CHIRP WAVEFORM DESIGN FOR WIRELESS COMMUNICATION, RADAR, AND ENERGY-HARVESTING SYSTEMS

Arijit Roy

CHIRP WAVEFORM DESIGN FOR WIRELESS COMMUNICATION, RADAR, AND ENERGY-HARVESTING SYSTEMS

A

Thesis Submitted

in Partial Fulfilment of the Requirements

for the Degree of

DOCTOR OF PHILOSOPHY

By

ARIJIT ROY

DEPARTMENT OF ELECTRONICS AND ELECTRICAL ENGINEERING

INDIAN INSTITUTE OF TECHNOLOGY GUWAHATI

GUWAHATI - 781039, ASSAM, INDIA

January, 2022

Declaration

I hereby declare that the thesis entitled "**Chirp Waveform Design for Wireless Communication, Radar, and Energy-harvesting Systems,**"submitted in the *Department of Electronics and Electrical Engineering, Indian Institute of Technology Guwahati, Assam, India*, for the award of the degree of **Doctor of Philosophy**, is a bonafide record of research work carried out by me under the supervision and guidance of Prof. Harshal B. Nemade and Prof. Ratnajit Bhattacharjee. The results embodied in this thesis are original and have not been submitted to any other University or Institute for the award of any degree or diploma.

Date: 11.01.2022

Place: Guwahati

Arijit Roy
Research Scholar
Department of Electronics and Electrical Engineering
Indian Institute of Technology Guwahati
Guwahati - 781039, Assam, India.

Certificate

This is to certify that the thesis entitled "**Chirp Waveform Design for Wireless Communication, Radar, and Energy-harvesting Systems,**" submitted by **Arijit Roy** (156102017), a research scholar in the *Department of Electronics and Electrical Engineering, Indian Institute of Technology Guwahati*, for the award of the degree of **Doctor of Philosophy**, is a record of an original research work carried out by him under our supervision and guidance. The thesis has fulfilled all requirements as per the regulations of the institute and in our opinion has reached the standard needed for submission. The results embodied in this thesis have not been submitted to any other University or Institute for the award of any degree or diploma.

Date: 11.01.2022

Place: Guwahati

Prof. Harshal B. Nemade **Prof. Ratnajit Bhattacharjee**

Department of Electronics and Electrical Engineering,

Indian Institute of Technology Guwahati,

Guwahati - 781039, Assam, India.

Dedicated to

My Parents

Acknowledgements

First and foremost, I feel it as a great privilege in expressing my deepest and most sincere gratitude to my supervisors Prof. Harshal B. Nemade and Prof. Ratnajit Bhattacharjee, for their excellent guidance throughout my PhD tenure. Their kindness, dedication and attention to the details have been a source of great inspiration to me. My heartfelt thanks to my supervisors for their unlimited support and patience that they have shown towards me. Their emphasis on clear communication helped me a lot. I cannot thank them enough for the patience shown by them while listening and clarifying my silliest of doubts. They have enriched my life in many significant ways. They have made an everlasting impression on my way of looking at problems, both professional and personal. I am grateful to them for providing an unbounded research environment. I thank them from the bottom of my heart for always being there with me during all kinds of distress.

I express my sincere gratitude to Dr. Salil Kashyap for assisting me with my research work in innumerable ways. His knowledge and experience have been a great boost for my research work. I am also thankful to Dr. Mahima Arrawatia for sharing her knowledge and providing valuable suggestions for my research.

I would also like to express my sincere gratitude to the members of doctoral committee members: Prof. Roy Paily Palathinkal, Prof. Rakhesh Singh Kshetrimayum, and Dr. Nagarjuna Nallam, for sparing time out of their busy schedule to evaluate my progress. They have enriched this work with their insightful suggestions and feedbacks. I extend my sincere thanks to all the staff members from EEE office and academic office for helping me out in all sorts of ways during my stay at IIT Guwahati.

During my PhD, I found really wonderful lab-mates and fellow research scholars. My lab-mates and research scholars of Communication Engineering Lab II Anoop P., Kaushik, Vijith, Sanjib, Mohit, and Rahul, have maintained the healthy and conducive lab environment necessary for good research. I had a great time with my many friends at IIT Guwahati including but not limited to Arijit Bhattacharjee, Pralay, Satyajit, Bikash, Chandan, Darpan, Manoranjan, Atanu, Aditya, Birjit, Arunangshu, Abhijit. These guys made my stay at IIT Guwahati memorable. I will cherish the time spent with them. I thank them all for their friendship. I also express my sincere thanks to my seniors Pawan Kumar, Prateek Rathore, Ramanand Sagar, and Sumantra Chaudhury for their encouragement and guidance.

My deepest gratitude goes to my family for their continuous love and support throughout my

studies. The opportunities they have given me and their unconditional sacrifices are the reasons where I am and what I have accomplished. My earnest gratitude and thanks to my parents to remain my source of inspiration in achieving every possible height during my journey. I extend my heartiest gratitude to my elder sister for her love and support. Finally, I would like to dedicate this thesis to my family, especially to my parents.

Arijit Roy

Abstract

A chirp waveform is a frequency modulated signal in which the signal duration and bandwidth can be adjusted independently. It finds applications in the fields of radar, sonar, and properties such as high processing gain, low power requirement, robustness to multipath interference make chirp based modulation an attractive alternative for wireless communication and Internet of Things (IoT) applications. Introduction of massive multiple-input multiple-output (MIMO) and 5G technologies make radio-frequency based wireless energy transfer (WET) a key enabling technique to effectively prolong operational lifetime of energy-constrained sensors. However, most works on WET are based on fixed-frequency waveform, and there exists scope to explore chirp waveform as a potential superior candidate. In this thesis, we perform an exhaustive study on the design of chirp waveforms and the analysis of associated systems employing the waveforms for wireless communication, radar, IoT, and WET applications. The design and analysis studies are broadly divided into three parts.

The first part covers chirp waveform design and system analysis for wireless communication where−
(i) Design of linear chirp (LC) waveform and a single user communication system based on surface acoustic wave (SAW)-chirp devices are proposed to transmit 3-bits per symbol duration. Symbol error rate (SER) performance of such system is analyzed under additive white Gaussian noise (AWGN) and Rayleigh fading channels, and its benefit over the available SAW-chirp systems is outlined.
(ii) Design of (a) phase-coded chirp waveforms using LC and nonlinear chirp (NLC) waveforms, and (b) a set of orthogonal up-chirp and orthogonal down-chirp waveforms are proposed to reduce multiple access interference (MAI) in a multiuser communication system where the later design minimizes bandwidth requirement as well. The performances of such systems are analyzed in terms of bit error rate (BER), for which closed form expressions are derived and evaluated over AWGN channel and over Rayleigh fading channel for (b).
(iii) We present a PSK-chirp-BOK system, to double the transmission rate while using only two correlators. Design of a set of completely orthogonal LCs is proposed to eliminate MAI in a multiuser system. Extending the design, a time domain multiplexing of orthogonal LC sets and associated signal demodulation using fractional Fourier transform are proposed to reduce the required system bandwidth. Analytical expressions of SER are derived for the system, and the associated performances evaluated under the effect of co-channel interference over Nakagami-m fading indicate a superior SER

performance over the reported chirp-BOK systems.

The second part covers chirp waveform design and system analysis for radar and IoT applications where−**(i)** Design of a set of discrete frequency-coding waveforms (DFCWs) using LC and pseudo-noise code sequence (DFCWs-PNLC) is proposed for MIMO and multiuser radar. A two stage optimization process is presented to improve autocorrelation sidelobe peak (ASP) and cross-correlation peak (CCP) levels of the waveforms. Analytical expressions of ambiguity functions are derived to analyze waveform performances, and it is observed that the DFCWs-PNLC outperforms other available DFCWs-LC. **(ii)** We propose a parameterized mathematical model for designing NLC waveform and present an optimization process based on genetic algorithm for appropriate selection of parameters value. Design of a set of DFCWs using parameterized NLC (DFCWs-NLC) is proposed for MIMO and multiuser radar, and a joint optimization of pulse type and frequency-ordering of DFCWs-NLC is performed that results in major improvement in ASP and CCP levels over the reported DFCW designs while attaining an increase in the number of available waveforms as well. **(iii)** Design of a new symmetry chirp waveform with multiple chirp rates (SC-MCR) is proposed for low-earth-orbit satellite IoT application. Extending the design, we present a time domain multiplexing of SC-MCR waveforms to improve the system data rate. For an M-ary system in a multiuser scenario, analytical expression for SER is derived and the system performance over a Rice-lognormal satellite channel indicates improved MAI as compared to SC waveform.

In the third part, the potential of chirp waveforms is investigated for downlink (DL) WET from a multi-antenna access point (AP) to a group of sensors over orthogonal subbands based on their channel estimates while maintaining the peak transmit power constraint. We propose a general design of chirp based waveforms and establish key properties required for optimizing WET. New analytical expressions using order statistics are derived for the average harvested energy based on DL-WET via superposed chirp waveforms, and max-min optimal power control coefficients in closed form are evaluated to ensure that the sensors placed at different distances from the AP harvest the same amount of energy. For comparison, we also present the corresponding analysis for fixed-frequency waveform. Furthermore, we analyze the max-min information transmitted on the uplink by the sensors. Through analysis and simulations, it is proved and elucidated that DL-WET via superposed chirp waveforms improves the max-min harvested energy, extends the operating range of WET, and widens the energy-information transfer region in comparison with DL-WET via fixed-frequency waveform.

Contents

List of Figures

List of Tables

List of Acronyms

AWGN	Additive White Gaussian Noise
ASP	Autocorrelation Sidelobe Peak
AP	Access Point
ASIC	Application Specific Integrated Circuit
ANLC	Asymmetric-type NLC
BER	Bit Error Rate
BOK	Binary Orthogonal Keying
BS	Base Station
CDMA	Code Division Multiple Access
CW	Continuous Wave
CCP	Cross-correlation Peak
CSI	Channel State Information
CSCG	Circularly Symmetric Complex Gaussian
CDF	Cumulative Distribution Function
CAF	Cross Ambiguity Function
DSP	Digital Signal Processor
DSSS	Direct-sequence Spread Spectrum
DPSK	Differential Phase Shift Keying
DQPSK	Differential Quadrature Phase Shift Keying
DFCW	Discrete Frequency-coding Waveform
DL	Downlink
DAF	Delay-Doppler Ambiguity Function
ETE	Energy Transfer Efficiency
EM	Electromagnetic

EH	Energy Harvesting
EU	Energy User
FM	Frequency Modulated
FPGAs	Field Programmable Gate Arrays
FDMA	Frequency Division Multiple Access
FHSS	Frequency-hopping Spread Spectrum
FMCW	Frequency Modulated Continuous Wave
FrFT	Fractional Fourier Transform
FER	Frame Error Rate
GA	Genetic Algorithm
HFH	Hyperbolic Frequency Hopping
IoT	Internet of Things
IFrFT	Inverse Fractional Fourier Transform
IDT	Interdigital Transducer
ID	Information Decoding
ICS	Interleaved Chirp Spreading
IU	Information User
LoRa	Long Range
LC	Linear Chirp
LFM	Linear FM
LTE	Long-Term Evolution
LPWAN	Low Power Wide Area Networks
LEO	Low-Earth-Orbit
MIMO	Multiple-Input-Multiple-Output
MAI	Multiple-Access Interference
MCR	Multiple Chirp Rates
MLW	Main-Lobe Width
MMSE	Minimum Mean Square Error
NLC	Nonlinear Chirp
NLFM	Nonlinear FM

NB	Narrow Band
NLOS	Non Line-of-Sight
NRZ	Non-Return-to-Zero
OFDM	Orthogonal Frequency Division Multiplexing
PAN	Personal Area Network
PDF	Probability Density Function
PS	Power-splitting
PSL	Peak Sidelobe Level
PN	Pseudo-noise
PSD	Power Spectral Density
PNLE	Polar NRZ Level Encoder
QPSK	Quadrature Phase Shift Keying
RF	Radio Frequency
RLS	Rice-Lognormal Satellite
SAW	Surface Acoustic Wave
SDMA	Space Division Multiple Access
SER	Symbol Error Rate
SNR	Signal-to-Noise Ratio
SINR	Signal-to-Interference-Plus-Noise Ratio
SF	Spreading Factor
SWIPT	Simultaneous Wireless Information and Power Transfer
SC	Symmetry Chirp
SISO	Single Input Single Output
S/P	Serial-to-Parallel
SNLC	Symmetric-type NLC
SEP	Symbol Error Probability
TDMA	Time Division Multiple Access
TS	Time-switching
TBP	Time-bandwidth Product
TDD	Time-Division-Duplexing

TDM	Time Domain Multiplexing
UL	Uplink
WPAN	Wireless Personal Area Network
WSN	Wireless Sensor Network
WET	Wireless Energy Transfer
WEIT	Wireless Energy and Information Transfer
WLAN	Wireless Local Area Network
WPT	Wireless Power Transfer
WIT	Wireless Information Transfer
WPCN	Wireless Powered Communication Networks

1

Introduction

Contents

A chirp is a frequency modulated (FM) waveform whose frequency varies with time [1]. Chirp waveform and associated pulse compression technique find wide applications in the field of radar, sonar and ultrasound [1, 2]. Advantages such as high processing gain, low power requirement, robustness to multipath interference and Doppler frequency offset make chirp based modulation an attractive alternative for wireless communication applications [3, 4], and recently, it has been successfully applied for LoRa (Long Range) communication intended for Internet of Things (IoT) applications [5]. It is also adopted as a physical layer implementation of IEEE 802.15.4a, the standard for wireless personal area network (WPAN) applications [6]. With the advent of wireless technologies such as massive multiple-input multiple-output (MIMO) and 5G, the operational lifetime of sensor nodes in an energy-constrained wireless sensor network (WSN) can be increased effectively through wireless energy transfer (WET) [7], and it holds enormous potential to power a massive number of IoT devices that are likely to get connected to the next generation wireless network [8]. It is expected that with appropriate design, chirp waveform can play an important role to address some of the design challenges associated with WET, and improve the harvested energy at the sensor nodes and energy transfer efficiency (ETE) of the WET system. In this thesis, we present chirp waveform designs for communication, radar, IoT, and wireless energy and information transfer (WEIT) systems to achieve an improved performance and analyze the associated systems to evaluate the corresponding improvements. In this introductory chapter brief overview of some of the associated technologies is presented to cover the background of the thesis. In the subsequent sections, a review on some of the available designs of chirp waveforms for the applications in communication, radar, and IoT systems along with the analysis of performance is presented followed by the discussion on some of the existing works on WET and WEIT. Thereafter, motivation, contribution, and organization of the thesis are outlined in this chapter.

1.1 Background

This section covers brief descriptions on chirp waveform, wireless communication and performance analysis, radar, IoT, WET, and highlights key properties of each of these technologies.

1.1.1 Chirp Waveform and Properties

A chirp is a waveform in which the instantaneous frequency varies as a function of time and it is categorized as up-chirp and down-chirp. For an up-chirp waveform, the instantaneous frequency

increases with time, while for a down-chirp signal the instantaneous frequency decreases with time [2]. A chirp waveform of unity amplitude and having a duration of T (in second) can be expressed as

$$s(t) = \cos\left[2\pi\phi(t)\right], \quad 0 \leq t \leq T, \tag{1.1}$$

where instantaneous frequency $f(t)$ of the waveform is defined as

$$f(t) = \frac{d\phi(t)}{dt}, \tag{1.2}$$

and the associated chirp rate $\mu(t)$ that defines the rate of change of instantaneous frequency [9] is given by

$$\mu(t) = \frac{df(t)}{dt}. \tag{1.3}$$

Therefore, for an up-chirp $\mu(t) > 0$ and for a down-chirp $\mu(t) < 0$. Based on the variation of chirp rate, chirp waveforms are primarily categorized as linear and nonlinear, i.e., for a linear chirp (LC) or linear FM (LFM) waveform, $\mu(t)$ remains constant throughout the signal duration whereas for a nonlinear chirp (NLC) or nonlinear FM (NLFM) waveform, $\mu(t)$ varies with time [1]. Following (1.1) and (1.2), instantaneous frequency for a linear up-chirp having bandwidth B (in Hz) [10] can be written as

$$f(t) = f_{\mathrm{L}} + \mu t, \tag{1.4}$$

where $B = f_{\mathrm{H}} - f_{\mathrm{L}}$, f_{L} is the starting frequency and f_{H} is the final frequency, and the chirp rate $\mu = \frac{B}{T}$ is a constant. Furthermore, the product of B and T is known as the time-bandwidth product of the chirp signal. Accordingly, the linear up-chirp waveform is given by

$$s_1(t) = \cos\left[2\pi\left(f_{\mathrm{L}}t + \frac{1}{2}\mu t^2\right)\right], \quad 0 \leq t \leq T. \tag{1.5}$$

Following similar steps a linear down-chirp waveform is expressed as

$$s_2(t) = \cos\left[2\pi\left(f_{\mathrm{H}}t - \frac{1}{2}\mu t^2\right)\right], \quad 0 \leq t \leq T. \tag{1.6}$$

In case a chirp signal is centered at $t = 0$, linear up-chirp and down-chirp waveforms are given by

$$s_i(t) = \cos\left[2\pi\left(f_0 t + (-1)^{(i-1)}\frac{1}{2}\mu t^2\right)\right], \quad -\frac{T}{2} \leq t \leq \frac{T}{2}, \tag{1.7}$$

where f_0 is the center frequency and $i = 1, 2$. $s_1(t)$ and $s_2(t)$ denote the up-chirp and down-chirp waveforms, respectively. Moreover, in equivalent complex form the chirp waveforms of (1.7) can be

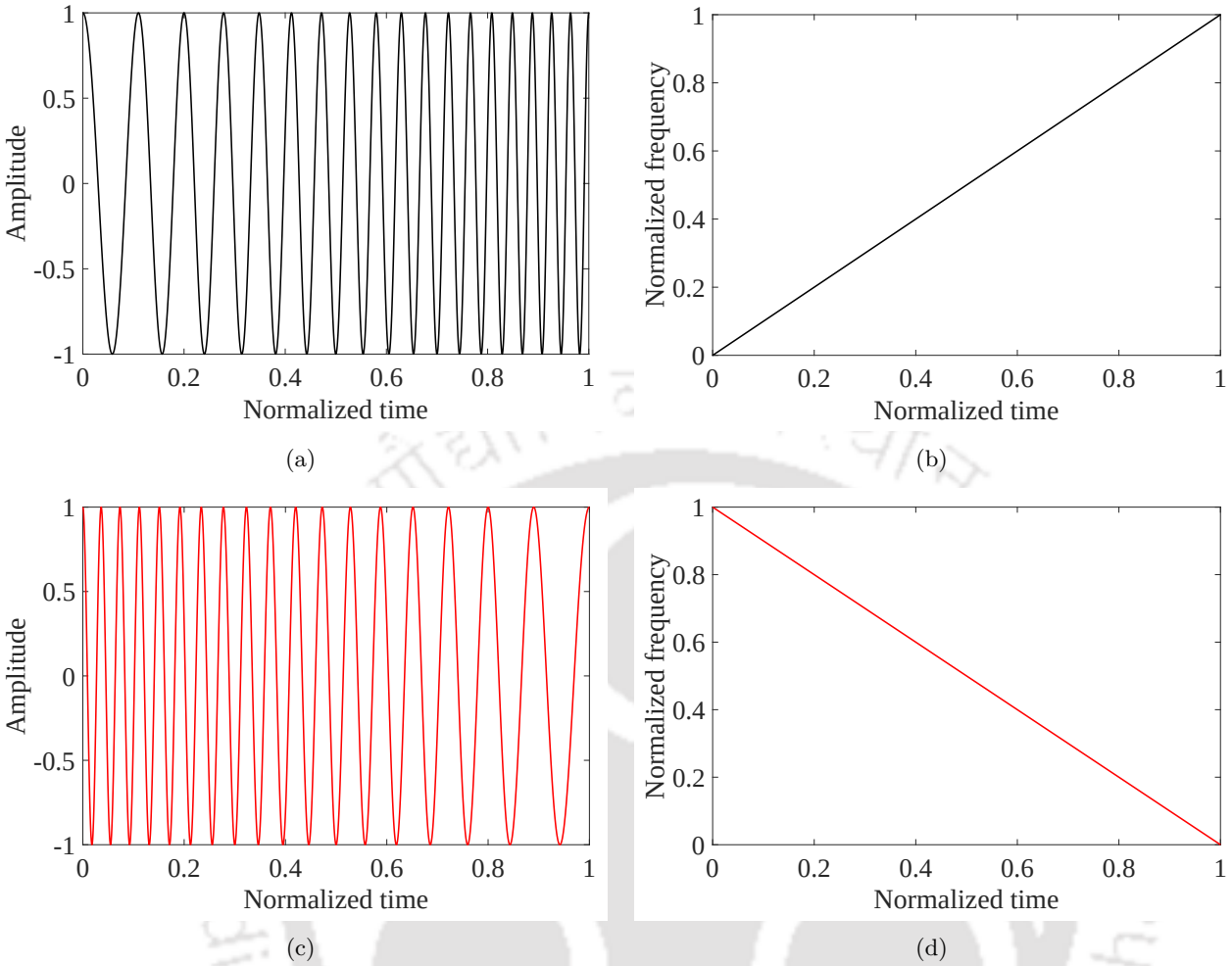

Figure 1.1: (a) Linear up-chirp waveform, (b) Instantaneous frequency variation for up-chirp, (c) Linear down-chirp waveform, (b) Instantaneous frequency variation for down-chirp.

given by [1]

$$\breve{s}_i(t) = e^{j2\pi\left(f_0 t + (-1)^{(i-1)}\frac{1}{2}\mu t^2\right)}, \quad -\frac{T}{2} \leq t \leq \frac{T}{2}, \tag{1.8}$$

and $s_i(t) = \Re\{\breve{s}_i(t)\}$ where $\Re\{\cdot\}$ indicates the real part. A linear up-chirp and the associated frequency variation of the waveform with time are shown in Figure 1.1(a) and Figure 1.1(b), respectively, while a linear down-chirp and its plot of instantaneous frequency versus time are shown in Figure 1.1(c) and Figure 1.1(d), respectively, where the chirp rate is considered as $\mu = 35$.

Matched filtering of a chirp waveform gives an output signal with a narrow peak at the chirp center frequency [1, 9] and thereby achieving the pulse compression. Further, the same output can also be achieved through auto-correlation of the chirp waveform [1,10]. Pulse compression, a signal processing technique, of a chirp waveform allows to accumulate the energy of the signal into a short pulse with

amplification in amplitude. It improves the range resolution and detection capability which is one of the main reasons chirp waveforms are widely used in radar applications. Given two signals $x(t)$ and $y(t)$, the associated correlation between them can be expressed as [11]

$$R'_{xy}(\tau) = \int_{-\infty}^{+\infty} x(t)y(t-\tau)dt. \tag{1.9}$$

Further, for a LC waveform given by (1.8), the correlation between up-chirp and down-chirp waveforms [1, 11] can be written in complex form as

$$R_{s_1s_2}(\tau) = \int_{-\infty}^{+\infty} \breve{s}_1(t)\breve{s}_2^*(t-\tau)dt, \tag{1.10}$$

where $(\cdot)^*$ denotes the conjugate operation, and $R'_{s_1s_2}(\tau) = \Re\{R_{s_1s_2}(\tau)\}$ gives the cross-correlation between $s_1(t)$ and $s_2(t)$. Setting $\breve{s}_2(t) = \breve{s}_1(t)$, (1.10) gives the autocorrelation output.

For a LC waveform given by (1.8), the autocorrelation output [1, 11] for up-chirp can be written in complex form using (1.10) as

$$\begin{aligned} R_{s_1s_1}(\tau) &= \int_{-\infty}^{+\infty} \breve{s}_1(t)\breve{s}_1^*(t-\tau)dt \qquad (1.11)\\ &= \int_{-\infty}^{+\infty} e^{j2\pi f_0\tau}e^{-j2\pi\frac{\mu}{2}\tau^2}e^{j2\pi\mu t\tau}dt = e^{j2\pi f_0\tau}e^{-j\pi\mu\tau^2}\int_{-\infty}^{+\infty} e^{j2\pi\mu t\tau}dt \\ &= (T-|\tau|)\,e^{j2\pi f_0\tau}\mathrm{sinc}[\mu\tau\,(T-|\tau|)], \qquad (1.12)\end{aligned}$$

where $|\tau| \leq T$, sinc$(\cdot)$ is the sinc function [1], and the autocorrelation of $s_1(t)$ is given by $R'_{s_1s_1}(\tau) = \Re\{R_{s_1s_1}(\tau)\}$. The associated output is shown in Figure 1.2(a) which indicates a sharp peak at $\tau = 0$. For down-chirp, its autocorrelation is identical to that of up-chirp [1] and is given by (1.12). Similarly, the cross-correlation between up-chirp and down-chirp waveforms [1] can be calculated using (1.10) as

$$\begin{aligned} R_{s_1s_2}(\tau) &= \int_{-\infty}^{+\infty} e^{j2\pi f_0\tau}e^{j2\pi\frac{\mu}{2}\tau^2}e^{j2\pi\mu t^2}e^{-j2\pi\mu t\tau}dt = e^{j2\pi f_0\tau}e^{j2\pi\frac{\mu}{2}\tau^2}e^{-j\frac{\pi}{2}\mu\tau^2}\int_{-\infty}^{+\infty} e^{j\frac{\pi}{2}\left[2\sqrt{\mu}t-\frac{\mu\tau}{\sqrt{\mu}}\right]^2}dt \\ &= \frac{1}{2\sqrt{\mu}}e^{j2\pi f_0\tau}e^{j\frac{\pi}{2}\mu\tau^2}\left[C'(\nu_2)+jS'(\nu_2)-C'(\nu_1)-jS'(\nu_1)\right], \qquad (1.13)\end{aligned}$$

where $|\tau| \leq T$, $\nu_2 = \sqrt{\mu}\,(T-|\tau|)$, $\nu_1 = \sqrt{\mu}\,(-T+|\tau|)$, $C'(u)$ and $S'(u)$ are Fresnel integrals [10], and $R'_{s_1s_2}(\tau) = \Re\{R_{s_1s_2}(\tau)\}$ gives the cross-correlation between $s_1(t)$ and $s_2(t)$. The associated unmatched output is shown in Figure 1.2(b) where value is normalized to maximum autocorrelation output.

Based on the application, chirp waveforms can be generated in different ways. Chirp waveforms can be generated using a surface acoustic wave (SAW) device. Advances in SAW technology offer a

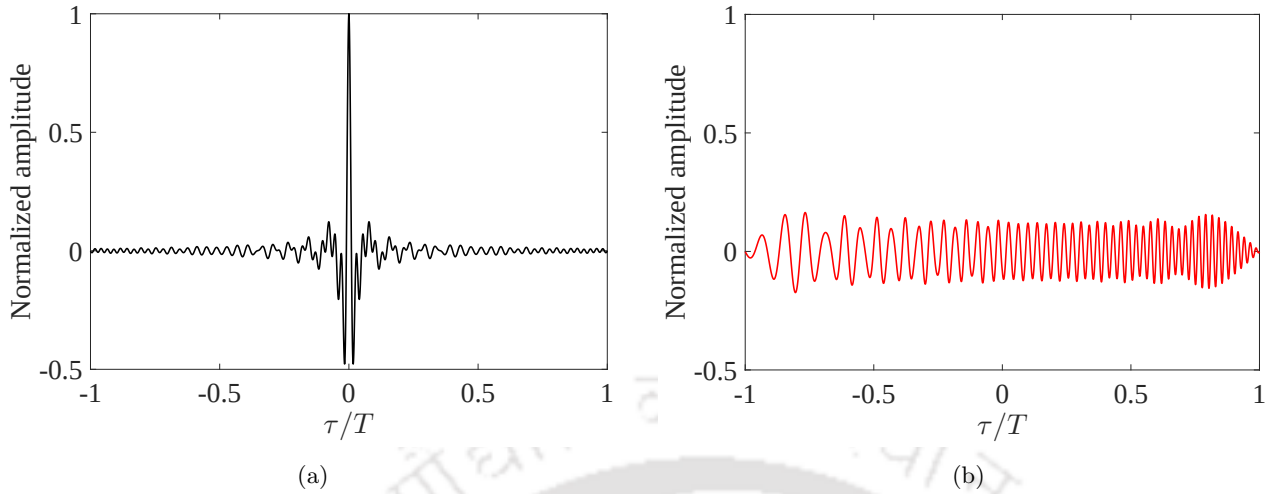

Figure 1.2: (a) Autocorrelation of LC waveform, (b) Cross-correlation between linear up-chirp and down-chirp waveforms.

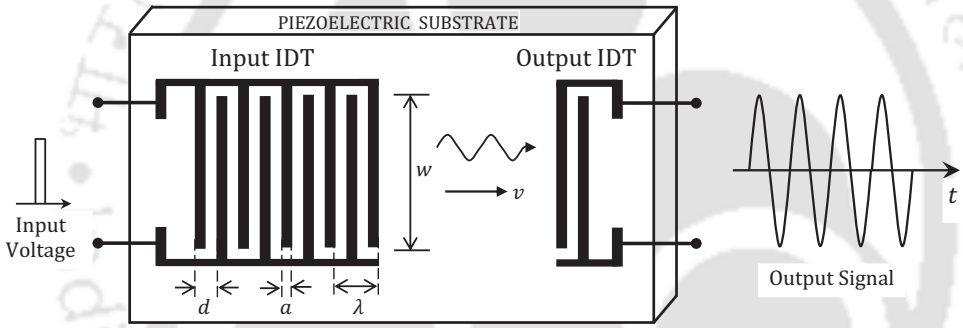

Figure 1.3: Block diagram of a basic SAW device.

rapid and efficient method for both generation and correlation of the chirp waveforms using completely passive and low cost SAW-chirp devices. The generation of chirp waveforms can also be realized using digital signal processor (DSP) or field programmable gate arrays (FPGAs) [12] which provides higher design flexibility over SAW device. In the thesis we consider ideal chirp waveforms for the proposed waveform designs and the analysis of the systems.

In its simplest form, a SAW device consists of two comb-like metal electrodes known as input interdigital transducer (IDT) and output IDT, placed on a piezoelectric substrate [13] as shown in Figure 1.3. When a radio frequency (RF) voltage is applied at the input IDT, acoustic waves are generated due to inverse piezoelectric effect [13]. The acoustic waves propagate on the substrate and reach the output IDT. At the output, the mechanical displacement caused by the acoustic waves generates a voltage difference due to the piezoelectric effect and produces an electric wave at the

output IDT. So, the second comb-like structure in the SAW serves as a transducer to convert the acoustic waves back into an electromagnetic signal. For an IDT structure having electrodes with uniform pitch (d), the associated wavelength λ of the acoustic wave is related as $d = 2a = \frac{\lambda}{2}$, and this provides ideally a waveform having a fixed-frequency with $\lambda = \frac{v}{f}$ where v is the acoustic wave velocity through the piezoelectric substrate, f is the frequency of RF signal, a is the electrode width, and w is the aperture [13]. However, by varying the pitch d along the length of the IDT structure, i.e., by progressively increasing or decreasing the electrodes width of input IDT, the output waveform can have frequency varying during its propagation time, thereby obtaining a chirp waveform [13, 14].

1.1.2 Wireless Communication and Performance Analysis

Wireless communication involves the transmission of information from one point to another wirelessly, i.e., without the use of any electrical wire connections. One of the most commonly used medium for enabling wireless communication is radio waves [15]. Wireless communication provides several advantages over the wired communication, e.g., it offers greater flexibility, allows constant connectivity and improves network speed, provides easy accessibility specially in remote areas, improves cost effectiveness of the network etc., and it has a vast range of applications in the fields of telecommunications, military, space, radar communication, IoT, and wireless power transmission. Wireless communication can be of two types− analog and digital. In analog communication the information signal modulates the carrier waveform by varying the amplitude, phase, and frequency. Amplitude modulation and frequency modulation are the most common form for the analog signal transmission. In digital communication, continuous-time analog signal is sampled and quantized in form of binary numbers, '0' and '1', which gives the digital signal, and the information is transferred in the form of amplitude, phase, or frequency of the carrier waveform. Advantages of digital communication over analog counterpart include− (i) more immunity to noise and external interference, (ii) easy storage and retrieval of digital information, (iii) higher security to the information, (iv) easier implementation of error correction and detection techniques, (v) cost effective and more reliable. Depending on the distance of communication, the operational range and type of devices used, current wireless communication systems and technology are categorized into different types such as (i) cellular communication systems, (ii) wireless local area network (WLAN) systems, (iii) wireless internet and other personal area network (PAN) systems, (iv) satellite communication systems, (v) low-cost, low-power wireless communication systems: Bluetooth and Zigbee [16]. Based on the application requirements, these systems are supported

by a number of transmission and multiple access technologies including frequency division multiple access (FDMA), time division multiple access (TDMA), code division multiple access (CDMA), space division multiple access (SDMA), different spread-spectrum technologies, e.g., direct-sequence spread spectrum (DSSS), frequency-hopping spread spectrum (FHSS), and other multi-carrier technologies to serve multiple user terminals and achieve the required system throughput.

During transmission, if the signal is affected by noise only, the associated channel is considered as additive white Gaussian noise (AWGN) channel. Whereas, if the signal, transmitted over wireless medium, gets affected by both noise and fading, the associated channel is considered as a fading channel. Fading indicates to the attenuation and distortion of the transmitted signal power during wireless propagation and categorized as large-scale and small-scale fading. Large-scale fading refers the power dissipation and attenuation in the received signal, and can be of two types: (i) path loss, which attenuates the power of the received signal due to propagation over a long distance, (ii) shadowing, which delineates the reduction in power of received signals due to the obstructions in the path of propagation. Small-scale fading refers to the fluctuations in signal strength and phase due to scattering, reflection, and diffraction of a signal during propagation and causes the reception of multiple replicas (or multipaths) of the signal at the receiver. Depending on the mobility of the transmitter/receiver with respect to each other, small-scale fading can be categorized as fast fading and slow fading. In fast fading channel condition varies rapidly, whereas in slow fading the channel experiences relatively slow variation over the symbol duration. Depending on the effect on signal frequency, small-scale fading can be further categorized as frequency-flat and frequency-selective fading. In case all frequency components of the signal observe almost the same amount of fading, it is termed as frequency-flat fading otherwise it is called frequency-selective fading.

Performance analysis process of a wireless communication system is broadly divided into two categories and can be performed either following a communication theoretic approach that includes evaluation of bit error rate (BER), symbol error rate (SER) etc., or following an information theoretic approach that includes evaluation of outage probability, channel capacity etc. Average BER or SER indicates the ratio of the number of erroneous bits or symbols detected at the receiver to the total number of transmitted bits or symbols. On the other hand, outage probability indicates the probability that the signal-to-noise ratio (SNR) level of the signal falls below a predetermined threshold, while channel capacity refers to the maximum data rate at which information can be transferred over a

communication channel with minimal probability of error. In this thesis, performance analysis of the communication systems using chirp waveforms is carried out in terms of BER, SER, and channel capacity.

1.1.3 Radar

Radar stands for radio detection and ranging and it performs operations such as detection, tracking, and recognizing objects, to name a few, for both civilian and military applications [17]. It works by transmitting RF electromagnetic (EM) signal towards a object, commonly known as the target, and studying the echo or waves reflected back from the target. The basic principle of a radar is shown in Figure 1.4. The radar signal, an RF EM wave, is produced at the transmitter. Output of the transmitter is delivered to the antenna where the signal is radiated. Use of a duplexer allows the same antenna to be used for both transmitter and receiver on a time sharing basis. After reception, the receiver amplifies the radar echoes and transfers them to the signal processing module. The processing block performs signal processing operations and decides whether a target is present or not (target detection). In case a target is present, other information about the target, i.e., range is estimated. If a target is present at a distance of D_o from the radar and the transmitted signal has taken time T_r to travel from radar to target and back to radar, then [17]

$$2D_o = C_o \times T_r \quad \Rightarrow \quad D_o = \frac{C_o T_r}{2}, \tag{1.14}$$

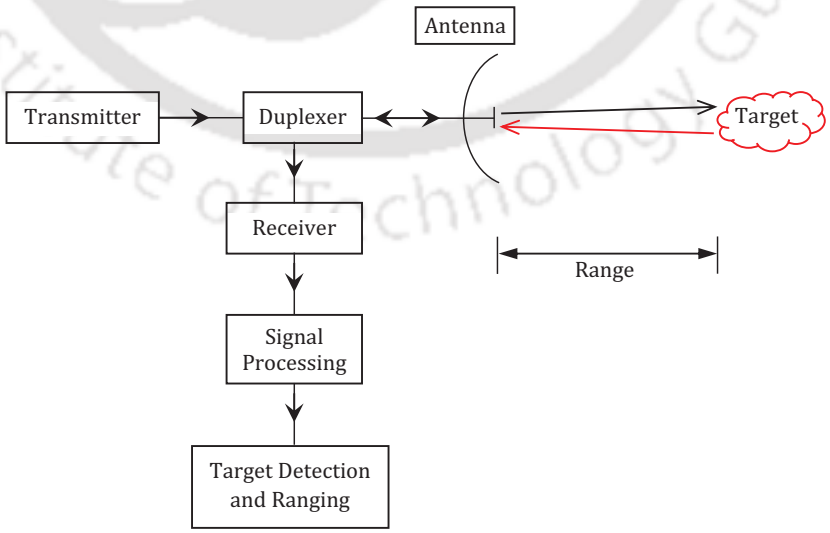

Figure 1.4: Block diagram of a pulse radar.

where C_o denotes the speed of light.

Performance of the radar systems mostly depends on the radiated waveforms, and thereby appropriate design of the radar waveforms is crucial for faithful detection of the targets [1, 11]. Based on the type of waveforms, radars are classified into pulse radar and continuous wave (CW) radar. As the name suggests, pulse radar operates with pulse type waveforms and CW radar operates with continuous waveforms. In case a CW radar incorporates frequency modulation for the design of the waveform, then the radar is termed as frequency modulated continuous wave (FMCW) Radar. Thereby, signal frequency for a FMCW radar varies with time, e.g., a chirp waveform [10, 17]. Use of FMCW in radar provides following advantages over CW (i) it can measure the target range and relative velocity simultaneously, (ii) it can determine very high accuracy of range measurement, (iii) it can operate with low peak power, (iv) it simplifies the realization of signal processing circuits as the processing can be performed at low frequency range. Therefore, chirp is a popular choice and is used widely for the design of radar waveforms [1, 10, 17]. Moreover, based on application requirements, different waveform modulation patterns through FMCW such as sawtooth modulation, triangular modulation, stepped modulation [1, 11] can be designed to attain an improved detection performance.

1.1.4 Internet of Things

The Internet of Things refers to a system of interrelated, internet-connected objects− sensors and devices, or "things", that have the ability to collect and transfer data over a wireless network without requiring human-to-human or human-to-computer interaction. With the emerging numerous new IoT applications spread across the areas of consumer and commercial to industrial and infrastructure including applications such as (i) smart home, (ii) wearables, (iii) smart cities, (iv) smart grids, (v) autonomous vehicles, (vi) industrial automation, (vii) smart retail and supply chain, and (viii) smart farming [18], thereby it is expected that more and more devices and sensors are to be connected to IoT networks and the number will exceed 20.4 billion by 2022 [19] as IoT offers numerous advantages including (i) easy monitoring and communications between devices, (ii) digitally and centrally controllable automation, (iii) improved system efficiency and operational time etc.

A number of wireless technologies have emerged for enabling the above mentioned IoT applications, and based on the coverage range the technologies are broadly categorized into two types− (i) short-range wireless technology, (ii) long-range wireless technology. Short-range technologies include Bluetooth, Zigbee, and WiFi, and intended to cover a maximum range of 100 m. Long-range technolo-

gies include LTE and 5G, and low power wide area networks (LPWAN) technologies [20]. While LTE and 5G are intended for power and data intensive applications, LPWAN technologies are intended to provide wide-area communications and large-scale connectivity for emerging IoT applications with low power, low cost, and low data rate devices. Further, LPWAN are divided into unlicensed and licensed LPWAN based on the operating spectrum resources (bands). LoRa and Sigfox technologies come under unlicensed LPWAN, whereas LTE-M and NB-IoT technologies come under licensed LPWAN [20].

Out of different enabling technologies for low power IoT networks, here, it is of particular interest to LoRa as it provides the following advantages over other LPWAN technologies for IoT– (i) reduced cost of deployment, since unlicensed bands are used, (ii) higher flexibility in terms of data rate and bidirectional communication over Sigfox, (iii) better security and mobility. Furthermore, LoRa performs signal modulation and demodulation employing chirp waveform [5] that spreads the signal over a wider channel bandwidth. It enables the transmitted waveform to become highly interference resilient and reduces the required signal-to-interference-plus-noise ratio (SINR) level for accurate data decoding, thereby improving the overall energy efficiency of the system [18]. LoRa supports a spreading factor (SF) from 7 to 12, which allows the system to achieve a variable data rates and tradeoff between throughput and coverage range or energy consumption [20].

1.1.5 Wireless Energy Transfer

The evolution and progress in silicon technology have helped reduce the power consumption and the size of wireless sensor nodes. Usually, these nodes are energy constrained because they depend on their batteries, which have limited capacity, to perform specific tasks in a wireless network. A convenient way to increase the lifetime of these sensors is by charging their batteries through WET [7]. WET is the transmission of energy from one place to another without wires. Nikola Tesla pioneered high-voltage, high-frequency electricity in wireless power transmission in his Colorado Springs lab in 1899 [21]. WET or wireless power transfer (WPT) is attractive and promising as it can provide seamless, constant and controllable on-demand energy to energy-constrained nodes and it provides a reliable way to energize nodes which may be placed at remote or hazardous locations. It does not require any intermediate grid for connections and can provide both non line-of-sight (NLOS) and LOS energy transfer at low maintenance cost. WET, also known as wireless charging, mainly falls into two categories, near field and far-field. For near field, non-radiative wireless charging based on inductive

coupling and capacitive coupling is used for energy transfer, whereas for far-field, radiative wireless charging based on electromagnetic waves, i.e., typically RF waves or microwaves are used for energy transfer [21].

Use of RF signal offers following advantages over non-conventional sources of energy: (i) the signal is controllable and can provide a deterministic energy harvesting method, i.e., based on the energy requirement, the transmit power level of the signals can be adjusted dynamically, and (ii) both information and power can be transferred simultaneously, independently or jointly. Thus, WET via RF signal can enable wirelessly powering energy-constrained nodes placed at a longer distance while effectively prolonging the operational lifetime and makes it more attractive for WSN. Electromagnetic energy carried via RF signal can be converted into electrical energy by employing rectenna at the energy-constrained nodes. Rectenna is basically formed by concatenating antenna and rectifier [22]. The received RF signal at the antenna is processed through a rectifier, which comprises of a diode, a low pass filter, and load, and converts the received RF signal into DC voltage. Integration of WET and conventional wireless information transfer (WIT) in a communication network is categorized into simultaneous wireless information and power transfer (SWIPT) networks and wireless powered communication networks (WPCN) [23] and it enables the wireless devices to perform simultaneous energy harvesting (EH) and information decoding (ID) using two practical receiver designs based on power-splitting (PS) and time-switching (TS) protocols [24]. Further, EH and usage techniques are broadly categorized into three protocols− harvest-use, harvest-store-use, and harvest-use-store [21]. In harvest-use technique, the incoming energy is directly used to power the communicating node and harvested energy is not buffered for future use. In harvest-store-use technique, harvested energy is first stored in a buffer and communication is initiated once a minimum amount of required energy is accumulated. In harvest-use-store technique, a fraction of the harvested energy is used to power the communicating node while the remaining energy is stored in a buffer for future use.

1.2 Literature Review

In this section, related works on the design of chirp waveform for the applications of communication, radar, and IoT are presented followed by the discussion on some of the reported waveform designs for WET and WEIT applications.

1.2.1 Chirp Waveform for Communication Applications

The use of chirp waveform for wireless communication applications was introduced by Winkler in 1962 [25]. Chirp communication system employing direct modulation scheme through up-chirp waveform has been presented in [26–30]. In particular, design and performance analysis of a single user chirp communication system using SAW-chirp delay line has been considered in [26–28] where transmission of 1 bit per symbol duration through differential phase shift keying (DPSK) modulation is presented in [26] and transmission of 2 bits per symbol duration through differential quadrature phase shift keying (DQPSK) and $\pi/4$-DQPSK modulation is presented in [27] and [28], respectively. All the systems in [26–28] have used a single LC waveform for data transmission. In [29], the authors have designed a single user chirp communication system considering DQPSK modulation and evaluated the system performance in presence of broadband jamming signal. The results indicate that chirp waveform can provide improved performance over a conventional system (without incorporating chirp). In [30], the authors have designed a single user chirp system with quadrature phase shift keying (QPSK) modulation and analyzed the performance. As the reported systems are designed and analyzed only for single user scenario, the effect of interference on the system performance remains unaddressed.

Chirp communication system employing binary orthogonal keying (BOK) scheme, where the transmitter consists of a pair of chirp waveforms– one up-chirp and one down-chirp mapped to binary '1' and binary '0', respectively for transmission of 1 bit per symbol, and the receiver consists of a pair of correlators for estimation of the symbol, has been presented in [6, 9, 31] for a single user and in [3, 25, 32–35] for multiuser systems. Specifically, in [6], the authors have shown that chirp-BOK improves the BER performance over conventional BOK system. The authors in [9] have presented a chirp-BOK system with a overlap between the transmitted up-chirp and down-chirp waveforms to improve data rate at the expense of overall increase in signal interference at the receiver. A chirp-BOK system using nonlinear quadratic chirp has been presented in [31] for underwater communication. The authors in [25] have designed a set of LCs with each chirp waveform having two different chirp rates for different time intervals while covering the same bandwidth, and each user has been allocated a pair of up-chirp and down-chirp waveforms. Since all the generated chirp signals occupy the same bandwidth are non-orthogonal, multiple-access interference (MAI) increases with the increase in the number of users. The authors in [32] have extended the design in [25] by combining the waveforms with the frequency hopping scheme. With the objective of reducing MAI, in [3], the authors have designed a

set of LC waveforms having the same initial frequency but different chirp rates for different users, and each user has been equipped with a pair of up-chirp and down-chirp waveforms. However, for both the designs in [3, 32], the system bandwidth is a function of the number of users resulting in higher bandwidth requirement. Moreover, owing to the fixed waveform duration and different chirp rates, time-bandwidth product (TBP) of the waveforms in [3] is different for each user and the signals with lower TBP are affected more by interference. In [33], the authors have extended the waveform designs of [25] and [3] to form a multilinear chirp signal and presented a waveform detection technique based on fractional Fourier transform (FrFT) for underwater acoustic sensor networks. The authors have extended the design of [3] for NLC waveforms in [34] for quadratic and exponential chirp waveforms, and in [35] for trigonometric and hyperbolic chirp waveforms.

To increase the data rate, the BOK transmission scheme has been extended to an M-ary data transmission using chirp modulation in [4, 36–38] where the receiver uses M correlators for the estimation of the transmitted symbol. The authors in [4] have presented a single user M-ary chirp communication system using LC modulation for coherent and non-coherent data transmission scheme, whereas, in [36] and [37] the authors have presented the performance of a single user M-ary LC communication system over different fading channels− frequency-selective and -nonselective fading channels, respectively. In [38], the authors have presented a single user M-ary chirp communication system using nonlinear hyperbolic frequency modulation for mobile underwater communication. However, the increased data rate for the M-ary systems has been achieved at the expense of increased system complexity, bandwidth and inter-chirp interference.

1.2.2 Chirp Waveform for Radar Applications

Design of radar waveforms having properties such as good Doppler tolerance, large TBP, low sidelobe level is necessary to achieve good range-resolution for the faithful detection of the target [1]. Further, the signals designed for MIMO and multiuser radar systems [39, 40] should maintain low cross-correlation levels as well as low autocorrelation sidelobe levels to enhance the detection performance. For this purpose, construction of radar waveforms through frequency diversity technique, i.e., discrete frequency-coding waveform (DFCW) has attracted much attention in recent years as it offers higher range-resolution with improved detection capability [39]. Design of DFCW involves the use of subpulses of different frequencies through a frequency hopping technique and the subpulse can be of fixed-frequency type or chirp type [39]. Various methods have been proposed for designing

discrete frequency-coding waveforms (DFCWs) to attain radar waveform diversity.

Design of DFCW with fixed-frequency pulses (DFCW-FF) for radar applications and associated performance have been presented in [40] for multiuser radar and in [41–44] for MIMO radar systems. In [40], Costas code has been used to determine the sequence of frequency hopping of the subpulses for the designed DFCW-FF and the subpulse coding has been performed through a process of cyclic shifting to maintain an acceptable cross-correlation peak (CCP) level. In [41], the authors have designed DFCWs-FF for netted radar systems where a simulated annealing algorithm based on statistical optimization technique has been presented for the optimization of the frequency hopping sequences. In [42], the authors have designed DFCWs-FF where the frequency firing order is optimized numerically through a genetic algorithm (GA). In [43], the authors have combined DFCW-FF with phase coding to improve peak sidelobe level (PSL) compared to traditional DFCW-FF. In [44], the authors have designed DFCW-FF with phase randomization of the subpulses that provides better autocorrelation sidelobe peak (ASP) and CCP performance over waveforms with polyphase sequences [45].

Chirp waveform offers favourable Doppler tolerance, large TBP, and therefore, is widely used for the design of radar waveforms [1, 39], and combining chirp with DFCW, the advantages of both DFCW and chirp can be reaped for the design of radar waveforms. Design of DFCW using LC subpulses (DFCW-LC), for automotive radar application, under the constraints of radar size and power has been presented in [46]. In [47], the authors have designed a DFCW-LC where the subpulses are composed of LC waveforms having random frequencies to improve the anti-jamming capability. Associated random sequences are generated through a Bernoulli map. Designs of DFCWs-LC to attain waveform diversity for MIMO radar have been presented in [39,48,49]. Specifically, in [39], the authors have designed a set of three DFCWs-LC where the associated frequency hopping sequences have been optimized through GA. Use of LC over fixed-frequency pulse improves the ASP and CCP levels as compared to DFCWs-FF. In [48], the authors have designed three pairs of DFCWs-LC, independently, for MIMO-SAR application. The formation of the LC subpulses in the DFCW has been decided by the entries of a random binary matrix. Although CCP performance of the waveforms in each pair has been reported, performance among different pairs remains unaddressed. The authors in [49] have designed a set of DFCWs using piecewise LC waveforms (DFCW-PWLC) with the objective of improvement in Doppler tolerance performance. However, the waveforms exhibit large CCP levels and limit their effectiveness.

Design of radar waveform using NLC improves the PSL performance over LC without using window functions or mismatch filtering which incurs loss in SNR at the receiver [50, 51]. Designs of DFCWs using NLC subpulses (DFCWs-NLC) for MIMO radar have been presented in [52, 53]. In [52], the authors have considered a nonlinear pulse based on *tan-sec* function for the design of DFCW-NLC. A set of three DFCWs-NLC has been designed for which the associated frequency hopping sequences are optimized using GA and the use of NLC has improved the ASP and CCP performances over DFCWs-LC. In [53], the authors have designed a set of four DFCWs-NLC using a tangential-type pulse where the duration of each pulse and its bandwidth have been kept asymmetric, and the associated frequency hopping sequences are optimized numerically to reduce the ASP and CCP levels. Although partial CCP performance between the first waveform with others combined has been presented, pairwise performances are not analyzed. Moreover, the design process has become complex with the increasing number of waveforms or number of subpulses, and it would limit the applicability of the waveforms.

1.2.3 Chirp Waveform for IoT Applications

Interconnectivity between systems through Internet of Things is gaining popularity around the world. The concept of IoT involves the interconnection of physical objects and is characterized by low power consumption, low data rate, ability to collect and transmit data. Chirp waveform has been successfully applied to design LoRa-based modulation intended for IoT applications for wide area networks [5]. In LoRa modulation, chirp waveform is used to design an M dimensional orthogonal signaling space by performing a cyclic shift of the linearly increasing waveform to transmit M-ary information where the associated SF determines M. The design and analysis of LoRa system have been presented in [5, 54–57]. In particular, the authors in [54] have derived the BER performance for a LoRa system over both AWGN and Rayleigh fading channels. In [55], the authors have analyzed the link-level performance of LoRa system while considering imperfect orthogonality between different SFs. In [56], the effect of frequency offset in the chirp waveform on the performance of LoRa system has been analyzed for different SF designs. The authors in [5] have designed an interleaved chirp spreading LoRa (ICS-LoRa) to enhance the data rates of LoRa-based LPWAN. An approximate BER expression has been derived to evaluate the capacity improvement for the LoRa networks. In [57], the performance of LoRa has been examined under AWGN channel and in presence of an interfering signal that is neither chirp nor phase-aligned with the target waveform for which the authors have derived SER and frame error rate (FER). In addition, an approximation for both SER and FER have

also been derived to reduce the computation complexity at the expense of performance degradation.

While the reported LoRa IoT systems have been performed for terrestrial communications only, in [58] the authors have shown that LoRa chirp waveforms are not suitable for the application of low-earth-orbit (LEO) satellite IoT communication due to high cross-correlation between the chirps with different starting frequencies. To minimize the cross-correlation, the authors have designed chirp waveforms that are symmetric in nature, i.e., symmetry chirp (SC), and the associated analysis has shown improved performance over LoRa chirp waveform. In addition, the authors have presented an acquisition method for SC waveforms in LEO satellite IoT communication in [59]. However, the cross-correlation performance of SC waveforms in a multiuser or an M-ary system is currently unavailable as only one pair of SC waveforms has been considered in [58] for a single user system. Therefore, the suitability of SC waveforms in presence of interference requires further investigations.

1.2.4 Waveform for WET Applications

In communication networks, such as WSNs, body area network, some nodes are not physically accessible in order to recharge or replace batteries. Operational life time of these sensor nodes depends on batteries and it can be increased through WET [7]. RF signal provides a convenient way to perform WET, in conjunction with information transfer over the same RF medium, in order to prolong the operational life time of the sensors.

Design of a SWIPT system via fixed-frequency single carrier with single antenna transmitter and receiver has been considered in [60, 61] assuming perfect channel state information (CSI). In [60], the authors have investigated the energy-information rate trade-off based on a dynamic PS scheme. In [61], the authors have studied transmit waveform optimization in a time-slotted SWIPT system, while considering a nonlinear EH model, to maximize the energy-information rate region in a network with both information users (IUs) and energy users (EUs). Use of multiple-antennas at the transmitter provides a promising way to improve the ETE, through spatial beamforming, over single antenna system [62]. Designs of WET, wireless energy and information transfer (WEIT), and SWIPT systems using fixed-frequency single carrier with multiple-antennas at the transmitter have been presented in [63–66]. In particular, the authors in [63] have proved that the effective range of WET can be improved through the use of massive number of antennas at the base station (BS) while maintaining a fixed target probability of outage in WET. The authors in [64] have obtained the optimal duration for channel estimation and WET to maximize the minimum information rate in a wireless powered

communication network with massive number of antennas at the BS. In [65], the authors have presented a massive MIMO simultaneous WEIT system to maximize the energy harvested by the EUs while maintaining the target data rate for IUs. The authors in [66] have designed a SWIPT system with massive number of antennas at the BS to obtain the max-min optimized rate-energy region for TS and PS protocols.

Use of multisine waveform [67], consisting of a set of fixed-frequency sinusoidal signals, having the same phase (e.g., 0°) improves the harvested energy over single carrier signal by enhancing the DC power level obtained from the received RF signal. Further, replacing multisine signal with orthogonal frequency division multiplexing (OFDM) which comprises of a set of fixed-frequency signals, transfer of both energy and information can be made over the same RF medium. Design of single input single output (SISO)-SWIPT system using OFDM based subcarrier set has been presented in [24, 68, 69]. The authors in [68] have considered PS protocol with continuous and discrete PS ratios to optimize the energy efficiency for the data communication while assuming perfect CSI at the receivers. However, acquiring CSI and its feedback to the transmitter would increase receiver complexity, energy requirement and limit the operational span. Assuming perfect CSI, the authors in [24] have obtained the transmit power policy to maximize the sum data rate subject to a constraint on the energy harvested by the TS receivers for TDMA based transmission and for PS receivers. For a single user with perfect CSI, the authors in [69] have designed an OFDM based WEIT system with the objective of maximizing the harvested energy where the sensor has assumed to have a set of bandpass filters for extracting the required RF signals to perform both information decoding and energy harvesting operations. However, the design leads to higher receiver complexity and degrades the ETE.

Use of multisine or OFDM in combination with multiple antennas at the transmitter for the design of WET, SWIPT systems has been reported in [22, 70–72]. Specifically, in [22, 70] the authors have optimized the amplitudes and phases of multisine waveform based on the channel response to improve the wireless power transfer (WPT) efficiency of a multisensor WPT system while considering a nonlinear EH model and assuming perfect CSI. For a single user, the authors in [71] have designed independent power and information waveforms for a single user SWIPT system to maximize the rate-energy region subject to a constraint on the total transmit power. For a single user, the authors in [72] have presented a two-phase channel training protocol over OFDM to maximize the harvested energy through subband selection. The scheme requires double the duration for channel training over

conventional designs, and the sensor needs to feedback the channel response that consumes additional energy. For an energy constrained sensor, the scheme poses an energy burden and limits the intended operational span.

1.3 Research Motivation

The analysis of the reported works described above indicates the importance of waveform design as appropriate design of chirp waveforms having low or zero mutual cross-correlation level boosts the performance of the communication and IoT systems. Moreover, chirp waveforms with low PSL for ASP and CCP lead to the improvement in the detection capability of the radar systems. The analysis on the design of chirp waveforms, in the above reported literature, indicates several shortcomings that require further investigation. The main findings and motivation behind carrying this research work are as follows:

(1) Design of communication systems using SAW-chirp delay line, as reported in the literature, is limited to a transmission of 2 bits per symbol duration while using single chirp waveform. The objective of achieving a transmission of symbols with a higher number of bits motivates us to explore system design using SAW-chirp delay line while maintaining the same system bandwidth.

(2) For an up-chirp and a down-chirp, occupying the same bandwidth, there exist a non-zero cross-correlation level between them. In the reported works on communication systems using chirp waveform, the design of waveforms either by changing chirp rate and (or) TBP to limit the cross-correlation value, leads to higher bandwidth requirement. This motivates us to investigate on the design properties of chirp with the objective of achieving a set of orthogonal chirp waveforms to minimize the MAI in a multiuser communication system. In the process, we also analyze possible designs of chirp waveforms by combining it with binary pseudo-noise (PN) code sequence.

(3) Design of waveform for radar systems depends on various characteristic parameters, e.g., PSL, main lobe width, Doppler sensitivity etc. From the designs on DFCWs, reported in literature, we find that the number of available waveforms is limited for many multiuser and MIMO radar applications. Furthermore, the associated performances can be improved further. These motivate us in the design of DFCWs using both LC and NLC with the objective of attaining a higher number of waveforms and better performance over the reported designs.

(4) From the analysis of SC waveforms in a multiuser scenario, for LEO satellite IoT communication, we observe high cross-correlation peak values at different delay that limit the system performance. The analysis on radar waveforms provides important insights about the minimization of overall cross-correlation levels, and this motivates us to design a new SC waveform with the objective of performance improvement over the reported designs.

(5) Most of the reported works on WET or WEIT systems perform fixed-frequency waveform based transmission over single or multiple carriers. Unlike fixed-frequency signal for which the waveform bandwidth is inversely related to its duration, waveform duration of a chirp can be varied independently of its bandwidth. Therefore, with appropriate design it is possible to allocate multiple chirp waveforms occupying the same bandwidth while maintaining orthogonality over the waveform duration and peak power constraint. This motivates us to replace the fixed-frequency waveforms by chirp waveforms with the objective of improving the energy harvested at the sensor nodes for WET systems and improving the energy-information transfer region in case of WEIT systems.

1.4 Contribution of the Thesis

The thesis aims at novel designs of chirp waveforms for wireless communication, radar, IoT, and WEIT applications, and the performance evaluation of the associated systems. Furthermore, it includes comparisons with the reported designs to analyze the improvement in performance. In particular, the main contributions of the thesis include–

- The design of chirp waveform for a single user communication system using SAW-chirp devices to achieve a transmission of 3 bits per symbol duration. Initially, we present a SAW communication system based on fixed-frequency waveform and subsequently extend it for LC waveform with appropriate modifications. We evaluate the system performance in terms of probability of BER and SER under AWGN and Rayleigh fading channels, and the results are compared to the reported designs.

- The design of phase-coded chirp waveforms by incorporating binary PN-code sequence within a chirp waveform, for both LC and NLC, to reduce the MAI in a multiuser communication system. We evaluate the system performance in terms of probability of BER and analyze the effects of the number of users on it.

- The design of a set of orthogonal up-chirp and a set of orthogonal down-chirp waveforms for multiuser chirp-BOK communication systems to minimize bandwidth requirement and MAI. We present the condition of orthogonality for a set of chirps and derive analytical expressions of BER for evaluating the system performance under AWGN and Rayleigh fading channels. Moreover, the results are compared with the reported designs.

- The design of a chirp communication system to double the transmission rate compared to a conventional chirp-BOK systems without increasing the number of correlators at the receiver. We propose a new design for the construction of a set of completely orthogonal chirp waveforms to eliminate MAI in a multiuser communication system. Extending it, we present time domain multiplexing of orthogonal chirp sets to reduce the required system bandwidth and the associated signal demodulation using FrFT in a multiuser scenario. We derive analytical expressions for SER and evaluate the system performance under the effect of co-channel interference over Nakagami-m fading. The effects of waveform type, channel conditions on the performance of the system are investigated while comparing it with the reported designs.

- The design of a set of DFCWs for MIMO and multiuser radar systems by combining LC subpulses and PN-code sequence where the frequency hopping of the pulses is decided according to hyperbolic frequency hopping (HFH) sequence. We formulate analytical expressions of auto-ambiguity and cross-ambiguity functions to analyze the performance of the waveforms. We formulate a two stage optimization process for the selection of appropriate frequency-firing order sequences and PN-code sequences to design a higher number of available waveforms while maintaining improved ASP and CCP levels over the reported designs.

- The design of a set of DFCWs using NLC waveforms (DFCWs-NLC) to achieve further improvement in PSL and an increase in the number of available waveforms. We present a parameterized waveform design model and derive NLC functions for designing the required NLC waveform. We perform an optimization process based on GA for the selection of appropriate parameter values and derive expressions for ambiguity functions to investigate waveform performance. We present a joint optimization of the NLC pulse type and the frequency firing order of the chirp pulses in the proposed DFCWs-NLC for improving ASP and CCP performance over the reported DFCW designs.

- The design of a new symmetry chirp waveform having multiple chirp rates (SC-MCR) to improve the cross-correlation performance over SC waveform [58] for LEO satellite IoT communication. Extending the design, we present a time domain multiplexing of the SC-MCR waveforms to improve the system data rate. We formulate analytical expressions of autocorrelation and cross-correlation for SC-MCR, and evaluate the performance of an M-ary system in terms of SER in a multiuser scenario over a Rice-lognormal satellite (RLS) channel. The effect of elevation angle on performance of the system is investigated and the results are compared with the reported designs.

- The design of superposed chirp waveforms for WET and WEIT applications. We establish key properties required for optimizing WET, and present the transmission strategies for downlink WET (DL-WET) from a multiantenna access point (AP) to a group of sensors over orthogonal subbands. We derive new analytical expressions for the average energy harvested by the sensor nodes based on the transmission of superposed chirp waveforms over subbands selected independently for each sensor based on their estimated channel gain. Further, we derive max-min optimal power control coefficients in closed form to ensure that sensors placed at different distances from the AP harvest an equal amount of energy. We also evaluate the max-min information transmitted on the uplink (UL) by the sensors. The effect of different system parameters on the DL harvested energy and the UL achievable rate for the WET, WEIT system, e.g., number of antennas at the AP, number of subbands, and number of sensors in the network, are investigated under Rayleigh fading and the results are compared with the reported designs based on fixed-frequency waveform.

1.5 Thesis Organization

This thesis is organized into five chapters. The summary of each chapter is briefly outlined as follows. A structural organization of the thesis is shown in Figure 1.5.

Chapter 1 : This chapter presents an overview of chirp waveform and its properties, wireless communication and performance analysis, radar system, Internet of Things, and wireless energy transfer. This chapter discusses fundamental concepts and terminologies which are used in the latter part of the thesis. It covers brief background and literature review of the designs based on chirp waveform for the applications of communication, radar, and IoT systems along with associated analysis of its per-

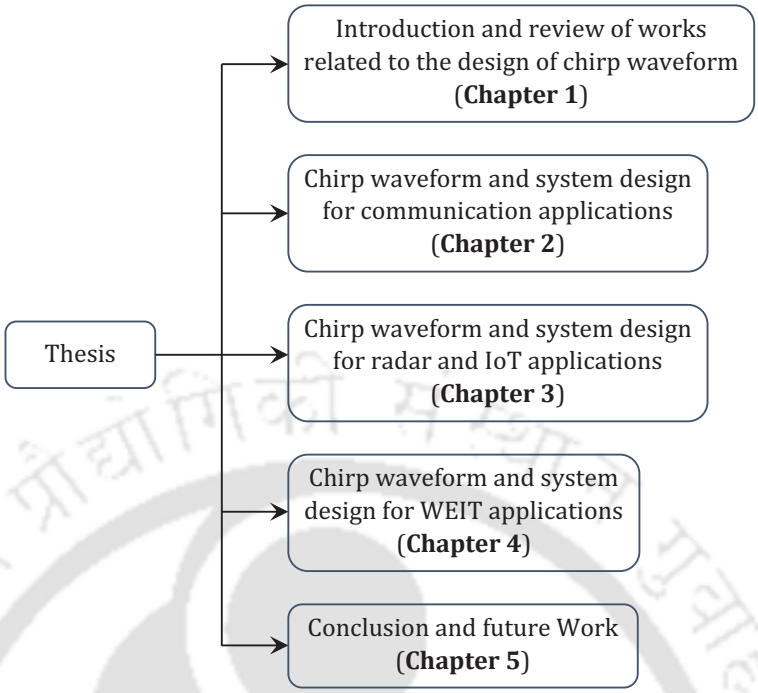

Figure 1.5: Thesis organization.

formance followed by some of the existing works on WET and WEIT that has motivated our present research. Subsequently, it summarizes the thesis contribution and provides an outline of the thesis organization.

Chapter 2 : This chapter presents the designs of chirp waveform for communication systems in a single and multiuser scenario and covers the following: (i) the design of a chirp system using SAW-chirp devices for transmission of 3 bits per symbol, (ii) the design of phase-coded chirp waveforms and design of a set of orthogonal up-chirp and set of orthogonal down-chirp waveforms for multiuser system to minimize MAI, (iii) the design of a set of completely orthogonal chirp waveforms, to eliminate MAI, and a chirp system with a data rate twice that of a conventional chirp-BOK scheme for multiuser scenario, (iv) the design of time domain multiplexing of orthogonal chirp sets, to reduce bandwidth requirement, and its demodulation using FrFT. We derive analytical expressions of BER or SER for the associated chirp communication systems to evaluate the performance and analyze the effect of different system parameters such as waveform type, number of users, channel conditions on the performance of the systems. In addition, the results are also compared with the reported works.

Chapter 3 : This chapter presents the design of DFCWs using linear and nonlinear chirp waveforms for MIMO and multiuser radar systems. For the design of DFCW-LC, LC pulses are binary

phase coded and positioned according to HFH sequence. We perform a two-stage optimization process to improve the ASP and CCP levels over reported designs. For the design of a set of DFCWs using NLC, we present a parameterized waveform design model and a waveform optimization process based on GA to design NLC waveforms and their optimization, respectively. For both the designs, we evaluate the performances through radar ambiguity functions and access the improvement over reported designs. This chapter also includes the design of SC-MCR waveforms and a time domain multiplexing of the SC-MCR waveforms for an M-ary chirp system, under a multiuser scenario, intended for LEO satellite IoT communication. We evaluate the system performance under RLS channel and analyze the effects of elevation angle while comparing it with the reported designs.

Chapter 4 : This chapter presents the design of chirp waveform for WET and WEIT applications. We present a general superposed chirp waveform design for a given configuration parameter and establish key properties required for optimizing DL-WET. For a multisensor WEIT system, we present the transmission strategy, and derive new analytical expressions for the average energy harvested by any sensor node for DL-WET via the transmission of superposed chirp waveforms as well as fixed-frequency waveform over the subbands selected based on their estimated channel strength. For both superposed chirp waveforms and fixed-frequency waveform based DL-WET with subband selection, we also derive the max-min power control coefficients in closed-form to ensure that sensors placed at different distances from the AP harvest an equal amount of energy. We also analyze the corresponding max-min information transmitted on the UL by the sensors. We present extensive numerical results to examine the joint impact of different design parameters on the system performance and benchmark our results against DL-WET via fixed-frequency waveform under Rayleigh fading channel.

Chapter 5 : This chapter concludes the research work presented in the thesis and discusses the scope for future research in the areas of communication, radar, and WET.

2

Design and Analysis of Chirp Waveform for Wireless Communication Systems

Contents

2.1 Introduction

Communication systems using chirp waveform, for single user, have been presented in [6,9,26–28,31, 73] whereas communication systems design using SAW-chirp device have been reported in [9,26–28,73] to attain a maximum transmission rate of 2 bits per symbol duration while considering single chirp waveform. On the other hand, multiuser chirp communication systems reported in [3, 25, 32, 34, 35] have employed set of non-orthogonal chirp waveforms that lead to an increase in MAI and limit the overall system performance. In this chapter chirp waveform designs are proposed starting for a single user SAW-chirp system to multiuser chirp-BOK system with the objective of improving data rate and minimizing MAI. Investigation on the waveforms design is carried out to improve bandwidth efficiency without compromising the system performance. The main contributions of this chapter are listed as follows:

(1) A SAW-chirp system and associated chirp waveforms are designed with a transmission rate of 3 bits per symbol. For the analysis, we consider SER as the performance metric and derive analytical expressions for quadrature phase shift keying modulated data.

(2) A design incorporating the combination of chirp waveforms and binary PN-code sequence is presented, considering LC and NLC, to reduce MAI in a multiuser communication system. For the analysis, we consider BER as the performance metric.

(3) In the process to minimize MAI, the design of a set of orthogonal up-chirp and orthogonal down-chirp waveforms for multiuser chirp-BOK system is proposed. Analytical expressions of the BER are derived under AWGN and Rayleigh fading environment.

(4) A modified chirp-BOK is proposed to double the transmission rate without increasing the number of correlators at the receiver. For a multiuser system, set of completely orthogonal chirp waveforms is designed to eliminate MAI. A time domain multiplexing of orthogonal chirp sets is proposed to improve bandwidth efficiency. Analytical expressions of the SER are derived under Nakagami-m fading to get a better insight of the dependence of performance on the fading parameters.

For all the proposed designs and systems, the associated performances are compared with the reported designs to analyze the improvement in performance. The detailed designs of these waveforms and systems are discussed in the subsequent sections in this chapter.

2.2 Communication System using SAW-Chirp Devices for Multibit Symbol Transmission

A SAW device allows an easy generation of waveforms, and based on the designs and arrangements of the metallic fingers in the form of IDT structure, one can obtain a fixed-frequency or a chirp waveform [2, 13]. Being a passive device, it consumes low power for the operation. Design of a single user communication system using SAW devices is reported in [74] for a transmission of 2 bits per symbol via fixed-frequency waveforms through QPSK modulation. In contrast, use of DQPSK modulation allows to maintain the same data rate without using any reference signal at the receiver for demodulation process, thereby simplifying the receiver design. Motivated from the fact that none of the reported works considered this modulation, in this work firstly we present a communication system using SAW devices based on fixed-frequency waveform and DQPSK modulation. BER analysis of the proposed DQPSK system is presented under AWGN and Rayleigh fading channels and the analytical results are verified through Monte-Carlo simulation. Furthermore, the proposed design acts as a base model and with appropriate modification the system model is extended for LC waveforms. Accordingly, in the next step, we present a chirp waveform modulation and demodulation scheme using SAW-chirp devices, for a single user system, to achieve an improved transmission rate of 3 bits per symbol.

2.2.1 System Model Based on Fixed-frequency Waveform

In a DQPSK signal, the symbol information is encoded as the phase difference of two consecutive transmitted signals. The receiver calculates the corresponding phase change instead of decoding each individual received signal to retrieve the transmitted symbol information, and eliminates the requirement of a reference carrier signal.

2.2.1.1 DQPSK Modulation using SAW Device

For DQPSK modulation, the input bits are grouped into 2-bit symbols. For a Gray encoded input bits, four possible combinations of 2 bits $b_1b_0 \in \{00, 01, 11, 10\}$ and associated phase mapping (θ) is given as $00 \equiv \frac{3\pi}{2}, 01 \equiv \pi, 11 \equiv \frac{\pi}{2}, 10 \equiv 0$. The corresponding mapping for DQPSK is shown in Figure 2.1. Accordingly, block diagram of the proposed DQPSK modulator using SAW device is shown in Figure 2.2. The pre-phase coder performs the mapping from the 2 bits binary input to the required phase difference based on the current input bits and the previous phase coder output bits. The phase of the current transmitted signal is calculated such that the phase difference between the

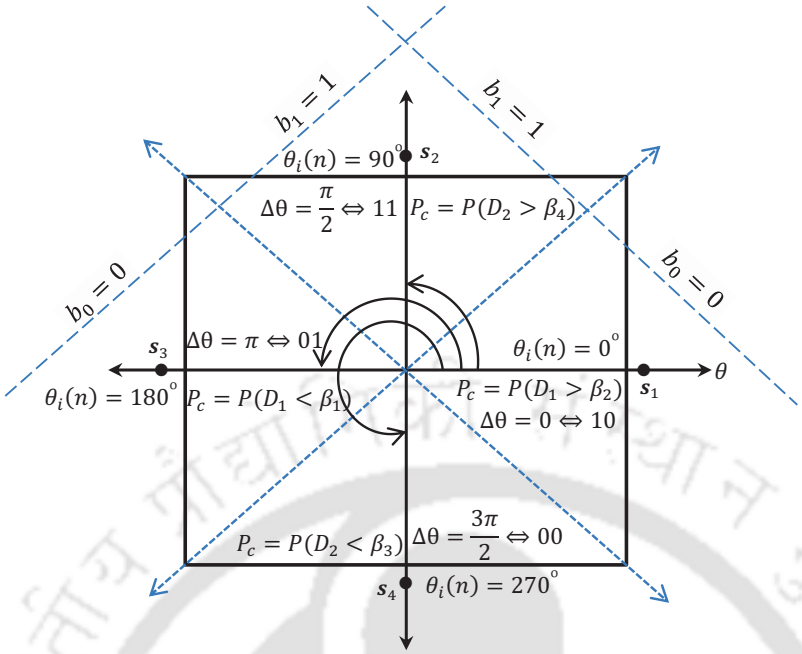

Figure 2.1: Two-bit encoding for DQPSK and QPSK.

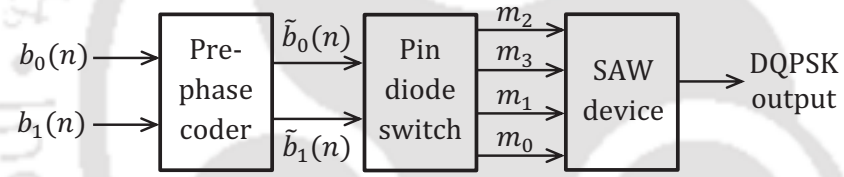

Figure 2.2: Block diagram of the DQPSK modulator using SAW device.

current and previous signals is equal to the phase assigned to the corresponding transmitted dibits. Therefore, from the calculation of the phase difference, the information about the transmitted bits can be extracted without the requirement of a local carrier. Based on the above criterion, the output of the pre-phase coder is formulated as given in Table 2.1 where $b_1(n)$ and $b_0(n)$ are the current input bits, $\tilde{b}_1(n-1)$ and $\tilde{b}_0(n-1)$ are the phase coder outputs in the previous symbol duration, and $\tilde{b}_1(n)$, $\tilde{b}_0(n)$ are the current phase coder outputs. In terms of phase, the pre-phase coder outputs can be presented [15] [16] as

$$\begin{aligned}
\theta(n) &= \theta(n-1), && \text{if} \quad b_1 b_0 = 10 \\
\theta(n) &= \theta(n-1) + \frac{\pi}{2}, && \text{if} \quad b_1 b_0 = 11 \\
\theta(n) &= \theta(n-1) + \pi, && \text{if} \quad b_1 b_0 = 01 \\
\theta(n) &= \theta(n-1) + \frac{3\pi}{2}, && \text{if} \quad b_1 b_0 = 00.
\end{aligned} \tag{2.1}$$

Table 2.1: Calculation of phase for DQPSK transmitted signal

$\tilde{b}_1\tilde{b}_0(n-1)$	$\theta(n-1)$	$b_1b_0(n)$	$\theta(n)$	$\tilde{b}_1\tilde{b}_0(n)$	$\triangle\theta$
00	270°	01	90°	11	180°
01	180°	01	0°	10	180°
11	90°	01	270°	00	180°
10	0°	01	180°	01	180°
00	270°	11	0°	10	90°
01	180°	11	270°	00	90°
11	90°	11	180°	01	90°
10	0°	11	90°	11	90°
00	270°	10	270°	00	0°
01	180°	10	180°	01	0°
11	90°	10	90°	11	0°
10	0°	10	0°	10	0°
00	270°	00	180°	01	270°
01	180°	00	90°	11	270°
11	90°	00	0°	10	270°
10	0°	00	270°	00	270°

To realise DQPSK signals using SAW device, the design of IDT is presented in Figure 2.3. To introduce phase delay, the gaps between the input and output IDTs are adjusted appropriately for the 4 pairs of IDTs which introduce a phase delay of 0, $\frac{\pi}{2}$, π, $\frac{3\pi}{2}$, respectively, in the output signal. According to the output phase of the pre-phase coder, appropriate input IDT of the SAW device is excited to get the corresponding phase delayed output signal

$$s_l(t) = \cos\left(2\pi f_0 t + \theta_l(t)\right), \quad 0 \leq t \leq T_\mathrm{s}, \tag{2.2}$$

where f_0 is the carrier frequency, T_s is the symbol duration, and $\theta(t)$ is the DQPSK transmitted signal phase that is equal to the corresponding pre-phase coder output phase for any particular transmission. Further, $l = 1, 2$ corresponds to the previous and current transmission instances, respectively. The appropriate input IDT of the SAW device is selected as

$$m_j = j = (2b_1 + b_0), \qquad \text{where} \quad b_1, b_0 \in \{0, 1\}. \tag{2.3}$$

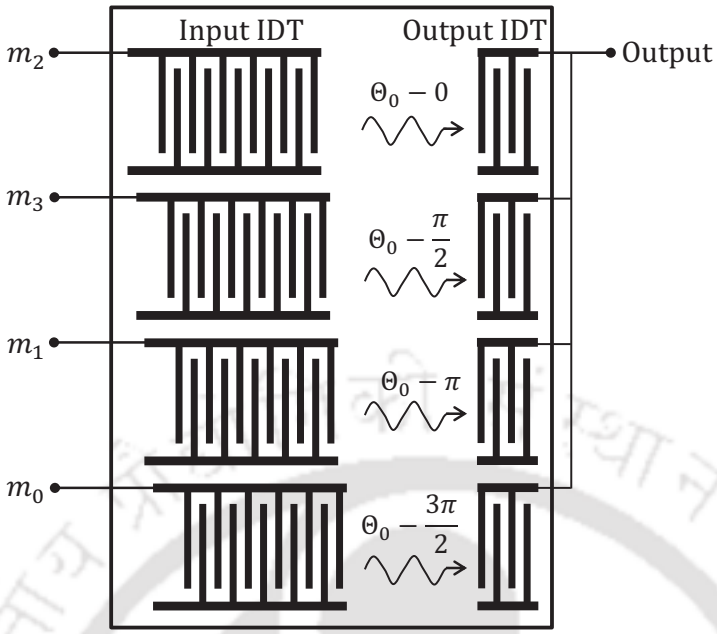

Figure 2.3: Schematic of the modulator SAW device. The gap between input and output IDTs corresponds to the 4 possible transmitted signal phases.

2.2.1.2 DQPSK Demodulation using SAW Device

The block diagram of the proposed DQPSK demodulator system using SAW device is shown in Figure 2.4. After amplification, the received DQPSK signal is fed to the SAW device which estimates the phase difference by the addition of two consecutive received signals. The output amplitudes of the SAW device are detected by the peak detectors and passed through the thresholding and decision block. Finally, the decoder estimates the transmitted bits from the output of the decision block.

The proposed SAW device for the demodulation of DQPSK signals is shown in Figure 2.5. It consists of two stages. The output of 'Stage 1' is the addition of the incoming signal and the signal obtained after introducing an additional delay of T_s, i.e., the signal received in the previous symbol duration. Mathematically, it can be written as

$$\begin{aligned} R_1 &= \cos\left(\omega_0 t + \theta_2(t)\right) + \cos\left(\omega_0 t + \theta_1(t - T_s)\right) \\ &= 2\cos\left(\frac{\theta_2(t) - \theta_1(t - T_s)}{2}\right)\cos\left(\omega_0 t + \left(\frac{\theta_2(t) + \theta_1(t - T_s)}{2}\right)\right), \end{aligned} \tag{2.4}$$

where $\omega_0 = 2\pi f_0$. The output of the peak detector of the added output signal is given as

$$D_1 = \left|2\cos\left(\frac{\theta_2(t) - \theta_1(t - T_s)}{2}\right)\right| = \left|2\cos\left(\frac{\Delta\theta}{2}\right)\right|. \tag{2.5}$$

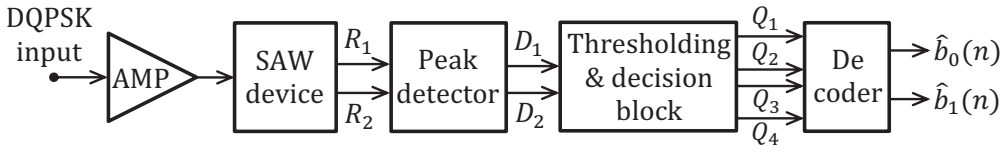

Figure 2.4: Block diagram of the DQPSK demodulator using SAW device.

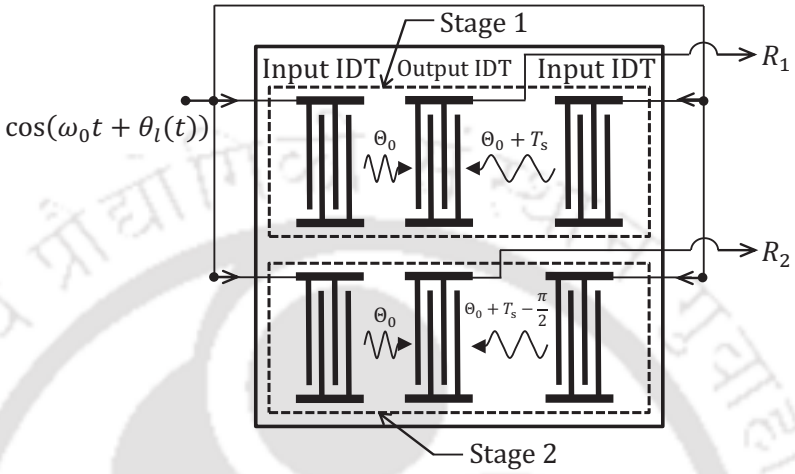

Figure 2.5: Schematic of the SAW device in the demodulator.

From (2.5) it can be found that the amplitude of the resultant signal is a function of the phase difference between two consecutive received signals. The detector is used to detect the peak values of the output signal having different phase values. From Table 2.1, it can be found that the phase difference between two consecutive incoming signals can have 4 possible values and from (2.5) the peak value can be one of 2, $\sqrt{2}$, 0. For the phase difference of $\frac{\pi}{2}$ and $\frac{3\pi}{2}$ the values of D_1 are equal to $\sqrt{2}$, which creates ambiguity in the decision block. In order to overcome this difficulty 'Stage 2' is introduced. The output of 'Stage 2' is the addition of the incoming signal and the signal received in the previous symbol duration delayed by an additional phase of $\frac{\pi}{2}$ which corresponds to additional path length of $\frac{\lambda}{4}$. Mathematically

$$\begin{aligned} R_2 &= \cos\left(\omega_0 t + \theta_2(t)\right) + \cos\left(\omega_0 t + \theta_1(t - T_s) + \frac{\pi}{2}\right) \\ &= 2\cos\left(\frac{\theta_2(t) - \theta_1(t - T_s)}{2} - \frac{\pi}{4}\right)\cos\left(\omega_0 t + \left(\frac{\theta_2(t) + \theta_1(t - T_s)}{2} + \frac{\pi}{4}\right)\right). \end{aligned} \tag{2.6}$$

The signal of the peak detector is given as

$$D_2 = \left|2\cos\left(\frac{\theta_2(t) - \theta_1(t - T_s)}{2} - \frac{\pi}{4}\right)\right| = \left|2\cos\left(\frac{\Delta\theta}{2} - \frac{\pi}{4}\right)\right|. \tag{2.7}$$

Table 2.2: Output of decoder based on detector and decision logic output for DQPSK

$\triangle\theta$	D_1	D_2	Q_1	Q_2	Q_3	Q_4	b_1	b_0
0°	2	$\sqrt{2}$	1	0	0	0	1	0
90°	$\sqrt{2}$	2	0	0	1	0	1	1
180°	0	$\sqrt{2}$	0	1	0	0	0	1
270°	$\sqrt{2}$	0	0	0	0	1	0	0

In this case the value of D_2 for $\triangle\theta = \frac{\pi}{2}, \frac{3\pi}{2}$ are distinct and can be used to remove ambiguity in D_1 explained above. The value of the peak detector are fed to the decision block. Table 2.2 summarizes the outputs for 4 cases of phase differences. If output of D_1 is 2 or 0, then it would select bits according to the logic of $\triangle\theta$. If the output of D_1 is other than 2 or 0, the decoder does not make any decision on the transmitted symbol. The decoded takes up the the output of D_2 to make decision in that case. Therefore, as a whole, the decoder uses the outputs from D_1 and D_2 for the estimation of the symbol.

Next, the proposed DQPSK demodulation process using SAW device is extended for the demodulation of a QPSK signal given by

$$s_i(t) = \cos\left(2\pi f_0 t + \theta_i(t)\right), \quad 0 \leq t \leq T_s, \tag{2.8}$$

where θ_i indicates the phase value that is constant for each dibit of the input bit stream [15] and associated phase mapping (θ_i) is given as $00 \equiv \frac{3\pi}{2}, 01 \equiv \pi, 11 \equiv \frac{\pi}{2}, 10 \equiv 0$. Conventionally, the QPSK demodulator systems require an additional local synchronizing signal. A QPSK demodulator system reported in [74] uses SAW device to add the incoming signal with the locally generated reference carrier. Here, we propose a QPSK demodulator using SAW device without the need of locally generated reference carrier. It may be noted that, the proposed demodulation scheme requires a preamble of a dibit as reference which is known apriori to both transmitter and receiver. Therefore, these two bits are the overhead in addition to actual data stream to be sent and it may be negligibly small when long streams of data are transmitted. The main difference between the proposed QPSK demodulator and the DQPSK demodulator described above is the modification in the logic of the decision block. The transmitted signal can have any one of the four possible phases based on the transmitted dibit. The structure of the receiver SAW device is shown in Figure 2.5, similar to the structure used in DQPSK. The amplitudes of the two outputs of SAW device are determined by the peak detectors and feed them to the decision block. As the phase of the previously transmitted signal is known to the receiver,

Table 2.3: Decoder output for different phases of the received QPSK signal

$\theta_{i_{n-1}}(t)$	$b_1b_0(n-1)$ Previous received bits	$\theta_{i_n}(t)$	$\triangle\theta$	D_1	D_2	$b_1b_0(n)$ Current received bits
180°	01	0°	180°	0	$\sqrt{2}$	10
180°	01	90°	270°	$\sqrt{2}$	0	11
180°	01	180°	0°	2	$\sqrt{2}$	01
180°	01	270°	90°	$\sqrt{2}$	2	00
90°	11	0°	270°	$\sqrt{2}$	0	10
90°	11	90°	0°	2	$\sqrt{2}$	11
90°	11	180°	90°	$\sqrt{2}$	2	01
90°	11	270°	180°	0	$\sqrt{2}$	00
0°	10	0°	0°	2	$\sqrt{2}$	10
0°	10	90°	90°	$\sqrt{2}$	2	11
0°	10	180°	180°	0	$\sqrt{2}$	01
0°	10	270°	270°	$\sqrt{2}$	0	00
270°	00	0°	90°	$\sqrt{2}$	2	10
270°	00	90°	180°	0	$\sqrt{2}$	11
270°	00	180°	270°	$\sqrt{2}$	0	01
270°	00	270°	0°	2	$\sqrt{2}$	00

from the phase difference between current and previous received signals, current received bits can be estimated using Table 2.3. Therefore, normal QPSK signals also can be decoded and transmitted bits can be extracted at the receiver side without the use of local reference carrier.

Simulation of the demodulator operation using SAW device for DQPSK is presented considering the sequence of transmitted bits $b_1 = [0, 0, 1, 1]$ and $b_0 = [0, 1, 1, 0]$ and reference bits $b_1b_0 = 10$. Two outputs R_1 and R_2 of the SAW device are shown in Figure 2.6(a) and Figure 2.6(b), respectively. The corresponding outputs D_1 and D_2 of the peak detectors are shown in Figure 2.6(c) and Figure 2.6(d), respectively. Addition operation performed by SAW device is also verified through simulation by designing a SAW structure using COMSOL Multiphysics as given in Figure 2.5. The substrate material for the SAW device is chosen 128° $Y-X$ $LiNbO_3$ with a surface acoustic wave velocity 3979 m/s [13], interdigital periodicity (λ) of 16 μm, and center frequency of 249 MHz. Split-electrode configurations are considered for input and output IDTs to minimize mechanical reflection [13]. The input and output IDTs have a length of 3λ and 2λ, respectively. Distance between the input and output IDT (Θ_0) is

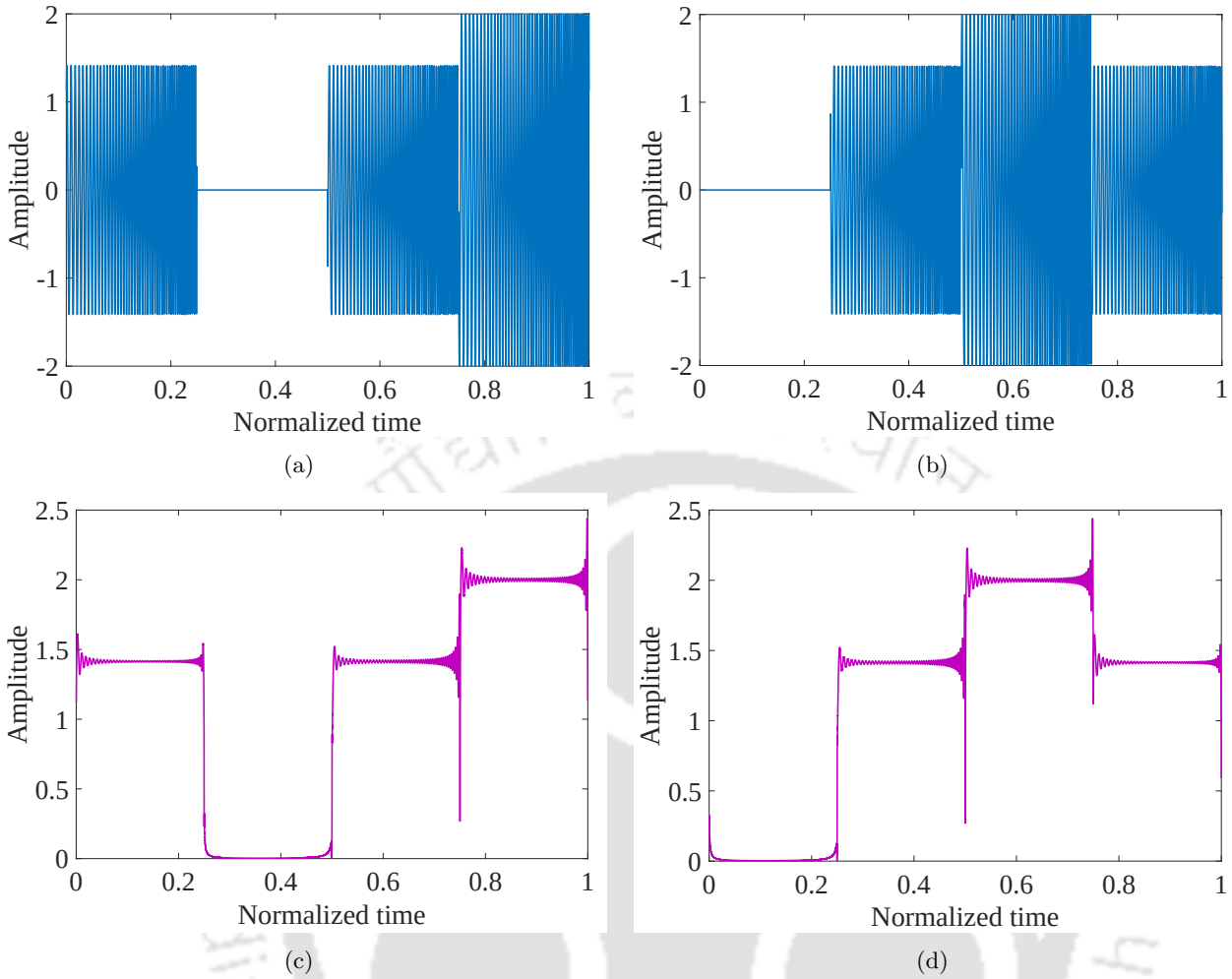

Figure 2.6: Result of simulation of DQPSK demodulator operation using SAW device for received dibits [00,01,11,10]. (a) Output of SAW device at R_1. (b) Output of SAW device at R_2. (c) Output of peak detector at D_1. (d) Output of peak detector at D_2.

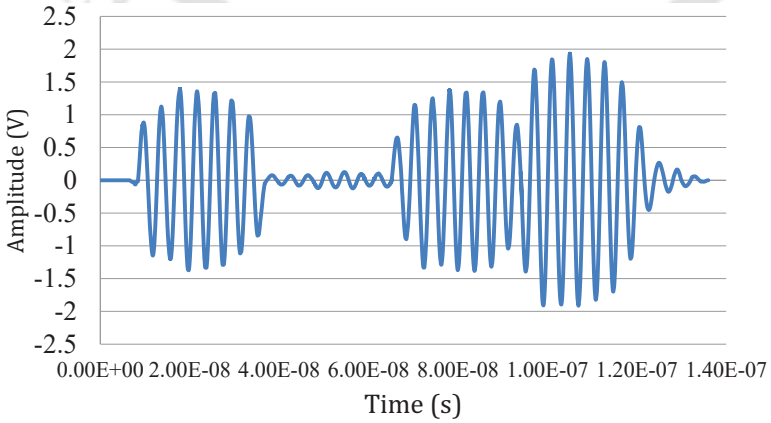

Figure 2.7: Output of SAW device at R_1 using COMSOL Multiphysics for received dibits [00,01,11,10].

chosen 3λ for simulation purpose. The input signal consists of 7 cycles having different starting phase and $T_s = 7\lambda$. The SAW device output is simulated for 'Stage 1' configuration. The added output at R_1 is shown in Figure 2.7 and its envelope closely matches with the ideal output shown in Figure 2.6(a).

2.2.1.3 Performance Analysis and Numerical Results

Performance of the proposed DQPSK system is evaluated in terms of BER firstly under AWGN channel followed by under Rayleigh fading channel. For the DQPSK system, at the receiver input the signal can be expressed using (2.2) as

$$y_l(t) = A\cos\left(\omega_0 t + \theta_l(t)\right) + w_l(t), \quad (l-1)T_s \leq t \leq lT_s, \tag{2.9}$$

where $l = 1, 2$, $A = \sqrt{2S}$ is the amplitude, S is the signal power, θ_l is the phase values associated with consecutive two transmitted signals, and $w(t)$ is the noise with zero mean and variance $\frac{N_0}{2}$. It is assumed that the phase of the received signal varies slowly and thus it is considered constant over two symbol duration. Accordingly, the output R_1 of 'Stage 1' and R_2 of 'Stage 2' of the SAW device is calculated using (2.4) and (2.6) as

$$R_1 = \sqrt{2}A\cos\left(\frac{\theta_2(t) - \theta_1(t-T_s)}{2}\right)\cos\left(\omega_0 t + \left(\frac{\theta_2(t) + \theta_1(t-T_s)}{2}\right)\right) + w_1'(t), \tag{2.10}$$

where $w_1'(t) = \frac{1}{\sqrt{2}}(w_1(t-T_s) + w_2(t))$, and

$$R_2 = \sqrt{2}A\cos\left(\frac{\theta_2(t) - \theta_1(t-T_s)}{2} - \frac{\pi}{4}\right)\cos\left(\omega_0 t + \left(\frac{\theta_2(t) + \theta_1(t-T_s)}{2} + \frac{\pi}{4}\right)\right) + w_2'(t), \tag{2.11}$$

where $w_2'(t) = \frac{1}{\sqrt{2}}(w_1\left((t-T_s) + \frac{\pi}{2}\right) + w_2(t))$. The corresponding peak detectors outputs are given by

$$D_1 = \left|\sqrt{2}A\cos\left(\frac{\Delta\theta}{2}\right) + w_1''(t)\right|, \tag{2.12}$$

$$D_2 = \left|\sqrt{2}A\cos\left(\frac{\Delta\theta}{2} - \frac{\pi}{4}\right) + w_2''(t)\right|, \tag{2.13}$$

where $w_1''(t)$ and $w_2''(t)$ are the noise present in the output signal at D_1 and D_2.

Using the symbol encoding process as shown in Figure 2.1 the probability regions for detection of correct symbols are presented in Figure 2.8. As $0 \leq \cos(\theta) \leq 1$, in absence of noise, from (2.12) and (2.13) it can be found that D_1 or D_2 can have values of 0, A, and $\sqrt{2}A$ for the 4 phase-difference values as shown in Table 2.1. In order to distinguish different transmitted symbols, the decision region is sub-divided in 3 parts having two threshold levels β_1 and β_2 for D_1 and two threshold levels β_3 and

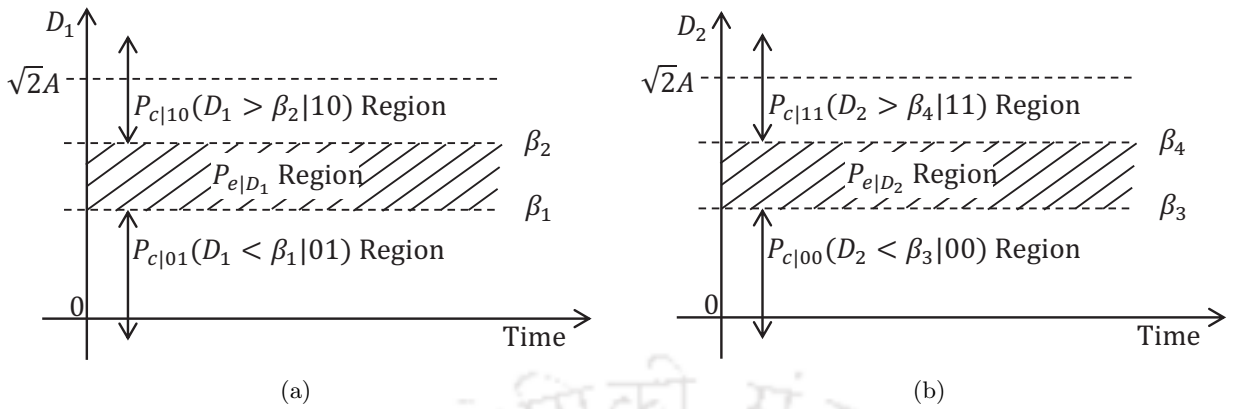

Figure 2.8: Schematic diagram of threshold levels for (a) D_1 and (b) D_2. P_c denotes the probability of correct detection and P_e denotes the probability that the symbol will fall in the erroneous decision region.

β_4 for D_2 as shown in Figure 2.8. Each phase-difference $\Delta\theta$ corresponds to specific symbol as shown in Figure 2.1. Assuming that the 2-bit symbols $\{00, 01, 11, 10\}$ are equally likely, the probability that the symbol will fall in the erroneous decision region as shown in Figure 2.8 can be calculated for both the peak detector outputs as

$$P_{eD_1} = Pr\{\beta_1 < D_1 < \beta_2\}. \tag{2.14}$$

$$P_{eD_2} = Pr\{\beta_3 < D_2 < \beta_4\}. \tag{2.15}$$

As the decoder uses the outputs from D_1 and D_2 for the estimation of the transmitted symbol, therefore, the symbol error probability (SEP) is given as

$$P_e = P_{eD_1} P_{eD_2}. \tag{2.16}$$

As D_1 follows a Gaussian distribution, P_{eD_1} can evaluated using (2.12) and simplified as

$$P_{eD_1} = \frac{1}{2}\,\mathrm{erfc}\left(\frac{\beta_1 - \left|\sqrt{2}A\cos\left(\frac{\Delta\theta}{2}\right)\right|}{\sqrt{2\sigma^2}}\right) - \frac{1}{2}\,\mathrm{erfc}\left(\frac{\beta_2 - \left|\sqrt{2}A\cos\left(\frac{\Delta\theta}{2}\right)\right|}{\sqrt{2\sigma^2}}\right), \tag{2.17}$$

where $\sigma^2 = N_0$, $\mathrm{erfc}\{\cdot\}$ is the complementary error function [15], and representing β_1 and β_2 in terms of bit energy, $\beta_1 = x_1\sqrt{E_\mathrm{b}}$ and $\beta_2 = x_2\sqrt{E_\mathrm{b}}$ where x_1, x_2 are positive real numbers and E_b is the bit energy. Substituting $A/\sqrt{2\sigma^2} = \sqrt{S/\sigma^2} = \sqrt{2E_\mathrm{b}/N_0}$ in (2.17), the bit error probability is given as

$$P_{eD_1} = \frac{1}{2}\,\mathrm{erfc}\left[\sqrt{\frac{E_\mathrm{b}}{N_0}}\left(\frac{x_1}{\sqrt{2}} - 2\left|\cos\left(\frac{\Delta\theta}{2}\right)\right|\right)\right] - \frac{1}{2}\,\mathrm{erfc}\left[\sqrt{\frac{E_\mathrm{b}}{N_0}}\left(\frac{x_2}{\sqrt{2}} - 2\left|\cos\left(\frac{\Delta\theta}{2}\right)\right|\right)\right]. \tag{2.18}$$

Similarly the bit error probability for D_2 can be calculated as

$$P_{eD_2} = \frac{1}{2}\,\mathrm{erfc}\left[\sqrt{\frac{E_\mathrm{b}}{N_0}}\left(\frac{x_3}{\sqrt{2}} - 2\left|\cos\left(\frac{\Delta\theta}{2} - \frac{\pi}{4}\right)\right|\right)\right] - \frac{1}{2}\,\mathrm{erfc}\left[\sqrt{\frac{E_\mathrm{b}}{N_0}}\left(\frac{x_4}{\sqrt{2}} - 2\left|\cos\left(\frac{\Delta\theta}{2} - \frac{\pi}{4}\right)\right|\right)\right], \tag{2.19}$$

where $\beta_3 = x_3\sqrt{E_\mathrm{b}}$ and $\beta_4 = x_4\sqrt{E_\mathrm{b}}$ and x_3, x_4 are positive real numbers. Finally from (2.18) and (2.19), the BER is expressed as

$$\begin{aligned} P_e = \frac{1}{4}&\left[\mathrm{erfc}\left(\sqrt{\frac{E_\mathrm{b}}{N_0}}\left(\frac{x_1}{\sqrt{2}} - 2\left|\cos\left(\frac{\Delta\theta}{2}\right)\right|\right)\right) - \mathrm{erfc}\left(\sqrt{\frac{E_\mathrm{b}}{N_0}}\left(\frac{x_2}{\sqrt{2}} - 2\left|\cos\left(\frac{\Delta\theta}{2}\right)\right|\right)\right)\right] \\ &\times\left[\mathrm{erfc}\left(\sqrt{\frac{E_\mathrm{b}}{N_0}}\left(\frac{x_3}{\sqrt{2}} - 2\left|\cos\left(\frac{\Delta\theta}{2} - \frac{\pi}{4}\right)\right|\right)\right) - \mathrm{erfc}\left(\sqrt{\frac{E_\mathrm{b}}{N_0}}\left(\frac{x_4}{\sqrt{2}} - 2\left|\cos\left(\frac{\Delta\theta}{2} - \frac{\pi}{4}\right)\right|\right)\right)\right]. \end{aligned} \tag{2.20}$$

Considering the DQPSK signal is received over a flat Rayleigh fading channel, it can be written as

$$y_l(t) = \alpha A\cos\left(\omega_0 t + \theta_l(t)\right) + w_l(t), \quad (l-1)T_\mathrm{s} \le t \le lT_\mathrm{s}, \tag{2.21}$$

where α is the channel fading coefficient with mean square value of $\overline{\alpha^2}$. The average BER of the proposed DQPSK modulation over a Rayleigh fading channel is computed by integrating the error probability in AWGN over the Rayleigh fading distribution [16] and is given by

$$\overline{P_e} = \int_0^\infty P_e(\gamma) f_\gamma(\gamma)\; d\gamma = \int_0^\infty P_e(\gamma)\frac{1}{\overline{\gamma}} e^{\left(-\frac{\gamma}{\overline{\gamma}}\right)}\; d\gamma, \tag{2.22}$$

where $\overline{\gamma}$ is average SNR and $P_e(\gamma)$ is the probability of bit error in AWGN channel and is a function of SNR γ. From (2.17) P_{eD_1} can be represented as

$$P_{eD_1} = P_{eD_{11}} - P_{eD_{12}}. \tag{2.23}$$

Simplifying $P_{eD_{11}}$ using (2.22) the average value is given by

$$\overline{P_{eD_{11}}} = \frac{1}{2}\left(1 - \sqrt{\frac{\rho_1}{1+\rho_1}}\right), \tag{2.24}$$

where $\rho_1 = \frac{\overline{\alpha^2}E_\mathrm{b}}{N_0}\left(\frac{x_1}{\sqrt{2\overline{\alpha^2}}} - 2\left|\cos\left(\frac{\Delta\theta}{2}\right)\right|\right)^2$. Similarly $\overline{P_{eD_{12}}}$ can be calculated and $\overline{P_{eD_1}}$ is given by

$$\overline{P_{eD_1}} = \frac{1}{2}\left[\left(1 - \sqrt{\frac{\rho_1}{1+\rho_1}}\right) - \left(1 - \sqrt{\frac{\rho_2}{1+\rho_2}}\right)\right], \tag{2.25}$$

where $\rho_2 = \frac{\overline{\alpha^2}E_b}{N_0}\left(\frac{x_2}{\sqrt{2\overline{\alpha^2}}} - 2\left|\cos\left(\frac{\Delta\theta}{2}\right)\right|\right)^2$. In a similar way using (2.19) and (2.22), $\overline{P_{eD_2}}$ can be calculated and the average BER for Rayleigh fading channel $\overline{P_e}$ is given by

$$\begin{aligned}\overline{P_e} &= \overline{P_{eD_1}}\ \overline{P_{eD_2}} \\ &= \frac{1}{4}\left[\left(1-\sqrt{\frac{\rho_1}{1+\rho_1}}\right)-\left(1-\sqrt{\frac{\rho_2}{1+\rho_2}}\right)\right]\left[\left(1-\sqrt{\frac{\rho_3}{1+\rho_3}}\right)-\left(1-\sqrt{\frac{\rho_4}{1+\rho_4}}\right)\right], \end{aligned} \tag{2.26}$$

where $\rho_3 = \frac{\overline{\alpha^2}E_b}{N_0}\left(\frac{x_3}{\sqrt{2\overline{\alpha^2}}} - 2\left|\cos\left(\frac{\Delta\theta}{2}-\frac{\pi}{4}\right)\right|\right)^2$ and $\rho_4 = \frac{\overline{\alpha^2}E_b}{N_0}\left(\frac{x_4}{\sqrt{2\overline{\alpha^2}}} - 2\left|\cos\left(\frac{\Delta\theta}{2}-\frac{\pi}{4}\right)\right|\right)^2$.

The DQPSK demodulation process using SAW device is extended for the demodulation of QPSK signal and the main difference in the proposed QPSK demodulator and DQPSK demodulator is the logic of the decision block. As the symbol information in QPSK is encoded according to the symbol-phase mapping as shown in Figure 2.1, QPSK demodulation becomes prone to error-propagation if conventional method of DQPSK demodulation is employed. The decoding logic presented in Table 2.3 for the proposed QPSK demodulator prevents error-propagation as explained in the following example shown in Figure 2.9. The solid path line represents the correct scenario, i.e., the last correctly received signal phase $\theta_{n-2}(t)$ is 0° corresponding to bits $b_1b_0(n-2)$ as 10. The received signal phase $\theta_{n-1}(t)$ in the subsequent time duration is 180° and the estimated bits $b_1b_0(n-1)$ are 01. If the present received signal phase $\theta_n(t)$ is 270°, the present bits $b_1b_0(n)$ will be estimated correctly as 00. In case of error, the received signal phase $\theta_{n-1}(t)$ may be 0°, 90° or 270° as indicated with dotted path in Figure 2.9. For the present received signal phase $\theta_n(t)$ of 270°, all 3 dotted paths lead to correct estimation of present bits $b_1b_0(n)$ as 00. Thus, the decision logic given in Table 2.3 leads to achieve

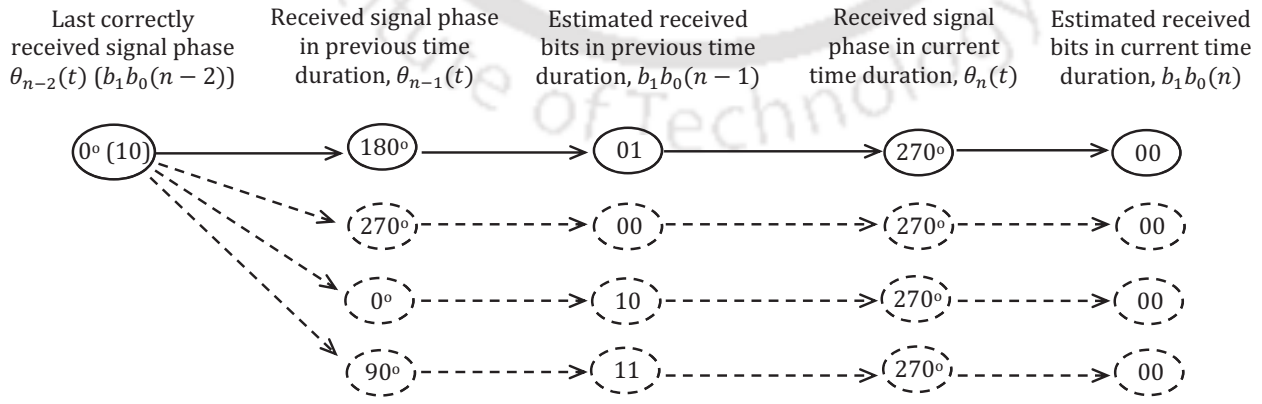

Figure 2.9: Flow diagram of the proposed QPSK demodulation process shows that though $\theta_{n-1}(t)$ is received incorrectly (dotted paths), the estimated $b_1b_0(n)$ are correct if $\theta_n(t)$ is received correctly.

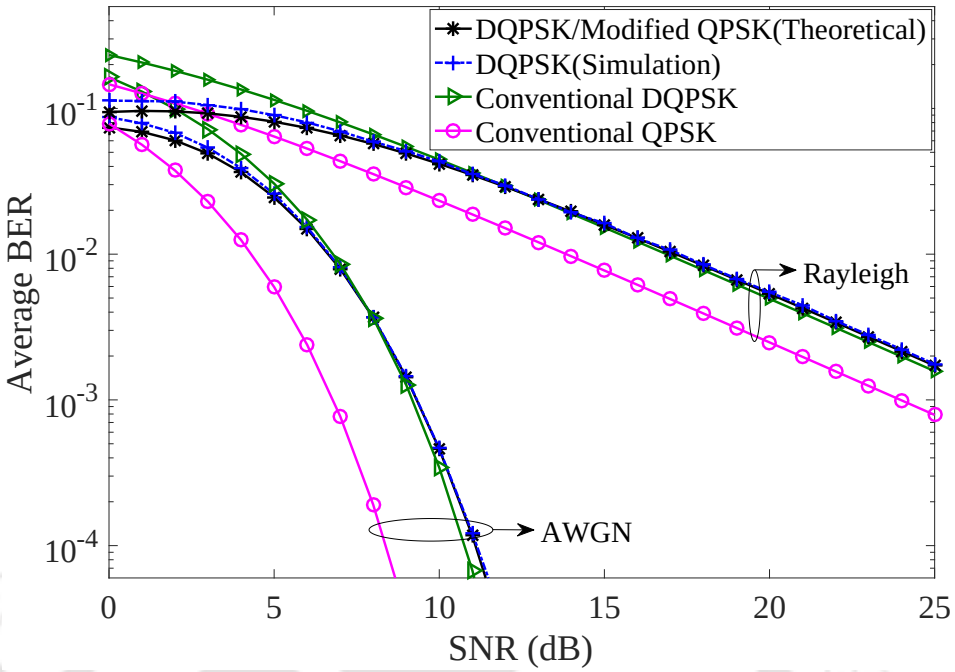

Figure 2.10: BER performance of the proposed DQPSK/QPSK systems employing SAW device.

correct estimation irrespective of erroneous bits estimated in the previous time duration. As the proposed demodulation processes for QPSK and DQPSK differ only in the decision logic, the BER performance of the proposed QPSK system would remain unchanged.

BER performance of the proposed DQPSK system using SAW device is shown in Figure 2.10 for AWGN and Rayleigh fading channels. Empirical BER based on Monte-Carlo simulation is also calculated and the results follow the theoretical counterpart. Performance of the proposed DQPSK system using SAW device is compared with conventional DQPSK system performance and found that its performance is almost similar to the conventional DQPSK system. It may be noted that the delay, multiplier, and integrator blocks in the conventional DQPSK system are replaced in the proposed design by a single SAW device, which performs the required delay and addition operations on the received signals in real time. The proposed QPSK system using DQPSK demodulator requires an additional $\approx$ 2.4 dB and $\approx$ 3 dB SNR as compared to conventional QPSK system to attain similar BER performance over AWGN and Rayleigh fading channels. It may be noted that the performance of the conventional QPSK system is calculated assuming the availability of a perfectly synchronous noise-free reference carrier at the receiver while the proposed QPSK has the advantage of performing the demodulation without the requirement of local reference carrier.

2.2.2 System Model Based on Linear Chirp Waveform

An up-chirp and the corresponding down-chirp covers the same signal bandwidth, thereby both waveforms can be used simultaneously without requiring additional bandwidth. Therefore, instead of using only single chirp waveform [26–28, 73], the system model presented in the previous section is extended in this section for LC waveforms, and a phase-coded chirp signal modulation-demodulation technique using both up-chirp and down-chirp through SAW-chirp devices is proposed to achieve a transmission rate of 3 bits per symbol duration. To the best of author's knowledge, design and performance analysis of such system has not yet been reported. Analytical expressions of SER performance of the system is derived and the performance of the system is evaluated under AWGN and Rayleigh fading channels.

2.2.2.1 Design of the Transmitter

For the proposed phase-coded chirp modulation using a SAW-chirp device, the input data stream is divided into 3-bit symbols, i.e., $b_2b_1b_0$ and possible combinations of a group of 3 bits can be $b_2b_1b_0 \in \{000, 001, 011, 010, 110, 111, 101, 100\}$. It can be found that for each possible symbol, the most significant bit (MSB), i.e., b_2 can be either 0 or 1. Thus, out of 3 bits, b_2 is encoded as the chirp-type of the transmitted signal, i.e., for $b_2 = 1$, up-chirp waveform is transmitted and for $b_2 = 0$, down-chirp waveform is transmitted. Modifying the encoding process of the previous design, b_1b_0 is encoded as the phase (θ_T) of the transmitted signal. The complete encoding process is presented in Table 2.4 and the block diagram of the proposed modulation for 3-bit symbol transmission is shown in Figure 2.11.

For a given signal duration and bandwidth, LC signal is generated through appropriate design of the IDT structures, i.e., changing the electrodes width and the spacing between the electrodes of the IDT of the SAW device [2, 13, 26, 28]. The schematic design of the SAW-chirp device is shown

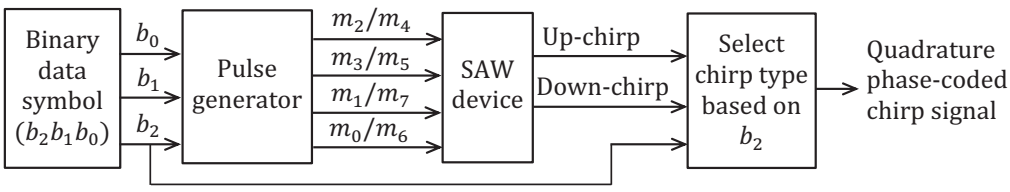

Figure 2.11: Block diagram of the proposed quadrature phase-coded chirp signal modulator using SAW-chirp device for 3-bit symbol transmission.

Table 2.4: Relation between input bits with signal phase and chirp type

Input MSB (b_2)	Carrier type	Input dibit (b_1b_0)	Carrier phase (θ_T)	Value of j in m_j
0	down-chirp	00	$\frac{3\pi}{2}$	0
1	up-chirp			4
0	down-chirp	01	π	1
1	up-chirp			5
0	down-chirp	11	$\frac{\pi}{2}$	3
1	up-chirp			7
0	down-chirp	10	0	2
1	up-chirp			6

in Figure 2.12. On applying an impulse, the same IDT structure provides both up-chirp and down-chirp waves traveling in opposite directions in a compact device as shown in Figure 2.12. To realize quadrature phase-coded chirp (QPCC) signal using SAW device, the gap between the input IDTs and the output IDTs is adjusted appropriately to introduce 4 possible phase delays of 0, $\pi/2$, π, $3\pi/2$, respectively, in the output signal. Considering gray coding for input bits, four possible combinations of 2 bits are $b_1b_0 \in \{10, 11, 01, 00\}$, and the corresponding mapping between b_1b_0 and signal phase is shown in Table 2.4. Based on $b_2b_1b_0$, the appropriate input IDT of the SAW device is selected as

$$m_j = 4b_2 + 2b_1 + b_0; \quad b_2, b_1, b_0 \in \{0, 1\}, \tag{2.27}$$

where $j = 0, 1, 2, \ldots, 7$. The selected IDT is excited by an impulse and based on b_2 either phase encoded up-chirp or phase encoded down-chirp is selected. Here, Θ_0 is the spacing between the input and the output IDT for $j = 2$ and 6. Using (1.7) and Table 2.4, a phase-coded up-chirp or down-chirp signal can be expressed as

$$s_i(t) = \cos\left[\omega_0 t + (-1)^{(i-1)}\pi\mu t^2 + \theta_T\right], \quad |t| \leq \frac{T}{2}, \tag{2.28}$$

where $i = 1, 2$, $\omega_0 = 2\pi f_0$, f_0 is the center frequency of the signal, T is the symbol duration, B is the signal bandwidth, $\mu = \frac{B}{T}$ is the chirp rate, and θ_T is the phase of the transmitted signal. $s_1(t)$ denotes phase-coded up-chirp signal and $s_2(t)$ denotes phase-coded down-chirp signal.

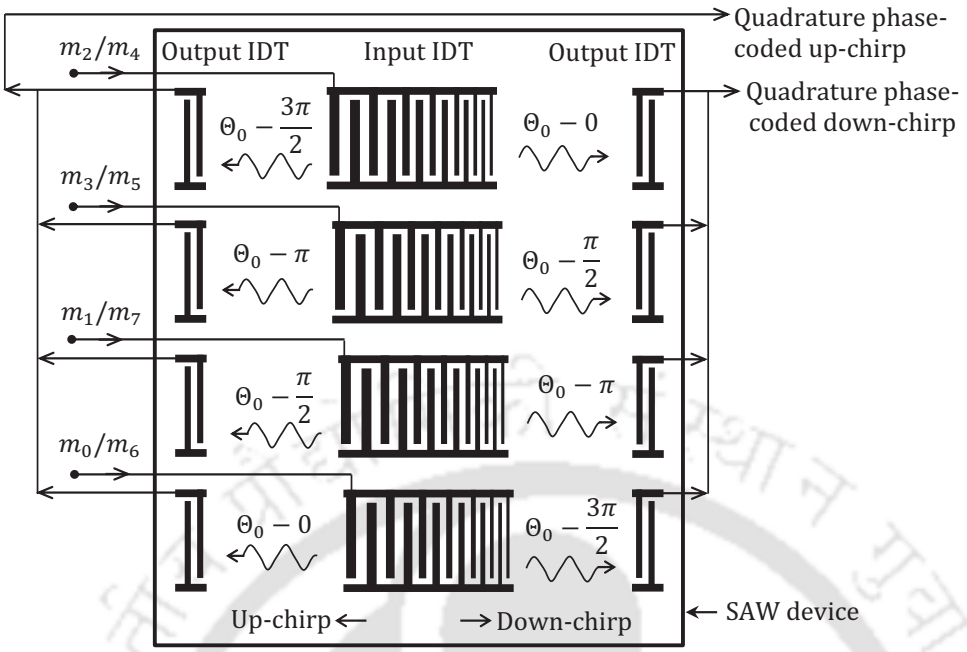

Figure 2.12: Block diagram of the modulator SAW-chirp device for quadrature phase-coded chirp signal modulation.

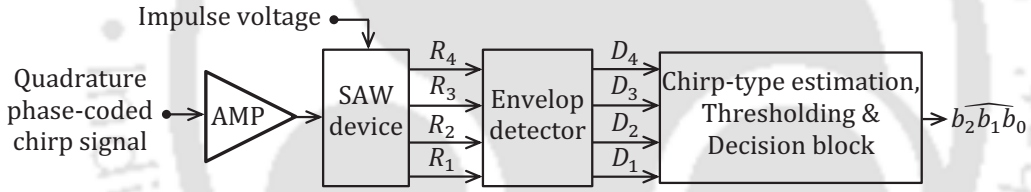

Figure 2.13: Block diagram of the demodulation process of quadrature phase-coded chirp signal using SAW-chirp device.

2.2.2.2 Design of the Receiver

The block diagram of the proposed QPCC signal demodulator using SAW-chirp device to demodulate 3-bit symbol is shown in Figure 2.13. The received signal is fed to the SAW-chirp device to estimate the phase of the transmitted chirp by addition of the received chirp signal with the locally generated chirp signal. The amplitudes of the output signals, obtained from the SAW device, are detected by the envelop detectors and passed through the thresholding and decision block. Based on the output of the decision block, the decoder estimates the transmitted bits.

The proposed SAW-chirp device, as shown in Figure 2.14, consists of two sections. In 'Section 1' addition of the incoming chirp signal with the locally generated chirp signals, $\cos\left(\omega_0 t + \pi\mu t^2 + \theta_0\right)$ and $\cos\left(\omega_0 t - \pi\mu t^2 + \theta_0\right)$, is performed. Considering that a quadrature phase-coded up-chirp is trans-

mitted, SAW-chirp device output, R_1 can be expressed as

$$\begin{aligned} R_1 &= \cos\left(\omega_0 t + \pi\mu t^2 + \theta_T\right) + \cos\left(\omega_0 t + \pi\mu t^2 + \theta_0\right) \\ &= 2\cos\left(\frac{\theta_T - \theta_0}{2}\right)\cos\left[\omega_0 t + \pi\mu t^2 + \left(\frac{\theta_T + \theta_0}{2}\right)\right], \end{aligned} \tag{2.29}$$

where θ_0 is the phase encoded in the locally generated chirp signal. Similarly, R_3 can be calculated as

$$\begin{aligned} R_3 &= \cos\left(\omega_0 t + \pi\mu t^2 + \theta_T\right) + \cos\left(\omega_0 t - \pi\mu t^2 + \theta_0\right) \\ &= 2\cos\left(\frac{\theta_T - \theta_0}{2} + \pi\mu t^2\right)\cos\left[\omega_0 t + \left(\frac{\theta_T + \theta_0}{2}\right)\right]. \end{aligned} \tag{2.30}$$

Output of the SAW device is passed through an envelop detector and the corresponding detector outputs for R_1 and R_3 are given by

$$D_1 = \left|2\cos\left(\frac{\theta_T - \theta_0}{2}\right)\right| = \left|2\cos\left(\frac{\Delta\theta}{2}\right)\right|, \tag{2.31}$$

$$D_3 = \left|2\cos\left(\frac{\theta_T - \theta_0}{2} + \pi\mu t^2\right)\right| = \left|2\cos\left(\frac{\Delta\theta}{2} + \pi\mu t^2\right)\right|, \tag{2.32}$$

where $\Delta\theta = \theta_T - \theta_0$. Considering $\theta_0 = 0$ and using Table 2.5, it can be found that the value of D_1 can be one of 2, $\sqrt{2}$, 0, and becomes equal to $\sqrt{2}$ for transmitted signal phase θ_T of $\pi/2$ and $3\pi/2$ which creates ambiguity in the decision block. Therefore, following a similar scheme from our previous design, 'Section 2' is introduced which performs the addition of the received signal with reference signal encoded with additional phase of $\pi/2$ as shown in Figure 2.14. The outputs, R_2 and R_4, of 'Section

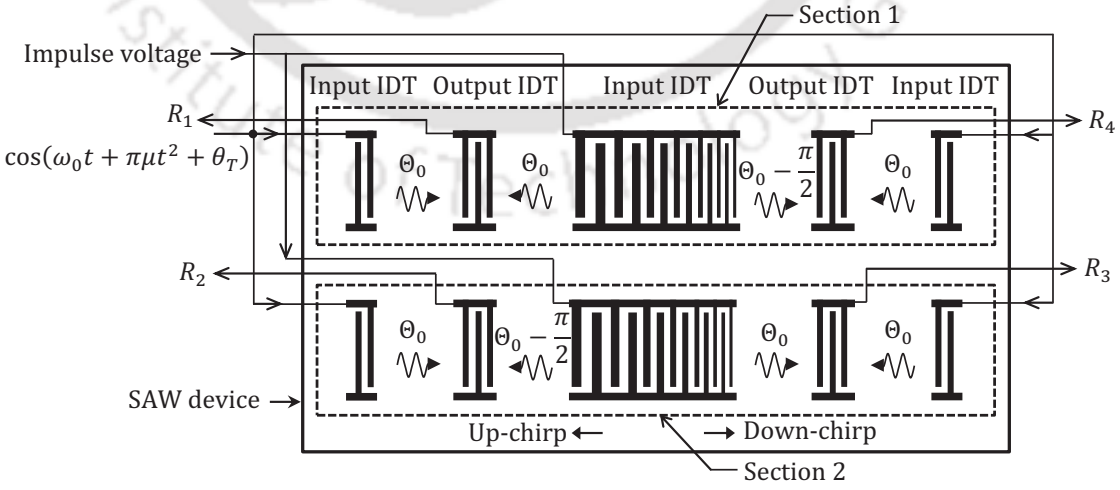

Figure 2.14: Schematic of the SAW-chirp device in the receiver.

Table 2.5: Outputs of envelop detectors for different phase differences

Up-chirp →	D_1	D_2	b_1b_0	D_3, D_4
Down-chirp→	D_3	D_4		D_1, D_2
$\triangle\theta \downarrow$				
0°	2	$\sqrt{2}$	10	≈ 2
90°	$\sqrt{2}$	2	11	≈ 2
180°	0	$\sqrt{2}$	01	≈ 2
270°	$\sqrt{2}$	0	00	≈ 2

2' can be calculated as

$$\begin{aligned} R_2 =& \cos\left(\omega_0 t + \pi\mu t^2 + \theta_T\right) + \cos\left(\omega_0 t + \pi\mu t^2 + \theta_0 + \frac{\pi}{2}\right) \\ =& 2\cos\left(\frac{\theta_T - \theta_0}{2} - \frac{\pi}{4}\right)\cos\left[\omega_0 t + \pi\mu t^2 + \left(\frac{\theta_T + \theta_0}{2} + \frac{\pi}{4}\right)\right]. \end{aligned} \tag{2.33}$$

$$\begin{aligned} R_4 =& \cos\left(\omega_0 t + \pi\mu t^2 + \theta_T\right) + \cos\left(\omega_0 t - \pi\mu t^2 + \theta_0 + \frac{\pi}{2}\right) \\ =& 2\cos\left(\frac{\theta_T - \theta_0}{2} - \frac{\pi}{4} + \pi\mu t^2\right)\cos\left[\omega_0 t + \left(\frac{\theta_T + \theta_0}{2} + \frac{\pi}{4}\right)\right]. \end{aligned} \tag{2.34}$$

Corresponding detector outputs are given by

$$D_2 = \left|2\cos\left(\frac{\Delta\theta}{2} - \frac{\pi}{4}\right)\right|. \tag{2.35}$$

$$D_4 = \left|2\cos\left(\frac{\Delta\theta}{2} - \frac{\pi}{4} + \pi\mu t^2\right)\right|. \tag{2.36}$$

It can be found that for $\Delta\theta = \pi/2, 3\pi/2$ the values of D_2 become distinct as given in Table 2.5 and solves the problem associated with D_1. Furthermore, as $0 \leq \cos(\theta) \leq 1$, D_3 and D_4 remain close to 2 due to the presence of the term $\pi\mu t^2$ as given in (2.32) and (2.36). Table 2.5 summaries the outputs of envelop detectors for different phase differences $\triangle\theta$ considering $\theta_0 = 0$. It also includes the envelop detector outputs if down-chirp is transmitted.

The outputs of the detectors are fed to the decision block for estimation of the chirp type as well as the phase of the transmitted signal. To identify the chirp type of the transmitted signal containing the information of b_2, the output of D_1 and D_2 is subtracted, i.e., $D_{12} = |D_1 - D_2|$ and the output of D_3 and D_4 is subtracted, i.e., $D_{34} = |D_3 - D_4|$. It can be found using Table 2.5 that, for transmission of

an up-chirp signal $D_{12} > D_{34}$ and $D_{34} \approx 0$ whereas for transmission of a down-chirp signal $D_{34} > D_{12}$ and $D_{12} \approx 0$. Thus, by comparing D_{12} and D_{34} one can find out the type of the transmitted chirp signal, and b_2 is estimated from the chirp type. The dibit, b_1b_0, is estimated according to Table 2.5 from the appropriate detector outputs– D_1, D_2 in case of up-chirp signal, i.e., if the output of D_1 is 2 or 0, then it would estimate the bits according to the logic of $\Delta\theta$, else logic block would consider the output of D_2 for the estimation of the dibit, and D_3, D_4 in case of down-chirp signal.

2.2.2.3 Performance Analysis over Rayleigh Fading Channel and Numerical Results

At the receiver, the received QPCC signal is given using (2.28) as

$$y_i(t) = \sqrt{E_s}\cos\left(\omega_0 t + (-1)^{(i-1)}\pi\mu t^2 + \theta_T\right) + w(t), \quad |t| \leq \frac{T}{2}, \tag{2.37}$$

where E_s is the symbol energy and $w(t)$ is AWGN with mean zero and variance $\frac{N_0}{2}$. Considering an up-chirp signal is transmitted, in absence of noise, D_1 and D_2 can have values 0, $\sqrt{2E_s}$ and $2\sqrt{E_s}$ while $\{D_3, D_4\} \approx 2\sqrt{E_s}$. Thus, a symbol error will occur if the receiver estimates the chirp type as down-chirp instead of up-chirp. Accordingly, the SEP can be expressed using (2.31), (2.32), (2.35), (2.36), and (2.37) as

$$P_{e_1} = Pr(|D_{34}| > |D_{12}| \ |\text{up-chirp}) \approx \frac{1}{2}\text{erfc}\left(\sqrt{\frac{E_D}{4N_0}}\right), \tag{2.38}$$

where E_D is the difference in energy from the outputs of D_{12} and D_{34}, and erfc$\{\cdot\}$ is the complementary error function [15]. Further, a symbol error will also occur when the chirp type, i.e., b_2 is estimated correctly but D_1 or D_2 is estimated incorrectly. To distinguish different transmitted dibits b_1b_0, encoded as the phase of the transmitted signal, a similar process described in Section 2.2.1.3 is considered, i.e., the decision region for D_1 and D_2 is divided into 3 parts with 2 threshold levels as shown in Figure 2.15. Thus, the probability of D_1 and D_2 to be in the erroneous decision region can be calculated as

$$P_{eD_1} = Pr\{\beta_1 < D_1 < \beta_2\}, \tag{2.39}$$

$$P_{eD_2} = Pr\{\beta_3 < D_2 < \beta_4\}, \tag{2.40}$$

where β_1 and β_2 are threshold levels for D_1 and β_3 and β_4 are threshold levels for D_2. Similarly, in case of transmission of down-chirp signal, the probability of D_3 and D_4 to be in the erroneous decision region can be calculated using Figure 2.15. Therefore, the probability of symbol error for the

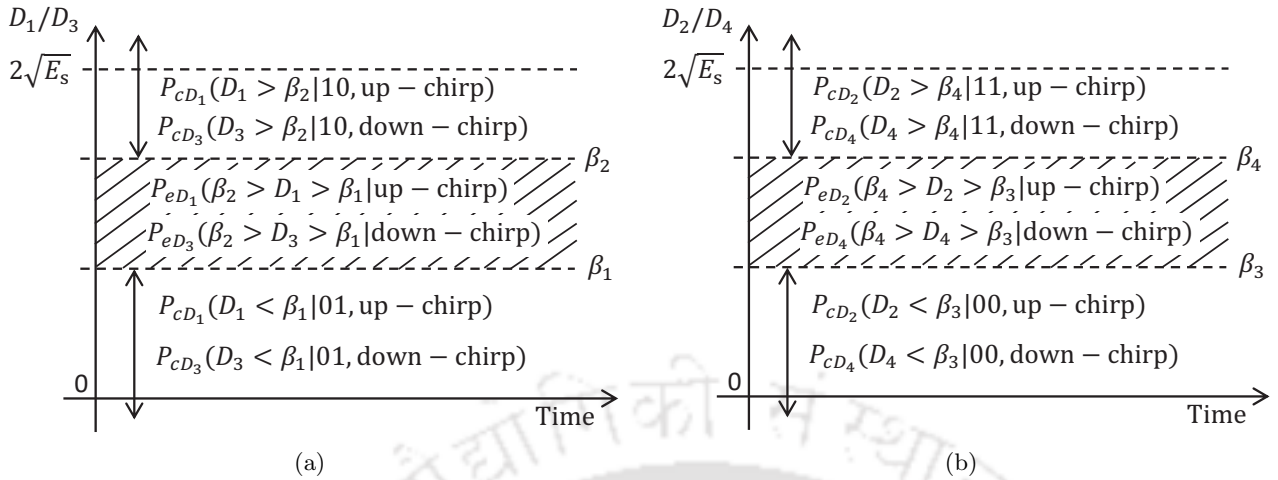

Figure 2.15: Schematic diagram of threshold levels for (a) D_1 and D_3, (b) D_2 and D_4. P_c denotes the probability of correct detection and P_e denotes the probability that the symbol will fall in the erroneous decision region.

communication system using SAW-chirp device for 3-bit symbol transmission can be expressed using (2.38), (2.39), and (2.40) as

$$P_e = 1 - (1 - P_{e_1})\left[1 - (P_{eD_1}P_{eD_2})\right]. \tag{2.41}$$

As the noise is considered to have Gaussian probability density function (PDF), P_{eD_1} can be simplified as

$$P_{eD_1} = \frac{1}{2}\,\text{erfc}\left(\frac{\beta_1 - \left|2\sqrt{E_s}\cos\left(\frac{\Delta\theta}{2}\right)\right|}{\sqrt{2\sigma^2}}\right) - \frac{1}{2}\,\text{erfc}\left(\frac{\beta_2 - \left|2\sqrt{E_s}\cos\left(\frac{\Delta\theta}{2}\right)\right|}{\sqrt{2\sigma^2}}\right), \tag{2.42}$$

where $\sigma^2 = N_0$.

Expressing β_1, β_2, β_3 and β_4 in terms of symbol energy, using (2.37), (2.39), and (2.42), P_{eD_1} can be given by

$$P_{eD_1} = \frac{1}{2}\,\text{erfc}\left[\sqrt{\frac{E_s}{2N_0}}\left(x_1 - 2\left|\cos\left(\frac{\Delta\theta}{2}\right)\right|\right)\right] - \frac{1}{2}\,\text{erfc}\left[\sqrt{\frac{E_s}{2N_0}}\left(x_2 - 2\left|\cos\left(\frac{\Delta\theta}{2}\right)\right|\right)\right], \tag{2.43}$$

where $\beta_1 = x_1\sqrt{E_s}$, $\beta_2 = x_2\sqrt{E_s}$, and x_1, x_2 are positive real numbers. Similarly, from the outputs of the 'Stage 2' of the SAW-chirp device, P_{eD_2} can be evaluated as

$$P_{eD_2} = \frac{1}{2}\,\text{erfc}\left[\sqrt{\frac{E_s}{2N_0}}\left(x_3 - 2\left|\cos\left(\frac{\Delta\theta}{2} - \frac{\pi}{4}\right)\right|\right)\right] - \frac{1}{2}\,\text{erfc}\left[\sqrt{\frac{E_s}{2N_0}}\left(x_4 - 2\left|\cos\left(\frac{\Delta\theta}{2} - \frac{\pi}{4}\right)\right|\right)\right], \tag{2.44}$$

where $\beta_3 = x_3\sqrt{E_s}$, $\beta_4 = x_4\sqrt{E_s}$, and x_3, x_4 are positive real numbers. Substituting (2.38), (2.43),

(2.44) in (2.41), the SER of the system is expressed as

$$P_e = 1 - \left[1 - \frac{1}{2}\,\mathrm{erfc}\left(\sqrt{\frac{E_D}{4N_0}}\right)\right]\left[1 - \frac{1}{4}\left(\left[\,\mathrm{erfc}\left(\sqrt{\frac{\gamma_s}{2}}\,(x_1-\rho_1)\right) - \,\mathrm{erfc}\left(\sqrt{\frac{\gamma_s}{2}}\,(x_2-\rho_1)\right)\right]\right.\right.$$
$$\left.\left.\times\left[\,\mathrm{erfc}\left(\sqrt{\frac{\gamma_s}{2}}\,(x_3-\rho_2)\right) - \,\mathrm{erfc}\left(\sqrt{\frac{\gamma_s}{2}}\,(x_4-\rho_2)\right)\right]\right)\right], \quad (2.45)$$

where $\gamma_s = \frac{E_s}{N_0}$, $\rho_1 = 2\left|\cos\left(\frac{\Delta\theta}{2}\right)\right|$, $\rho_2 = 2\left|\cos\left(\frac{\Delta\theta}{2} - \frac{\pi}{4}\right)\right|$.

Considering the signal is received over a flat Rayleigh fading channel with channel fading coefficient α and $\Omega = \overline{\alpha^2}$, the average SER $\overline{P_e}$ for the system is calculated by integrating the error probability in AWGN, given by (2.45), over the Rayleigh fading distribution [16] and can be evaluated as

$$\overline{P_e} = 1 - \left[1 - \frac{1}{2}\left(1 - \sqrt{\frac{\Omega E_D}{4N_0 + \Omega E_D}}\right)\right]$$
$$\times\left[1 - \frac{1}{4}\left(\left[\left(\frac{\Omega E_s\left(\frac{x_2}{\sqrt{\Omega}} - \rho_1\right)^2}{2N_0 + \Omega E_s\left(\frac{x_2}{\sqrt{\Omega}} - \rho_1\right)^2}\right)^{\frac{1}{2}} - \left(\frac{\Omega E_s\left(\frac{x_1}{\sqrt{\Omega}} - \rho_1\right)^2}{2N_0 + \Omega E_s\left(\frac{x_1}{\sqrt{\Omega}} - \rho_1\right)^2}\right)^{\frac{1}{2}}\right]\right.$$
$$\left.\times\left[\left(\frac{\Omega E_s\left(\frac{x_4}{\sqrt{\Omega}} - \rho_2\right)^2}{2N_0 + \Omega E_s\left(\frac{x_4}{\sqrt{\Omega}} - \rho_2\right)^2}\right)^{\frac{1}{2}} - \left(\frac{\Omega E_s\left(\frac{x_3}{\sqrt{\Omega}} - \rho_2\right)^2}{2N_0 + \Omega E_s\left(\frac{x_3}{\sqrt{\Omega}} - \rho_2\right)^2}\right)^{\frac{1}{2}}\right]\right)\right]. \quad (2.46)$$

SER performance of the proposed quadrature phase-coded-SAW-chirp system for transmission of 3-bit symbol using LC signals is shown in Figure 2.16 under AWGN and Rayleigh fading channels. System performance is also evaluated considering that the system is using LCs generated from SAW devices through finite element simulation in COMSOL Multiphysics. Simulation parameters for the SAW device are as follows– the substrate material is chosen as 128° Y-X $LiNbO_3$ having a surface acoustic wave velocity of 3979 m/s [13], the center frequency is considered as 80 MHz with a signal duration T of 5 μs and bandwidth B of 3 MHz. The performances match closely with the corresponding analytical results. Performances of the proposed system are compared with that of the SAW-chirp communication systems reported in [27, 28, 73], considering that the systems transmit 3-bit symbol using 8-PSK modulation as the systems used single chirp carrier. The systems [27, 28, 73] provide similar level of SER performances, as shown in Figure 2.16, and the performance curves get overlapped. The simulation results in Figure 2.16 indicate that the proposed system provides better performance over the SAW-chirp systems in [27, 28, 73], e.g., for an SER of 10^{-2}, a gain of 2.5 dB and 3.2 dB in SNR, $\frac{E_s}{N_0}$, is observed for AWGN and Rayleigh fading channels, respectively. Improved performance is achieved mainly due to less number of comparisons as two carriers– up-chirp and down-chirp are used.

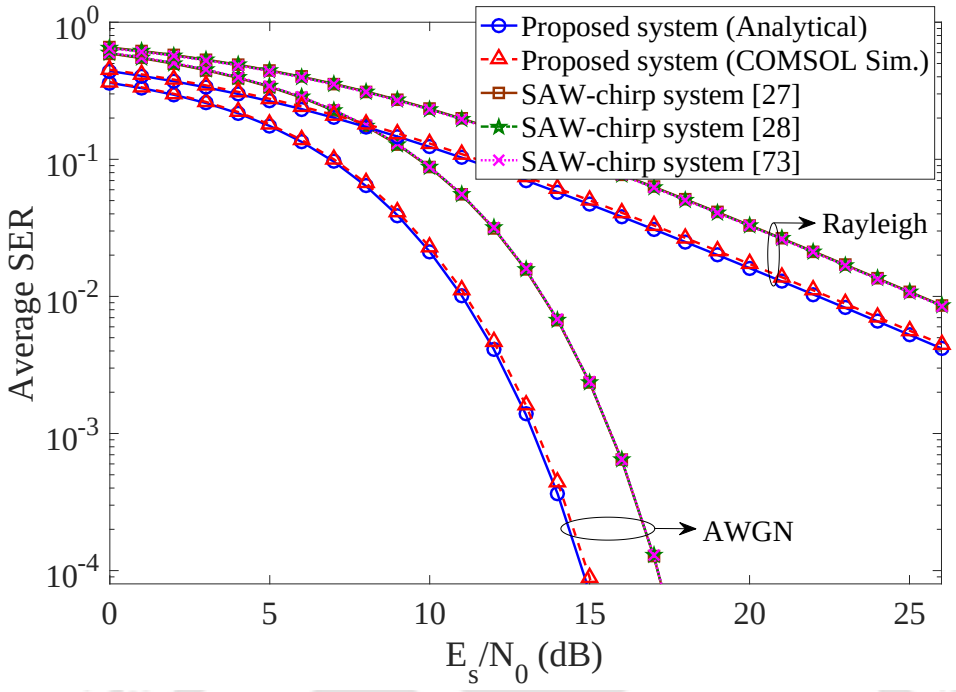

Figure 2.16: SER performance of the proposed quadrature phase-coded-SAW-chirp system for transmission of 3-bit symbol using linear chirps in AWGN and Rayleigh fading channels.

Moreover, the system does not require additional bandwidth. Chirp communication systems employing chirp-BOK type scheme [9] would require three sets of up-chirp and down-chirp waveforms [4] for the transmission of 3-bit symbols and thus, it would require much higher bandwidth as compared to the proposed design which requires only one set of up-chip and down-chirp. The data rate of the system will depend on the symbol duration and can be varied according to the application requirement.

2.3 Phase-Coded Chirp Waveforms for Multiuser Communication System

The system presented in the previous section is intended for single user scenario, whereas in general, most of the communication systems operate in a multiuser scenario. Inclusion of multiple users, operating simultaneously, leads to the fact that along with the required signal, the receiver also receives signals intended for other users resulting in interference at the receiver and thereby affecting the performance of the system. To enable serving multiple users through chirp waveform, in this work, design of phase-coded chirp waveform is presented considering both linear and nonlinear chirp waveforms in which a PN-code sequence is embedded within a single chirp signal. The associated system performance is evaluated in a multiuser scenario where the use of PN-code helps to reduce the

MAI. In this context, firstly, a general design for n^{th} order chirp is presented.

Given a bandwidth B with starting and ending frequencies f_{L} and f_{H} respectively and the dispersion time T, a chirp waveform with n^{th} order can be constructed as follows:

(1) The chirp function ψ is defined, e.g., for an n^{th} order chirp, $\psi_n(t) = \left(\frac{t}{T}\right)^n$ with $n \geq 1$. In case of LC $n = 1$.

(2) Perform the integral

$$\varrho_n(t) = \int_0^t \psi_n(\tau)\ d\tau = \frac{T}{n+1}\left(\frac{t}{T}\right)^{n+1}. \tag{2.47}$$

(3) The up-chirp and down-chirp waveforms can be represented using (1.5) and (1.6) as

$$s_1^n(t) = \cos\left[2\pi\left(f_{\text{L}}t + \vartheta\varrho_n(t)\right)\right] = \cos\left[2\pi\left(f_{\text{L}}t + \frac{\vartheta T}{n+1}\left(\frac{t}{T}\right)^{(n+1)}\right)\right], \quad 0 \leq t \leq T, \tag{2.48}$$

$$s_2^n(t) = \cos\left[2\pi\left(f_{\text{H}}t - \vartheta\varrho_n(t)\right)\right] = \cos\left[2\pi\left(f_{\text{H}}t - \frac{\vartheta T}{n+1}\left(\frac{t}{T}\right)^{(n+1)}\right)\right], \quad 0 \leq t \leq T, \tag{2.49}$$

where the parameter ϑ is equal to $f_{\text{H}} - f_{\text{L}}$, i.e., B for an n^{th} power chirp.

2.3.1 Proposed Design of Phase-Coded Chirp Waveform

The principle for designing the proposed phase-coded chirp waveform lies in calculating the number of cycles present in the waveform and the associated time instant at which each cycle starts so that the phase of each cycle can be adjusted according to the entries of a binary PN-code sequence.

2.3.1.1 Using Linear Chirp

The chirp waveform in (2.48) can be expressed for LC by substituting $n = 1$ and is given by

$$\begin{aligned} s_1(t) &= \cos\left[2\pi\left(f_{\text{L}}t + \frac{(f_{\text{H}} - f_{\text{L}})T}{2}\left(\frac{t}{T}\right)^2\right)\right]\text{rect}\left(\frac{t - \frac{T}{2}}{T}\right), \quad 0 \leq t \leq T \\ &= \cos\left[2\pi\left(f_{\text{L}}t + \frac{\mu}{2}t^2\right)\right]\text{rect}\left(\frac{t - \frac{T}{2}}{T}\right), \end{aligned} \tag{2.50}$$

where $\mu = \frac{f_{\text{H}} - f_{\text{L}}}{T} = \frac{B}{T}$, $\text{rect}\left(\frac{t}{T}\right)$ indicates a rectangular function with $|t| \leq \frac{T}{2}$ and center at $t = 0$. Now, if the number of cycles present in the chirp waveform is N_{c}, it can be related to the phase of the signal and expressed using (2.48) and (2.50) as

$$\begin{aligned} 2\pi N_{\text{c}} &= 2\pi\left[(f_{\text{L}}T + \vartheta\varrho(T)) - (\vartheta\varrho(0))\right] \\ \Rightarrow N_{\text{c}} &= \frac{(f_{\text{H}} + f_{\text{L}})T}{2} \approx f_0 T, \end{aligned} \tag{2.51}$$

where f_0 is the center frequency. Moreover, maximum number of possible phase transitions in a LC signal would be the number of cycles N_c present in it and the phase-transition points at time instants t_n, $n = 0, 1, 2, \ldots, N_c - 1$, can be evaluated using (2.50) and (2.51) as

$$2\pi\left(f_L t_n + \frac{\mu}{2}t_n^2\right) = 2\pi n$$

$$t_n = \frac{f_L}{\mu}\left[-1 + \left(1 + \frac{2\mu n}{f_L^2}\right)^{\frac{1}{2}}\right]. \tag{2.52}$$

Considering a binary PN-code sequence C of length N such that $N_c = zN$, i.e., change in phase happens after every z number of cycles in the signal. Using (2.50) and (2.52) a binary phase-coded linear up-chirp waveform can be represented as

$$p_1(t) = \sum_{n=0}^{N_c-1} C(n') \cos\left[2\pi\left(f_L t + \frac{\mu}{2}t^2\right)\right] \text{rect}\left[\frac{\left(t - \frac{T}{2}\right) - t_n}{T_n}\right], \quad 0 \le t \le T, \tag{2.53}$$

where $n' = \lfloor \frac{n}{z} \rfloor$, $z \ge 1$, $\lfloor \cdot \rfloor$ denotes the floor operator, $C(n') = \pm 1$ denotes the n'^{th} index value of C, and $T_n = t_{n+1} - t_n$. Similarly, a binary phase-coded linear down-chirp waveform can be expressed using (2.49) and (2.51) as

$$p_2(t) = \sum_{n=0}^{N_c-1} C(n') \cos\left[2\pi\left(f_H t - \frac{\mu}{2}t^2\right)\right] \text{rect}\left[\frac{\left(t - \frac{T}{2}\right) - t_n}{T_n}\right], \quad 0 \le t \le T, \tag{2.54}$$

where $T_n = t_{n+1} - t_n$ and t_n is calculated as

$$t_n = \frac{f_H}{\mu}\left[1 + \left(1 - \frac{2\mu n}{f_H^2}\right)^{\frac{1}{2}}\right], \quad n = 0, 1, 2, \ldots, N_c - 1. \tag{2.55}$$

The associated autocorrelation and cross-correlation for phase-coded LC waveforms $p_i(t)$, $i \in \{1, 2\}$, can be expressed using (1.9), (1.10), and (1.13) as

$$R'_{ii'}(\tau) = \int_{-\infty}^{+\infty} p_i(t) p_{i'}(t - \tau) dt, \tag{2.56}$$

where $i, i' \in \{1, 2\}$ and for a given C, N_c, and z, the value of $R'_{ii'}(\tau)$ can be evaluated numerically. For $i = i'$, $R'_{ii}(\tau)$ gives the autocorrelation output of $p_i(t)$ while for $i \ne i'$, $R'_{ii'}(\tau)$ gives the cross-correlation output $p_i(t)$. Examples of phase-coded linear up-chirp and down-chirp signals are illustrated in Figure 2.17(a) and Figure 2.17(b), respectively, considering $z = 3$.

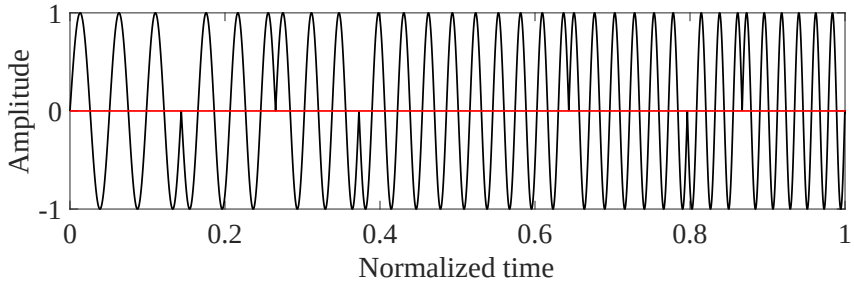

(a)

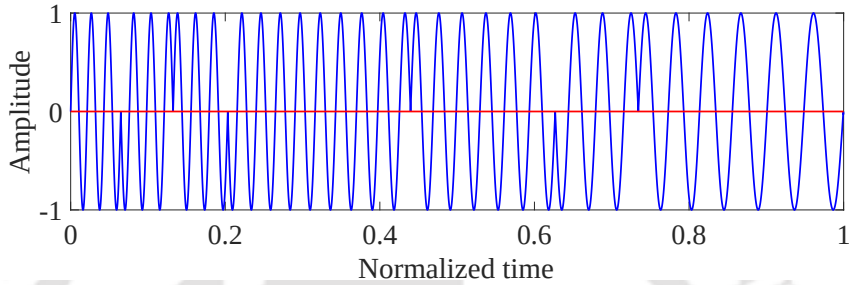

(b)

Figure 2.17: (a) A linear up-chirp signal phase-coded with sequence [1 0 1 0 0 1 1 0 1 1], (b) A linear down-chirp signal phase-coded with sequence [1 0 1 0 0 1 1 0 1 1].

2.3.1.2 Using Nonlinear Chirp

For an exponential type NLC, the instantaneous frequency $f(t)$ can be expressed as

$$f(t) = f_{\mathrm{L}}\vartheta^{\psi(t)}, \tag{2.57}$$

where the parameters $\vartheta = \frac{f_{\mathrm{H}}}{f_{\mathrm{L}}}$ and $\psi(t) = \frac{t}{T}$, and the associated chirp waveform is given using (1.1) as

$$s(t) = \cos\left[2\pi\phi(t)\right] \mathrm{rect}\left(\frac{t-\frac{T}{2}}{T}\right), \quad 0 \le t \le T, \tag{2.58}$$

where $\phi(t) = \int_0^t f(t)dt = \frac{\vartheta^{\frac{t}{T}}-1}{\ln\left(\vartheta^{\frac{1}{T}}\right)}$, $\ln(\cdot)$ denotes the natural logarithm. Accordingly, simplifying (2.58) gives the exponential up-chirp waveform as

$$s_1(t) = \cos\left[2\pi f_{\mathrm{L}}\left(\frac{\beta_1^t - 1}{\ln(\beta_1)}\right)\right] \mathrm{rect}\left(\frac{t-\frac{T}{2}}{T}\right), \quad 0 \le t \le T, \tag{2.59}$$

where $\beta_1 = \vartheta^{\frac{1}{T}} = \left(\frac{f_{\mathrm{H}}}{f_{\mathrm{L}}}\right)^{\frac{1}{T}}$ is the chirp rate of the exponential chirp signal. Following a similar design process as that of phase-coded LC waveform, the number of cycles N_{c} and the phase transition time

instants t_n for an exponential up-chirp waveform can be given by

$$N_{\mathrm{c}} = f_{\mathrm{L}} \left(\frac{\beta_1^T - 1}{\ln(\beta_1)} \right) = \frac{f_{\mathrm{H}} - f_{\mathrm{L}}}{\ln\left(\left(\frac{f_{\mathrm{H}}}{f_{\mathrm{L}}} \right)^{\frac{1}{T}} \right)}, \tag{2.60}$$

$$t_n = \frac{\ln\left(\frac{n \ln(\beta_1)}{f_{\mathrm{L}}} + 1 \right)}{\ln(\beta_1)}, \quad n = 0, 1, \ldots, N_{\mathrm{c}} - 1, \tag{2.61}$$

and using (2.59), (2.60), and (2.61), a binary phase-coded exponential up-chirp waveform can be represented as

$$v_1(t) = \sum_{n=0}^{N_{\mathrm{c}}-1} C(n') \cos\left[2\pi f_{\mathrm{L}} \left(\frac{\beta_1^t - 1}{\ln(\beta_1)} \right) \right] \mathrm{rect}\left[\frac{\left(t - \frac{T}{2}\right) - t_n}{T_n} \right], \quad 0 \le t \le T, \tag{2.62}$$

where C is a binary PN-code sequence of length N with $C(n') = \pm 1$ such that $N_{\mathrm{c}} = zN$, $n' = \lfloor \frac{n}{z} \rfloor$, $z \ge 1$, and $T_n = t_{n+1} - t_n$. Similarly a binary phase-coded exponential down-chirp waveform can be expressed as

$$v_2(t) = \sum_{n=0}^{N_{\mathrm{c}}-1} C(n') \cos\left[2\pi f_{\mathrm{H}} \left(\frac{\beta_2^t - 1}{\ln(\beta_2)} \right) \right] \mathrm{rect}\left[\frac{\left(t - \frac{T}{2}\right) - t_n}{T_n} \right], \quad 0 \le t \le T, \tag{2.63}$$

where $\beta_2 = \left(\frac{f_{\mathrm{L}}}{f_{\mathrm{H}}} \right)^{\frac{1}{T}}$, $T_n = t_{n+1} - t_n$, and t_n can be calculated as

$$t_n = \frac{\ln\left(\frac{n \ln(\beta_2)}{f_{\mathrm{H}}} + 1 \right)}{\ln(\beta_2)}, \quad n = 0, 1, \ldots, N_{\mathrm{c}} - 1. \tag{2.64}$$

The associated autocorrelation and cross-correlation for phase-coded exponential chirp waveforms $v_i(t)$, $i \in \{1, 2\}$, given in (2.62) and (2.63) can be evaluated numerically from (2.56).

2.3.2 System Model

A multiuser communication system is considered with K pairs of transmitters and receivers communicating simultaneously. The block diagram of the system using binary phase-coded LC signals shown in Figure 2.18 is essentially a multiuser chirp-BOK system. In case, the communication system is using NLC waveforms, the phase-coded LCs will be replaced by the phase-coded exponential chirp waveforms. It is considered that binary data symbol $b = \{1, 0\}$ is independent and equally likely where '1' is represented by phase-coded up-chirp signal ($i = 1$) and '0' is represented by phase-coded down-chirp signal ($i = 2$). It is assumed that the chirp waveforms have the same center frequency and bandwidth for all the communicating users. To distinguish between signals transmitted for different

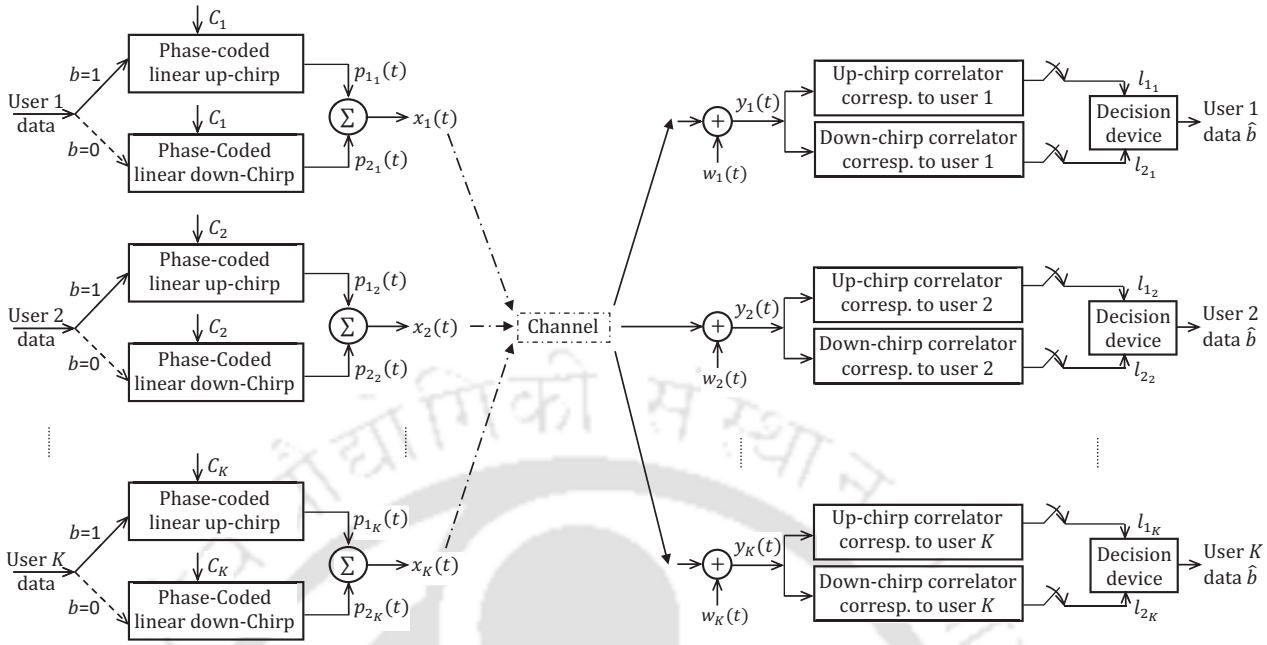

Figure 2.18: Block diagram of a multiuser communication system using binary phase-coded LC signals.

users, PN spreading codes having low cross-correlation values are used [75]. At every transmitter, the linear up and down chirp signals are modulated with a unique PN-spreading code, e.g., $C_1, C_2, \ldots, C_K$ and can be expressed for k^{th} transmitter as

$$p_{i_k}(t) = \sum_{n=0}^{N_c-1} C_k(n') \cos\left[2\pi\left((f_L + (i-1)B)\,t + (-1)^{i-1}\frac{\mu}{2}t^2\right)\right] \text{rect}\left[\frac{\left(t-\frac{T}{2}\right)-t_n}{T_n}\right], \quad 0 \le t \le T, \tag{2.65}$$

where $i \in \{1, 2\}$ and $k = 1, 2, \ldots, K$. Accordingly, the received signal at the k^{th} receiver can be expressed using (2.65) as

$$y_k(t) = \sum_{r=1}^{K} \sqrt{E_s}\, p_{i_r}(t) + w_k(t), \tag{2.66}$$

where $p_{i_r}(t)$ is the transmitted signal for r^{th} receiver and can be either $p_1(t)$ or $p_2(t)$ depending upon the transmitted data symbol. E_s is the signal energy and $w_k(t)$ is white Gaussian noise with zero mean and variance $N_0/2$. Each receiver consists of a pair of correlators– up-chirp correlator and down-chirp correlator. The received signal is fed to the correlators to compute the cross-correlation of the input signal with the reference chirps, given by (2.65) for k^{th} receiver, and the outputs are compared to estimate the transmitted data symbol b_k for k^{th} receiver, i.e., if l_{1_k} and l_{2_k} are the sampled outputs of up-chirp correlator and down-chirp correlator, respectively, then b_k will be estimated as '1' for $l_{1_k} > l_{2_k}$ else b_k will be estimated as '0'. In case of phase-coded NLC, exponential chirps are modulated using

C_k and are expressed for k^{th} transmitter as

$$v_{i_k}(t) = \sum_{n=0}^{N_c-1} C_k(n') \cos\left[2\pi \left(f_L + (i-1)B\right)\left(\frac{\beta_i^t - 1}{\ln(\beta_i)}\right)\right] \text{rect}\left[\frac{\left(t - \frac{T}{2}\right) - t_n}{T_n}\right], \quad 0 \le t \le T, \tag{2.67}$$

where $i \in \{1, 2\}$. The associated $y_k(t)$ in (2.66) is obtained by replacing $p_{i_r}(t)$ with $v_{i_r}(t)$.

2.3.3 Performance Analysis

At the k^{th} receiver, as shown in Figure 2.18, the received chirp signal is fed to both up-chirp correlator and down-chirp correlator. Each correlator performs multiplication of the input signal $y_k(t)$ with respective reference chirps, given in (2.65) for phase-coded LC or in (2.67) for phase-coded NLC, followed by integration. The sampled output of the up-chirp correlator, considering for the transmission of $b_k = 1$, can be expressed as

$$l_{1_k} = \sqrt{E_s}\zeta_{1_k 1_k} + \sum_{r=1; r\neq k}^{K} \sqrt{E_s}\zeta_{1_k i_r} + w'_{1_k}, \tag{2.68}$$

where $\zeta_{1_k 1_k}$, $\zeta_{1_k i_r}$, and w'_{1_k} are the sampled correlation outputs corresponding to the desired signal, the signal for other receivers, and the noise, respectively, and are evaluated using (2.56). Similarly, the sampled output of the down-chirp correlator can be expressed as

$$l_{2_k} = \sqrt{E_s}\zeta_{2_k 1_k} + \sum_{r=1; r\neq k}^{K} \sqrt{E_s}\zeta_{2_k i_r} + w'_{2_k}, \tag{2.69}$$

where $\zeta_{2_k 1_k}$, $\zeta_{2_k i_r}$, and w'_{2_k} are evaluated using (2.56). At the receiver, the transmitted symbol is estimated by comparing the outputs of the correlators, i.e., according to the following decision logic [76]

$$l_{1_k} \underset{\widehat{b}_k=0}{\overset{\widehat{b}_k=1}{\gtrless}} l_{2_k}. \tag{2.70}$$

Considering that $b_k = 1$ is transmitted ($i = 1$), the associated probability of bit error for k^{th} receiver can be expressed as [36, 76]

$$P_{e_k} = Pr(l_{1_k} \le l_{2_k} \mid p_{1_k}(t)), \tag{2.71}$$

and following [3, 76, 77], the BER for the k^{th} receiver can be evaluated using (2.68), (2.69) as

$$P_{e_k} = Q\left[\left\{\frac{E_s\left(1 - \rho_2^{kk}\right)}{N_0 + \sum_{r=1; r\neq k}^{K} E_s \rho^{kr}}\right\}^{\frac{1}{2}}\right], \tag{2.72}$$

where $\rho^{kr} = \rho_1^{kr} - \rho_2^{kr}$, and ρ_2^{kk}, ρ_1^{kr}, and ρ_2^{kr} are the normalized values of $\zeta_{2_k 1_k}$, $\zeta_{1_k i_r}$, and $\zeta_{2_k i_r}$, respectively. $Q\{\cdot\}$ is the Q-function [16]. Under the scenario of multiple users (K), following central limit theorem the interference at the receiver is expected to be Gaussian for large value of K.

2.3.4 Numerical Results and Discussion

The BER performance of the proposed multiuser communication system using binary phase-coded linear and nonlinear chirp signals are simulated through Monte-Carlo simulation. We have considered a TB product of 43 with $z = 8$ for the phase-coded chirp waveforms while for the phase encoding Gold code sequences of length $N = 63$ are used. The results shown in Figure 2.19(a) and Figure 2.19(b) present the system performance for different number of users under AWGN channel considering phase-coded LC and phase-coded NLC waveforms, respectively. Results indicate that with the increase of the number of users, the performance of the system degrades due to the increase of interference as the up-chirp and the down-chirp are not strictly orthogonal. Further, it is found that, the system performances under phase-coded linear and nonlinear chirp waveforms are nearly similar, and use of NLC waveform does not particularly provide any additional advantages over LC waveform.

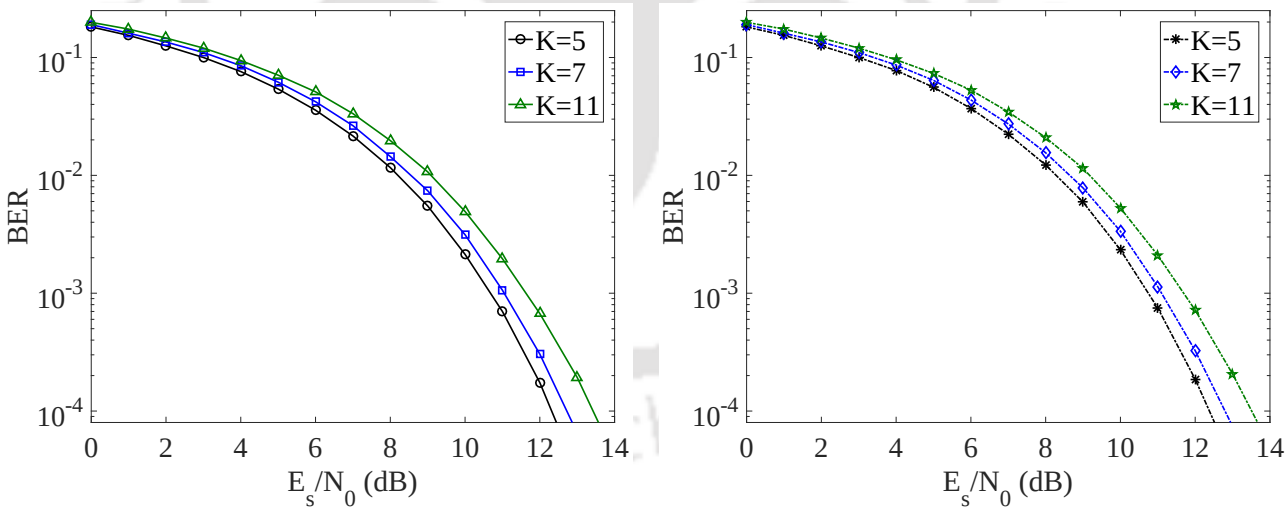

Figure 2.19: BER performance of multiuser communication system employing (a) Binary phase-coded LC waveforms, (b) Binary phase-coded NLC waveforms.

2.4 Chirp Waveforms of Equal Chirp Rate for Multiuser Communication System

The analysis on phase-coded chirp waveforms indicates that the correlation between the waveforms for different users depends on the properties of the associated PN-code sequences which in turn controls the MAI. As a suitable alternative, use of orthogonal waveforms can improve the overall MAI. Therefore, in an attempt to minimize the cross-correlation between chirp waveforms, in this work a set of orthogonal up-chirp and orthogonal down-chirp waveforms is designed for multiuser chirp-BOK system and associated system performance is evaluated.

2.4.1 Proposed Design of Chirp Waveform with Equal Chirp Rate

An LC waveform having bandwidth B and dispersion time T can be expressed, following (1.7), as

$$s_{i=1,2}(t) = \cos\left[2\pi\left(f_0 t + (-1)^{(i-1)}\frac{1}{2}\mu t^2\right)\right], \quad -\frac{T}{2} \le t \le \frac{T}{2}, \tag{2.73}$$

In the proposed set of LC waveforms, it is considered that all up-chirp or all down-chirp signals have the same chirp rate and bandwidth. The associated frequency variation of the waveforms is shown in Figure 2.20 where each pair of up-chirp and down-chirp waveforms shares the same center frequency and adjacent pairs maintain a frequency separation of Δf. Considering the signal set consists of K number of up-chirp and down-chirp waveforms, using (2.73), k^{th} pair of chirp waveforms can be represented as

$$s_{i_k}(t) = \cos\left[2\pi\left(f_{0_k} t + \frac{1}{2}(-1)^{(i-1)}\mu t^2\right)\right], \quad -\frac{T}{2} \le t \le \frac{T}{2}, \tag{2.74}$$

where $i = 1, 2$, $k = 1, 2, \ldots, K$, f_{0_k} is the center frequency of the k^{th} chirp waveform with $\Delta f = f_{0_{k+1}} - f_{0_k}$, $s_{1_k}(t)$ and $s_{2_k}(t)$ indicate the up-chirp and down-chirp waveforms, respectively, and B_{total} is the overall bandwidth. In addition, keeping Δf constant for adjacent chirp signals and an overlap between their bandwidths restricts the total bandwidth B_{total} requirement as shown in Figure 2.20. In equivalent complex form the chirp waveforms in (2.74) can be given using (1.8) as

$$\breve{s}_{i_k}(t) = e^{j2\pi\left(f_{0_k} t + \frac{1}{2}(-1)^{(i-1)}\mu t^2\right)}, \quad -\frac{T}{2} \le t \le \frac{T}{2}, \tag{2.75}$$

where $s_{i_k}(t) = \Re\{\breve{s}_{i_k}(t)\}$ and $\Re\{\cdot\}$ indicates the real part.

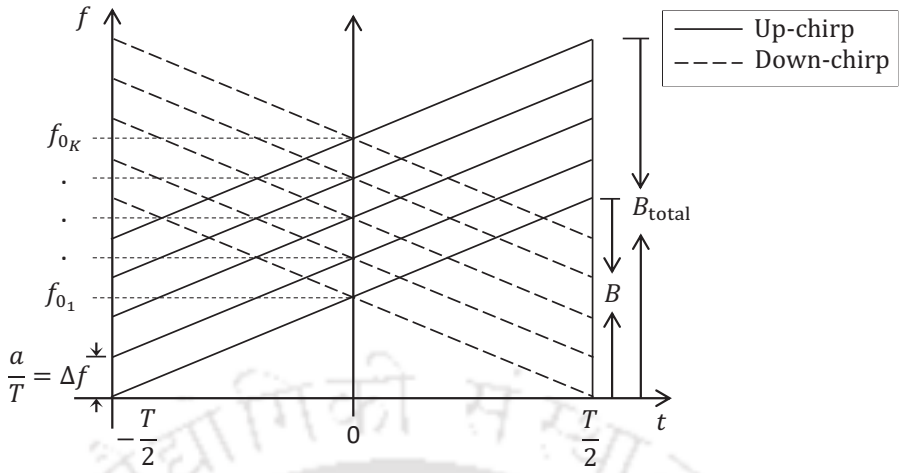

Figure 2.20: Plot of instantaneous frequency of the proposed linear chirp signals having the same chirp rate $\left(\frac{B}{T}\right)$ and constant difference (Δf) in initial frequency between the adjacent up-chirp or down-chirp signals.

2.4.1.1 Correlation Analysis of Waveforms

Given the proposed chirp waveforms having equal chirp rate, the cross-correlation between any two up-chirp waveforms $s_{1_n}(t)$ and $s_{1_m}(t)$, $n, m \in \{1, 2, \ldots, K\}$, $n \neq m$, can be evaluated using (1.11) and (2.75) as

$$\begin{aligned} R_{1_n 1_m}(\tau) &= \int_{-\infty}^{+\infty} \breve{s}_{1_n}(t)\breve{s}^*_{1_m}(t-\tau)dt \qquad (2.76)\\ &= e^{j2\pi f_{0_m}\tau} e^{-j\pi\mu\tau^2} \int_{-\infty}^{+\infty} e^{j2\pi(f_{0_n}-f_{0_m})t} e^{j2\pi\mu t\tau} dt \\ &= e^{j2\pi f_{0_m}\tau} e^{-j\pi\mu\tau^2} e^{j\pi\{(f_{0_n}-f_{0_m})+\mu\tau\}\tau} \frac{\sin\left[\pi((f_{0_n}-f_{0_m})+\mu\tau)\,(T-\tau)\right]}{\pi((f_{0_n}-f_{0_m})+\mu\tau)} \\ &= (T-|\tau|)\, e^{j\pi(f_{0_n}+f_{0_m})\tau} \text{sinc}[((f_{0_n}-f_{0_m})+\mu\tau)\,(T-|\tau|)], \quad |\tau| \leq T, \qquad (2.77) \end{aligned}$$

where $(\cdot)^*$ denotes the conjugate operation, sinc$(\cdot)$ denotes the sinc function [1], and $R'_{1_n 1_m}(\tau) = \Re\{R_{1_n 1_m}(\tau)\}$. For $n = m$, (2.77) reduces to the autocorrelation of $s_{1_n}(t)$ and is given by

$$R_{1_n 1_n}(\tau) = (T-|\tau|)\, e^{j2\pi f_{0_n}\tau} \text{sinc}[\mu\tau\,(T-|\tau|)], \quad |\tau| \leq T, \qquad (2.78)$$

where $R'_{1_n 1_n}(\tau) = \Re\{R_{1_n 1_n}(\tau)\}$. Similarly, it can be found that the correlation between any two down-chirp waveforms $R'_{2_n 2_m}(\tau)$ is the same as that of the correlation between any two up-chirp waveforms, and can be given by (2.77).

For the proposed waveforms the cross-correlation between any up-chirp and down-chirp waveforms

$s_{1_n}(t)$ and $s_{2_m}(t)$, $n, m \in \{1, 2, \ldots, K\}$, can be evaluated using (2.75) and (2.76) as

$$\begin{aligned} R_{1_n 2_m}(\tau) &= \int_{-\infty}^{+\infty} \breve{s}_{1_n}(t)\breve{s}^*_{2_m}(t-\tau)dt \\ &= e^{j2\pi f_{0_m}\tau} e^{j\pi\mu\tau^2} \int_{-\infty}^{+\infty} e^{j2\pi(f_{0_n}-f_{0_m})t} e^{j2\pi\mu t^2} e^{-j2\pi\mu t\tau} dt \\ &= \frac{e^{j2\pi f_{0_m}\tau} e^{j\pi\mu\tau^2}}{2\sqrt{\mu}} e^{-j\frac{\pi}{2}\left[\frac{(f_{0_n}-f_{0_m})-\mu\tau}{\sqrt{\mu}}\right]^2} \left[C'(\nu_2) + jS'(\nu_2) - C'(\nu_1) - jS'(\nu_1)\right], \end{aligned} \tag{2.79}$$

where $|\tau| \leq T$, ν_2 and ν_1 are given by $\nu_2 = \sqrt{\mu}T + \frac{(f_{0_n}-f_{0_m})-\mu|\tau|}{\sqrt{\mu}}$ and $\nu_1 = 2\sqrt{\mu}\left(-\frac{T}{2} + |\tau|\right) + \frac{(f_{0_n}-f_{0_m})-\mu|\tau|}{\sqrt{\mu}}$, respectively and the Fresnel integrals $C'(u)$ and $S'(u)$ [10] are defined as

$$C'(u) = \frac{2}{\sqrt{2\pi}} \int_0^u \cos(t^2)dt, \qquad S'(u) = \frac{2}{\sqrt{2\pi}} \int_0^u \sin(t^2)dt. \tag{2.80}$$

$R'_{1_n 2_m}(\tau) = \Re\{R_{1_n 2_m}(\tau)\}$ gives cross-correlation between $s_{1_n}(t)$ and $s_{2_m}(t)$. For $n = m$, (2.79) reduces to

$$R_{1_n 2_n}(\tau) = \frac{e^{j2\pi f_{0_n}\tau} e^{j\frac{\pi}{2}\mu\tau^2}}{2\sqrt{\mu}} \left[C'(\nu_2) + jS'(\nu_2) - C'(\nu_1) - jS'(\nu_1)\right], \quad |\tau| \leq T, \tag{2.81}$$

where $\nu_2 = \sqrt{\mu}\,(T - |\tau|)$ and $\nu_1 = \sqrt{\mu}\,(-T + |\tau|)$.

2.4.1.2 Condition for Orthogonality

In case all the chirp signals are provided with a bandwidth not overlapping with any neighbor user's signal, unlike for the waveforms shown in Figure 2.20, ideally the system would be interference free. However, this type of design would lead to a higher requirement of bandwidth. The total system bandwidth requirement can be restricted by keeping the instantaneous frequency difference of the adjacent chirp signals constant and allowing an overlap between their bandwidths. Although, the condition for which the interference between chirp signals gets minimum needs to be evaluated which in this case is the condition for orthogonality.

For two chirp waveforms to be orthogonal, the cross-correlation output between them at the sampled instant, i.e., at $\tau = 0$ should be zero. Hence substituting $\tau = 0$ in (2.77) the correlation output for any two up-chirp waveforms gives

$$R_{1_n 1_m}(0) = T\text{sinc}[(f_{0_n} - f_{0_m})T], \tag{2.82}$$

and setting (2.82) to zero gives

$$f_{0_n} - f_{0_m} = \Delta f = \frac{a}{T}, \tag{2.83}$$

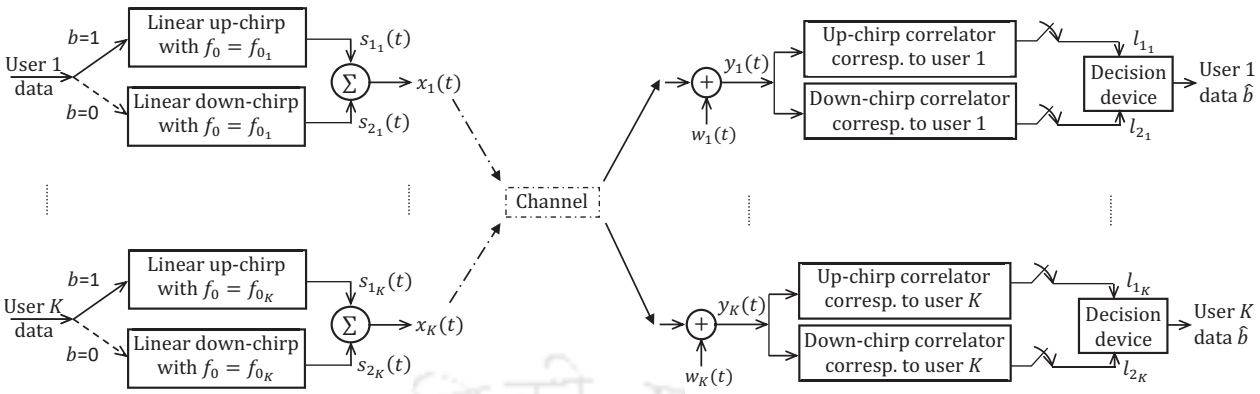

Figure 2.21: Block diagram of a multiuser communication system based on the proposed chirp signals having the same chirp rate and different initial frequency.

where $a \geq 1$ can be any integer number. As the minimum separation between the center frequency of two adjacent up-chirp or down-chirp waveforms can be Δf, satisfying the condition $\Delta f = \frac{a}{T}$ allows to design a set of mutually orthogonal up-chirp waveforms as well as a set of mutually orthogonal down-chirp waveforms.

2.4.2 System Model

A similar system model based on chirp-BOK scheme as considered for phase-coded chirp waveforms is also adopted here by replacing the phase-coded chirps with the proposed set of orthogonal up-chirps and orthogonal down-chirps given in (2.74). The system is having K pairs of transmitters and receivers that are communicating simultaneously where each transmitter is allocated a pair of up-chirp and down-chirp waveforms for transmission of 1-bit data symbol $b_k \in \{1, 0\}$, $k = 1, 2, \ldots, K$. Binary '1' is represented by up-chirp signal ($i = 1$) and binary '0' is represented by down-chirp signal ($i = 2$) and system block diagram is shown in Figure 2.21. Accordingly, the received signal at the k^{th} receiver can be expressed using (2.74) as

$$y_k(t) = \sum_{r=1}^{K} \alpha_{kr} \sqrt{E_{\text{s}}} s_{i_r}(t) + w_k(t), \tag{2.84}$$

where $i \in \{1, 2\}$, $s_{i_r}(t)$ is the transmitted signal for r^{th} receiver and can be either $s_1(t)$ or $s_2(t)$ depending on the transmitted data symbol. E_{s} is the signal energy, α_{kr} is the channel fading coefficient between k^{th} receiver and r^{th} transmitter, and $w_k(t)$ is white Gaussian noise with zero mean and variance $N_0/2$. It is considered that at k^{th} receiver the received interfering signals from the other users are originated from approximately the same distance and are assumed to be mutually independent

and with equal power. As shown in Figure 2.21, at the k^{th} receiver, the received chirp signal is fed to up-chirp correlator and down-chirp correlator to perform the cross-correlation of the input signal $y_k(t)$ with the reference chirps, given by (2.74) for k^{th} receiver. The sampled output of the up-chirp correlator, considering for the transmission of $b_k = 1$, can be expressed as

$$l_{1_k} = \alpha_{kk}\sqrt{E_{\text{s}}}\zeta_{1_k1_k} + \sum_{r=1;r\neq k}^{K} \alpha_{kr}\sqrt{E_{\text{s}}}\zeta_{1_ki_r} + w'_{1_k}, \tag{2.85}$$

where $\zeta_{1_k1_k}$, $\zeta_{1_ki_r}$, and w'_{1_k} are the sampled correlation outputs for the desired signal, the signal for other receivers, and the noise, respectively. Similarly, the sampled output of the down-chirp correlator can be expressed as

$$l_{2_k} = \alpha_{kk}\sqrt{E_{\text{s}}}\zeta_{2_k1_k} + \sum_{r=1;r\neq k}^{K} \alpha_{kr}\sqrt{E_{\text{s}}}\zeta_{2_ki_r} + w'_{2_k}, \tag{2.86}$$

where $\zeta_{2_k1_k}$ is the sampled correlation output between up-chirp and down-chirp of the same user, and the outputs $\zeta_{1_k1_k}$, $\zeta_{2_k1_k}$, $\zeta_{1_ki_r}$, $\zeta_{2_ki_r}$, w'_{1_k}, and w'_{2_k} can be evaluated using (2.77), (2.79), and (1.9). Following the decision logic [36, 76] given in (2.70) and using (2.71), (2.72), (2.85), (2.86), at k^{th} receiver, the probability of bit error [3, 76, 77] can be expressed as

$$P_{e_k} = Q\left[\left\{\frac{\alpha_{kk}^2 E_{\text{s}}\left(1-\rho_2^{kk}\right)}{N_0 + \sum_{r=1;r\neq k}^{K}\alpha_{kr}^2 E_{\text{s}}\rho^{kr}}\right\}^{\frac{1}{2}}\right], \tag{2.87}$$

where $\rho^{kr} = \rho_1^{kr} - \rho_2^{kr}$, and ρ_2^{kk}, ρ_1^{kr}, and ρ_2^{kr} are the normalized values of $\zeta_{2_k1_k}$, $\zeta_{1_ki_r}$, and $\zeta_{2_ki_r}$, respectively.

2.4.3 Performance Analysis Over Rayleigh Fading Channel

From (2.87), the signal-to-interference plus noise ratio (SINR) γ_k corresponding to the k^{th} receiver can be given in the following form

$$\gamma_k = \frac{\alpha_{kk}^2 E_{\text{s}}\left(1-\rho_2^{kk}\right)}{N_0 + \sum_{r=1;r\neq k}^{K}\alpha_{kr}^2 E_{\text{s}}\rho^{kr}} = \frac{S_k}{N_0 + \sum_{r=1;r\neq k}^{K} I_r} = \frac{X_k}{1 + \sum_{r=1;r\neq k}^{K} V_r}, \tag{2.88}$$

where X_k denotes the instantaneous SNR corresponding to the desired signal and V_r denotes the instantaneous interference-to-noise ratio (INR) corresponding to the r^{th} interferer. Considering the fading channel as a flat Rayleigh fading channel, the desired instantaneous SNR of the output signal

is exponential distributed random variable with PDF given by [16]

$$f_{X_k}(x) = \frac{1}{\overline{\gamma}_{\mathrm{s}_k}} e^{\left(-\frac{x}{\overline{\gamma}_{\mathrm{s}_k}}\right)}, \quad x \geq 0, \tag{2.89}$$

where $\overline{\gamma}_{\mathrm{s}_k} = \frac{\Omega_{kk} E_{\mathrm{s}} \left(1-\rho_2^{kk}\right)}{N_0}$, $\Omega = \mathbb{E}\left\{\alpha^2\right\}$ denotes the mean square value, and $\mathbb{E}\left\{\cdot\right\}$ denotes the expectation operation. It is assumed that the interfering signals are mutually independent and having equal power. This assumption helps in obtaining the closed-form expression which otherwise become difficult to obtain analytically. Then, $Z_k = \sum_{r=1; r\neq k}^{K} V_r$ follows gamma distribution with PDF [16]

$$f_{Z_k}(z) = \left(\frac{1}{\overline{\gamma}_{\mathrm{I}_k}}\right)^L \frac{z^{L-1}}{\Gamma(L)} e^{\left(-\frac{z}{\overline{\gamma}_{\mathrm{I}_k}}\right)}, \quad z \geq 0, \tag{2.90}$$

where $L = K-1$, $\Gamma(\cdot)$ is gamma function [16], and $\overline{\gamma}_{\mathrm{I}_k} = \sum_{r=1; r\neq k}^{K} \frac{E_{\mathrm{s}}}{N_0} \Omega_{kr} \rho^{kr}$ is the average INR at the k^{th} receiver. Therefore, the PDF of the SINR, $\gamma = \frac{X}{1+Z}$ given in (2.88) (without subscript), can be written as

$$f_\gamma(\gamma) = \int_0^\infty (1+z) f_X\left((1+z)\gamma\right) f_Z(z) dz, \quad \gamma \geq 0. \tag{2.91}$$

Substituting (2.89) and (2.90) in (2.91) gives [78]

$$\begin{aligned} f_\gamma(\gamma) &= \int_0^\infty (1+z) \frac{1}{\overline{\gamma}_{\mathrm{s}}} e^{-\frac{(1+z)\gamma}{\overline{\gamma}_{\mathrm{s}}}} \frac{z^{L-1}}{{\overline{\gamma}_{\mathrm{I}}}^L \Gamma(L)} e^{-\frac{z}{\overline{\gamma}_{\mathrm{I}}}} dz \\ &= \frac{1}{\overline{\gamma}_{\mathrm{s}} {\overline{\gamma}_{\mathrm{I}}}^L \Gamma(L)} e^{-\frac{\gamma}{\overline{\gamma}_{\mathrm{s}}}} \int_0^\infty (1+z) z^{L-1} e^{\left[-z\left(\frac{\gamma}{\overline{\gamma}_{\mathrm{s}}} + \frac{1}{\overline{\gamma}_{\mathrm{I}}}\right)\right]} dz. \end{aligned} \tag{2.92}$$

Expressing Q-function in terms of the complementary error function [16] as $Q(u) = \frac{1}{2}\mathrm{erfc}\left(\frac{u}{\sqrt{2}}\right)$, $u \geq 0$, and using (2.87), (2.88), (2.92), the average BER for k^{th} receiver can be obtained as

$$\overline{P}_{e_k} = \int_0^\infty P_{e_k}(\gamma_k) f_{\gamma_k}(\gamma_k) d\gamma_k \tag{2.93}$$

$$\begin{aligned} &= \int_0^\infty \frac{1}{2}\mathrm{erfc}\left(\sqrt{\frac{\gamma_k}{2}}\right) \frac{1}{\overline{\gamma}_{\mathrm{s}_k} {\overline{\gamma}_{\mathrm{I}_k}}^L \Gamma(L)} e^{-\frac{\gamma_k}{\overline{\gamma}_{\mathrm{s}_k}}} \int_0^\infty (1+z) z^{L-1} e^{\left[-z\left(\frac{\gamma_k}{\overline{\gamma}_{\mathrm{s}_k}} + \frac{1}{\overline{\gamma}_{\mathrm{I}_k}}\right)\right]} dz \, d\gamma_k \\ &= \frac{1}{2} \frac{1}{\overline{\gamma}_{\mathrm{s}_k} {\overline{\gamma}_{\mathrm{I}_k}}^L \Gamma(L)} \int_0^\infty (1+z) z^{L-1} e^{-\frac{z}{\overline{\gamma}_{\mathrm{I}_k}}} \frac{2\Gamma\left(\frac{3}{2}\right)}{\sqrt{\pi}} {}_2F_1\left(1, \frac{3}{2}; 2; -\frac{2(1+z)}{\overline{\gamma}_{\mathrm{s}_k}}\right) dz, \end{aligned} \tag{2.94}$$

where ${}_2F_1\left(m, m+\frac{1}{2}; m+1; v\right)$ is the hypergeometric function [78]. From (2.94), for $m=1$ it can be expressed as [79]

$${}_2F_1\left(m, m+\frac{1}{2}; m+1; v\right) = \frac{\sqrt{\pi}\Gamma(m+1)}{\Gamma(m+\frac{1}{2}) v^m} \left[(1-v)^{-\frac{1}{2}} - 1\right]. \tag{2.95}$$

Substituting (2.95) into (2.94) and after simplification average BER for k^{th} receiver can be written as

$$\overline{P}_{e_k} = \frac{1}{2}\left[1 - \left(\frac{\overline{\gamma}_{\mathrm{s}_k}}{2\overline{\gamma}_{\mathrm{I}_k}}\right)^{\frac{1}{2}} \xi^{\left(L-\frac{1}{2}\right)} U\left(L; L+\frac{1}{2}; \xi\right)\right], \tag{2.96}$$

where $\xi = \frac{2+\overline{\gamma}_{\mathrm{s}_k}}{2\overline{\gamma}_{\mathrm{I}_k}}$, $\overline{\gamma}_{\mathrm{s}_k}$ and $\overline{\gamma}_{\mathrm{I}_k}$ are the average SNR and INR, respectively corresponding to k^{th} receiver and $U(a;b;v)$ is the confluent hypergeometric function of the second kind [80].

2.4.4 Numerical Results and Discussion

The BER performance of a multiuser communication system using the proposed LC signals having the same chirp rate but different center frequency is simulated. The presented chirp signal set consists of five up-chirp and five down-chirp signals as shown in Figure 2.20. Total signal bandwidth B_{total} of 36 kHz with each chirp signal is having a TB product of 40 and $B = 20$ kHz is considered. The center frequency separation Δf between two consecutive up-chirps or down-chirps is set to 2 kHz. The result shown in Figure 2.22 presents the system performance for single user and multiuser $K = 5$ communication under AWGN and Rayleigh fading. Results indicate that system performance has degraded with increased number of users due to the increase of interference as the up-chirp and the down-chirp are not strictly orthogonal.

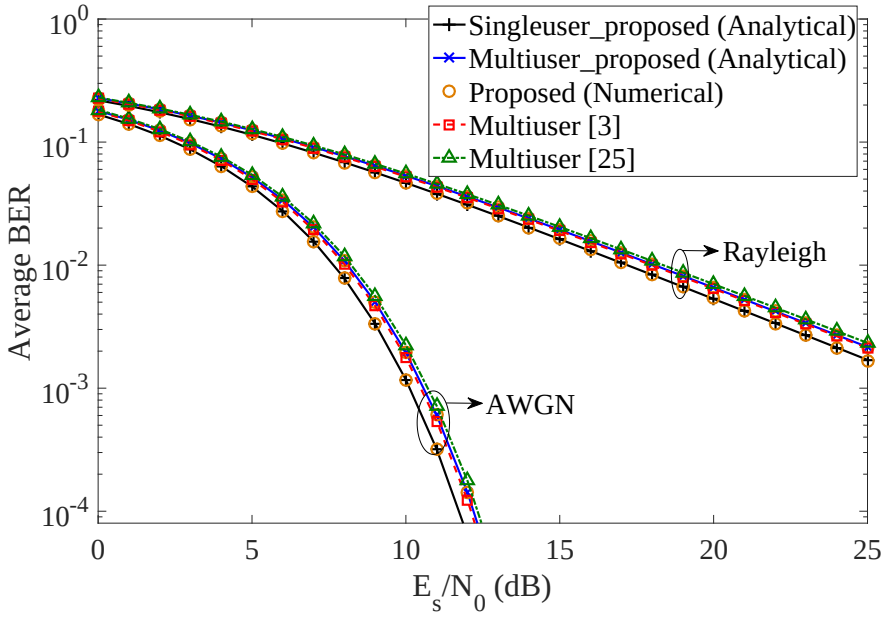

Figure 2.22: BER performance of a chirp-BOK system employing the proposed chirp signals having the same chirp rate and different center frequencies for $K = 1, 5$, and performance comparison with two different multiuser LC communication systems, one using the technique given in [3] and the other using the technique given in [25], considering $K = 5$.

Performance of the presented multiuser system is compared with two different multiuser LC communication systems, one using the technique given in [3] and the other using the technique given in [25]. From [3] the required bandwidth for a K user system is given by $B_K = (2K-1)B_1$, where B_1 is lowest bandwidth for user 1. With $B_1 = 20$ kHz, the system would require a bandwidth of 180 kHz for five users. From the results simulated for five users under AWGN and Rayleigh fading as shown in Figure 2.22, it is found that performance of the proposed system is on a par with the system in [3] in spite of using much less bandwidth and is better than the system in [25] while using the same bandwidth, e.g., we observe an improvement of 0.18 dB in $\frac{E_s}{N_0}$ for a BER of 0.2×10^{-3} in case of AWGN channel and an improvement of 0.4 dB in $\frac{E_s}{N_0}$ for a BER of 0.3×10^{-2} in case of Rayleigh fading channel.

2.5 PSK-Chirp-BOK Waveform for Multiuser Communication System Under Co-Channel Interference

The analysis on chirp waveforms having equal chirp rate in a chirp-BOK system indicates improvement in MAI performance in a multiuser scenario, as it is able to cancel out the interference between the up-chirp waveforms or the down-chirp waveforms while serving a transmission rate of 1 bit per symbol. However, from the fact that up-chirp and down-chirp waveforms are non-orthogonal, interference remains present in the system. In an attempt to improve the data rate, in this work, firstly, a chirp communication system is proposed to double the transmission rate over conventional chirp-BOK system [6] without increasing the number of correlators at the receiver for demodulation. Secondly, for a multiuser system, the design of a set of orthogonal chirp waveforms is proposed to eliminate the MAI and a time domain multiplexing of orthogonal chirp sets is presented to reduce the required system bandwidth. In addition, system performance is analyzed under Nakagami-m fading and in presence of co-channel interference.

2.5.1 Proposed System Model incorporating PSK-Chirp-BOK Waveform

Incorporating the phase shift keying (PSK) in a chirp-BOK scheme, a modified chirp-BOK system is presented where PSK modulation is combined with the pulse compression property of the chirp signal. The modified system namely 'PSK-chirp-BOK' system along with binary PSK (BPSK) modulation is capable of supporting data rate twice that of a conventional chirp-BOK system [6] and can perform demodulation using only two correlators instead of four. Accordingly, the proposed

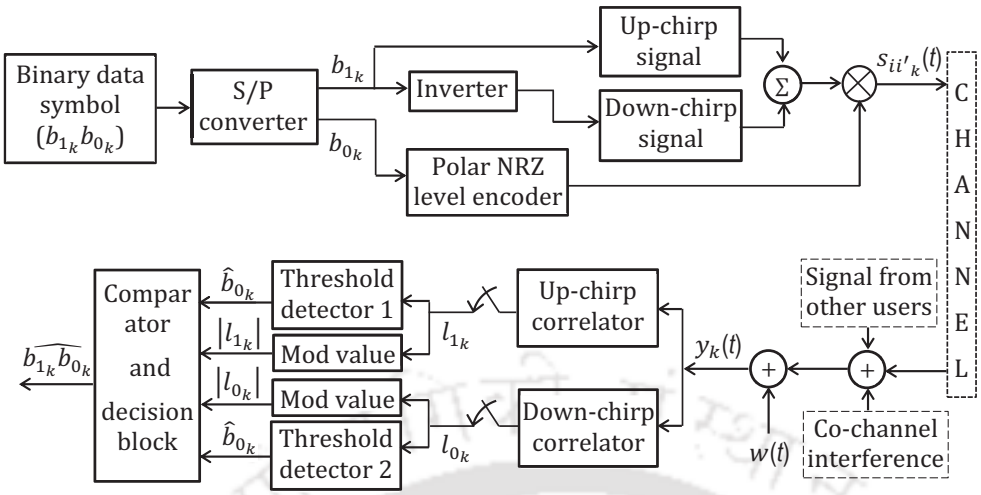

Figure 2.23: Proposed BPSK-chirp-BOK communication system for k^{th} user for transmission of 2 bits per symbol using linear chirp signal.

PSK-chirp-BOK system is designed considering binary phase shift in the chirps and termed as 'BPSK-chirp-BOK' system. For a K-user environment, block level design of the proposed BPSK-chirp-BOK system for k^{th} user is shown in Figure 2.23. Each user is allocated a pair of chirps– up-chirp and down-chirp. Therefore, a total of $2K$ chirps are required to design the K-user system. For the design of the waveform, initially, it is considered that all the up-chirps and all the down-chirps have equal chirp rate of μ while center frequencies f_{0_k} of the chirp signals $s_k(t)$ for different users $k = 1, 2, \ldots, K$ are separated by a frequency offset of $\Delta f = \frac{a}{T}$, $a \geq 1$ and an integer. Following (2.74), the chirp waveform set can be rewritten as

$$s_{c_k}(t) = \cos\left[2\pi\left(f_{0_k}t + \frac{1}{2}(-1)^{(1-c)}\mu t^2\right)\right], \quad -\frac{T}{2} \leq t \leq \frac{T}{2}, \tag{2.97}$$

where $c = 1, 0$, $s_{1_k}(t)$ and $s_{0_k}(t)$ indicate the up-chirp and down-chirp waveforms, respectively, $\mu = \frac{B}{T}$ is the chirp rate, and the total required bandwidth is given by $B_{\text{total}} = B + (K-1)\Delta f$.

2.5.1.1 Design of the Transmitter

From an implementation aspect of the proposed system as shown in Figure 2.23, for each individual user, at the transmitter the input data stream is grouped into 2-bit symbols represented as $b_{ii'} = b_1 b_0$ where $i, i' \in \{1, 0\}$. The data symbols $b_{ii'} = \{11, 10, 01, 00\}$ to be transmitted, are considered as independent and equally likely. Out of two bits obtained through the serial-to-parallel (S/P) converter, b_1 decides the chirp type to be transmitted and b_0 decides the phase of the selected chirp. Two chirp

signals, from the up-chirp and the down-chirp waveform generators, are used to uniquely map b_1, i.e., for $b_1 = 1$, the up-chirp signal is selected, while for $b_1 = 0$, the down-chirp signal is selected. b_0 is fed to a polar non-return-to-zero (NRZ) level encoder to obtain $+1$ or -1 levels corresponding to the input binary '1' or binary '0', respectively. Finally, the selected chirp waveform is multiplied with the output of polar NRZ level encoder (PNLE), using a multiplier, to obtain the phase-coded chirp waveform. Accordingly, the transmitted chirp signal for $b_{ii'}$ is obtained as follows: $b_{11}-$ up-chirp, $b_{10}-$ inverted up-chirp, $b_{01}-$ down-chirp, $b_{00}-$ inverted down-chirp where $i \in \{1, 0\}$ determines the chirp signal type, i.e., up-chirp or down-chirp and $i' \in \{1, 0\}$ determines the phase of the selected chirp signal. Thus, for k^{th} user, based on the input bits b_{1_k} and b_{0_k}, corresponding phase-coded chirp signal for $b_{ii'_k}$ is given by using (2.97) as

$$s_{ii'_k}(t) = (-1)^{(1-i')} \cos\left[2\pi\left(f_{0_k}t + \frac{1}{2}(-1)^{(1-i)}\mu t^2\right)\right], \quad -\frac{T}{2} \leq t \leq \frac{T}{2}, \tag{2.98}$$

where $k = 1, 2, \ldots, K$.

2.5.1.2 Design of the Receiver

Considering D number of interferers are present in the network, the corresponding received signal, at the k^{th} receiver, in presence of co-channel interference can be written as

$$y_k(t) = \sum_{r=1}^{K} \alpha_{kr}\sqrt{E_{\text{s}}}s_{ii'_r}(t) + \sum_{d=1}^{D} \alpha_{kd}\sqrt{E_{\text{I}}}u_d(t) + w_k(t), \tag{2.99}$$

where E_{s} is the symbol energy, $w_k(t)$ is noise with zero mean and variance $\frac{N_0}{2}$, and α_{kr} is the channel fading coefficient between k^{th} receiver and r^{th} transmitter. E_{I} is the energy of the co-channel interfering signals $u_d(t)$, $d = 1, 2, \ldots, D$, and α_{kd} is the channel fading coefficient between k^{th} receiver and d^{th} interferer. Data demodulation at the receiver can be considered as a combination of chirp and PSK demodulation schemes. Frequency sweep of the chirp signal is considered to be equal to the chirp signal bandwidth. At the receiver, as shown in Figure 2.23, the received chirp signal is fed to the up-chirp correlator and the down-chirp correlator to perform the cross-correlation of the input signal $y_k(t)$ with the reference chirps, given by (2.97) for k^{th} receiver where $c = 1, 0$. Accordingly, the sampled value of the output of the up-chirp ($c = 1$) correlator and down-chirp ($c = 0$) correlator corresponding to the k^{th} user can be expressed as

$$l_{c_k} = \alpha_{kk}\sqrt{E_{\text{s}}}\zeta^{kk}_{c_{ii'}} + \sum_{r=1;r\neq k}^{K} \alpha_{kr}\sqrt{E_{\text{s}}}\zeta^{kr}_{c_{ii'}} + \sum_{d=1}^{D} \alpha_{kd}\sqrt{E_{\text{I}}}\zeta^{kd}_{c} + w'^{k}_{c}, \quad c = 1, 0, \tag{2.100}$$

where $\zeta_{c_{ii'}}^{kk}$, $\zeta_{c_{ii'}}^{kr}$, ζ_c^{kd}, w'^k_c are the sampled cross-correlation output of the reference chirps $s_{c_k}(t)$ with the desired signal, the signal from other users, the interfering signals, and the noise, respectively and are evaluated in next subsection 2.5.1.3. The correlator outputs, l_{c_k}, are fed to two threshold detectors and passed through the mod-value block to obtain the 'mod' value $|l_{c_k}|$. Using $|l_{c_k}|$ and the outputs of the threshold detectors, estimation of $b_{ii'_k}$ is performed in the comparator and decision block (CDB) that contains a comparator along with a data selector. As an example, considering b_{11_k} is transmitted, in absence of noise and interference, $|l_{1_k}|$ from the up-chirp correlator will be greater than $|l_{0_k}|$ from the down-chirp correlator. Comparing the outputs, $|l_{1_k}|$ and $|l_{0_k}|$, in the CDB, b_{1_k} among the two transmitted bits can be estimated, i.e., $\widehat{b}_{1_k} = 1$ if $|l_{1_k}| > |l_{0_k}|$ else $\widehat{b}_{1_k} = 0$ ($|l_{0_k}| > |l_{1_k}|$). The estimation of b_{0_k} can be done using PSK demodulation scheme. For the input l_{c_k}, each threshold detector with a threshold '0' provides an estimated b_{0_k} as shown in Figure 2.23. Depending on the estimated b_{1_k} ($\widehat{b}_{1_k}$), data selector selects the output of the corresponding threshold detector as the final estimated b_{0_k} ($\widehat{b}_{0_k}$), i.e., if $\widehat{b}_{1_k} = 1$, the output of threshold detector 1 is chosen as $\widehat{b}_{0_k}$ else the output of threshold detector 2 is chosen as $\widehat{b}_{0_k}$. Thus, the conditional probability of symbol error for k^{th} user is given by

$$P_e^k = 1 - \left[(1 - P_{e_1}^k(\gamma_1^k))(1 - P_{e_2}^k(\gamma_2^k))\right], \tag{2.101}$$

where $P_{e_n}^k(\gamma_n^k) = Q\big(\sqrt{\gamma_n^k}\big)$, $n = 1, 2$, and $Q(\cdot)$ denotes the Q-function [16]. $P_{e_1}^k$ and $P_{e_2}^k$ are the probabilities of incorrect estimation of b_{1_k} and b_{0_k}, respectively, and

$$\gamma_1^k = \frac{\alpha_{kk}^2 E_{\text{s}} \left(1 - |\rho_0^{kk}|\right)}{N_0 + \sum_{r=1;r\neq k}^{K} \alpha_{kr}^2 E_{\text{s}} |\rho^{kr}| + \sum_{d=1}^{D} \alpha_{kd}^2 E_{\text{I}} |\xi^{kd}|} \tag{2.102}$$

$$\gamma_2^k = \frac{\alpha_{kk}^2 2E_{\text{s}}}{N_0 + \sum_{r=1;r\neq k}^{K} \alpha_{kr}^2 E_{\text{s}} \rho_1^{kr} + \sum_{d=1}^{D} \alpha_{kd}^2 E_{\text{I}} \xi_1^{kd}} \tag{2.103}$$

where $\rho^{kr} = |\rho_1^{kr}| - |\rho_0^{kr}|$ and $\xi^{kd} = |\xi_1^{kd}| - |\xi_0^{kd}|$. ρ_c^{kr}, ρ_c^{kk}, and ξ_c^{kd} are the normalized value of ζ_c^{kr}, ζ_c^{kk}, and ζ_c^{kd}, respectively (subscript ii' omitted). Block level implementation of the system is described here and for actual hardware implementation, based on the application requirement, the scheme can be realized using DSP or application-specific integrated circuit (ASIC) or FPGA which is out of the scope of the current work.

From the aspect of hardware complexity overhead, compared to a conventional chirp-BOK system with a transmission rate of 1 bit per symbol [6], the proposed system requires additional hardware blocks of P/S converter, polar NRZ level encoder, multiplier at the transmitter side, and threshold detector, mod value detector, multiplexer (data selector) at the receiver side. It can be seen that

all these additional blocks do not introduce much hardware complexity while realizing the proposed system to achieve data rate twice that of a conventional chirp-BOK system. Further, a chirp-BOK system with a transmission rate of 2 bits per symbol uses four correlators and two sets of up-chirp and down-chirp waveforms [3, 4]. In comparison, the proposed system has offered reduction in hardware complexity as only two correlators are needed for the design at the receiver and at the same time it saves valuable spectral resources as only a pair of chirp waveform− one up-chip and one down-chirp is required.

2.5.1.3 Correlation Analysis of Waveforms

For the calculation of $\zeta_{c_{ii'}}^{kr}$, $\zeta_{c_{ii'}}^{kk}$, and ζ_{c}^{kd}, the chirp waveforms $s_{c_k}(t)$ given by (2.97) and $s_{ii'_r}(t)$ given by (2.98) can be expressed in equivalent complex form as

$$\breve{s}_{c_k}(t) = e^{j2\pi\left(f_{0_k}t+(-1)^{(1-c)}\frac{1}{2}\mu t^2\right)}, \tag{2.104}$$

$$\breve{s}_{ii'_r}(t) = (-1)^{(1-i')}e^{j2\pi\left(f_{0_r}t+(-1)^{(1-i)}\frac{1}{2}\mu t^2\right)}, \tag{2.105}$$

where $|t| \leq \frac{T}{2}$, $c = 1, 0$, and $s_{ii'_r}(t) = \Re\left\{\breve{s}_{ii'_r}(t)\right\}$. $\Re\{\cdot\}$ indicates the real part. Given the chirp waveforms, the cross-correlation between $\breve{s}_{ii'_r}(t)$ and $\breve{s}_{c_k}(t)$ is given using (1.10) as

$$\begin{aligned} R_{c_{ii'}}^{kr}(\tau) &= \int_{-\infty}^{+\infty} \breve{s}_{ii'_r}(t)\breve{s}_{c_k}^{*}(t-\tau)dt \\ &= \int_{-\infty}^{+\infty} (-1)^{(1-i')}e^{j2\pi\left(f_{0_r}t+(-1)^{(1-i)}\frac{1}{2}\mu t^2\right)}e^{-j2\pi\left(f_{0_k}(t-\tau)+(-1)^{(1-c)}\frac{1}{2}\mu(t-\tau)^2\right)}dt, \end{aligned} \tag{2.106}$$

where $(\cdot)^*$ denotes the conjugate operation. For $i = c$, $R_{c_{ii'}}^{kr}(\tau)$ can be simplified using (2.77) as

$$R_{c_{ii'}}^{kr}(\tau) = (-1)^{(1-i')}e^{j2\pi f_{0_k}\tau}e^{j\pi\left(f_{0_r}-f_{0_k}\right)\tau}\,\frac{\sin\left[\pi\left(\left(f_{0_r}-f_{0_k}\right)+(-1)^{(1-c)}\mu\tau\right)(T-|\tau|)\right]}{\pi\left(\left(f_{0_r}-f_{0_k}\right)+(-1)^{(1-c)}\mu\tau\right)}, \tag{2.107}$$

where $|\tau| \leq T$. Now, for $i = (1-c)$, $R_{c_{ii'}}^{kr}(\tau)$ can be evaluated using (2.79) and (2.106) as

$$\begin{aligned} R_{c_{ii'}}^{kr}(\tau) = \frac{(-1)^{(1-i')}}{2\sqrt{\mu}}&e^{j2\pi f_{0_k}\tau}e^{(-1)^{c}j\pi\mu\tau^2}e^{-j\frac{\pi}{2\mu}\left[\left(f_{0_r}-f_{0_k}\right)+(-1)^{(1-c)}\mu\tau\right]^2} \\ &\times\left[C'(\nu_2)+jS'(\nu_2)-C'(\nu_1)-jS'(\nu_1)\right], \end{aligned} \tag{2.108}$$

where $|t| \leq T$, $\nu_2 = \sqrt{\mu}T + \frac{\left(f_{0_r}-f_{0_k}\right)+(-1)^{(1-c)}\mu|\tau|}{\sqrt{\mu}}$, $\nu_1 = 2\sqrt{\mu}\left(-\frac{T}{2}+|\tau|\right) + \frac{\left(f_{0_r}-f_{0_k}\right)+(-1)^{(1-c)}\mu|\tau|}{\sqrt{\mu}}$. The required output $\zeta_{c_{ii'}}^{kr}$ is obtained from (2.107) and (2.108) as $\zeta_{c_{ii'}}^{kr} = \Re\left\{R_{c_{ii'}}^{kr}(\tau)\right\}$ and by setting $\tau = 0$. For $r = k$, $\zeta_{c_{ii'}}^{kk}$ can be calculated from (2.107) and (2.108).

Considering co-channel interferer ($u_d(t)$) can be both up and down type chirps, using (2.99) and

(2.100), $R_c'^{kd}(\tau)$ can be written as $R_c'^{kd}(\tau) = \int_{-\infty}^{+\infty} u_d(t) s_{c_k}(t-\tau)dt$, and ζ_c^{kd} is calculated from $R_c'^{kd}(\tau)$ by setting $\tau = 0$. Accordingly the normalized value for ζ_c^{kd} would lies between $0 \leq \zeta_c^{kd} < 1$.

2.5.2 Proposed Design for Set of Orthogonal Chirp Waveforms

Up-chirps and down-chirps that are used in the multiuser system have overlap in bandwidth and as they are not completely orthogonal, cross-correlation between the chirps results in interference. A process to design $2K$ number of orthogonal chirps using the same bandwidth of B_{total} that is used in the K-user system is presented below. It is considered that the chirp rate μ for all the chirps is equal, frequency separation Δf between two adjacent chirp or chirp-component is fixed and $\frac{B}{2} - (K-1)\Delta f = \Delta f$. Accordingly, the design process is stated as follows:

(1) First, determine all the up-chirps covering individual bandwidth in a continuous manner and let the number of this type of chirps be K.

(2) For each up-chirp, to replace the corresponding down-chirp, a two-segment up-chirp namely 'segmented up-chirp' within the same signal bandwidth is designed such that the first segment covers the upper half of B from $t = -\frac{T}{2}$ to $t = 0$ and the second segment covers the lower half of B with $t = 0$ to $t = \frac{T}{2}$. The associated frequency variation is shown in Figure 2.24.

The instantaneous frequency of the up-chirp and the 'segmented up-chirp' for k^{th} user are given by

$$f_{c_k}(t) = \begin{cases} \left(f_{0_k} + (1-c)\frac{B}{2}\right) + \mu t, & -\frac{T}{2} \leq t < 0, \\ \left(f_{0_k} - (1-c)\frac{B}{2}\right) + \mu t, & 0 \leq t \leq \frac{T}{2}, \end{cases} \tag{2.109}$$

where $c = 1$ is for up-chirp and $c = 0$ is for 'segmented up-chirp', respectively, $\Delta f = \frac{a}{T}$, $a \geq 1$ and an integer, f_{0_k} is the center frequency for k^{th} user's chirp, and $k = 1, 2, \ldots, K$. The corresponding chirp signals are given using (1.1) as

$$s_{c_k}(t) = \cos\left[2\pi\phi_{c_k}(t)\right], \quad -\frac{T}{2} \leq t \leq \frac{T}{2}, \tag{2.110}$$

where $\phi_{c_k}(t)$ is calculated using (1.2) and (2.109) as

$$\phi_{c_k}(t) = \int_0^t f_{c_k}(\tau)d\tau = \begin{cases} \left(f_{0_k} + (1-c)\frac{B}{2}\right)t + \frac{1}{2}\mu t^2, & -\frac{T}{2} \leq t < 0, \\ \left(f_{0_k} - (1-c)\frac{B}{2}\right)t + \frac{1}{2}\mu t^2, & 0 \leq t \leq \frac{T}{2}. \end{cases} \tag{2.111}$$

It can be readily proved that, any two chirp signals $s_{c_k}(t)$ and $s_{c_{k'}}(t)$, $k, k' \in \{1, 2, \ldots, K\}$, $k \neq k'$, are

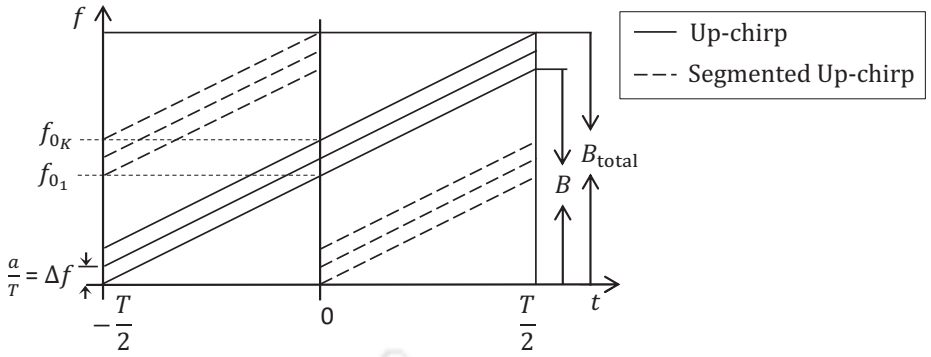

Figure 2.24: Plot of instantaneous frequency versus time of the proposed set of orthogonal linear chirp waveforms.

mutually orthogonal, i.e., $\int_{-\frac{T}{2}}^{\frac{T}{2}} s_{c_k}(t)s_{c_{k'}}(t)dt = \delta(k-k')$ where $\delta(\cdot)$ is Kronecker delta function [15]. Therefore, using the proposed design, within each chirp-signal bandwidth two orthogonal chirps– up-chirp and 'segmented up-chirp' can be formed as shown in Figure 2.24. In addition, for a given signal bandwidth B, proposed design can provide double the number of orthogonal LCs, in continuous-time domain, as compared to [81] where only set of up-chirps are considered, i.e., considering $B = 10$ kHz, $T = 1$ ms, and $\Delta f = \frac{1}{T}$, B_{total} would be 14 kHz for 5 chirp waveforms according to [81], whereas a set of 10 chirp waveforms can be designed within the same B_{total} using the proposed design technique.

2.5.3 Time Domain Multiplexing of Orthogonal Chirps: A Transmission Scheme for Multiuser System

For the design of the proposed K-user BPSK-chirp-BOK system, a set of $2K$ orthogonal chirps and a bandwidth of B_{total} are required. Use of LCs enables us to transmit a set of chirps before the completion of previously transmitted chirp-set and accordingly, a transmission technique of time domain multiplexing (TDM) of set of only K orthogonal chirps is proposed. Two set of chirps, set1 having K orthogonal chirps and designed according to (2.109) and a time shifted version of set1, i.e., set2, with a time separation of $\frac{T}{4}$ is considered as shown in Figure 2.25. Thus, a total of $2K$ chirps can be obtained within a duration of $T + \frac{T}{4}$ and for large number of repetition (M) of the chirp sets, $MT + \frac{T}{4} \rightarrow MT$ which means effectively $2K$ chirps can be obtained within a duration of T while achieving a bandwidth gain of $B_g = \frac{B_{\text{total}} - B + \Delta f}{2} = \frac{K\Delta f}{2}$. Although K chirps in every set are mutually orthogonal and cover the signal bandwidth B, within 0 to T duration the chirps of set2 (given by dashed lines in Figure 2.25) do not cover the entire signal bandwidth while the chirps from set1 do. Due to the partial coverage of bandwidth by the chirps of set2, as can be seen from Figure 2.25,

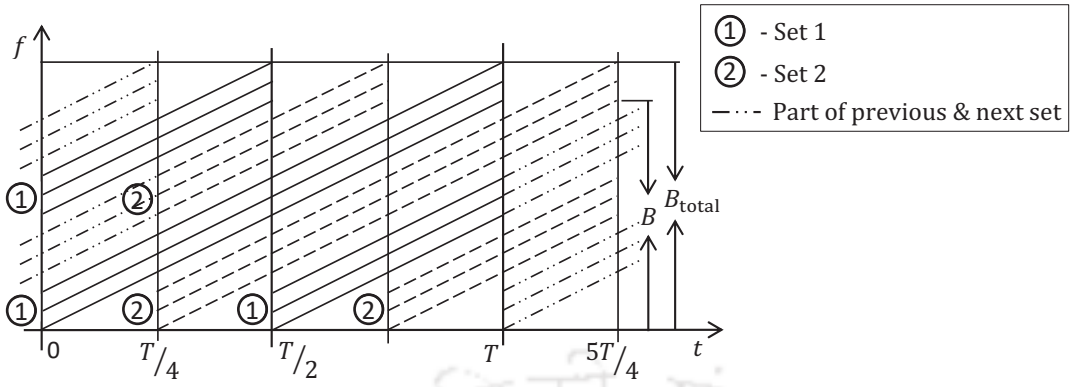

Figure 2.25: Time domain multiplexed orthogonal chirp sets.

cross-correlation between the chirp waveforms of set1 and set2 gives non-zero values and it makes the chirps of set1 and set2 non-orthogonal to each other.

Fractional Fourier transform (FrFT) and inverse FrFT (IFrFT) processes [82] are used to remove the undesired chirps and attain orthogonality for each set. FrFT can be considered as a generalization of conventional Fourier transform. FrFT performed at an optimal order p on an LC signal gives an impulse in FrFT domain, and p is related to the chirp rate μ of the signal as $p = -\frac{2}{\pi}\tan^{-1}\left(\frac{f_s^2/C_s}{\mu}\right)$ where f_s is the sampling frequency, C_s is the number of samples, and in FrFT domain the position of the impulse will depend on the starting frequency of the chirp signal [83].

Block diagram of the FrFT process at the receiver of k^{th} user is given in Figure 2.26. After the reception of the composite signal $y_k(t)$, considering that set1 is the desired set for k^{th} user, signal duration is divided into two equal halves corresponding to the two segments of the segmented up-chirp set where the 1$^{\text{st}}$ half $y_{1_k}(t)$ is from 0 to $\frac{T}{2}$ and the 2$^{\text{nd}}$ half $y_{2_k}(t)$ is from $\frac{T}{2}$ to T. As the chirp rate (μ) is same for all the chirps, fractional Fourier-based rotation, i.e., FrFT $\mathfrak{F}_p(\cdot)$ performed at an order p on each half $y_{\varepsilon_k}(t)$, $\varepsilon = 1, 2$, gives set of impulses $y_{\varepsilon_k}(u)$ parallel to v axis in FrFT domain and makes the chirps separable along u axis due to different initial frequency as shown in Figure 2.27(a) for the 1$^{\text{st}}$ half. A rectangular window ($\Pi(\cdot)$) can be used for masking the unwanted peaks by setting the sample values as 0, in turn removing the undesired signals. After masking operation, IFrFT at an

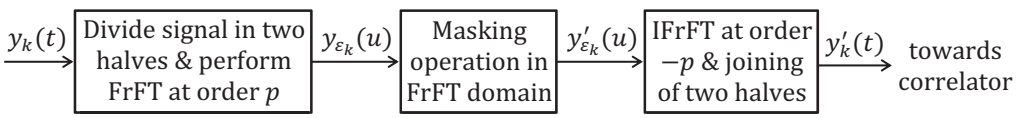

Figure 2.26: Block diagram of the FrFT based filtering process at the receiver.

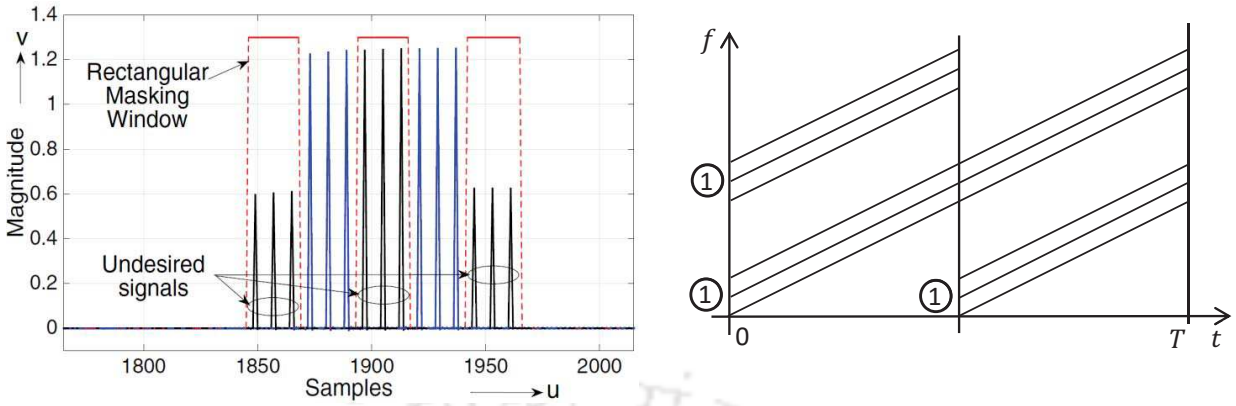

Figure 2.27: (a) Masking operation on the output of FrFT of 1st half of set1 chirps mixed with the chirps of other sets, (b) Concatenation of two halves of set1 after IFrFT process.

order $-p$ ($\mathfrak{F}_{-p}(\cdot)$) is performed to get back the filtered signal $y'_{\varepsilon_k}(t)$ in time domain and concatenation of two halves gives the required time domain signal $y'_k(t)$ as shown in Figure 2.27(b). Mathematically it can be expressed as

$$y'_{\varepsilon_k}(t) = \mathfrak{F}_{-p}\left[\Pi\left[\mathfrak{F}_p\left(y_{\varepsilon_k}(t)\right)\right]\right], \quad \varepsilon = 1, 2 \tag{2.112}$$

$$y'_k(t) = y'_{1_k}(t) + y'_{2_k}(t)\text{rect}\left(t - \frac{T}{2}\right), \tag{2.113}$$

where

$$y_{\varepsilon_k}(u) = \mathfrak{F}_p\left(y_{\varepsilon_k}(t)\right) = \int_{-\infty}^{\infty} y_{\varepsilon_k}(t) K_p^{'}(t,u)dt, \tag{2.114}$$

$$y_{\varepsilon_k}(t) = \mathfrak{F}_{-p}\left(y_{\varepsilon_k}(u)\right) = \int_{-\infty}^{\infty} y_{\varepsilon_k}(u) K_{-p}^{'}(t,u)du, \tag{2.115}$$

and $K_p^{'}(t,u)$ is the FrFT kernel defined in [82]. Thus, FrFT based filtering removes the undesired chirps from the required chirp set and can also partially remove the co-channel interference.

2.5.4 Performance Analysis Over Nakagami-m Fading Channel

Considering that the transmitted signal is received over slowly varying flat fading channel, from (2.102) and (2.103), γ_n^k, $n = 1, 2$, can be rewritten as

$$\begin{aligned}\gamma_n^k &= \frac{\alpha_{kk}^2 n E_{\text{s}} \tilde{\rho}_n^{kk}}{N_0 + \sum_{r=1;r\neq k}^{K} \alpha_{kr}^2 E_{\text{s}} \tilde{\rho}_n^{kr} + \sum_{d=1}^{D} \alpha_{kd}^2 E_{\text{I}} \tilde{\xi}_n^{kd}} \\ &= \frac{X_{\text{s}_n}^k}{1 + \sum_{r=1;r\neq k}^{K} V_n^{kr} + \sum_{d=1}^{D} W_n^{kd}} = \frac{X_{\text{s}_n}^k}{1 + Y_{\text{o}_n}^k + Z_{\text{I}_n}^k},\end{aligned} \tag{2.116}$$

where $X_{\mathrm{s}_n}^k = \alpha_{kk}^2 n E_\mathrm{s} \tilde{\rho}_n^{kk}/N_0$ is the SNR of the desired output signal for k^{th} user, $W_n^{kd} = \alpha_{kd}^2 E_\mathrm{I} \tilde{\xi}_n^{kd}/N_0$ is the INR of the d^{th} co-channel interferer, $V_n^{kr} = \alpha_{kr}^2 E_\mathrm{s} \tilde{\rho}_n^{kr}/N_0$ is the INR due to r^{th}th user. $Z_{\mathrm{I}_n}^k = \sum_{d=1}^{D} W_n^{kd}$ and $Y_{\mathrm{o}_n}^k = \sum_{r=1;r\neq k}^{K} V_n^{kr}$. Moreover, from (2.102), (2.103), and (2.116)

(i) for $n = 1$, $\tilde{\rho}_1^{kk} = 1 - |\rho_0^{kk}|$, $\tilde{\rho}_1^{kr} = |\rho^{kr}|$, $\tilde{\xi}_1^{kd} = |\xi^{kd}|$,

(ii) for $n = 2$, $\tilde{\rho}_2^{kk} = 1$, $\tilde{\rho}_2^{kr} = \rho_1^{kr}$, $\tilde{\xi}_2^{kd} = \xi_1^{kd}$.

Considering Nakagami-m fading channel where m is the fading severity parameter, using (2.116) cumulative distribution function (CDF) of $X_{\mathrm{s}_n}^k$ can be given as $F_{X_{\mathrm{s}_n}^k}(x) = \frac{1}{\Gamma(m_\mathrm{s})}\gamma\left(m_\mathrm{s}, \frac{m_\mathrm{s} x}{\Omega_{kk}\vartheta_n^k}\right)$ where $\Gamma(\cdot)$ is gamma function, $\gamma(\cdot,\cdot)$ is lower incomplete gamma function [78], $\Omega = \mathbb{E}\{\alpha^2\}$ is the mean square value and $\vartheta_n^k = \left(nE_\mathrm{s}\tilde{\rho}_n^{kk}\right)/N_0$. The associated PDF of $X_{\mathrm{s}_n}^k$ can be given by

$$f_{X_{\mathrm{s}_n}^k}(x) = \left(\frac{m_\mathrm{s}}{\overline{\gamma_{\mathrm{s}_n}^k}}\right)^{m_\mathrm{s}} \frac{x^{m_\mathrm{s}-1}}{\Gamma(m_\mathrm{s})} e^{-\frac{m_\mathrm{s} x}{\overline{\gamma_{\mathrm{s}_n}^k}}}, \quad x \geq 0, \tag{2.117}$$

where $\overline{\gamma_{\mathrm{s}_n}^k}$ is the average SNR. Assuming equal power and mutually independent interfering signals, the PDF of $Z_{\mathrm{I}_n}^k = \sum_{d=1}^{D} \alpha_{kd}^2 E_\mathrm{I} \tilde{\xi}_n^{kd}$ and $Y_{\mathrm{o}_n}^k = \sum_{r=1;r\neq k}^{K} \alpha_{kr}^2 E_\mathrm{s} \tilde{\rho}_n^{kr}$ is given as [84]

$$f_{Z_{\mathrm{I}_n}^k}(z) = \left(\frac{m_\mathrm{I}}{\overline{\gamma_{\mathrm{I}_n}^k}}\right)^{m_\mathrm{I} D} \frac{z^{m_\mathrm{I} D-1}}{\Gamma(m_\mathrm{I} D)} e^{-\frac{m_\mathrm{I} z}{\overline{\gamma_{\mathrm{I}_n}^k}}}, \quad z \geq 0, \tag{2.118}$$

$$f_{Y_{\mathrm{o}_n}^k}(y) = \left(\frac{m_\mathrm{o}}{\overline{\gamma_{\mathrm{o}_n}^k}}\right)^{m_\mathrm{o} L} \frac{y^{m_\mathrm{o} L-1}}{\Gamma(m_\mathrm{o} L)} e^{-\frac{m_\mathrm{o} y}{\overline{\gamma_{\mathrm{o}_n}^k}}}, \quad y \geq 0, \tag{2.119}$$

where $\overline{\gamma_{\mathrm{I}_n}^k}$ is the average co-channel INR, $\overline{\gamma_{\mathrm{o}_n}^k}$ is the average INR caused by other users and $L = K-1$. m_s, m_o and m_I are the Nakagami fading parameters for desired signal, other users' signals and co-channel interfering signals, respectively. From (2.116), total INR can be given by $G_{\mathrm{I}_n}^k = Y_{\mathrm{o}_n}^k + Z_{\mathrm{I}_n}^k$, and using (2.118) and (2.119) PDF of $G_{\mathrm{I}_n}^k$ can be calculated as

$$f_{G_{\mathrm{I}_n}^k}(g) = \int_0^g f_{Z_{\mathrm{I}_n}^k}(g-y) f_{Y_{\mathrm{o}_n}^k}(y) dy \tag{2.120}$$

$$= \left(\frac{m_\mathrm{I}}{\overline{\gamma_{\mathrm{I}_n}^k}}\right)^{m_\mathrm{I} D} \left(\frac{m_\mathrm{o}}{\overline{\gamma_{\mathrm{o}_n}^k}}\right)^{m_\mathrm{o} L} \frac{g^{m_\mathrm{o} L + m_\mathrm{I} D - 1}}{\Gamma(m_\mathrm{I} D + m_\mathrm{o} L)} e^{-\frac{m_\mathrm{I} g}{\overline{\gamma_{\mathrm{I}_n}^k}}} {}_1F_1\left[m_\mathrm{o} L; m_\mathrm{I} D + m_\mathrm{o} L; \left(\frac{m_\mathrm{I}}{\overline{\gamma_{\mathrm{I}_n}^k}} - \frac{m_\mathrm{o}}{\overline{\gamma_{\mathrm{o}_n}^k}}\right) g\right], \tag{2.121}$$

where ${}_1F_1(\cdot;\cdot;\cdot)$ is confluent hypergeometric function of the first kind [78]. Thus, using (2.116), (2.117), and (2.121) the PDF of signal-to-interference plus noise ratio (SINR), $\gamma_n^k = \frac{X_{\mathrm{s}_n}^k}{1+G_{\mathrm{I}_n}^k}$ can be calculated

as

$$f_{\gamma_n^k}(\gamma_n^k) = \int_0^\infty (1+g) f_{X_{\mathrm{s}_n}^k}\left((1+g)\gamma_n^k\right) f_{G_{\mathrm{I}_n}^k}(g)\, dg \tag{2.122}$$

$$= \left(\frac{m_{\mathrm{s}}}{\overline{\gamma_{\mathrm{s}_n}^k}}\right)^{m_{\mathrm{s}}} \left(\frac{m_{\mathrm{I}}}{\overline{\gamma_{\mathrm{I}_n}^k}}\right)^{m_{\mathrm{I}}D} \left(\frac{m_{\mathrm{o}}}{\overline{\gamma_{\mathrm{o}_n}^k}}\right)^{m_{\mathrm{o}}L} \frac{(\gamma_n^k)^{m_{\mathrm{s}}-1}}{\Gamma(m_{\mathrm{s}})\Gamma(\varphi)} e^{-\frac{m_{\mathrm{s}}\gamma_n^k}{\overline{\gamma_{\mathrm{s}_n}^k}}}$$

$$\times \sum_{i=0}^{m_{\mathrm{s}}} \binom{m_{\mathrm{s}}}{i} \Gamma(\varphi+i)\lambda^{-(\varphi+i)} {}_2F_1\left[\varphi+i, m_{\mathrm{o}}L; \varphi; \frac{\chi}{\lambda}\right], \tag{2.123}$$

where $\varphi = m_{\mathrm{I}}D + m_{\mathrm{o}}L$, $\lambda = \frac{m_{\mathrm{s}}\gamma_n^k}{\overline{\gamma_{\mathrm{s}_n}^k}} + \frac{m_{\mathrm{I}}}{\overline{\gamma_{\mathrm{I}_n}^k}}$, $\chi = \frac{m_{\mathrm{I}}}{\overline{\gamma_{\mathrm{I}_n}^k}} - \frac{m_{\mathrm{o}}}{\overline{\gamma_{\mathrm{o}_n}^k}}$, and ${}_2F_1(\cdot,\cdot;\cdot;\cdot)$ is the Gauss hypergeometric function [78]. Expressing $Q\left(\sqrt{\gamma_n^k}\right)$ in terms of upper incomplete Gamma function [84], $\Gamma(\cdot,\cdot)$, and using (2.93), (2.101), and (2.123) average $P_{e_n}^k(\gamma_n^k)$ for k^{th} user can be expressed as

$$\overline{P_{e_n}^k} = \left(\frac{m_{\mathrm{I}}}{\overline{\gamma_{\mathrm{I}_n}^k}}\right)^{m_{\mathrm{I}}D} \left(\frac{m_{\mathrm{o}}}{\overline{\gamma_{\mathrm{o}_n}^k}}\right)^{m_{\mathrm{o}}L} \left(\frac{\overline{\gamma_{\mathrm{s}_n}^k}}{2m_{\mathrm{s}}}\right)^{\frac{1}{2}} \frac{\Gamma(m_{\mathrm{s}}+\frac{1}{2})}{\Gamma(m_{\mathrm{s}}+1)\Gamma(\varphi)}$$

$$\times \int_0^\infty \frac{(1+g)^{m_{\mathrm{s}}} g^{\varphi-1}}{2\sqrt{\pi}(\Psi+g)^{m_{\mathrm{s}}+\frac{1}{2}}} e^{-\frac{m_{\mathrm{s}}\gamma_n^k}{\overline{\gamma_{\mathrm{s}_n}^k}}} {}_1F_1\left[m_{\mathrm{o}}L; \varphi; \chi g\right] {}_2F_1\left[1, m_{\mathrm{s}}+\frac{1}{2}; m_{\mathrm{s}}+1; \frac{1+g}{\Psi+g}\right] dg, \tag{2.124}$$

where $\Psi = 1 + \frac{\overline{\gamma_{\mathrm{s}_n}^k}}{2m_{\mathrm{s}}}$, and ${}_2F_1(\cdot,\cdot;\cdot;\cdot)$ can be simplified as [79]

$${}_2F_1\left[1, m_{\mathrm{s}}+\frac{1}{2}; m_{\mathrm{s}}+1; a\right] = \frac{\sqrt{\pi}\Gamma(m_{\mathrm{s}}+1)}{\Gamma(m_{\mathrm{s}}+\frac{1}{2})a^{m_{\mathrm{s}}}}\left[(1-a)^{-\frac{1}{2}} - \sum_{i=0}^{m_{\mathrm{s}}-1}\binom{2i}{i}\left(\frac{a}{4}\right)^i\right]. \tag{2.125}$$

Substituting (2.125) in (2.124), solving the integral, and after simplification $\overline{P_{e_n}^k}$ can be evaluated as

$$\overline{P_{e_n}^k} = \frac{1}{2}\left(\frac{m_{\mathrm{I}}}{\overline{\gamma_{\mathrm{I}_n}^k}}\right)^{m_{\mathrm{I}}D} \left(\frac{m_{\mathrm{o}}}{\overline{\gamma_{\mathrm{o}_n}^k}}\right)^{m_{\mathrm{o}}L} \left(\frac{\overline{\gamma_{\mathrm{s}_n}^k}}{2m_{\mathrm{s}}}\right)^{\frac{1}{2}} \left[\left(\left(\frac{2m_{\mathrm{s}}}{\overline{\gamma_{\mathrm{s}_n}^k}}\right)^{\frac{1}{2}} \left(\frac{m_{\mathrm{I}}}{\overline{\gamma_{\mathrm{I}_n}^k}}\right)^{-\varphi} {}_2F_1\left[m_{\mathrm{o}}L, \varphi; \varphi; \frac{\chi}{\frac{m_{\mathrm{I}}}{\overline{\gamma_{\mathrm{I}_n}^k}}}\right]\right)\right.$$

$$\left. - \left(\sum_{i=0}^{m_{\mathrm{s}}-1}\binom{2i}{i}\left(\frac{1}{4}\right)^i \sum_{j=0}^{i}\binom{i}{j}\sum_{u=0}^{\infty}\frac{\Gamma(m_{\mathrm{o}}L+u)\Gamma(\psi)}{\Gamma(m_{\mathrm{o}}L)\Gamma(\varphi+u)u!}\chi^u\Psi^{\psi-i-\frac{1}{2}}U\left[\psi; \psi+\frac{1}{2}-i; \Psi\frac{m_{\mathrm{I}}}{\overline{\gamma_{\mathrm{I}_n}^k}}\right]\right)\right], \tag{2.126}$$

where $\psi = m_{\mathrm{I}}D + m_{\mathrm{o}}L + j + u$ and $U(\cdot;\cdot;\cdot)$ is the confluent hypergeometric function of the second kind [78]. When set of orthogonal chirps or time domain multiplexed set of chirps along with FrFT based filtering is used at the receiver of k^{th} user, cross-correlation with the chirps of other users become negligible. Thus, considering $\tilde{\rho}_n^{kr} \approx 0$, $G_{\mathrm{I}_n}^k = Z_{\mathrm{I}_n}^k$ and after modifying (2.126) accordingly $\overline{P_{e_n}^k}$ can be expressed as

$$\overline{P_{e_n}^k} = \frac{1}{2} - \left(\frac{m_{\mathrm{I}}}{\overline{\gamma_{\mathrm{I}_n}^k}}\right)^{m_{\mathrm{I}}D} \left(\frac{\overline{\gamma_{\mathrm{s}_n}^k}}{2m_{\mathrm{s}}}\right)^{\frac{1}{2}} \sum_{i=0}^{m_{\mathrm{s}}-1}\binom{2i}{i}\left(\frac{1}{4}\right)^i \sum_{j=0}^{i}\binom{i}{j}\frac{\Gamma(\ell)\Psi^{\ell-i-\frac{1}{2}}}{2\Gamma(m_{\mathrm{I}}D)} U\left[\ell; \ell+\frac{1}{2}-i; \Psi\frac{m_{\mathrm{I}}}{\overline{\gamma_{\mathrm{I}_n}^k}}\right], \tag{2.127}$$

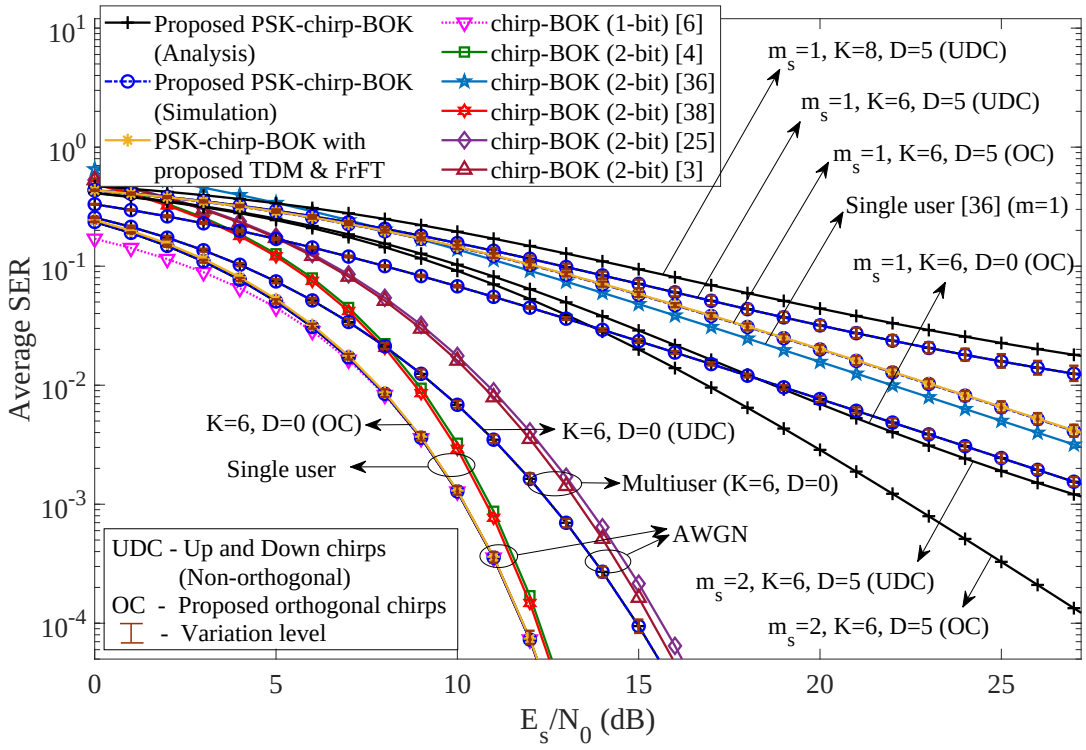

Figure 2.28: Average SER performance of the proposed BPSK-chirp-BOK communication system in a multiuser environment affected by co-channel interference under a Nakagami-m fading channel using (i) up and down chirp sets, (ii) proposed orthogonal chirp set, (iii) proposed time domain multiplexed chirp sets and FrFT based filtering at the receiver. Performance of the BPSK-chirp-BOK system is compared with different chirp-BOK systems reported in [3, 4, 6, 25, 36, 38].

where $\ell = m_{\mathrm{I}} D + j$. Using (2.101), (2.126), and (2.127) average SER of BPSK-chirp-BOK system for k^{th} user can be calculated as

$$\overline{P_e^k} = 1 - \left[\left(1 - \overline{P_{e_1}^k}\right)\left(1 - \overline{P_{e_2}^k}\right)\right]. \tag{2.128}$$

2.5.5 Numerical Results and Discussion

Average SER performance of the proposed PSK-chirp-BOK system using binary phase modulation for transmission of 2-bit symbol in a multiuser environment and in presence of co-channel interference is presented in Figure 2.28 under Nakagami-m fading channel. LC signal having $B = 32$ kHz, $T = 0.4$ ms with $K = 6$ and 8 are considered. A group of 5 interferers ($D = 5$), each with INR of 3 dB at the receiver input are chosen. Signals from other users and co-channel interfering signals are assumed to be Rayleigh faded ($m_{\mathrm{o}} = 1, m_{\mathrm{I}} = 1$). It is observed that the system performance improves with the improvement in channel condition (m_{s}) of the desired signal. Use of the proposed set of orthogonal chirps indicates substantial improvement in SER performance over a system using up-chirps and down-

chirps, i.e., for $K = 6$, a gain of 2.8 dB and 7.5 dB in SNR for a SER of 10^{-2} is observed considering AWGN and Rayleigh fading ($m_s = 1$) channels, respectively and the gain increases as SER decreases. The results of Monte-Carlo simulation, with the average value, match closely with the corresponding analytical results and the amount of variation obtained with individual values is also indicated. System with the proposed time domain multiplexed chirp sets and FrFT based filtering at the receiver performs as good as to the system having orthogonal chirp waveforms without time overlap and it indicates that the proposed transmission scheme is able to successfully eliminate the interference due to the chirps from other users. The value of order p for FrFT process is calculated as 0.95. As a special case, performance of the proposed system using orthogonal chirps with no interference is also given in Figure 2.28 and the system provides best performance, as expected.

Considering single user case, performance of the BPSK-chirp-BOK system approaches the performance of a conventional 1-bit chirp-BOK system [6] for high SNR in AWGN channel, in spite of double transmission rate. For 2-bit symbol transmission, compared to single user [4, 36, 38] and multiuser ($K = 6$) [3, 25] chirp-BOK systems, the proposed PSK-chirp-BOK system performs better as can be seen from Figure 2.28 due to the requirement of fewer comparisons and use of set of orthogonal chirps in spite of using less system bandwidth. Further, adopting M-PSK modulation along with set of orthogonal chirps, design of a M-ary M-PSK-chirp-BOK system is possible to provide high speed data communication.

2.6 Summary

In this chapter, design of chirp waveforms for wireless communication applications is investigated and analyzed. Particularly, in the first work, presented in Section 2.2, the design of a SAW communication system for single user is presented considering fixed-frequency waveform and it is extended for chirp waveform where an LC waveform modulation and demodulation scheme using SAW-chirp devices incorporating quadrature phase modulation capable of transmitting 3-bit symbols is preformed. It has been shown that, use of both up-chirp and down-chirp in the proposed design allows to map additional bit in a single symbol which in turn increases the data rate without increasing modulation order or use of additional bandwidth. Analysis on the SER performances under AWGN and Rayleigh fading channels has indicated that the system provides improved SER performance over the reported SAW-chirp communication systems adapted for transmission of 3-bit data symbols. The second work,

in Section 2.3, has presented the design of binary phase-coded linear and nonlinear chirp waveforms for multiuser communication system. The associated analysis on the system performance has indicated that the performance is dependent on the number of available users in the network. Design of chirp waveforms with equal chirp rate to attain set of orthogonal up-chirp and orthogonal down-chirp waveforms has been described in the next work, presented in Section 2.4, to improve the MAI performance. The condition of orthogonality for the chirp waveforms is derived and analytical expressions of correlation values between different chirp signals are presented. Closed-form expressions have been derived to analyze the average BER performance of the system under Rayleigh fading channel, and the results indicate that employing the proposed waveform has allowed to attain better performance while using the same bandwidth over reported work [25]. In the fourth work, a PSK-chirp-BOK system and associated chirp waveform design are presented in Section 2.5 and the proposed system is capable of doubling the transmission rate as compared to conventional chirp-BOK system while using the same number of correlators, and thus saving valuable spectral resources. In addition, a design of $2K$ orthogonal chirps within B_{total} using up-chirps and segmented up-chirps for K-user chirp-BOK system has been presented to eliminate MAI in a multiuser system, and a transmission scheme using TDM of the same chirp sets along with FrFT based filtering at the receiver has been presented to attain bandwidth gain without compromising system performance. Moreover, closed-form expressions of the average SER performance of a BPSK-chirp-BOK system, in a multiuser scenario and affected by co-channel interference, have been derived under Nakagami-m fading. The associated results have shown considerable improvement in SER performance by using the proposed set of orthogonal chirps which provide zero cross-correlations between chirps of different users. Thus, the PSK-chirp-BOK system along with set of orthogonal chirps and TDM transmission scheme provides a flexible way to design a chirp communication system to meet the required data rate or bandwidth or both.

3

Design and Analysis of Chirp Waveform for Radar and IoT Systems

Contents

3.1 Introduction

The previous chapter presented the design of chirp waveforms and systems to achieve improvement in data rate and performance compared to the reported works in literature. Apart from communication, chirp waveform has also been widely used in radar applications as it provides improved pulse compression, low sidelobe levels, good Doppler tolerance, large TBP etc. at the radar receiver [1, 17] over fixed-frequency type waveform. Design of radar waveforms through frequency hopping technique, i.e., DFCW has attracted much attention in recent years [39], as it offers higher range-resolution with improved detection capability. Since the reported DFCW designs are limited in number of available waveforms [39, 46, 48, 49], in this chapter design of DFCWs using chirp subpulses is proposed for multiuser and MIMO radar applications with the objective of designing higher number of waveforms along with improved performance over the reported designs. Investigation on the waveforms design is carried out to improve the ASP and CCP performances among the waveforms, and the associated analysis provides important insights about the minimization of overall cross-correlation levels in the design of a new set of SC waveform, for LEO satellite IoT communication, to improve the system performance over the reported SC waveform [58]. The main contributions of this chapter are as follows:

(1) A set of DFCWs by combining LC subpulses and PN-code sequence is designed, to attain waveform diversity, for MIMO and multiuser radar systems. A two stage optimization process for the selection of appropriate frequency-firing order sequences and PN-code sequences is proposed for which appropriate radar ambiguity functions are formulated in order to maintain improved ASP and CCP levels over reported designs.

(2) Another DFCW design incorporates NLC waveform for further improvement in PSL and increase in the number of available waveforms where a parameterized waveform design model and an optimization process, based on GA, are proposed for designing NLC. A joint optimization of NLC pulse type and the frequency firing order of the chirp pulses, of the designed DFCW-NLC, is proposed for improving the ASP and CCP performance over the reported DFCW designs.

(3) In the process to minimize the cross-correlation peak values of SC waveform occurring at different delay, the design of a new symmetry chirp waveform having multiple chirp rates, i.e., SC-MCR is proposed for an M-ary multiuser chirp system for LEO satellite IoT communication. Extending the design, a time domain multiplexing of the SC-MCR waveforms is proposed to improve the

system data rate. Analytical expressions of SER of the system are derived under RLS channel, and the system performance is analyzed to get a better insight of the dependence of performance on the fading parameters.

For all the proposed designs and systems, the associated performances are compared with the reported designs to demonstrate the improvement in performance. The detailed designs of these waveforms and systems are discussed in the subsequent sections in this chapter.

3.2 DFCW-PNLC for MIMO and Multiuser Radar Systems

Design of DFCWs to attain waveform diversity for MIMO and multiuser radar application is performed in this work, where firstly, a set of DFCW is designed using LC pulse and PN-code sequence. Secondly, a two-stage optimization process is proposed to achieve minimum cross-correlation levels between different waveforms and improve the ASP and CCP levels for the designed DFCWs over the reported LC based DFCW designs.

3.2.1 Design of DFCW-PNLC

An LC signal (up-chirp) having bandwidth B and signal duration T, in complex form, can be expressed using (1.5), (1.8) as

$$p(t) = e^{j2\pi\left(f_s t+\frac{1}{2}\mu t^2\right)}, \quad 0 \le t \le T, \tag{3.1}$$

where f_s is the starting frequency and $\mu = \frac{B}{T}$ is the chirp rate of the signal [1]. Considering a DFCW-LC waveform to consist of N chirp subpulses, a total of N waveforms can be formed by performing frequency-hopping of the available pulses. Thus, i^{th} subpulse of n^{th} waveform can be expressed using (3.1) as

$$p_n(t-(i-1)T) = e^{j2\pi((f_s+H_n(i)\Delta f-\Delta f)(t-(i-1)T))}e^{j\pi\mu(t-(i-1)T)^2}, \quad (i-1)T \le t \le iT, \tag{3.2}$$

where $i = 1, 2, \ldots, N$, Δf indicates the frequency step size, H_n is the n^{th} hyperbolic frequency hopping (HFH) sequence [85] for determining the sequence of frequency-firing of chirp pulses, n denotes the sequence number, i is the index number of the sequence, and the corresponding index value is given by $H_n(i)$. The HFH sequence can be formed as [85]

$$H_n(i) = ni^{-1} (\text{mod } g), \tag{3.3}$$

where g is a prime number and $1 \leq i,\ n \leq g-1$. Therefore, a set of $N = g-1$ HFH sequences with each sequence having a length of $N = g-1$ can be generated. Using (3.2) and (3.3) n^{th} DFCW-PNLC can be written as

$$s_n(t) = \sum_{i=1}^{N} C(i) p_n(t-(i-1)T), \tag{3.4}$$

where C is the PN-code sequence of length N, and $C(i) = \pm 1$. The instantaneous frequency of one of the DFCW-PNLC is shown in Figure 3.1.

For radar applications, Gold codes are preferred as the desired PN-code sequences due to their low cross-correlation property [75]. Gold codes can be generated by combining the outputs of two maximal-length sequence generators [75]. As the length of the PN-code sequence is N, the PN-code set would consist at least N number of Gold code sequences. Moreover, any DFCW-LC can be encoded with any available PN-code sequences. Therefore, the general form of n^{th} DFCW-LC encoded with l^{th} PN-code sequence can be expressed using (3.2) and (3.4) as

$$s_n^l(t) = \sum_{i=1}^{N} C_l(i) p_n(t-(i-1)T). \tag{3.5}$$

It is considered that no two DFCW-LC, $s_n(t)$ and $s_m(t)$, are encoded with the same PN-code sequence, i.e., for two waveforms $s_n^l(t)$ and $s_m^q(t)$, $l \neq q$.

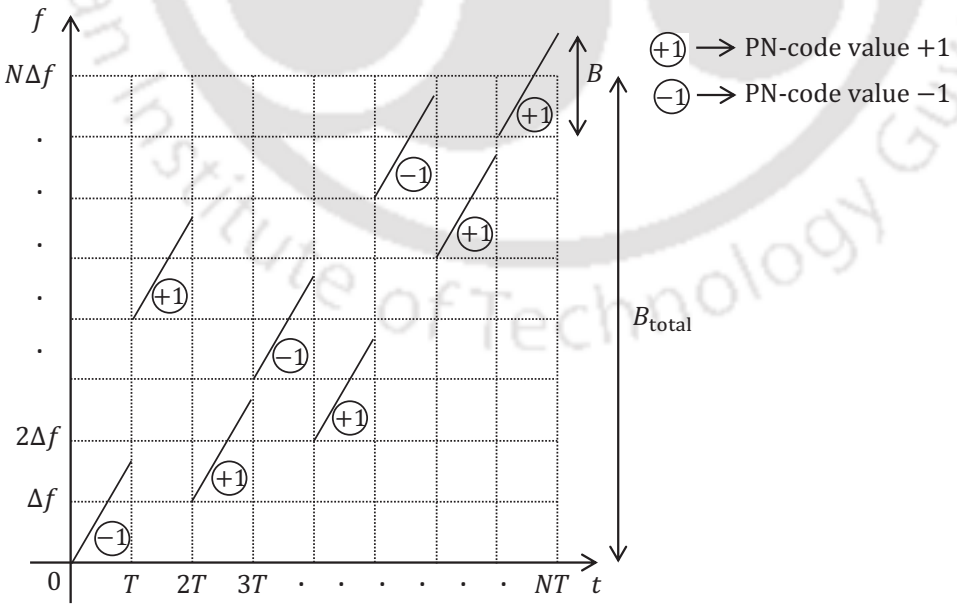

Figure 3.1: Instantaneous frequency versus time of one of the DFCW-PNLC.

3.2.1.1 Analysis of Ambiguity Function for DFCW-PNLC

The performance of the proposed DFCW-PNLC can be evaluated from the analysis of its auto-ambiguity function and cross-ambiguity function (CAF) [86]. CAF between two waveforms $s_n^l(t)$ and $s_m^q(t)$ is given by

$$\chi_{s_n^l s_m^q}(\tau,\varphi) = \int_{-\infty}^{\infty} s_n^l(t) s_m^{q^*}(t-\tau) e^{j2\pi\varphi t} dt, \tag{3.6}$$

where $(\cdot)^*$ denotes the conjugate operation, φ accounts the Doppler shift, and τ is the delay time. Using (3.5), (3.6) can be simplified and expressed as

$$\begin{aligned}
\chi_{s_n^l s_m^q}(\tau,\varphi) &= \int_{-\infty}^{\infty} \sum_{i=1}^{N} C_l(i) \sum_{i'=1}^{N} C_q(i') e^{j2\pi\left((f_s+H_n(i)\Delta f-\Delta f)(t-(i-1)T)+\frac{1}{2}\mu(t-(i-1)T)^2\right)} \\
&\quad \times e^{-j2\pi((f_s+H_m(i')\Delta f-\Delta f)((t-(i'-1)T)-\tau))} e^{-j\pi\mu((t-(i'-1)T)-\tau)^2} e^{j2\pi\varphi t} dt \qquad (3.7) \\
&= \sum_{i=1}^{N}\sum_{i'=1}^{N} C_l(i) C_q(i') e^{j2\pi f_s[(i'-i)T+\tau]} e^{-j2\pi\Delta f[(i'-i)T+\tau]} e^{j2\pi\Delta f[T(H_m(i')(i'-1)-H_n(i)(i-1))+H_m(i')\tau]} \\
&\quad \times e^{j\pi\mu[((i-1)^2-(i'-1)^2)T^2-2(i'-1)T\tau-\tau^2]} \int_{-\infty}^{\infty} e^{j2\pi\Delta f[H_n(i)-H_m(i')]t} e^{j2\pi\mu((i'-i)T+\tau)t} e^{j2\pi\varphi t} dt \\
&= \sum_{i=1}^{N}\sum_{i'=1}^{N} C_l(i) C_q(i') e^{j2\pi(f_s-\Delta f)[(i'-i)T+\tau]} \\
&\quad \times e^{j2\pi\Delta f[T(H_m(i')(i'-1)-H_n(i)(i-1))+H_m(i')\tau]} e^{j\pi\mu[(i-i')(i+i'-2)T^2-2(i'-1)T\tau-\tau^2]} \chi_{ii'}, \qquad (3.8)
\end{aligned}$$

where $\chi_{ii'} = \int_{t_1}^{t_2} e^{j2\pi(\beta_{ii'}\Delta f+\varphi)t} e^{j2\pi\mu((i'-i)T+\tau)t} dt$ and $\beta_{ii'} = H_n(i) - H_m(i')$. In every subpulse duration, for $0 \le \tau \le T$, the lower and upper limits of $\chi_{ii'}$ can be given by $t_1 = \tau$ and $t_2 = T$. For $l = q$ and $n = m$, (3.6) reduces to auto-ambiguity function and using (3.7) it can be simplified as

$$\begin{aligned}
\chi_{s_n^l s_n^l}(\tau,\varphi) &= \int_{-\infty}^{\infty} s_n^l(t) s_n^{l^*}(t-\tau) e^{j2\pi\varphi t} dt \qquad (3.9) \\
&= \sum_{i=1}^{N}\sum_{i'=1}^{N} C_l(i) C_l(i') e^{j2\pi(f_s-\Delta f)[(i'-i)T+\tau]} \\
&\quad \times e^{j2\pi\Delta f[T(H_n(i')(i'-1)-H_n(i)(i-1))+H_n(i')\tau]} e^{j\pi\mu[(i-i')(i+i'-2)T^2-\tau^2-2(i'-1)T\tau]} \zeta_{ii'}, \qquad (3.10)
\end{aligned}$$

where $\zeta_{ii'} = \int_{t_1}^{t_2} e^{j2\pi(\varrho_{ii'}\Delta f+\varphi)t} e^{j2\pi\mu((i'-i)T+\tau)t} dt$ and $\varrho_{ii'} = H_n(i) - H_n(i')$.

3.2.2 Proposed Optimization for Waveform Selection

In a multiuser radar system, consider that K users are operating simultaneously where K is less than the number of pulses N. Considering that all the waveforms transmitted from different radar

users are different, for a particular user the received echo from a target not only consists of the required signal but also have the signals of other radar systems. Thus, minimization of the cross-correlation levels between transmitted signals is required for optimal detection performance. The multiuser radar ambiguity function for v^{th} user can be expressed as

$$\chi_v^{Multiuser}(\tau,\varphi) = \int_{-\infty}^{\infty} \sum_{k=1}^{K} u_k(t) u_v^*(t-\tau) e^{j2\pi\varphi t} dt, \tag{3.11}$$

where $u_k(t)$ is the radar signal for k^{th} user, $u_k(t) = s_{n_k}^{l_k}(t)$, with $k, v \in \{1, 2, \ldots, K\}$, n_k denotes n^{th} HFH sequence and l_k denotes l^{th} PN-code sequence selected for k^{th} radar signal. Simplifying (3.11) gives

$$\chi_v^{Multiuser}(\tau,\varphi) = \sum_{k=1}^{K} \int_{-\infty}^{\infty} s_{n_k}^{l_k}(t) s_{n_v}^{l_v\,*}(t-\tau) e^{j2\pi\varphi t} dt. \tag{3.12}$$

The values of n and l of the radar signals corresponding to different users will be different. Therefore, replacing n_k, l_k and n_v, l_v, related to user k and v, with the corresponding selected n and l values, the inner integral of (3.12) takes a similar form to that of (3.6) and it can be evaluated using (3.8) (An example of n and l values, selected for different values of k is presented in Table 3.2). In order to achieve optimal detection performance the ASP level and CCP level of the correlated output of the composite received radar signal, $\chi_v^{Multiuser}(\tau,\varphi)$, should be as low as possible. Further, for a MIMO radar system where K radar signals are operating simultaneously through multiple antennas, the received composite signal is processed through a bank of matched filters. The associated MIMO radar ambiguity function can be expressed as [44]

$$\chi_K^{MIMO}(\tau,\varphi) = \int_{-\infty}^{\infty} \sum_{k=1}^{K} \sum_{k'=1}^{K} u_k(t) u_{k'}^*(t-\tau) e^{j2\pi\varphi t} dt \tag{3.13}$$

$$= \sum_{k=1}^{K} \sum_{k'=1}^{K} \int_{-\infty}^{\infty} s_{n_k}^{l_k}(t) s_{n_{k'}}^{l_{k'}\,*}(t-\tau) e^{j2\pi\varphi t} dt. \tag{3.14}$$

Similar to (3.12), the inner integral of (3.14) can be solved using (3.8). Minimum cross-correlation between different transmitted signals allow maximum contribution from each of the signals as achieving complete orthogonality between different received signals is nearly impossible in practice [44]. Thus, appropriate selection of proposed discrete frequency-coding waveforms with phase-coded linear chirp pulses is necessary.

From (3.8) and (3.10), for a given B, Δf and T, it can be observed that the maximum level of

ASP and CCP between two waveforms depends upon the HFH sequence H_n, i.e., frequency-firing sequence and the PN-code sequence C_l. Thus, an optimization process is presented for the selection of DFCW-PNLC to minimize ASP level and CCP level of $\chi_v^{Multiuser}(\tau,\varphi)$ and $\chi_K^{MIMO}(\tau,\varphi)$.

The optimization process consists of two stages. In the first stage, following processes are performed:

(1) Selection of two HFH sequences H_n is performed for which the corresponding DFCW-LC given by

$$\tilde{p}_n(t) = \sum_{i=1}^{N} p_n(t-(i-1)T), \tag{3.15}$$

provides minimum cross-correlation peak level, i.e., we need to minimize $\chi_{\tilde{p}_n\tilde{p}_m}(\tau)$ where

$$\chi_{\tilde{p}_n\tilde{p}_m}(\tau) = \int_{-\infty}^{\infty} \tilde{p}_n(t)\tilde{p}_m^*(t-\tau)dt, \tag{3.16}$$

and $1 \leq n, m \leq g-1$.

(2) Considering that a total of K waveforms are to be selected, select the remaining $K-2$ waveforms in an iterative process, e.g., for the 3^{rd} HFH sequence and corresponding waveform such that the total cross-correlation level remains as low as possible, i.e., minimize

$$\chi_{\tilde{p}_m}(\tau) = \int_{-\infty}^{\infty} \sum_{k=1}^{z} \tilde{p}_{n_k}(t)\tilde{p}_m^*(t-\tau)dt, \tag{3.17}$$

where $z=2$, n_k denotes n^{th} HFH sequence for k^{th} waveform, given by $\tilde{p}_{n_k}(t)$, and $m \neq n_k$.

(3) Repeat the process of step 2 for the selection of the remaining waveforms.

Thus, first stage performs the optimization of the cross-correlation between DFCW-LC. In the second stage, following processes are performed:

(1) Once the selection of discrete frequency-coding waveforms with LC subpulses is completed, select any two optimized DFCW-LC (out of K) and for these two waveforms select two Gold code sequences (C_l) such that the two DFCW-PNLC, given by using (3.5) and (3.15) as

$$s_{n_k}^{l_k}(t) = \sum_{i=1}^{N} C_{l_k}(i)p_{n_k}(t-(i-1)T), \quad k=1,2, \tag{3.18}$$

provide minimum cross-correlation peak level, i.e., using (3.6) and (3.18) minimize the CAF

Table 3.1: Design parameters for the construction of the proposed DFCW-PNLC

Parameter	Value
Chirp subpulse bandwidth (B)	2 MHz
Duration of chirp subpulse (T)	400 ns
g	127
Frequency step (Δf)	$(B_{\text{total}} - B)/g$
Number of users or radar signals (K)	6
Doppler frequency span (φ)	$\pm$10 kHz

while considering $\varphi = 0$ as

$$\chi_{s_{n_1}^{l_1} s_{n_2}^{l_2}}(\tau, 0) = R_{s_{n_1}^{l_1} s_{n_2}^{l_2}}(\tau) = \int_{-\infty}^{\infty} s_{n_1}^{l_1}(t) s_{n_2}^{l_2{}^*}(t-\tau) dt, \tag{3.19}$$

where $1 \leq l_k \leq g - 1$.

(2) After selection of two DFCW-PNLC, similar to the selection of HFH sequences in step 2 of first stage, encode the next optimized DFCW-LC with PN-code such that overall cross-correlation peak level remains as low as possible, e.g., for the 3$^{\text{rd}}$ optimized DFCW-LC with PN-code to minimize

$$\chi_{s_{n_3}^{l_3}}(\tau, 0) = \int_{-\infty}^{\infty} \sum_{k=1}^{z} s_{n_k}^{l_k}(t) s_{n_3}^{l_3{}^*}(t-\tau) dt. \tag{3.20}$$

(3) Repeat the process of step 2 for the selection of PN-code sequences of the remaining DFCW-LC.

3.2.3 Performance Analysis and Discussion

Based on the proposed optimization process, presented in Section 3.2.2, a set of DFCW-PNLC is obtained. It is considered that the discrete frequency-coding waveforms can cover a total bandwidth B_{total} of 20 MHz. The design parameters considered for the construction of the proposed waveforms are given in Table 3.1. For $K = 6$, the output of the optimization process provides the selection of HFH sequences and code sequences as presented in Table 3.2. It is worth mentioning here that the length of the Gold code sequences is $2^r - 1$, $r = 2, 3, 4, 5, 6, 7$, and the number of subpulses used for the formation of the waveform is 126 (N). Thus, we have considered the Gold code sequences of length 127 and the last element of the code sequence is dropped to match the length with the number of subpulses. Cross-correlation between two radar DFCW-PNLC $u_1(t)$ and $u_2(t)$, selected though the optimization process, is shown in Figure 3.2(a) with maximin CCP level as -25.33 dB

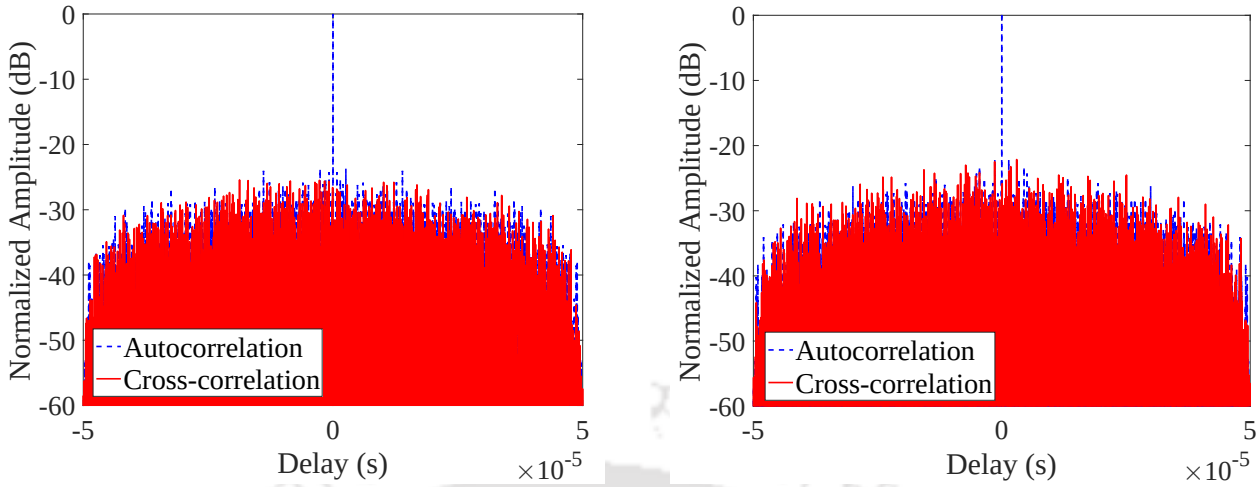

Figure 3.2: (a) Autocorrelation and cross-correlation of two DFCW-PNLC $u_1(t)$ and $u_2(t)$, selected through the optimization process, where $u_1(t) = s_9^{13}(t)$ and $u_2(t) = s_{23}^{55}(t)$. (b) Autocorrelation and cross-correlation of two DFCW-PNLC chosen arbitrarily.

while for the autocorrelation of $u_1(t)$, maximum ASP level is calculated as -23.82 dB. Performance of autocorrelation and cross-correlation considering arbitrary n and l is shown in Figure 3.2(b) with maximin ASP and CCP levels as -22.14 dB and -22.17 dB, respectively which clearly indicates that the proposed optimization process effectively minimizes the ASP and CCP levels.

Performance of a radar user (for 3$^{\text{rd}}$ user, i.e., $v = 3$) in a multiuser radar system for $K = 6$ is presented in Figure 3.3(a) where the received signal is mixed with signals from all other 5 users. The output is shown for zero Doppler scenario. The maximum sidelobe peak level of the correlated output is calculated as -16.44 dB when the signal of the desired user ($v = 3$) is present, whereas

Table 3.2: HFH sequence number n and PN-code sequence number l selected through the optimization process considering $K = 6$

Radar signal number k	HFH sequence number - n (Corresponding HFH sequence - H_n)	PN-code sequence number - l (Corresponding Gold code sequence - C_l)
1	9	13
2	23	55
3	47	26
4	67	69
5	73	102
6	46	96

Table 3.3: Comparison of maximum sidelobe peak levels for multiuser radar system with $K = 6$

Waveform type	Max. sidelobe peak level (dB) (when signal of desired user is available)	Max. CCP level (dB) (when signal of desired user is not available)
Proposed DFCW-PNLC	-16.44	-17.13
DFCW-LC [39]	-15.01	-15.65
DFCW-FF [41, 42]	-14.37	-14.93
DFCW-FF with random phase [44]	-15.52	-16.11
Spread spectrum coded chirp [86]	-14.62	-15.41
DFPCW [43]	-15.57	-16.19

if the receiver receives signals from other radar systems only, maximum CCP level is calculated as -17.13 dB. Performance of a multiuser radar system using waveforms designed according to different techniques [39, 41–44, 86], considering the same sequence length (N), is compared with the proposed one and the corresponding maximum cross-correlation levels are listed in Table 3.3. It can be observed that the proposed DFCW-PNLC provides a cross-correlation gain of 1.48 dB, 1.72 dB, 2.2 dB, 1.02 dB, and 0.94 dB as compared to [39], [86], [41], [44] and [43], respectively.

For a MIMO radar system, considering the number of transmitting and receiving antennas as 6, 6 optimized radar signals ($u_k(t)$) are transmitted through different antennas. The received composite

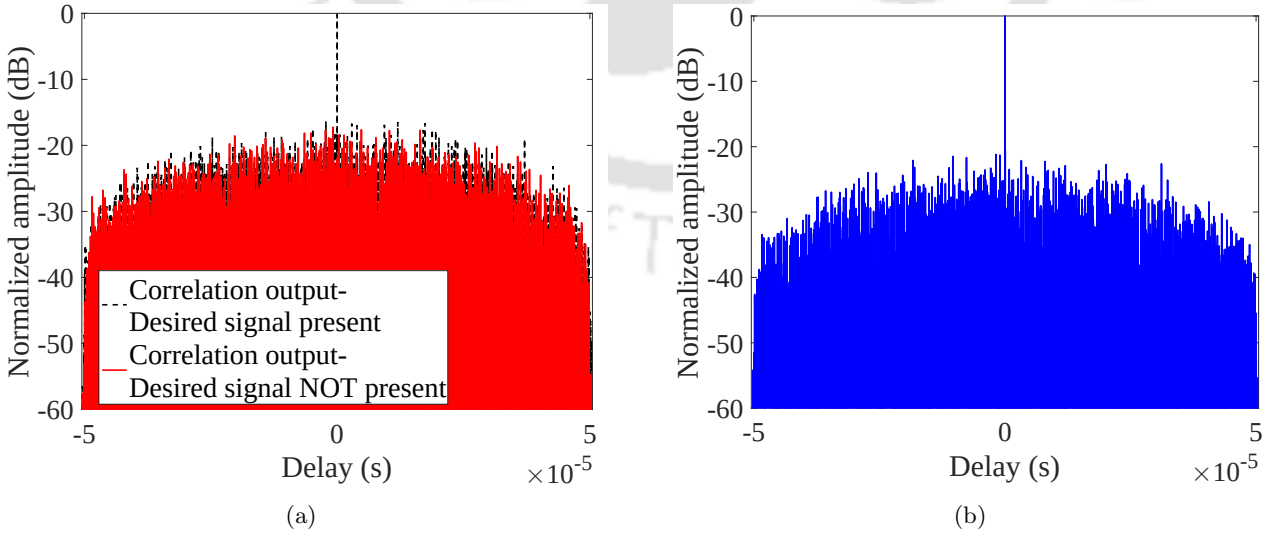

Figure 3.3: (a) Plot of multiuser radar ambiguity function for radar user 3 ($v = 3$) and considering $K = 6$. (b) Plot of MIMO radar ambiguity function considering $K = 6$.

Table 3.4: Comparison of maximum sidelobe peak levels for MIMO radar system with $K = 6$

Waveform type	Max. sidelobe peak level (dB)
Proposed DFCW-PNLC	-21.32
DFCW-LC [39]	-19.64
DFCW-FF [41, 42]	-18.89
DFCW-FF with random phase [44]	-19.05
Spread spectrum coded chirp [86]	-17.73
DFPCW [43]	-18.92

signal can be analyzed through MIMO radar ambiguity function given by (3.13). The output correlated signal at zero Doppler is shown in Figure 3.3(b) with maximum sidelobe peak level is measured as -21.32 dB. In this context, pairwise cross-correlation between different transmitted DFCW-PNLC is calculated through simulation and maximum CCP level is found to be approximately -25.41 dB while maximum ASP level is approximately -23.74 dB. The performance of the proposed waveforms for MIMO radar system is compared with the performance of the MIMO radar systems designed using different available radar waveforms such as DFCW-FF, DFCW-LC [39, 41–44, 86] considering the same sequence length (N). The comparison is listed in Table 3.4. It can be observed that combination of PN-code sequence with DFCW-LC and the selection of sequences through the proposed optimization process provides better performance in terms of maintaining lower sidelobe peak level as compared to

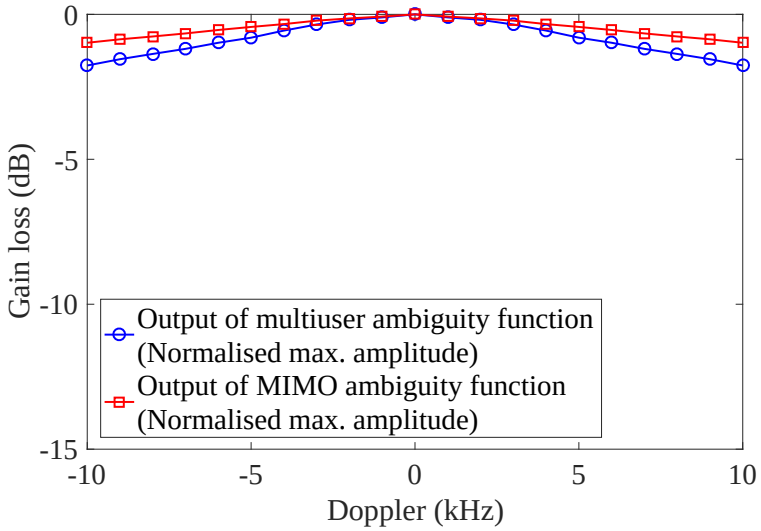

Figure 3.4: Gain loss due to variation in Doppler frequency.

other MIMO radar systems designed with different available waveforms.

Considering a Doppler variation of 10 kHz, Figure 3.4 presents the gain loss due to the effect of Doppler frequency variation in the received signal. It can be found that MIMO radar system is more resilient as compared to multiuser radar system for the same Doppler variation, while the level of the sidelobe peaks remains approximately same during the variation.

3.3 Nonlinear Chirp Waveform for MIMO and Multiuser Radar Systems

It may be noted that for a conventional LC waveform its first peak sidelobe level appears at -13.2 dB [17, 50], and this limits the ASP performance of the DFCWs-LC. On the other hand NLC can provide an improved PSL performance over LC [50, 51] without using window functions or mismatch filtering which incurs SNR loss at the receiver and the reported designs on DFCWs-NLC [52, 53] indicate the superiority of DFCW-NLC over DFCW-LC in terms of ASP and CCP performances. However, very limited works related to DFCW-NLC are currently available, and the reported designs are restricted to three or four waveforms only. In addition, the design of NLC waveform, to be used as subpulses for DFCW-NLC, influences the performance of the DFCWs. Furthermore, as opposed to LC waveform, NLC can be of different types [17, 50, 51] and in general depends on the target application. Thus, unlike the reported works with standalone design of NLC from scratch, design of the required NLC waveform with desired properties through a parameterized waveform design model can greatly simplify the overall waveform design process. In this work, to address the paucity of DFCWs-NLC in attaining waveform diversity for MIMO and multiuser radar applications, firstly, a parameterized mathematical model is proposed for designing NLC waveform. The adaptive model can provide the design of different types of NLC functions and associated waveforms, based on the application requirement, to simplify the overall waveform design process. Secondly, an optimization process based on genetic algorithm is presented for the selection of appropriate values of the input parameters for the parameterized NLC waveforms, derived from the parameterized model, to achieve the desired waveform characteristic, e.g., ASP level, main-lobe width (MLW), and CCP level. After the waveform design and its optimization, finally, the design of a set of DFCWs using NLC to achieve waveform diversity for radar applications is proposed where a joint optimization of the chirp-pulse type and the frequency firing order of the chirp pulses is presented to minimize ASP and CCP levels.

3.3.1 Proposed Parameterized Model for Nonlinear Chirp Waveform Design

The parameterized mathematical model is constructed for designing NLC waveform with the consideration that the waveforms have a bandwidth B, starting frequency f_{L}, ending frequency f_{H}, center frequency f_0 and duration T. A chirp function $f(t)$ with second-degree polynomial is given by

$$f(t) = f_{\mathrm{L}} + \alpha t + \beta t^2, \quad 0 \leq t \leq T, \tag{3.21}$$

where $f(t)$ is the instantaneous frequency variation, α and β are the parameters to control the variation with $0 \leq \alpha, \beta \leq 1$, and $\alpha + \beta = 1$. Extending $f(t)$ in (3.21) for x^{th} degree having normalized time variable can be expressed as

$$f(t) = f_{\mathrm{L}} + B\left[\alpha\left(\frac{t}{T}\right) + \beta\left(\frac{t}{T}\right)^x\right], \quad 0 \leq t \leq T. \tag{3.22}$$

The parameterized function $f(t)$ has the following properties:

(1) For the designed chirp waveform, $f(t)$ always covers the bandwidth B in a duration of T while maintaining appropriate f_0.

(2) A polynomial with a variable degree for $f(t)$ provides design flexibility, and the curvature of $f(t)$ can be varied independently within a range to achieve the desired frequency profile.

(3) LC can be obtained as a special form of the proposed designs.

To accomplish the above design properties, the single $\frac{t}{T}$ term with x^{th} degree in (3.22) is split into two terms of $\frac{t}{T}$ having independent degrees x_1 and x_2 while maintaining the same number of input parameters for $f(t)$ by considering $\beta = 1 - \alpha$. Accordingly, $f(t)$ is modified into

$$f_i(t) = (f_{\mathrm{L}} + (i-1)B) + (-1)^{(i-1)}B\left[\alpha\left(\frac{t}{T}\right) + \frac{1-\alpha}{2}\left(\frac{t}{T}\right)^{x_1} + \frac{1-\alpha}{2}\left(\frac{t}{T}\right)^{x_2}\right], \quad 0 \leq t \leq T, \tag{3.23}$$

where $f_{\mathrm{H}} = f_{\mathrm{L}} + B$, and $i \in \{1, 2\}$. $f_1(t)$ and $f_2(t)$ represent the up-chirp and down-chirp frequency functions, respectively. The input parameters α, x_1, x_2 can have following values while designing a chirp: $0 \leq \alpha \leq 1$, and $x_1, x_2 \geq 1$. The parameterized function $f_i(t)$ given in (3.23) serves as the base model for the design of different asymmetric-type NLC (ANLC) functions, e.g., concave chirp [50], parabolic chirp, exponential chirp [17], quadratic chirp, hyperbolic chirp functions as shown in Figure 3.5. The associated values of the input parameters are also indicated. It may be noted that

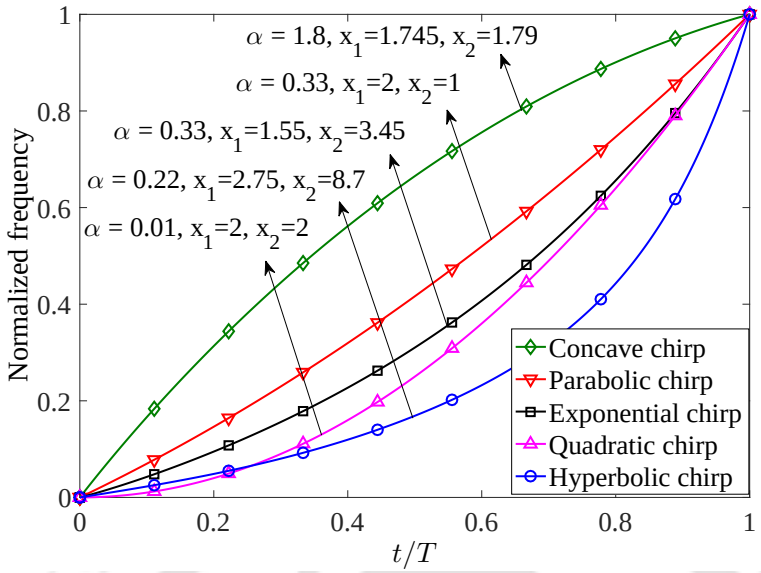

Figure 3.5: Frequency profiles of different asymmetric-type NLC designed using the parameterized chirp function given in (3.23). The corresponding values of the input parameters are mentioned.

for $1 \leq x_1, x_2 \leq 2$, α has a range $0 \leq \alpha \leq 2$. Also, for $\alpha = 1$, (3.23) reduces to an LC function.

Further, suitable modification in the proposed parameterized mathematical model, given in (3.23), allows us to design different symmetric-type NLC (SNLC) functions, i.e., tangential, sine, and cosine chirp functions. Instantaneous frequency variation of a tangential-type and sine-type chirp function can be viewed as antisymmetric with respect to $\frac{T}{2}$ in the interval of 0 to T. Therefore, with appropriate modification in (3.23), a tangential-type chirp function can be expressed as

$$f_i(t) = f_0 + (-1)^{(i-1)}\vartheta B\left[\frac{\alpha}{2}\left(2\vartheta\left(\frac{t}{T}-\frac{1}{2}\right)\right)^{x_1} + \frac{1-\alpha}{2}\left(2\vartheta\left(\frac{t}{T}-\frac{1}{2}\right)\right)^{x_2}\right], \quad 0 \leq t \leq T, \tag{3.24}$$

where $i \in \{1, 2\}$, $0 \leq \alpha \leq 1$, $x_1, x_2 \geq 1$, $\vartheta = (-1)^{\left[\text{round}\left(1-\frac{t}{T}\right)\right]}$ and round$(\cdot)$ is the round off function.

In addition, using (3.23) and (3.24), a sine-type chirp function can be given by

$$f_i(t) = f_0 + (-1)^{(i-1)}\xi B\left[\frac{\alpha}{2}\left(2\xi\left(\frac{t}{T}-\nu\right)\right)^{x_1} + \frac{1-\alpha}{2}\left(2\xi\left(\frac{t}{T}-\nu\right)\right)^{x_2} - \frac{1}{2}\right], \quad 0 \leq t \leq T, \tag{3.25}$$

where $i \in \{1, 2\}$, $0 \leq \alpha \leq 1$, $x_1, x_2 \geq 1$, $\xi = (-1)^{\nu}$, and $\nu = \text{round}\left(\frac{t}{T}\right)$.

In case of a cosine-type chirp function, the instantaneous frequency starts and ends at the same frequency value and has a maximum value at $t = \frac{T}{2}$. Accordingly, modifying the tangential-type chirp

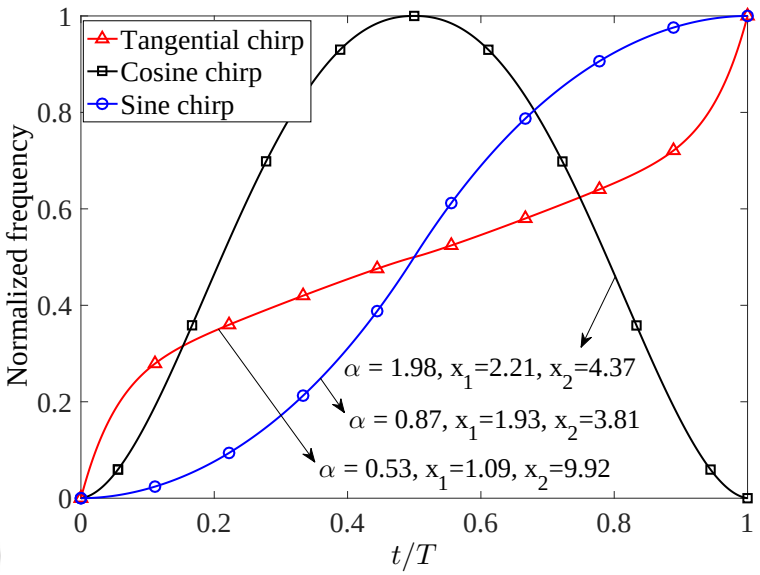

Figure 3.6: Frequency profiles of different symmetric-type NLC designed using the parameterized chirp functions given in (3.24), (3.25), and (3.26). The corresponding values of the input parameters are mentioned.

function given in (3.24), the cosine-type chirp function can be expressed as

$$f_i(t) = f_0 + (-1)^{(i-1)} 2B \left[\frac{\alpha}{2} \left(2\vartheta \left(\frac{t}{T} - \frac{1}{2} \right) \right)^{x_1} + \frac{1-\alpha}{2} \left(2\vartheta \left(\frac{t}{T} - \frac{1}{2} \right) \right)^{x_2} - \frac{1}{4} \right], \quad 0 \le t \le T, \quad (3.26)$$

where $i \in \{1, 2\}$, $0 \le \alpha \le 1$ and $x_1, x_2 \ge 1$. It is worth noting that for small values of x_1 and x_2 with $x_1 \le x_2$, bound on α for the NLC functions in (3.24), (3.25), and (3.26) can be relaxed and can have values more than 1. Furthermore, for $\alpha = 1$ and $x_1 = 1$, the NLC functions in (3.24), (3.25), and (3.26) reduce to LC functions.

For different values of α, x_1, and x_2, corresponding symmetric-type NLC functions are plotted in Figure 3.6. Moreover, based on the design requirement, a range of variations on the designed chirp can be achieved through the proposed parameterized NLC functions which in turn simplify the waveform design process. As an example, the design of a set of tangential-type chirp functions, using (3.24), are plotted in Figure 3.7, and the associated parameter values are also indicated.

The corresponding parameterized NLC waveforms are given by

$$s_i(t) = e^{j2\pi\phi_i(t)}, \quad 0 \le t \le T, \quad (3.27)$$

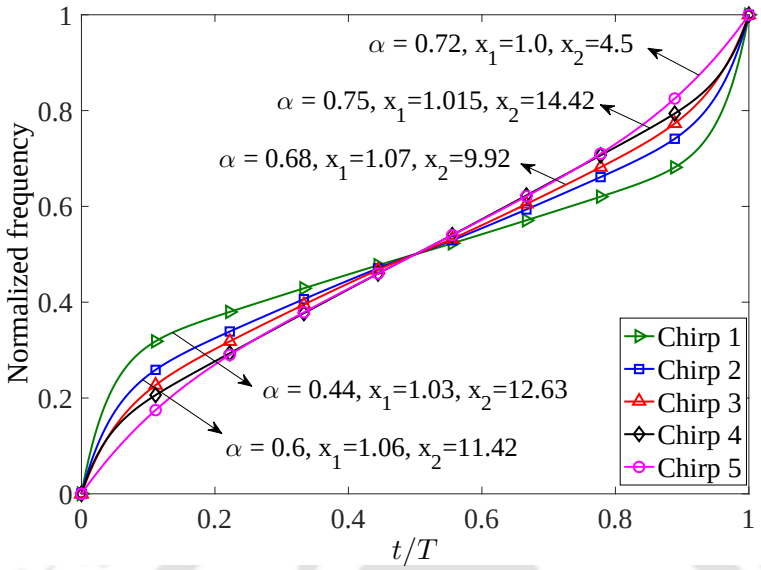

Figure 3.7: Frequency profiles of a set of tangential-type chirp designed using the parameterized NLC function in (3.24).

where $i \in \{1, 2\}$. $s_1(t)$ and $s_2(t)$ represent the up-chirp and down-chirp signals, respectively, and $\phi_i(t)$ is calculated as

$$\phi_i(t) = \int_0^t f_i(t)\ dt, \tag{3.28}$$

where $f_i(t)$ is given in (3.23), (3.24), (3.25), and (3.26).

3.3.1.1 Correlation Analysis for NLC Waveforms

Given the proposed parameterized NLC waveforms, the cross-correlation between the up-NLC and down-NLC waveforms can be evaluated using (3.19), (3.27), and (3.28) as

$$R_{s_i s_{i'}}(\tau) = \int_{-\infty}^{+\infty} s_i(t) s_{i'}^*(t-\tau) dt = \int_{-\infty}^{+\infty} e^{j2\pi\phi_i(t)} e^{-j2\pi\phi_{i'}(t-\tau)} dt \tag{3.29}$$

$$\overset{(a)}{=} e^{j2\pi\left[f_{\mathrm{L}}+(i'-1)B-(-1)^{(i'-1)}\frac{\alpha B\tau}{2T}\right]\tau}\ \Psi_{i,i'}^{\mathrm{ANLC}}(\alpha, x_1, x_2, \tau), \tag{3.30}$$

$$\overset{(b)}{=} e^{j2\pi f_0\tau}\ \Psi_{i,i'}^{\mathrm{Tan}}(\alpha, x_1, x_2, \tau), \tag{3.31}$$

$$\overset{(c)}{=} e^{j2\pi f_0\tau}\ \Psi_{i,i'}^{\mathrm{Sine}}(\alpha, x_1, x_2, \tau), \tag{3.32}$$

$$\overset{(d)}{=} e^{j2\pi f_0\tau}\ \Psi_{i,i'}^{\mathrm{Cosine}}(\alpha, x_1, x_2, \tau), \tag{3.33}$$

where $(\cdot)^*$ denotes the conjugate operation, $i, i' \in \{1, 2\}$, and (a), (b), (c), and (d) represent the cross-correlation outputs corresponding to the chirp functions derived in (3.23), (3.24), (3.25), and (3.26), respectively. Furthermore,

$$\Psi_{i,i'}^{\text{ANLC}}(\alpha, x_1, x_2, \tau) = \int_{t_1}^{t_2} e^{j2\pi B\left[(i-i')+(-1)^{(i'-1)}\frac{\alpha\tau}{T}\right]t} e^{j\pi\frac{B(1-\alpha)T}{x_1+1}\left[(-1)^{(i-1)}\left(\frac{t}{T}\right)^{x_1+1}-(-1)^{(i'-1)}\left(\frac{t-\tau}{T}\right)^{x_1+1}\right]} \times e^{j\pi B\alpha T\left[(-1)^{(i-1)}-(-1)^{(i'-1)}\right]\left(\frac{t}{T}\right)^2} e^{j\pi\frac{B(1-\alpha)T}{x_2+1}\left[(-1)^{(i-1)}\left(\frac{t}{T}\right)^{x_2+1}-(-1)^{(i'-1)}\left(\frac{t-\tau}{T}\right)^{x_2+1}\right]} dt, \tag{3.34}$$

$$\Psi_{i,i'}^{\text{Tan}}(\alpha, x_1, x_2, \tau) = \int_{t_1}^{t_2} e^{j\pi\frac{BT\alpha}{2(x_1+1)}\left[(-1)^{(i-1)}\left(2\vartheta\left(\frac{t}{T}-\frac{1}{2}\right)\right)^{x_1+1}-(-1)^{(i'-1)}\left(2\vartheta\left(\frac{t-\tau}{T}-\frac{1}{2}\right)\right)^{x_1+1}\right]} \times e^{j\pi\frac{BT(1-\alpha)}{2(x_2+1)}\left[(-1)^{(i-1)}\left(2\vartheta\left(\frac{t}{T}-\frac{1}{2}\right)\right)^{x_2+1}-(-1)^{(i'-1)}\left(2\vartheta\left(\frac{t-\tau}{T}-\frac{1}{2}\right)\right)^{x_2+1}\right]} dt, \tag{3.35}$$

$$\Psi_{i,i'}^{\text{Sine}}(\alpha, x_1, x_2, \tau) = \int_{t_1}^{t_2} e^{j\pi\frac{BT\alpha}{2(x_1+1)}\left[(-1)^{(i-1)}\left(2\xi\left(\frac{t}{T}-\nu\right)\right)^{x_1+1}-(-1)^{(i'-1)}\left(2\xi\left(\frac{t-\tau}{T}-\nu\right)\right)^{x_1+1}\right]} \times e^{j\pi\frac{BT(1-\alpha)}{2(x_2+1)}\left[(-1)^{(i-1)}\left(2\xi\left(\frac{t}{T}-\nu\right)\right)^{x_2+1}-(-1)^{(i'-1)}\left(2\xi\left(\frac{t-\tau}{T}-\nu\right)\right)^{x_2+1}\right]} \times e^{j\pi\frac{BT}{2}\left[(-1)^{(i'-1)}\frac{2\xi(t-\tau)}{T}-(-1)^{(i-1)}\frac{2\xi t}{T}\right]} dt, \tag{3.36}$$

$$\Psi_{i,i'}^{\text{Cosine}}(\alpha, x_1, x_2, \tau) = \int_{t_1}^{t_2} e^{j\pi\frac{BT\alpha}{\vartheta(x_1+1)}\left[(-1)^{(i-1)}\left(2\vartheta\left(\frac{t}{T}-\frac{1}{2}\right)\right)^{x_1+1}-(-1)^{(i'-1)}\left(2\vartheta\left(\frac{t-\tau}{T}-\frac{1}{2}\right)\right)^{x_1+1}\right]} \times e^{j\pi\frac{BT(1-\alpha)}{\vartheta(x_2+1)}\left[(-1)^{(i-1)}\left(2\vartheta\left(\frac{t}{T}-\frac{1}{2}\right)\right)^{x_2+1}-(-1)^{(i'-1)}\left(2\vartheta\left(\frac{t-\tau}{T}-\frac{1}{2}\right)\right)^{x_2+1}\right]} \times e^{j\pi\frac{BT}{\vartheta}\left[(-1)^{(i'-1)}\frac{\vartheta(t-\tau)}{T}-(-1)^{(i-1)}\frac{\vartheta t}{T}\right]} dt, \tag{3.37}$$

where the values of t_1 and t_2 for $0 \leq \tau \leq T$ are given as, $t_1 = \tau$ and $t_2 = T$. For $i' = i$, (3.29) gives the autocorrelation output for $s_i(t)$. For a given value of α, x_1 and x_2, the correlation outputs given in (3.30)–(3.33) can be easily computed numerically using common mathematical software such as Matlab or Mathematica.

3.3.2 NLC Parameter Optimization

Based on the design requirements of the NLC waveforms, e.g., chirp function type, ASP and CCP levels, the input parameters of the parameterized NLC waveforms, presented in Section 3.3.1, need to be chosen appropriately. Hence, it can be considered as parameter optimization problems and can be solved easily through an optimization process using GA.

GA is a search based algorithm and it is developed on the concepts of natural selection and genetics [87]. It provides the optimized solution through an iterative search process [39, 87] and consists of the following steps: generation of population, evaluation of fitness function, selection,

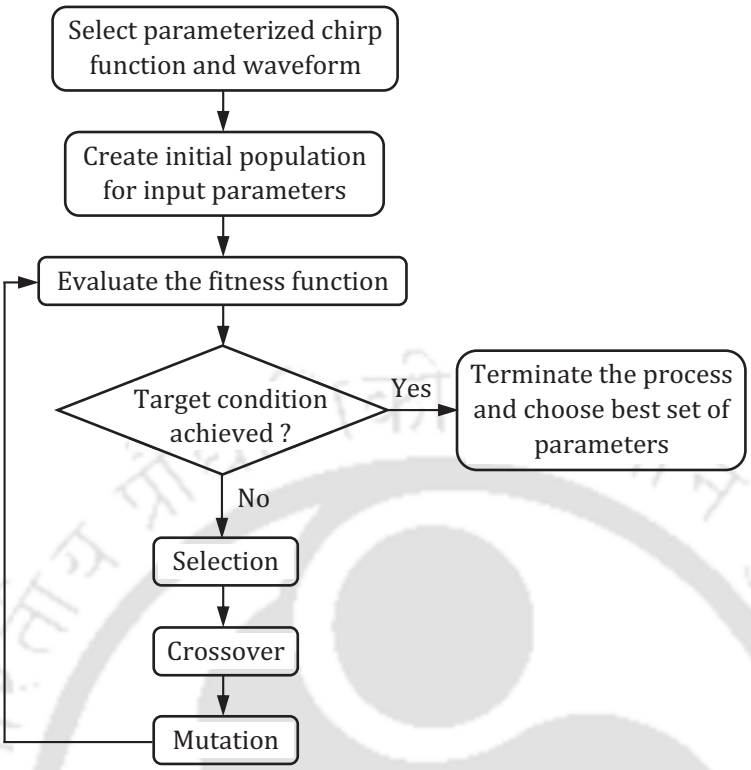

Figure 3.8: Flowchart of the optimization process based on GA.

crossover, and mutation. The optimization process used for the parameter optimization of the chirp waveform is given in the following steps while a flowchart of the process is illustrated in Figure 3.8.

(1) Based on the application, choose appropriate chirp function type and corresponding chirp waveform, presented in Section 3.3.1, since the input parameters related to the selected function are to be optimized to achieve the target requirement, e.g., ASP and CCP levels. Here, the process steps are presented in general form and no specific criterion is considered; however, some examples are presented in this context as follows– (i) sine and cosine type chirps are used for communication applications [88], (ii) hyperbolic and exponential chirps are considered for multiuser communication [34,35], and for sensing and tracking applications [89], (iii) tangential type chirp is considered for radar, sonar application [51], (iv) concave type chirps are considered as a means for pulse compression applications [50].

(2) For each input parameter, an equal number of random individuals are generated within the specified range-level to form an initial population. A method based on random initialization is performed to initialize the population treated as the candidate solutions in GA. Subsequently,

sets of random individuals are formed such that each set consists of one random individual for each of the input parameters corresponding to the selected parameterized chirp waveform.

(3) For each set of the input parameters, the evaluation of the fitness function is performed. The formulation of the associated function is described below.

(4) If the target condition is achieved, e.g., if the cost function achieves a predefined threshold while maintaining the design constraints if any, the process is stopped, and the best set of inputs is selected. Based on application or design requirement the target condition can be the ASP level, or CCP level, or MLW value, or a combination of these.

(5) Otherwise, in the selection phase, a portion of the population most suitable based on the fitness function output is selected, and a new population is formed through crossover and mutation operations.

(6) During crossover more than one parent is selected and they are combined to form a new offspring (chromosome). For the present optimization process single point crossover [87] with crossover probability of 0.6 is considered. Mutation can be considered as a process of altering or tweaking in the chromosome, to obtain a new solution, and bit-flip mutation [87] with mutation probability of 0.1 is considered for the present optimization process. Accordingly, the newly formed sets become the input to Step 3 for the evaluation of the fitness function.

The cost function and fitness function associated with the parameterized NLC waveform can be formulated as follows: to design an NLC waveform with required ASP level, for the given chirp type and the values of the input parameters, the corresponding autocorrelation output $R_{s_i s_i}(\tau)$ is calculated using (3.29). Next, the ASP values are calculated numerically from $R_{s_i s_i}(\tau)$ and given as $\zeta = [\zeta_1, \zeta_2, \zeta_3, ...]$, and are used to form the fitness function. The associated cost function is given as $E = \max(\zeta)$. Alternatively, it can be evaluated as $E = \max|R_{s_i s_i}(\tau)|_{\tau \neq 0}$. In case of a given MLW constraint, E is minimized while maintaining the constraint.

The parameter values used for optimization purpose are listed in Table 3.5. These values are chosen after performing rigorous simulations to ensure the convergence of the search process.

Examples of NLC waveform optimization are presented below. Firstly, we consider a concave NLC function, i.e., curve model III given in [50], and the associated NLC signal provides an ASP level of -15.87 dB for a $TB = 40$ and $T = 5$ μs. Also, the -3 dB MLW is calculated as $0.028T$ as

Table 3.5: Parameter values used for the optimization process based on GA

Parameter	Value or type
Population set	150 individuals
Number of generations	100
Crossover type	Single point crossover
Crossover probability	0.6
Mutation type	Bit-flip mutation
Mutation probability	0.1

shown in Figure 3.9(a). Now, using the proposed NLC function given by (3.23), obtained from the parameterized model, the associated NLC signal and its ASPs are calculated using (3.27) and (3.30). Accordingly, optimal values of the input parameters α, x_1, x_2 need to be obtained to minimize the peak sidelobe level while maintaining the same MLW. After performing the optimization process, the values of the input parameters are optimized as $\alpha = 0.47$, $x_1 = 1.002$, and $x_2 = 12.8$, and it provides an ASP level of -18.66 dB as shown in Figure 3.9(a) which indicates an improvement of 2.79 dB in peak sidelobe level over [50].

Secondly, for the optimization of symmetric-type NLC signal, the chirp function type is chosen as a tangential-type chirp. A tangential-type chirp signal designed using the chirp function given

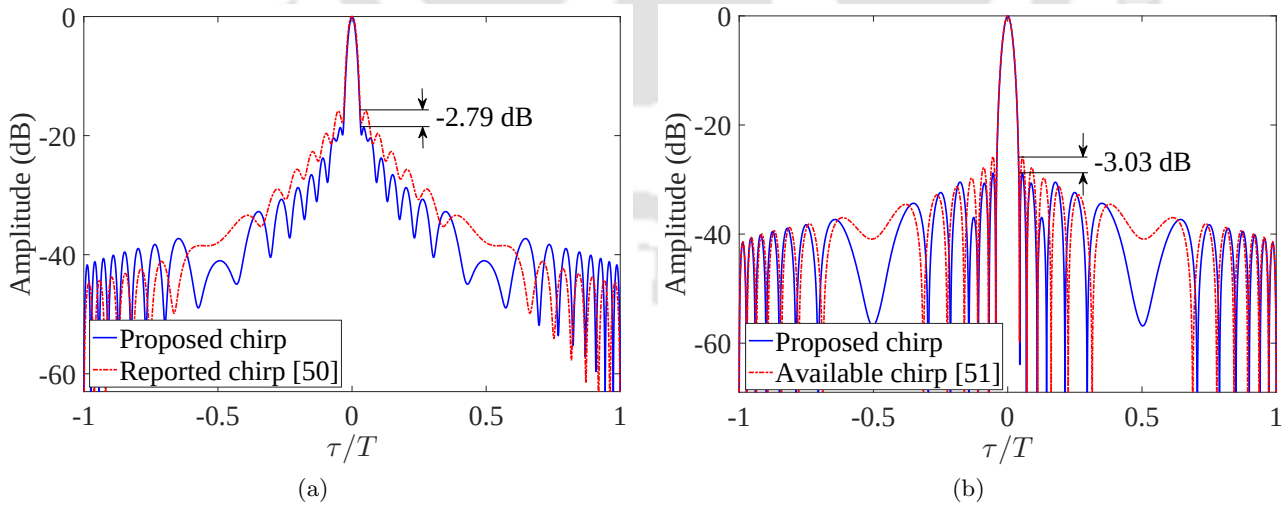

Figure 3.9: (a) Comparison of autocorrelation sidelobe peaks between the NLC given in [50] and the designed parameterized asymmetric-type NLC with optimized input parameters for $TB = 40$ and equal MLW. (b) Comparison of autocorrelation sidelobe peaks between the NLC given in [51] and the designed parameterized symmetric-type NLC with optimized input parameters for $TB = 40$ and equal MLW.

in [51], for a $TB = 40$ and $T = 5$ μs, provides an ASP level of -25.81 dB as shown in Figure 3.9(b) with a -3 dB MLW of $0.03T$. Now, to design a tangential-type chirp, the proposed tangential-type chirp function given in (3.24) is used. The associated chirp signal and ASPs are calculated using (3.27) and (3.31). Compared to the chirp function in [51] which needs to calculate M coefficients with $M = 30$, the proposed NLC function requires to calculate only three parameters, thereby providing a simpler design process. The optimization process output, to minimize the peak sidelobe level while maintaining the same MLW value, provides the optimized values of the input parameters as $\alpha = 0.352$, $x_1 = 1.084$, and $x_2 = 8.212$, with an ASP level of -28.84 dB. The output, shown in Figure 3.9(b), indicates an improvement of 3.03 dB in ASP level over [51]. Thus, the designed parameterized NLC functions not only provide the required waveforms but also provide improved performance over the existing ones.

3.3.3 Proposed Design for Set of DFCW-NLC

Construction of discrete frequency-coding waveforms consisting of pulses designed using the parameterized NLC, given in Section 3.3.1, is presented in this section. Based on the requirement, the set of waveforms can be used for MIMO and multiuser radar applications. In this context, the correlation properties of the proposed waveforms are analyzed and are compared with DFCWs designed using linear and nonlinear chirp waveforms reported in [39, 40, 46, 48, 49, 52, 53].

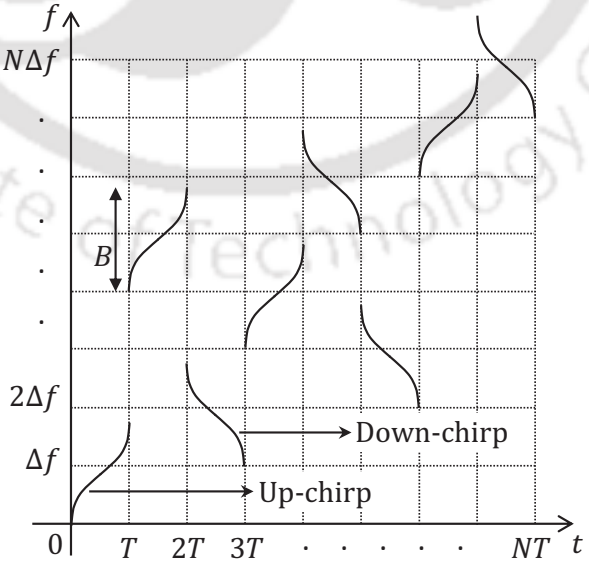

Figure 3.10: Time-frequency plot of one of the DFCW-NLC designed using the parameterized tangential-type NLC.

The waveform, namely discrete frequency-coding waveform with nonlinear chirp pulses, i.e., DFCW-NLC, consists of N frequency hopping pulses having a frequency step size of Δf, and each pulse having a duration of T, and bandwidth of B. In the proposed design, in a particular DFCW-NLC, each one of the N pulses can be either up-chirp or down-chirp, as shown in Figure 3.10. The pulse type is considered as tangential-type chirp, obtained using (3.24) and (3.27), for the construction of DFCW-NLC. Considering that the waveform set consists of K DFCWs-NLC, k^{th} waveform can be expressed as

$$s_k(t) = \sum_{n=0}^{N-1} p_{i,n}^k(t - nT), \tag{3.38}$$

where $i \in \{1, 2\}$, $k = 1, 2, \ldots, K$, the waveform duration is $T_{\text{d}} = NT$, and $p_{1,n}^k(t)$ and $p_{2,n}^k(t)$ represent the up-chirp pulse and down-chirp pulse, respectively. Using (3.27) $p_{i,n}^k(t)$ is given as

$$p_{i,n}^k(t) = e^{j2\pi\phi_{i,n}^k(t)}, \quad 0 \le t \le T. \tag{3.39}$$

The associated instantaneous frequency function $f_{i,n}^k(t)$ is expressed using (3.24) as

$$f_{i,n}^k(t) = (f_0 + G_k(n)\Delta f) + (-1)^{(i-1)}\vartheta B\left[\frac{\alpha}{2}\left(2\vartheta\left(\frac{t}{T} - \frac{1}{2}\right)\right)^{x_1} + \frac{1-\alpha}{2}\left(2\vartheta\left(\frac{t}{T} - \frac{1}{2}\right)\right)^{x_2}\right], \tag{3.40}$$

and $\phi_{i,n}^k(t)$ is calculated using (3.28) and (3.40) as

$$\begin{aligned}\phi_{i,n}^k(t) = {} & (f_0 + G_k(n)\Delta f)\, t + (-1)^{(i-1)}\frac{BT}{4} \\ & \times\left[\frac{\alpha}{x_1+1}\left(2\vartheta\left(\frac{t}{T} - \frac{1}{2}\right)\right)^{x_1+1} + \frac{1-\alpha}{x_2+1}\left(2\vartheta\left(\frac{t}{T} - \frac{1}{2}\right)\right)^{x_2+1}\right].\end{aligned} \tag{3.41}$$

Here, G_k is a sequence of length N and represents the frequency firing order of the chirp pulses for k^{th} DFCW-NLC. The sequence is a unique permutation of sequence $\{0, 1, \ldots, N-1\}$ and n is the index number of the sequence with the corresponding value given by $G_k(n)$ where $G_k(n) \in \{0, 1, \ldots, N-1\}$.

3.3.4 Waveform Optimization and Selection

Performance of the proposed DFCW-NLC can be evaluated through CAF. Using (3.6) and (3.38) the CAF between two waveforms, $s_k(t)$ and $s_l(t)$, $k, l \in \{1, 2, \ldots, K\}$, $k \ne l$, can be expressed as

$$\chi_{s_k s_l}(\tau, \varphi) = \int_{-\infty}^{+\infty} s_k(t) s_l^*(t - \tau) e^{j2\pi\varphi t} dt, \tag{3.42}$$

$$= \sum_{n=0}^{N-1}\sum_{m=0}^{N-1}\int_{-\infty}^{+\infty} p_{i,n}^k(t - nT)\; p_{i',m}^{l*}(t - mT - \tau) e^{j2\pi\varphi t} dt, \tag{3.43}$$

where $i, i' \in \{1, 2\}$ and φ accounts the Doppler offset. For $l = k$, (3.43) reduces to delay-Doppler ambiguity function (DAF) given by $\chi_{s_k s_k}(\tau, \varphi)$. Whereas, the CAF between two pulse waveforms, $p_{i,n}^{k}(t)$ and $p_{i',m}^{l}(t)$, can be evaluated using (3.31), (3.39), and (3.43) as

$$\begin{aligned}\Upsilon_{p_{i,n}^{k} p_{i',m}^{l}}(\tau, \varphi) &= \int_{-\infty}^{+\infty} p_{i,n}^{k}(t) p_{i',m}^{l^*}(t-\tau) e^{j2\pi\varphi t} dt \\ &= e^{j2\pi(f_0 + G_l(m)\Delta f)\tau} \ \Psi_{i,k,n,i',l,m}^{(\text{DFCW-NLC})}(\alpha, x_1, x_2, \tau, \varphi), \end{aligned} \tag{3.44}$$

where $\Psi_{i,k,n,i',l,m}^{(\text{DFCW-NLC})}(\alpha, x_1, x_2, \tau, \varphi)$ is given by

$$\begin{aligned}\Psi_{i,k,n,i',l,m}^{(\text{DFCW-NLC})}(\alpha, x_1, x_2, \tau, \varphi) = \int_{-\infty}^{\infty} & e^{j2\pi[(G_k(n) - G_l(m))\Delta f + \varphi]t} \\ & \times e^{j\pi \frac{BT\alpha}{2(x_1+1)} \left[(-1)^{(i-1)} \left(2\vartheta\left(\frac{t}{T} - \frac{1}{2}\right)\right)^{x_1+1} - (-1)^{(i'-1)} \left(2\vartheta\left(\frac{t-\tau}{T} - \frac{1}{2}\right)\right)^{x_1+1} \right]} \\ & \times e^{j\pi \frac{BT(1-\alpha)}{2(x_2+1)} \left[(-1)^{(i-1)} \left(2\vartheta\left(\frac{t}{T} - \frac{1}{2}\right)\right)^{x_2+1} - (-1)^{(i'-1)} \left(2\vartheta\left(\frac{t-\tau}{T} - \frac{1}{2}\right)\right)^{x_2+1} \right]} dt, \end{aligned} \tag{3.45}$$

and substituting (3.44) in (3.43), $\chi_{s_k s_l}(\tau, \varphi)$ can be evaluated. Here, for the analysis of correlation properties of the DFCW-NLC, φ is considered to be zero. Accordingly the cross-correlation between the pulses, $p_{i,n}^{k}(t)$ and $p_{i',m}^{l}(t)$, can be calculated from (3.44) as

$$R_{p_{i,n}^{k} p_{i',m}^{l}}(\tau) = \Upsilon_{p_{i,n}^{k} p_{i',m}^{l}}(\tau, 0). \tag{3.46}$$

Setting $l = k$, $m = n$, and $i' = i$, the autocorrelation of $p_{i,n}^{k}(t)$ can be calculated from (3.46).

Since in the proposed design each pulse can be of up-chirp or down-chirp type, for a given T and B, we need to determine appropriate input parameters, α, x_1, x_2, such that cross-correlation between the up-chirp and the down-chirp pulse waveforms, i.e., $R_{p_i p_{i'}}(\tau)$, calculated from $R_{p_{i,n}^{k} p_{i',m}^{l}}(\tau)$ (l, k, m, n ignored), should be minimized while maintaining chirp autocorrelation, calculated from $R_{p_i p_{i'}}(\tau)$ for $i' = i$, within a threshold level. Hence, a joint optimization of ASP level of the chirp and CCP level between the up-chirp and the down-chirp pulses is performed. The associated cost function can be formulated as

$$E_{\text{pulse}} = \max(\zeta_{\text{CCP}}(\tau)) + \max(\zeta_{\text{ASP}}(\tau)), \tag{3.47}$$

where $\zeta_{\text{ASP}}(\tau) = |R_{p_i p_i}(\tau)|_{\tau \neq 0}$ and $\zeta_{\text{CCP}}(\tau) = |R_{p_i p_{i'}}(\tau)|$ constitute the fitness functions and satisfy the condition: $\max(\zeta_{\text{CCP}}(\tau)) \leq \max(\zeta_{\text{ASP}}(\tau))$. In radar applications where multiple waveforms are used simultaneously, CCP level between different DFCWs-NLC should be as low as possible to maximize the performance. From (3.43) and (3.44) it can be found that for each DFCW $s_k(t)$, $k \in \{1, 2, \ldots, K\}$, the

associated sequence G_k and the chirp type (i) of each pulse $p_{i,n}^k(t)$ needs to be optimized to improve the overall cross-correlation performance. Accordingly, the optimal sequence for the constructed DFCW-NLC can be obtained through the GA based optimization process, presented in Section 3.3.2, and using (3.43) and (3.46) the associated cost function is given by

$$E_{\text{DFCW-NLC}} = \sum_{k=1}^{K} \max|\chi_{s_k s_k}(\tau,0)|_{\tau\neq 0} + \sigma_1 \sum_{k=1}^{K} \sum_{l=1,l\neq k}^{K} \max|\chi_{s_k s_l}(\tau,0)|, \tag{3.48}$$

where σ_1 is the weight coefficient to control the relative weight of the two summation terms. The ASP and CCP levels calculated from (3.48) constitute the associated fitness functions. In the optimization process, the number of generations is kept large to ensure the convergence of the search process and is set to 100.

3.3.5 Performance Analysis and Discussion

In this work, the design of a set of eight DFCWs-NLC, i.e., $K = 8$, is performed and it provides double the number of waveforms as compared to the designs in [52,53]. For the given design parameters of $N = 32$, $TB = 32$, and $T\Delta f = 4$, the optimized values of the input parameters for the tangential-type chirp pulse, obtained from the optimization process, are $\alpha = 0.6598$, $x_1 = 1.0049$, $x_2 = 4.6608$, and are used to construct the DFCWs-NLC. The corresponding ASP level is -26.73 dB and CCP level between the up-chirp and the down-chirp pulse is -15.51 dB. In the next step, the frequency firing order sequence, G_k, and the chirp type (i) of each pulse associated with each DFCW-NLC are optimized considering σ_1 as 1. The optimized sequences G_k along with the chirp type i of the corresponding NLC pulses are listed in Table 3.6. The associated ASP and CCP values of the proposed DFCWs are presented in Table 3.7. The CCP values indicate a good level of separation, in terms of cross-correlation performance, between the DFCWs and make them a suitable candidate for MIMO radar and multiuser radar applications. Further, as an example, the autocorrelation performances of the eight DFCWs-NLC are shown in Figure 3.11.

Performance of the proposed set of DFCWs-NLC is compared with the reported DFCWs designed using LC [39], PWLC [49], tansec-type chirp [52], i.e., DFCW-TSC, and tangential-type chirp [53], i.e., DFCW-TC, for MIMO radar applications, considering the same value of K, N, TB and Δf. Results, given in Table 3.8, indicate that the proposed set of DFCWs, designed using the optimized tangential-type chirp pulse in combination with the optimized frequency hopping sequence (G_k) and pulse type (i), provide significant improvement in average sidelobe peak level performances for both

Table 3.6: Frequency firing order sequence (G_k) along with the type (i) of the associated chirp pulses of the DFCW-NLC with $K = 8$

$n \downarrow$	G_1	i	G_2	i	G_3	i	G_4	i	G_5	i	G_6	i	G_7	i	G_8	i
0	13	2	6	1	8	1	3	1	16	1	27	1	31	2	1	1
1	6	2	0	1	3	1	28	1	22	2	28	2	4	2	4	2
2	23	2	14	2	17	1	4	2	5	2	21	1	14	2	10	2
3	18	2	26	2	1	1	1	2	23	1	2	2	21	2	0	2
4	21	1	5	1	25	2	27	2	3	2	8	1	11	2	18	1
5	10	1	27	1	18	2	6	1	6	1	25	2	2	1	9	1
6	0	1	24	2	10	1	9	1	25	1	14	2	17	1	7	1
7	15	2	22	1	19	1	24	1	20	2	15	2	30	2	26	2
8	25	1	30	2	31	2	12	2	7	1	31	1	25	1	28	1
9	22	2	13	1	2	1	16	2	29	1	20	2	16	1	23	2
10	24	2	18	1	27	2	19	2	18	1	3	1	28	1	20	2
11	17	1	29	1	16	1	2	2	8	2	1	2	6	2	29	2
12	31	1	15	1	6	1	5	2	9	1	12	1	3	2	27	1
13	12	1	4	2	23	2	15	1	10	1	29	1	26	1	19	2
14	5	2	7	1	13	1	0	2	21	1	5	2	22	1	21	1
15	28	2	17	2	11	2	14	1	28	2	23	2	7	2	31	1
16	7	2	31	1	30	2	30	1	31	2	9	2	8	1	30	1
17	27	1	21	2	0	2	26	1	19	2	30	1	18	2	15	2
18	19	1	19	2	21	2	11	1	11	2	22	2	15	2	14	1
19	11	2	23	1	20	2	23	1	14	1	4	1	10	2	24	1
20	1	1	1	1	24	1	20	1	2	2	16	2	5	2	6	2
21	26	2	12	2	7	2	10	2	0	1	0	2	24	2	22	1
22	4	1	10	1	15	1	31	2	12	1	19	1	12	2	5	2
23	29	2	8	1	12	1	25	1	13	2	24	2	23	2	12	2
24	2	1	20	1	26	2	8	2	30	1	18	1	29	2	25	2
25	8	2	3	2	14	1	13	2	15	2	13	1	1	1	2	2
26	3	1	25	1	5	1	17	2	1	2	6	1	0	1	17	2
27	20	1	28	2	28	1	29	2	17	1	7	2	20	2	16	1
28	30	2	11	2	4	1	7	1	4	1	10	1	13	1	3	1
29	9	1	9	2	9	1	18	1	27	2	11	1	9	2	13	1
30	14	2	16	2	29	1	21	2	26	1	17	2	27	2	11	1
31	16	1	2	1	22	2	22	1	24	1	26	2	19	2	8	1

autocorrelation and cross-correlation operations over [39, 49, 52, 53]. The designed DFCWs-NLC provide an average ASP level gain of 5.45 dB, 7.39 dB, 3.92 dB, 3.44 dB, and an average CCP level gain

Table 3.7: ASP and CCP values in dB of the designed DFCWs-NLC for $K = 8$, $N = 32$, $TB = 32$, and $T\Delta f = 4$

	s_1	s_2	s_3	s_4	s_5	s_6	s_7	s_8
s_1	−27.48	−26.43	−26.62	−26.79	−26.29	−26.36	−26.22	−26.20
s_2	−26.43	−27.65	−26.27	−26.22	−26.24	−26.39	−26.51	−26.37
s_3	−26.62	−26.27	−27.50	−26.26	−26.46	−26.38	−26.29	−26.55
s_4	−26.79	−26.22	−26.26	−27.66	−26.36	−26.47	−26.53	−26.31
s_5	−26.29	−26.24	−26.46	−26.36	−27.81	−26.34	−26.44	−26.27
s_6	−26.36	−26.39	−26.38	−26.47	−26.34	−28.00	−26.49	−26.32
s_7	−26.22	−26.51	−26.29	−26.53	−26.44	−26.49	−27.68	−26.25
s_8	−26.20	−26.37	−26.55	−26.31	−26.27	−26.32	−26.25	−28.03

of 5.76 dB, 6.61 dB, 5.90 dB, 3.72 dB as compared to [39], [49], [52], and [53], respectively. Thus, the improved CCP performance of the proposed DFCWs, while maintaining a low ASP level, makes them a superior candidate for MIMO radar applications.

For multiuser radar system, considering a pair of waveforms, e.g., s_6 and s_8, the associated ASP

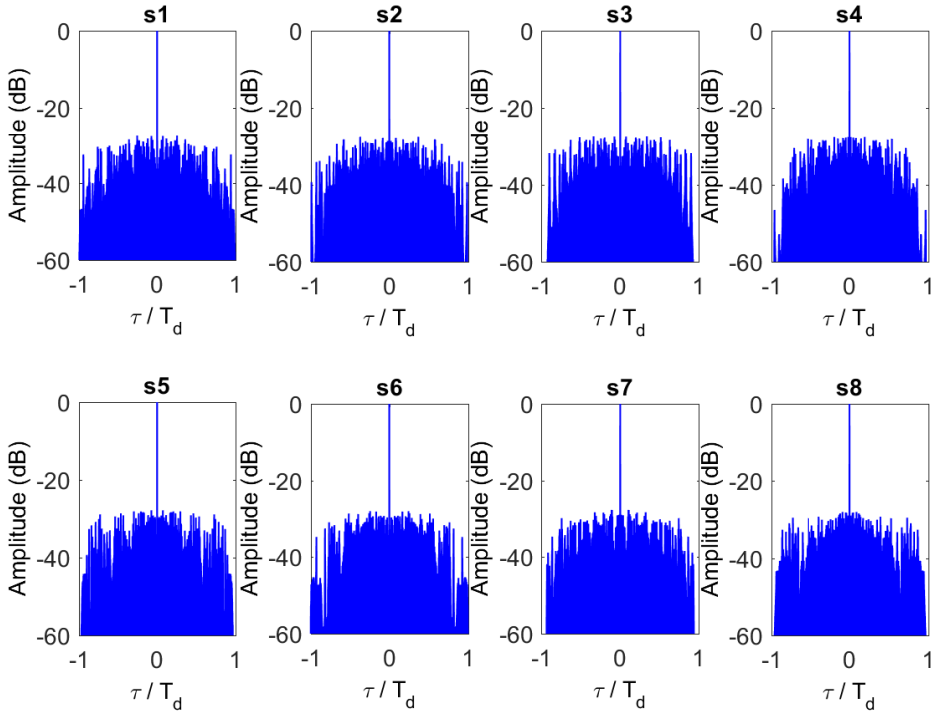

Figure 3.11: Autocorrelation outputs of the designed DFCWs-NLC with $TB = 32$, $N = 32$, $T\Delta f = 4$, and $K = 8$.

Table 3.8: Comparison of different DFCWs for $K = 8$, $N = 32$, $TB = 32$, and $T\Delta f = 4$

	Average ASP level	Average CCP level
Proposed DFCW-NLC	−27.73 dB	−26.38 dB
DFCW-LC [39]	−22.28 dB	−20.62 dB
Proposed DFCW-PNLC (Sec. 3.2)	−23.11 dB	−21.03 dB
DFCW-PWLC [49]	−20.34 dB	−19.77 dB
DFCW-TSC [52]	−23.81 dB	−20.48 dB
DFCW-TC [53]	−24.29 dB	−22.66 dB

Table 3.9: ASP and CCP performance for a pair of DFCWs with $N = 32$, $TB = 32$, and $T\Delta f = 4$

	Average ASP level	Average CCP level
Proposed DFCW-NLC	−28.01 dB	−26.32 dB
DFCW waveform [40]	−24.13 dB	−22.14 dB
DFCW waveform [46]	−22.21 dB	−21.67 dB
DFCW waveform [48]	−24.16 dB	−21.93 dB

and CCP performances of the proposed DFCWs are compared with the designs reported in [40, 46, 48] while maintaining the same value of N, TB and Δf. The results, given in Table 3.9, indicate a superior sidelobe peak level performance by the proposed DFCWs with an average ASP level gain of 3.88 dB, 5.80 dB, 3.85 dB, and an average CCP level gain of 4.18 dB, 4.65 dB, 4.39 dB as compared to [40], [46], and, [48], respectively. We find that the designed DFCWs-NLC perform equally good, in terms of correlation performances, for both MIMO and multiuser radar applications, and this indicates the effectiveness of the proposed parameterized model and the waveform design process to attaining radar waveform diversity.

3.4 SC-MCR Waveform for Satellite IoT Communication

Chirp waveform modulation, apart from the radar systems, has recently found its application for LEO satellite IoT communication where design of symmetry chirp (SC) waveforms [58] is used for low data rate communication. However, the reported waveform is considered for single user and only one pair of SC waveforms has been used, therefore it constitutes an interesting opportunity to explore further about the waveform and its potentiality in M-ary and multiuser environment. Thereby, in this work, firstly, the cross-correlation performance of multiple SC waveforms is analyzed to find its

suitability in presence of interference. Secondly, from the analysis and understanding of the proposed radar waveforms related to minimization of overall cross-correlation level, design of a new symmetry chirp with multiple chirp rates, SC-MCR, is proposed to achieve improved overall cross-correlation performance as compared to SC waveforms. Thirdly, a design of time domain multiplexed SC-MCR waveforms is presented to improve the overall system data rate, and finally SER performance of an M-ary communication system employing the SC-MCR waveforms is evaluated over an Rice-lognormal satellite (RLS) channel [90] in a multiuser scenario.

3.4.1 SC Waveform Analysis

In the design of SC waveforms presented in [58], for a given bandwidth B, waveform duration T, and spreading factor SF, starting frequency of the waveforms is given by

$$\nu_n = B_n \frac{B}{2^{SF}}, \tag{3.49}$$

where $B_n \in \{0, 1, 2, \ldots, 2^{SF} - 1\}$, $BT = 2^{SF}$, and $SF = 6, 7, \ldots, 12$. The associated symmetric chirp waveform in time-domain [58] is given by

$$s_n(t) = \begin{cases} \sqrt{\frac{E_s}{T}} e^{j2\pi\left(\frac{B}{2T}t^2 + \nu_n t\right)}, & 0 \le t < T_n, \\ \sqrt{\frac{E_s}{T}} e^{j2\pi\left(\frac{B}{2T}t^2 + \nu_n t - Bt\right)}, & T_n \le t < T, \end{cases} \tag{3.50}$$

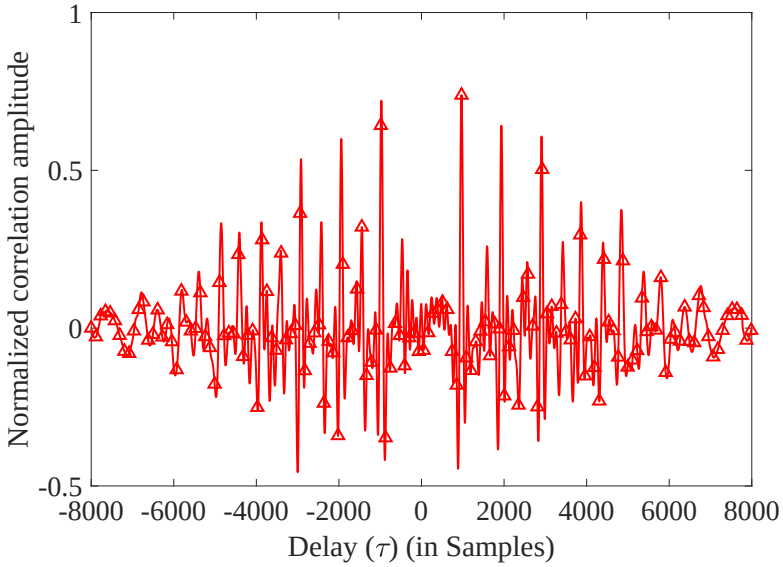

Figure 3.12: Cross-correlation performance of SC waveforms [58] considering 8 waveforms and $SF = 6$.

where $T_n = \left(1 - \frac{\nu_n}{B}\right) T$, $n \in \{0, 1, 2, \ldots, 2^{SF} - 1\}$, and E_s is the symbol energy.

Consider a set of 8 SC waveforms, with $SF = 6$ and $B_n = 3, 6, 9, \ldots, 24$, operating simultaneously in a multiuser communication scenario. Cross-correlation of the SC waveform of a particular user with the received signal comprising of SC waveforms of rest of the users is calculated and is shown in Figure 3.12. It indicates presence of multiple large cross-correlation peaks, with maximum normalized peak value exceeding 0.7 at different delay positions. The main reason for the formation of the peaks is the cross-correlation of chirp sections of one SC waveform with that of the other SC waveforms. As the chirp rate is the same for different sections of SC waveforms, overlap of the chirp sections of SC waveforms at different delay generates localized peaks and when multiple SC waveforms operate simultaneously, accumulation of localized peaks results in a large one.

3.4.2 Proposed Design of SC-MCR Waveform

Fixed chirp rate in SC waveforms leads to high cross-correlation peaks and the cross-correlation between chirp waveforms can be reduced by keeping the chirp rates different [1]. Thus, minimization of the localized cross-correlation peak values between the sections of different SC waveforms while maintaining the symmetry nature of the waveform can be achieved by dividing each half of the waveform into subsections and applying different chirp rates for each subsection. Accordingly, the design of a new set of chirps namely symmetry chirp with multiple chirp rates, SC-MCR, is presented to reduce the overall cross-correlation level caused by possible delays in LEO satellite communication. The proposed SC-MCR waveforms, for a given bandwidth B, waveform duration T, and SF, can be constructed as follows:

(1) Frequency variation of the chirp is symmetric with respect to $\frac{T}{2}$ in the interval of 0 to T.

(2) Each half is divided into two subsections with two different chirp rates and each half of the chirp covers the entire bandwidth. For each subsection, the out-of-band frequency portion is wrapped around such that it stays within the signal bandwidth.

(3) Different chirp signals can be designed by shifting the starting frequency of the chirp. The frequency shift between chirps is integral multiple of Δf and $\Delta f = \frac{B}{2^{SF}}$.

The plot of instantaneous frequency of the SC-MCR waveform is shown in Figure 3.13. Based on the chirp rate of the first sub-section of the chirp having a duration of l, two kinds of SC-MCR are

designed: up-SC-MCR and down-SC-MCR when the chirp rate is positive and negative, respectively. A generalized design process of the instantaneous frequency of k^{th} up-SC-MCR waveform can be formulated as

$$f_k(t) = \begin{cases} k\Delta f + \frac{B}{2} + \mu_0 t, & 0 \le t \le T_1 \ \& \ k\Delta f + \frac{B}{2} + \mu_0 t \le B \\ k\Delta f - \frac{B}{2} + \mu_0 t, & t \le T_1 \\ k\Delta f + x_1 B - \mu_1 t, & t \le T_2 \ \& \ k\Delta f + x_1 B - \mu_1 t \ge 0 \\ k\Delta f + x_2 B - \mu_1 t, & t \le T_2 \\ k\Delta f - x_2 B + \mu_1 t, & t \le T_3 \ \& \ k\Delta f - x_2 B + \mu_1 t \le B \\ k\Delta f - x_3 B + \mu_1 t, & t \le T_3 \\ k\Delta f + x_4 B - \mu_0 t, & t \le T \ \& \ k\Delta f + x_4 B - \mu_0 t \ge 0 \\ k\Delta f + x_5 B - \mu_0 t, & t \le T. \end{cases} \tag{3.51}$$

Similarly, the generalized design process of the instantaneous frequency for k^{th} down-SC-MCR waveform is given by

$$f_k(t) = \begin{cases} k\Delta f - \frac{B}{2} - \mu_0 t, & 0 \le t \le T_1 \ \& \ k\Delta f - \frac{B}{2} - \mu_0 t \ge 0 \\ k\Delta f + \frac{B}{2} - \mu_0 t, & t \le T_1 \\ k\Delta f - x_1 B + \mu_1 t, & t \le T_2 \ \& \ k\Delta f - x_1 B + \mu_1 t \le B \\ k\Delta f - x_2 B + \mu_1 t, & t \le T_2 \\ k\Delta f + x_2 B - \mu_1 t, & t \le T_3 \ \& \ k\Delta f + x_2 B - \mu_1 t \ge 0 \\ k\Delta f + x_3 B - \mu_1 t, & t \le T_3 \\ k\Delta f - x_4 B + \mu_0 t, & t \le T \ \& \ k\Delta f - x_4 B + \mu_0 t \le B \\ k\Delta f - x_5 B + \mu_0 t, & t \le T, \end{cases} \tag{3.52}$$

where l denotes the duration of the first sub-section, i.e., $T_1 = l$, $T_2 = \frac{T}{2}$, $T_3 = T - l$, and $0 < l < \frac{T}{2}$ and $l \neq \frac{T}{4}$. $BT = 2^{SF}$, $k \in \{0, 1, 2, \ldots, 2^{SF} - 1\}$, $\Delta f = \frac{B}{2^{SF}}$, and SF is an integer with $SF \ge 1$. Values for x_1, x_2, x_3, x_4, and x_5 are given as $x_1 = \frac{l}{T-2l} - \frac{1}{2}$, $x_2 = \frac{1}{2}\left(\frac{T}{T-2l}\right)$, $x_3 = \frac{1}{2}\left(2 + \frac{T}{T-2l}\right)$, $x_4 = \frac{1}{2}\left(\frac{T}{l} - 1\right)$, and $x_5 = \frac{1}{2}\left(\frac{T}{l} + 1\right)$. Different chirp rates are calculated as $\mu_0 = \frac{B}{2l}$ and $\mu_1 = \frac{B}{T-2l}$.

In each sub-section of the up-SC-MCR and the down-SC-MCR, the out-of-band portion is wrapped around and the transition time instant T_{k_i}, for i^{th} section of k^{th} chirp, can be obtained from (3.51)

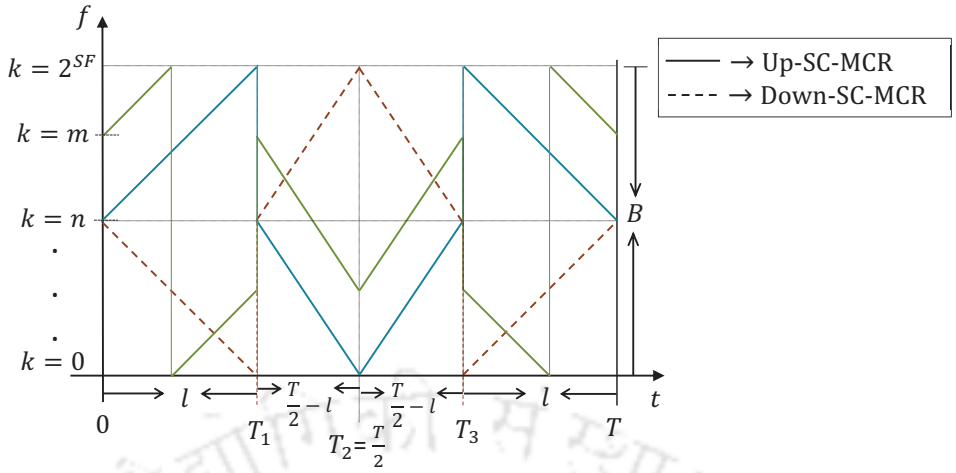

Figure 3.13: Plot of time-frequency of the proposed SC-MCR. Two up-SC-MCRs ($k = n$ and $k = m$) are shown in solid lines and one down-SC-MCR ($k = n$) is shown in dashed line.

and (3.52), respectively where $i = 1, 2, 3, 4$. As an example, using (3.51), corresponding T_{k_i} can be calculated as

$$\begin{aligned}
T_{k_1} = t \quad &\text{for} \quad k\Delta f + \frac{B}{2} + \mu_0 t = B, \quad 0 < t < T_1 \\
T_{k_2} = t \quad &\text{for} \quad k\Delta f + x_1 B - \mu_1 t = 0, \quad T_1 < t < T_2 \\
T_{k_3} = t \quad &\text{for} \quad k\Delta f - x_2 B + \mu_1 t = B, \quad T_2 < t < T_3 \\
T_{k_4} = t \quad &\text{for} \quad k\Delta f + x_4 B - \mu_0 t = 0, \quad T_3 < t < T,
\end{aligned} \tag{3.53}$$

where $T_2 = \frac{T}{2}$. Corresponding SC-MCR waveforms, in complex form, can be written as

$$s_k(t) = e^{j2\pi\phi_k(t)}, \quad 0 \le t \le T, \tag{3.54}$$

where $\phi_k(t) = \int_0^t f_k(t)dt$, and $f_k(t)$ is given in (3.51) and (3.52) for up-SC-MCR and down-SC-MCR, respectively.

3.4.2.1 Correlation Analysis of Waveforms

Given the proposed SC-MCR waveforms, the cross-correlation between any two SC-MCR waveforms $s_n(t)$ and $s_m(t)$, $n, m \in \{0, 1, \ldots, 2^{SF} - 1\}$, given by (3.54) and $m > n$, can be calculated using (1.10) in a generalized form as

$$R_{s_n s_m}(\tau) = \int_{-\infty}^{+\infty} s_n(t) s_m^*(t-\tau)dt = \sum_{i=0}^{3} \int_{T_i}^{T_{i+1}} s_n(t) s_m^*(t-\tau)dt, \tag{3.55}$$

where $(\cdot)^*$ denotes the conjugate operation, $T_0 = 0$ and $T_4 = T$. In case there is a transition within a subsection, the integral for that section can be calculated as the summation of individual integrals, i.e., using (3.55)

$$\int_{T_i}^{T_{i+1}} s_n(t)s_m^*(t-\tau)dt = \int_{T_i}^{T_{m_{i+1}}} s_n(t)s_m^*(t-\tau)dt + \int_{T_{m_{i+1}}}^{T_{i+1}} s_n(t)s_m^*(t-\tau)dt. \tag{3.56}$$

Thus, total correlation can be considered as a sum of correlations between different subsections of the two chirps. The instantaneous frequency of the subsections of SC-MCRs, given in (3.51) and (3.52), can be written in a general form, for any up-chirp subsection, as

$$f_k^c(t) = k\Delta f + \xi_k + \mu_{c_k} t, \quad t_1 \le t \le t_2, \tag{3.57}$$

and for any down-chirp subsection as

$$f_k^c(t) = k\Delta f + \xi_k - \mu_{c_k} t, \quad t_1 \le t \le t_2, \tag{3.58}$$

where $c \in \{0, 1\}$ and ξ incorporates the constant terms. Corresponding chirp signal of the subsection is given using (3.54), (3.57), and (3.58) as

$$s_k^c(t) = e^{j2\pi\phi_k^c(t)}, \tag{3.59}$$

where $\phi_k^c(t) = \int_0^t f_k^c(t)dt$. Using (3.51), (3.52), (3.54), (3.55), and (3.57) cross-correlation between two subsections of the SC-MCR waveforms $s_n(t)$ and $s_m(t)$, considering that both the subsections have up-chirps, is given by

$$\begin{aligned} R_{s_n^p s_m^q}(\tau) &= \int_{t_1}^{t_2} s_n^p(t) s_m^{q^*}(t-\tau)dt \qquad (3.60)\\ &= \int_{t_1}^{t_2} e^{j2\pi\left[(n\Delta f+\xi_n)t+\frac{\mu_{p_n}}{2}t^2\right]} e^{-j2\pi\left[(m\Delta f+\xi_m)(t-\tau)+\frac{\mu_{q_m}}{2}(t-\tau)^2\right]}dt \\ &= e^{-j\pi\mu_{q_m}\tau^2} e^{j2\pi(m\Delta f+\xi_m)\tau} e^{-j\pi\frac{\left[(n-m)\Delta f+(\xi_n-\xi_m)+\mu_{q_m}\tau\right]^2}{(\mu_{p_n}-\mu_{q_m})}} \\ &\quad \times \int_{t_1}^{t_2} e^{j\pi\left[\sqrt{\mu_{p_n}-\mu_{q_m}}t+\frac{(n-m)\Delta f+(\xi_n-\xi_m)+\mu_{q_m}\tau}{\sqrt{\mu_{p_n}-\mu_{q_m}}}\right]^2} dt \\ &= \frac{e^{-j\pi\mu_{q_m}\tau^2} e^{j2\pi(m\Delta f+\xi_m)\tau}}{\sqrt{2(\mu_{p_n}-\mu_{q_m})}} e^{-j\pi\frac{\chi^2}{(\mu_{p_n}-\mu_{q_m})}} \left[C'(z_2)+jS'(z_2)-C'(z_1)-jS'(z_1)\right], \qquad (3.61) \end{aligned}$$

where $\chi = (n-m)\Delta f + (\xi_n - \xi_m) + \mu_{q_m}\tau$, $z_{\varepsilon=1,2} = \sqrt{\frac{2}{\mu_{p_n}-\mu_{q_m}}}\left[(\mu_{p_n}-\mu_{q_m})t_\varepsilon + \chi\right]$ and $p, q \in \{0, 1\}$. $C'(z)$ and $S'(z)$ are Fresnel integrals [10]. For $n = m$ and $p = q$, (3.61) gives the autocorrelation of

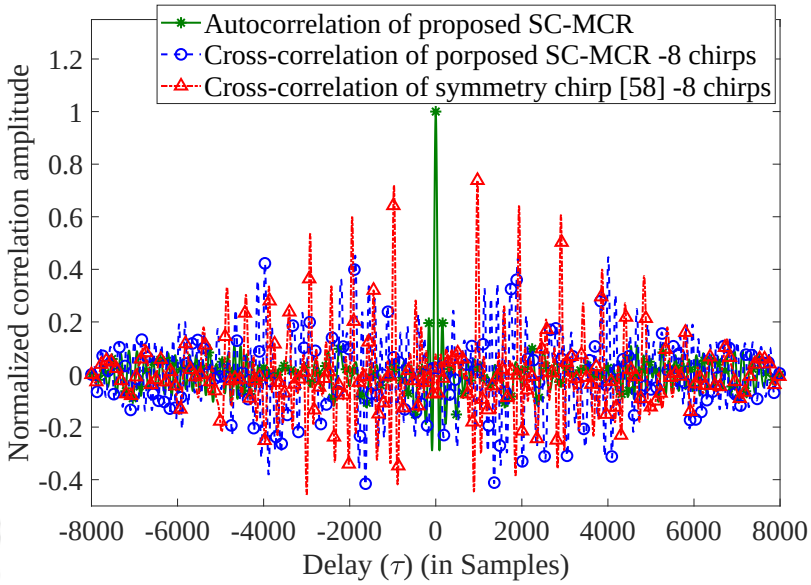

Figure 3.14: Cross-correlation performance of SC waveforms [58] and up-SC-MCR waveforms considering 8 waveforms, $SF = 6$ and $l = 0.3T$. Also autocorrelation of up-SC-MCR is shown.

$s_n^p(t)$. Similarly, if chirp-types of two subsections are opposite, i.e., one is up-chirp while the other is down-chirp, the cross-correlation can be calculated using (3.54), (3.55), (3.57), (3.58), and (3.60) as

$$\begin{aligned} R_{s_n^p s_m^q}(\tau) &= \int_{t_1}^{t_2} e^{j2\pi\left[(n\Delta f+\xi_n)t+\frac{\mu_{p_n}}{2}t^2\right]} e^{-j2\pi\left[(m\Delta f+\xi_m)(t-\tau)-\frac{\mu_{q_m}}{2}(t-\tau)^2\right]} dt \\ &= \frac{e^{j2\pi(m\Delta f+\xi_m)\tau} e^{j\pi\mu_{q_m}\tau^2}}{\sqrt{2(\mu_{p_n}+\mu_{q_m})}} e^{-j\pi\frac{\psi^2}{(\mu_{p_n}+\mu_{q_m})}} \left[C'(z_2)+jS'(z_2)-C'(z_1)-jS'(z_1)\right], \end{aligned} \tag{3.62}$$

where $\psi = (n-m)\Delta f + (\xi_n - \xi_m) - \mu_{q_m}\tau$, $z_{\varepsilon=1,2} = \sqrt{\frac{2}{\mu_{p_n}+\mu_{q_m}}}\,[(\mu_{p_n}+\mu_{q_m})t_\varepsilon + \psi]$.

Cross-correlation of the up-SC-MCR waveforms considering 8 chirps, $SF = 6$ and $l = 0.3T$ is plotted in Figure 3.14. Result indicates that maximum cross-correlation level of the proposed SC-MCR waveforms is lower than that of SC waveforms. For different delay τ, SC-MCR waveforms are able to maintain the normalized overall cross-correlation level below 0.5, whereas for SC waveforms it exceeds 0.7 for certain delay values. Thus, for a multiuser or M-ary communication scenario, SC-MCR minimizes MAI compared to SC.

3.4.3 Time Domain Multiplexed SC-MCR Waveforms: A Transmission Scheme to Improve Data Rate

For a K user environment with each user using an M-ary chirp system where $M = 2^d$ and $KM = 2^{SF}$, the data rate for the entire system is given by $R_{\text{total}} = \frac{dK}{T}$ bits/s. In an attempt to

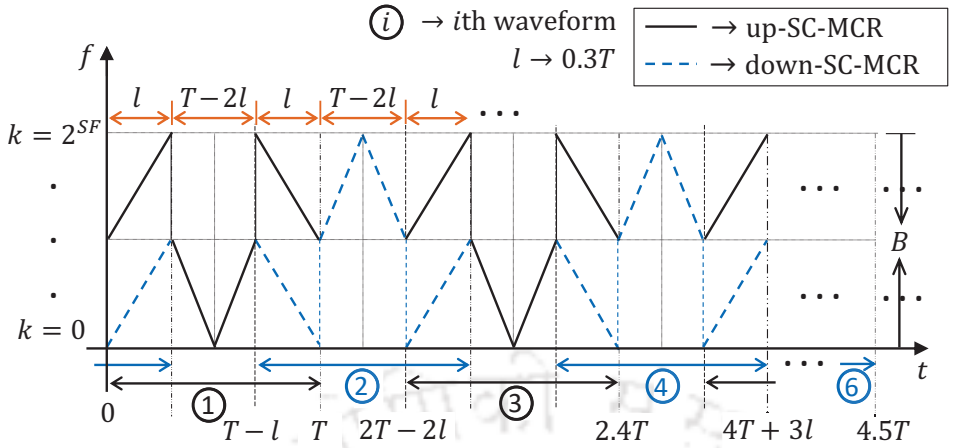

Figure 3.15: Time domain multiplexed chirps constructed using up-SC-MCR and down-SC-MCR with the overlap of $0.3T$.

improve the data rate a design of a time domain multiplexed (TDM) SC-MCR waveform is presented here for a the multiuser system. Both up-SC-MCR and down-SC-MCR waveforms are used for the design as shown in Figure 3.15 with l is chosen as $0.3T$. Overlapping of chirp waveforms is the basis of the proposed design. In time domain, a set of 2^{SF} up-SC-MCR and a set of 2^{SF} down-SC-MCR are placed such that the last subsection of the waveforms in one set overlaps with the first subsection of the waveforms in the next set. The two sets are repeated to obtain the TDM SC-MCR. Since the chirp rate of the first subsection of the waveforms in a set is the same as the chirp rate of the last subsection of waveforms in the previous set, complete overlap of the subsections boosts the autocorrelation output level for both the chirp waveforms during the demodulation at the receiver. However, for partial overlap of subsections, the cross-correlation depends on the amount of overlap. The corresponding chirp waveforms of a subsection for up-SC-MCR and down-SC-MCR can be obtained using (3.51), (3.52), (3.57), (3.58), and (3.59), and all the correlation values can be evaluated using (3.55), (3.60), and (3.62). For an overlap of $0.3T$, it can be found using Figure 3.15 that 6 waveforms can be transmitted in a duration of $4.5T$. Thus, the lower bound on the overall data rate for TDM SC-MCR is $\tilde{R}_{\text{total}} = \frac{2dK}{1.5T}$ bits/s which is higher than R_{total}.

3.4.4 System Model and Performance Analysis Over RLS Channel

A multiuser scenario with K users (IoT nodes) is considered. Each user is equipped with an M-ary system, designed using the up-SC-MCR waveforms, and to transmit a d-bit symbol a set of M SC-MCR waveforms are used for mapping each symbol uniquely [4, 36] where $M = 2^d$. Using (3.51)

and (3.54), chirp signals corresponding to the k^{th} user can be written as

$$s_{k_u}(t) = e^{j2\pi\phi_{(kM+u)}(t)}, \quad 0 \leq t \leq T, \tag{3.63}$$

where u denotes the u^{th} chirp out of M chirps allocated for k^{th} user, $u \in \{0, 1, \ldots, M-1\}$, and $k \in \{0, 1, \ldots, K-1\}$. For a given SF, the values for M and K are chosen such that all the available waveforms can be used, i.e., $KM = 2^{SF}$. At k^{th} receiver, the received signal is given by

$$y_k(t) = \sqrt{E_{\text{s}}} s_{k_u}(t) + \sum_{r=0; r\neq k}^{K-1} \sqrt{E_{\text{s}}} s_{r_i}(t) + w_k(t), \tag{3.64}$$

where $i \in \{0, 1, \ldots, M-1\}$ and denotes the i^{th} waveform transmitted for r^{th} user. E_{s} is the symbol energy, $w_k(t)$ is additive white Gaussian noise with zero mean and variance $\frac{N_0}{2}$, and a process similar to [59] is assumed for acquisition of the received signal. At the receiver, cross-correlation of the received signal $y_k(t)$ with the reference chirp waveforms, constituted from (3.63), would result in only intended correlator to produce high output and lead to estimation of d-bit data symbol [4, 36]. Accordingly, following [4] and using (2.87), for k^{th} user the SEP can be bounded and given by

$$P_{e_k} \leq \frac{1}{M} \sum_{u=0}^{M-1} \sum_{v=0; v\neq u}^{M-1} Q\left[\left(\frac{E_{\text{s}} \left(1 - \rho_{kk}^{vu}\right)}{N_0 + \sum_{r=0; r\neq k}^{K-1} E_{\text{s}} \tilde{\rho}_{kr}^{uv}} \right)^{\frac{1}{2}} \right], \tag{3.65}$$

where $\tilde{\rho}_{kr}^{uv} = \rho_{kr}^{ui} - \rho_{kr}^{vi}$. ρ_{kk}^{vu}, ρ_{kr}^{ui}, and ρ_{kr}^{vi} are normalized sampled values of $R_{s_{k_v} s_{k_u}}(\tau)$, $R_{s_{k_u} s_{r_i}}(\tau)$, and $R_{s_{k_v} s_{r_i}}(\tau)$, respectively, and are calculated using (3.55), (3.61), (3.62), and (3.64). $Q\{\cdot\}$ is the Q-function [16].

Use of the proposed TDM SC-MCR waveforms in the chirp system allows us to increase the number of users, hence increasing the overall data rate, without increasing SF. A set of K M-ary users can be identified by assigning a set of 2^{SF} up-SC-MCR waveforms and another set of K users can be given a set of 2^{SF} down-SC-MCR waveforms. Waveforms in each set have a waveform duration of T and the repetition interval for each set is given by $2T - 2l$, as shown in Figure 3.15. Accordingly, the SEP for k^{th} user, designed using the up-SC-MCR waveforms of the TDM SC-MCR, can be given, after appropriately modifying (3.65), as

$$P_{e_k} \leq \frac{1}{M} \sum_{u=0}^{M-1} \sum_{v=0; v\neq u}^{M-1} Q\left[\left(\frac{E_{\text{s}} \left(1 - \rho_{kk}^{vu} + \hat{\rho}_{kk}^{uv}\right)}{N_0 + \sum_{r=0; r\neq k}^{K-1} E_{\text{s}} \left(\tilde{\rho}_{kr}^{uv} + \hat{\rho}_{kr}^{uv}\right)} \right)^{\frac{1}{2}} \right], \tag{3.66}$$

where $\hat{\rho}_{kr}^{uv} = \acute{\rho}_{kr}^{up'q'} - \acute{\rho}_{kr}^{vp'q'}$ and $\acute{\rho}_{kr}^{up'q'} = \rho_{kr}^{up'} + \rho_{kr}^{uq'}$. $\rho_{kr}^{up'}$ and $\rho_{kr}^{uq'}$ are normalized sampled values of

$R_{s_{k_u}s'_{r_p}}(\tau)$ and $R_{s_{k_u}s'_{r_q}}(\tau)$, respectively, and are calculated using (3.61) and (3.62). For $u = v$, $\acute{\rho}_{kr}^{vp'q'}$ is calculated from $\acute{\rho}_{kr}^{up'q'}$. Within the interval of 0 to T, $s'_{r_p}(t)$ and $s'_{r_q}(t)$ corresponding to the last and the first subsections of down-SC-MCR waveforms, obtained using (3.51), (3.52), (3.54), and (3.64), overlap with the first and the last subsections of up-SC-MCR waveforms, respectively. Further, $\hat{\rho}_{kk}^{uv}$ is obtained from $\hat{\rho}_{kr}^{uv}$ by setting $r = k$.

The performance of the system is analyzed under an RLS channel model [90] which represents a LEO satellite channel, modeled for the L-band, and its PDF is given by

$$f_h(h) = \int_0^\infty \frac{2(\grave{K}+1)h}{\sqrt{2\pi}g\sigma S^3} e^{-\left[(\grave{K}+1)\frac{h^2}{S^2}+\grave{K}+\left(\frac{\ln S-\psi}{\sqrt{2}g\sigma}\right)^2\right]} I_0\left[\frac{2h}{S}(\grave{K}(\grave{K}+1))^{\frac{1}{2}}\right] dS, \tag{3.67}$$

where h is the envelop of the received signal, $\grave{K}$ is the Rice factor, S is shadowing, I_0 is the zero order modified Bessel function of the first kind, and $g = (\ln 10)/20$. The model parameters $\grave{K}$, ψ, σ are functions of the elevation angle α as defined in [90]. Using the PDF, performance of the chirp system is evaluated through numerical simulations.

3.4.5 Numerical Results and Discussion

The SER performance of the multiuser M-ary system, with $SF = 6$, $l = 0.3T$, $K = 8$, and $M = 8$, for LEO satellite IoT communication, is presented in Figure 3.16. From the results it can be found that

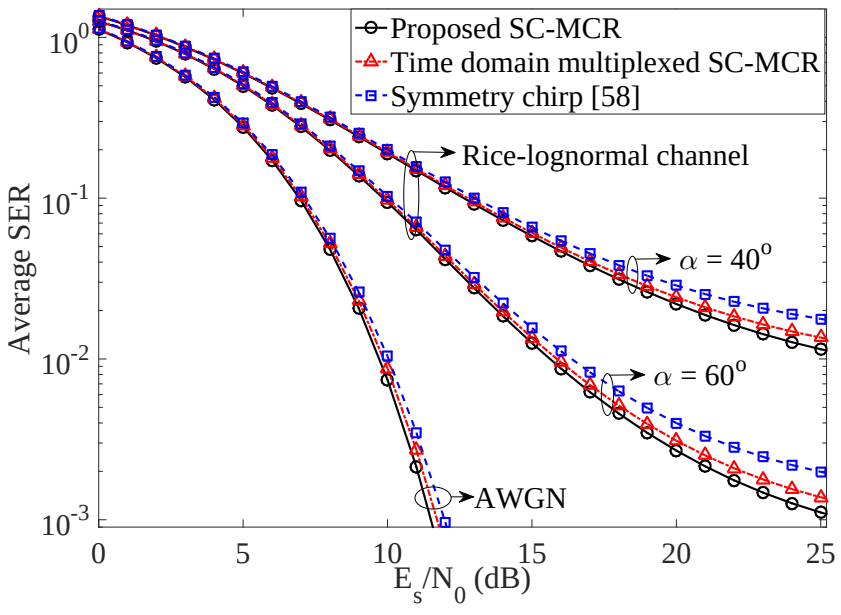

Figure 3.16: SER performance of an M-ary communication system with transmission rate of 3 bits per symbol employing the proposed up-SC-MCR waveforms, the proposed TDM SC-MCR waveforms, and the symmetry chirp waveforms [58] in a multiuser environment considering $SF = 6$ and $l = 0.3T$.

the use of SC-MCR waveforms result in better performance over SC waveforms for both AWGN and RLS channels. With the increment of elevation angle α, i.e., from 40° to 60°, the system performances improve, because of increase in $\grave{K}$ and decrease in σ [90].

The system using TDM SC-MCR waveforms shows slightly poor performance compared to the system using up-SC-MCR waveforms, due to increase in the number of users. However, it performs better compared to the system using SC waveforms while providing higher data rate. For the given system with SC, the overall data rate R_{total} can be given as 15000 bits/s whereas using TDM SC-MCR, the overall data rate $\tilde{R}_{\text{total}}$ is given by 20000 bits/s , which is 1.33 times higher. Based on application requirement, data rate of the system can be increased by varying B and SF appropriately. For SER level of 2×10^{-3} and $\alpha = 60°$, the systems with up-SC-MCR and TDM SC-MCR provide a gain of 3.6 dB and 2.7 dB in $\frac{E_s}{N_0}$, respectively over the system with SC, as shown in Figure 3.16, indicating that SC-MCR waveforms provide better interference immunity over SC waveforms.

3.5 Summary

In this chapter, design of chirp waveforms is investigated for radar and LEO satellite IoT applications, and the associated results are analyzed to evaluate the corresponding improvements in performance. Particularly, in the first work, presented in Section 3.2, design of DFCW with phase-coded LC pulses is carried out for multiuser and MIMO radar systems where HFH sequences are used to control the frequency-firing order of the waveforms. The associated auto-ambiguity and cross-ambiguity functions are derived to analyze the performance of the waveforms. An optimization process consisting of two stages with the selection of appropriate HFH sequences and PN-code sequences in the first and second stages, respectively has been presented, and the associated simulation results have demonstrated the effectiveness of the proposed design technique and the optimization process in terms of providing improved ASP and CCP level performance over existing DFCW-LC. Design of a set of DFCWs-NLC is described in the next work, in Section 3.3, for which a parameterized mathematical model is proposed. Both symmetric and asymmetric type NLC functions can be obtained from the model and an optimization process based on GA has been presented to achieve optimal values of input parameters of the NLC waveforms based on the targeted output. In addition, analytical expressions of autocorrelation and cross-correlation for the parameterized NLC waveforms that have been used in optimization process are derived. Related simulation results have indicated that the parameterized NLC

waveforms in combination with the optimization process are not only able to provide chirp waveforms with desired properties but also improve the ASP and CCP performances over the existing designs while using fewer input variables, and thereby simplifying the waveform design process. A set of eight DFCWs-NLC are designed where the duration and bandwidth of the NLC pulse remain the same but the chirp type (up-chirp or down-chirp) varies across DFCW. A tangential-type NLC waveform, obtained from the model, serves as the building block for the DFCW where the input parameters of the waveform are optimized to improve the ASP and CCP levels. Analytical expressions of CAF and DAF for the analysis of the sidelobe peak levels of the proposed DFCWs have been derived, and a joint optimization of the frequency hopping sequences and the chirp type at each frequency slot of the DFCWs-NLC has been performed to attain further improvement in ASP and CCP levels of the DFCWs. The numerical results confirm that the proposed design is able to provide a large set of DFCWs while minimizing the overall ASP levels and CCP levels between the DFCWs. Moreover, in comparison to the reported DFCW designs, the proposed design provides an average gain of ≈ 5.0 dB and ≈ 5.47 dB in ASP and CCP levels while considering waveforms for MIMO radar, and an average gain of ≈ 4.51 dB and ≈ 4.41 dB in ASP and CCP levels while considering waveforms for multiuser radar. Hence, it makes the designed set of DFCWs a superior candidate for high range-resolution radar applications and indicates the effectiveness of the proposed parameterized model and the waveform design process. In the third work, in Section 3.4, design of SC-MCR waveform is presented to improve overall cross-correlation level over SC waveforms [58] for which high cross-correlation peaks are observed under multiuser scenario. The generalized design of two types of SC-MCR, i.e., up-SC-MCR and down-SC-MCR has been discussed and analytical expressions for cross-correlation and autocorrelation of the SC-MCR waveforms have been derived. In addition, analysis on the SER performance of an M-ary system over an RLS channel in a multiuser scenario indicates that employing SC-MCR waveform reduces cross-correlation and provides better performance over SC waveforms. Moreover, the proposed TDM SC-MCR by combining the up-SC-MCR and down-SC-MCR has allowed to increase in the overall system data rate with minor degradation in performance. Thus, the proposed SC-MCR waveforms are able to provide a more reliable LEO satellite IoT communication and maintain a higher data rate compared to that of SC waveforms.

4

Design and Analysis of Chirp Waveform for WEIT in Multisensor System over Multiantenna and Multibands

Contents

4.1 Introduction[1]

Design of waveforms and systems based on chirp for communication and radar applications have been explored and investigated in the previous chapters. In the era of 5G and massive MIMO wireless technology, WEIT has recently gained significant attention [71] as it makes use of RF signal for simultaneous operation of WET and WIT. WET becomes appealing by essentially providing a perpetual supply of energy for energy-limited networks, e.g., WSN, IoT etc., low power electronic devices in order to prolong the lifetime of the energy-constrained nodes [24]. However, most of the existing works have studied WET or WEIT based on the transmission of fixed-frequency waveform on the downlink (DL) either for single carrier [63–66] or for multi-carrier systems like OFDM [22, 24, 69–72]. As a waveform, chirp exhibits some unique properties which are given below:

(1) Unlike fixed-frequency waveform in which the signal bandwidth is inversely related to its duration, the duration of a chirp can be varied independently of its bandwidth [1].

(2) Since, the instantaneous frequency of chirps varies as a function of time, with appropriate design it can be ensured that identical signal frequencies corresponding to distinct chirps do not appear at a given time instant. This is the reason why the instantaneous power contained at any frequency satisfies the peak power constraint irrespective of the number of chirps that are superposed within a subband, in a multiband system, while keeping the waveform bandwidth equal to the subband bandwidth. Thereby, with appropriate design, the instantaneous frequency of each of these chirp waveforms that are placed within a subband can be separated by a fixed amount, and they would remain mutually uncorrelated over the waveform duration.

In this chapter, design chirp waveform has been investigated to exploit its key property for the applications of WET where a superposition of multiple distinct chirp waveforms is transmitted on the DL over select subbands with relatively higher channel gains to make use of frequency diversity without violating the peak power constraint, i.e., the instantaneous power contained at any frequency of the waveform to improve the ETE and overall harvested energy at the sensor end. To the best of the authors' knowledge, this is the first work that (i) proposes application of chirp for DL-WET and quantifies the gains obtained over DL-WET via fixed-frequency waveform, (ii) presents DL-WET to a group of sensors placed at different distances from the access point (AP) where energy is transferred

[1]Dr. Salil Kashyap, Dept. of EEE, IIT Guwahati, is associated with this work.

over selected subbands with relatively higher channel strengths independently to each sensor in an OFDM system, (iii) presents the design of optimal power and subband allocation strategies for both fixed-frequency and superposed chirp waveforms to maximize the minimum harvested energy in the sensor network. Specifically, a WSN is considered where an AP with M antennas is involved in DL energy transfer (to) and uplink (UL) information transfer (from) the K single-antenna sensor nodes. We have focused on a scenario where the entire system bandwidth is divided into multiple orthogonal subbands (N). Given this set-up, the main contributions are listed as follows:

(1) A general chirp based waveform design with configuration parameter ξ is proposed and key properties required for optimizing DL-WET are established.

(2) Novel analytical expressions for the average energy harvested by any sensor node are derived for DL-WET based on transmission of superposed chirp waveforms and based on transmission of fixed-frequency waveform over subbands selected based on their estimated channel strength. The mathematical analysis exploits the order statistics of the subband channel estimates acquired through UL pilot signalling.

(3) For both superposed chirps and fixed-frequency waveform based DL-WET with subband selection, max-min power control coefficients are derived in closed-form to ensure that sensors placed at different distances from the AP harvest an equal amount of energy.

(4) Given a constraint on the peak power level per subband, two simple algorithms are presented to compute the number of best subbands for superposed chirp waveforms and fixed-frequency waveform based transmission while satisfying the max-min fairness on harvested energy and the peak power constraint.

(5) As a benchmark, the corresponding results with perfect CSI are also presented. In addition, the corresponding max-min information transmitted on the UL by the sensors is analyzed.

(6) Extensive numerical results are performed to analyze the joint impact of different design parameters such as the number of chirps that are placed within a subband, number of subbands selected, number of antennas at the AP, number of sensors in the network, channel estimation error, distance between the AP and the sensor on WET and WEIT systems. The computed results are also benchmarked against DL-WET via fixed-frequency waveforms with and without

subband selection. Furthermore, Monte-Carlo simulations are conducted to validate our derived analytical results.

4.2 Proposed Design of Chirp Waveform for WET

In this work, signal design for WET based on chirp waveform is investigated. A chirp waveform with bandwidth B and duration T_{o} over subband n and corresponding to sensor k can be mathematically expressed using (1.5) as

$$s_{\mathrm{c}_{n,k}}(t) = \cos\left[2\pi\left(\left(f_{\mathsf{s}} + (n-1)B\right)t + \frac{1}{2}\mu t^2\right)\right], \quad 0 \le t \le T_{\mathrm{o}}, \tag{4.1}$$

where the subband index $n \in \{1, 2, \ldots, N\}$, the sensor index $k \in \{1, 2, \ldots, K\}$, f_{s} is the initial frequency, $B = \frac{B_{\mathrm{total}}}{N} = \frac{1}{T_{\mathrm{o}}}$, and $\mu = \frac{B}{T_{\mathrm{o}}}$ denotes the chirp rate. Furthermore, the inter-subband spacing Δf is considered equal to B. Note that the instantaneous frequency $f_{\mathrm{c}_{n,k}}(t)$ of the chirp varies with time and is given by

$$f_{\mathrm{c}_{n,k}}(t) = f_{\mathsf{s}} + (n-1)B + \mu t, \quad 0 \le t \le T_{\mathrm{o}}. \tag{4.2}$$

An important point to note is that based on the chirp factor μ, the duration of a chirp waveform, unlike a fixed-frequency waveform of bandwidth B, can be varied independently of its bandwidth.

We exploit this property so that the duration of a chirp waveform can be varied without affecting its bandwidth to transmit a superposition of chirp waveforms in a given subband of bandwidth B. This can be essentially done by designing a waveform that is obtained through a superposition of these chirps with increased duration within a given subband while ensuring that the superposed chirps remain uncorrelated to each other and maintain the same signal-bandwidth B. Furthermore, the waveforms thus designed satisfy the peak power constraint P_{peak}, since any instantaneous frequency corresponding to these superposed waveforms appears at distinct time instants. In a general form, a chirp waveform with configuration factor ξ can be expressed as

$$s_{\mathrm{cl}_{n,k}}(t) = \begin{cases} \cos\left[2\pi\left(f_{\mathrm{c}}(n,l,\xi)t + \frac{1}{2}\mu t^2\right)\right], & 0 \le t \le T'_{\mathrm{cl}}, \\ \cos\left[2\pi\left(\left(f_{\mathrm{c}}(n,l,\xi) - B\right)t + \frac{1}{2}\mu t^2\right)\right], & T'_{\mathrm{cl}} < t \le T_{\mathrm{c}}, \end{cases} \tag{4.3}$$

where ξ is a positive integer, $l \in \{1, 2, \ldots, \xi\}$, $f_{\mathrm{c}}(n,l,\xi) = f_{\mathsf{s}} + \frac{B(l-1)}{\xi} + (n-1)B$, $\mu = \frac{B}{T_{\mathrm{c}}}$, $T'_{\mathrm{cl}} = T_{\mathrm{c}}\left(1 - \frac{l-1}{\xi}\right)$, and $T_{\mathrm{c}} = \xi T_{\mathrm{o}}$. The factor ξ denotes the number of chirps that are superposed within the

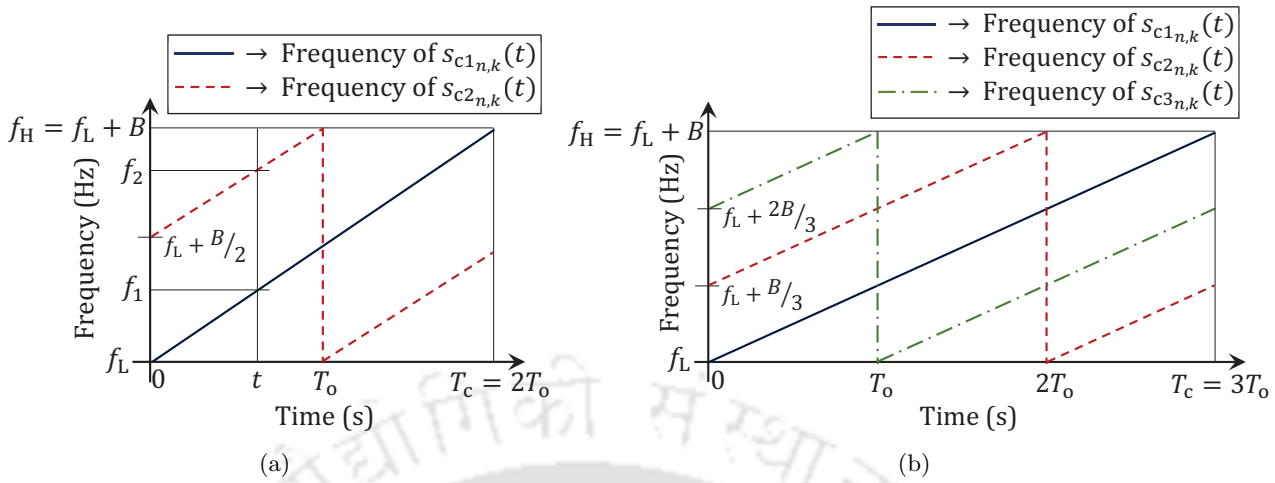

Figure 4.1: (a) Instantaneous frequency of chirp waveforms in chirp-2 configuration ($\xi = 2$) in a subbnad of bandwidth B. (b) Instantaneous frequency of chirp waveforms in chirp-3 configuration ($\xi = 3$) in a subbnad of bandwidth B.

same time and signal bandwidth B. Furthermore, the separation in instantaneous frequency between any two adjacent chirp waveforms in this set of ξ waveforms is $\frac{B}{\xi}$. An example of instantaneous frequency variation of the proposed chirp waveforms with $\xi = 2$ configuration (i.e., chirp-2) where two chirps are superposed within the same signal-bandwidth of B and with $\xi = 3$ configuration (i.e., chirp-3) where three chirps are superposed within the same signal-bandwidth of B is shown in Figure 4.1(a) and Figure 4.1(b), respectively. Note that, the lower and upper limit of the y-axis label are considered as f_L and f_H where f_L denotes the start frequency and f_H denotes the end frequency of the waveform, $f_L, f_H > 0$, such that $f_H - f_L = B$. Next, we have stated two results to highlight the key properties of these chirp waveforms as described in (4.3).

4.2.1 Properties of the Waveform

Lemma 1. The chirp signals corresponding to different $l \in \{1, 2, \ldots, \xi\}$ as described in (4.3) satisfy the following relation over any subband n of bandwidth B:

$$\int_0^{T_c} \left(s_{c1_{n,k}}(t) + s_{c2_{n,k}}(t) + \ldots + s_{c\xi_{n,k}}(t) \right)^2 dt = \int_0^{T_c} \left(s^2_{c1_{n,k}}(t) + s^2_{c2_{n,k}}(t) + \ldots + s^2_{c\xi_{n,k}}(t) \right) dt. \quad (4.4)$$

Proof: The proof is given in Appendix A.1. □

Remark 1. For $\xi = 2$, the chirp signals within a subband are not only mutually uncorrelated but also orthogonal to each other. In other words, $\int_0^{T_c} s_{c1_{n,k}}(t) s_{c2_{n,k}}(t) dt = 0$.

Lemma 2. The superposed waveform $S_{c_{m,k}}(t)$ of the set of chirp waveforms over subband m

described in (4.3) is mutually orthogonal to the superposed waveform $S_{c_{n,k}}(t)$ of the set of chirp waveforms over a distinct subband n, where $n \neq m$, i.e., they satisfy the following relation:

$$\int_0^{T_c} S_{c_{m,k}}(t) S_{c_{n,k}}(t) dt = 0, \tag{4.5}$$

where $S_{c_{i,k}}(t) = s_{c1_{i,k}}(t) + s_{c2_{i,k}}(t) + \ldots + s_{c\xi_{i,k}}(t)$, $i \in \{n, m\}$ and $n, m \in \{1, 2, \ldots, N\}$.

Proof: The proof is given in Appendix A.2. □

4.3 System Model

We have considered a WSN comprising of an AP with M antennas involved in DL energy transfer (to) and UL information transfer (from) the K single-antenna sensor nodes in an OFDM system as shown in Figure 4.2. A time-division-duplexing (TDD) mode of operation is considered so that the DL channel from the AP to the sensors is identical to the UL channel from the sensors to the AP. The total system bandwidth B_{total} is divided into N subbands with an inter-subband spacing $\Delta f = B = \frac{B_{\text{total}}}{N} \leq B_{\text{ch}}$, where B_{ch} is the coherence bandwidth. The complex baseband channel vector $\mathbf{g}_{n,k} \in \mathbb{C}^{M \times 1}$ between the M antennas at the AP and the k^{th} sensor over the n^{th} subband is given by $\mathbf{g}_{n,k} = \sqrt{\beta_k}\mathbf{h}_{n,k}$, where β_k models large-scale fading comprising of distance-dependent path-loss, $\mathbf{h}_{n,k} \in \mathbb{C}^{M \times 1}$ captures small-scale fading and it is a random vector with independent and identically distributed (i.i.d.) zero mean unit variance circularly symmetric complex Gaussian (CSCG) entries,

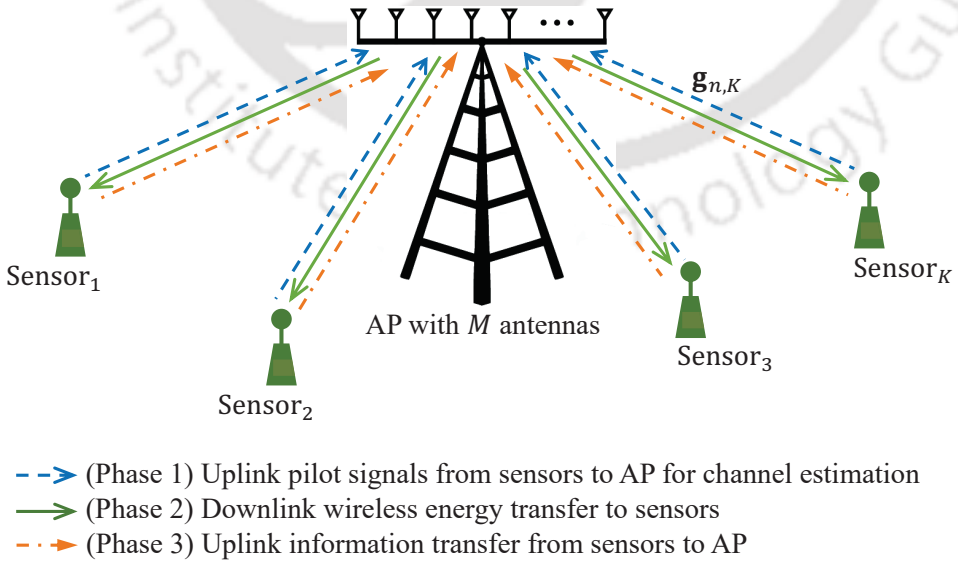

Figure 4.2: System model for WEIT system.

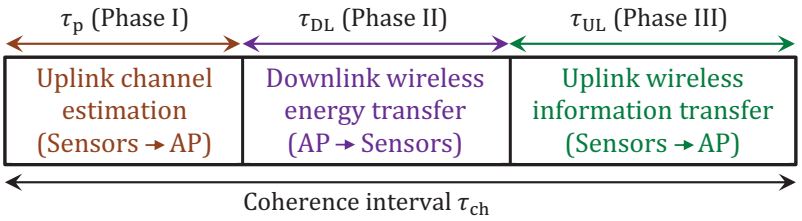

Figure 4.3: Three phase communication protocol for WEIT system.

i.e., $[\mathbf{h}_{n,k}]^m = h_{n,k}^m \sim \mathcal{CN}(0,1)$. Since, the inter-subband spacing is less than the coherence bandwidth, the channel over each subband experiences frequency-flat fading. Also, $[\mathbf{g}_{n,k}]^m = g_{n,k}^m = \sqrt{\beta_k} h_{n,k}^m$, where $m = 1, 2, \ldots, M$, $n = 1, 2, \ldots, N$, and $k = 1, 2, \ldots, K$. In matrix form, the UL channel coefficient matrix $\mathbf{G}_n \in \mathbb{C}^{M \times K}$ between M antennas at the AP and K sensors over the n^{th} subband is given by $\mathbf{G}_n = [\mathbf{g}_{n,1}, \mathbf{g}_{n,2}, \ldots, \mathbf{g}_{n,K}]$.

It is considered that the channel remains time-invariant over a coherence block of length τ_{ch} seconds and varies independently across blocks. Therefore, channel estimation must be done after every coherence block. In each interval of length τ_{ch}, the communication between the AP and the sensors takes place in three different phases as illustrated in Figure 4.3. In the first phase, every sensor transmits a pilot of length τ_{p} on the UL to facilitate channel estimation at the AP. In the second phase of length τ_{DL}, based on the estimated channel, the AP beamforms energy to the sensors on the DL. Subsequently, in the third phase of length τ_{UL}, the sensors transmit information on the UL. Note that $\tau_{\text{ch}} = \tau_{\text{p}} + \tau_{\text{DL}} + \tau_{\text{UL}}$. For the presented work, the transmission of wireless power is performed over multiple subbands and the signal transmitted on the DL from AP across multiple subbands and to multiple sensors is subject to an average transmit power constraint of P_{tx} where the averaging is done with respect to the channel fading distribution. In a multicarrier system having N subbands, the harvested energy at the sensor can be improved by allocating more power to the subbands having relatively higher channel gains [72]. Therefore, allocating power to subbands with relatively lower channel gain will contribute little to power received at the sensor and will degrade the efficiency of energy transfer of the system due to high signal attenuation over those subbands. By dropping the subbands having low channel gains and increasing allocation of power to the set of subbands with high gains will lead to improvement in the harvested energy. For a system performing transmission with equal power over N subbands and K sensors, the peak power of a signal P_{peak} over a band can be given by $P_{\text{peak}} = \frac{P_{\text{tx}}}{NK}$, while in case, a set of $\widetilde{N}$ subbands ($\widetilde{N} < N$) with relatively higher channel gains

is employed, the new $P_{\text{peak}} = \frac{P_{\text{tx}}}{\widetilde{N}K}$ which is greater than the previous P_{peak}. Thereby with $\widetilde{N} \leq N$ the value of $P_{\text{peak}} = \frac{P_{\text{tx}}}{\widetilde{N}K} \geq \frac{P_{\text{tx}}}{NK}$. Furthermore, the instantaneous power $P_{n,k}$ contained in a frequency of a signal at a given time transmitted over the n^{th} subband towards the k^{th} sensor satisfies the condition $0 \leq P_{n,k} \leq P_{\text{peak}}\ \forall\ n, k$.

4.3.1 Channel Estimation

The pilot signal $s_{\mathbf{\Phi}_{n,k}}(t)$ transmitted over the n^{th} subband by the k^{th} sensor is given by

$$s_{\mathbf{\Phi}_{n,k}}(t) = \sum_{p=1}^{\zeta_{\text{p}}} \mathbf{\Phi}_k(p) s_{\text{c1}_{n,k}}(t - (p-1)T_{\text{c}}), \tag{4.6}$$

where $s_{\text{c1}_{n,k}}(t) = e^{j2\pi\left[(f_{\text{s}}+(n-1)B)t+\frac{1}{2}\mu t^2\right]}$ for $0 \leq t \leq T_{\text{c}}$, denotes the complex form of chirp-1 signal ($\xi = 1$) with unit average power and of duration $T_{\text{c}} = T_{\text{o}} = \frac{1}{B}$ over the n^{th} subband corresponding to the k^{th} sensor. $\mathbf{\Phi}_k \in \mathbb{C}^{1\times\zeta_{\text{p}}}$ denotes the ζ_{p}-length pilot sequence assigned to the k^{th} sensor. The pilot sequences assigned to the K sensors are chosen such that

$$\frac{1}{\zeta_{\text{p}}}\mathbf{\Phi}_k\mathbf{\Phi}_{k'}^{\text{H}} = \delta_{kk'} = \begin{cases} 1, & k = k' \\ 0, & k \neq k', \quad k, k' \in \{1, 2, \ldots, K\}, \end{cases} \tag{4.7}$$

where $(\cdot)^{\text{H}}$ denotes the conjugate transpose operation. To ensure that assigned pilot sequences are mutually orthogonal, $\zeta_{\text{p}} \geq K$. Note that the duration τ_{p} of the pilot signal $s_{\mathbf{\Phi}_{n,k}}(t)$ equals $\tau_{\text{p}} = \zeta_{\text{p}}T_{\text{c}} < \tau_{\text{ch}}$.

Then, the signal received at the AP over the n^{th} subband and for $0 \leq t \leq \zeta_{\text{p}}T_{\text{c}}$ is given by

$$\mathbf{y}_{\text{p}_n}(t) = \sqrt{\frac{P_{\text{p}}}{N}} \sum_{k'=1}^{K} \mathbf{g}_{n,k'} s_{\mathbf{\Phi}_{n,k'}}(t) + \mathbf{w}_{\text{p}_n}(t), \tag{4.8}$$

where P_{p} denotes the pilot power, $\mathbf{g}_{n,k'} \in \mathbb{C}^{M\times 1}$ denotes the complex baseband channel vector between the M-antennas at the AP and the k'^{th} sensor over the n^{th} subband and $s_{\mathbf{\Phi}_{n,k'}}(t)$ denotes the pilot signal transmitted over the n^{th} subband by the k'^{th} sensor and is given by (4.6). Furthermore, $\mathbf{w}_{\text{p}_n}(t)$ denotes the thermal noise vector at the AP and is independent of $\mathbf{g}_{n,k'}$.

A sufficient statistics for estimating the channel $\mathbf{g}_{n,k}$ to the k^{th} sensor is

$$\mathbf{y}_{\text{p}_{n,k}} = \frac{1}{\sqrt{\zeta_{\text{p}}T_{\text{c}}}} \int_0^{\zeta_{\text{p}}T_{\text{c}}} \mathbf{y}_{\text{p}_n}(t) s_{\mathbf{\Phi}_{n,k}}^{\text{H}}(t)dt = \sqrt{\frac{E_{\text{p}}}{N}}\mathbf{g}_{n,k} + \mathbf{w}_{\text{p}_{n,k}}, \tag{4.9}$$

where $\int_0^{\zeta_{\text{p}}T_{\text{c}}} s_{\mathbf{\Phi}_{n,k'}}(t) s_{\mathbf{\Phi}_{n,k}}^{\text{H}}(t)dt = \zeta_{\text{p}}T_{\text{c}}$ if $k = k'$ and equals 0 otherwise, $\mathbf{y}_{\text{p}_{n,k}} \in \mathbb{C}^{M\times 1}$, $E_{\text{p}} = P_{\text{p}}\zeta_{\text{p}}T_{\text{c}}$

is the energy spent in UL pilot transmission by any sensor, and $\mathbf{w}_{\mathrm{p}_{n,k}} \in \mathbb{C}^{M\times 1}$ is CSCG noise vector. Furthermore, $\mathbf{w}_{\mathrm{p}_{n,k}} \sim \mathcal{CN}(\mathbf{0}, \sigma^2\mathbf{I}_M)$, where σ^2 denotes the noise power spectral density (PSD) and $\mathbf{I}_M$ indicates an $M \times M$ identity matrix.

Based on $\mathbf{y}_{\mathrm{p}_{n,k}}$ in (4.9), the minimum mean square error (MMSE) estimate $\widehat{\mathbf{g}}_{n,k}$ of the channel vector $\mathbf{g}_{n,k}$ to the k^{th} sensor over the n^{th} subband equals [63]

$$\widehat{\mathbf{g}}_{n,k} = \mathbf{g}_{n,k} + \widetilde{\mathbf{g}}_{n,k}, \tag{4.10}$$

where $\widetilde{\mathbf{g}}_{n,k}$ denotes the channel estimation error that is uncorrelated to $\widehat{\mathbf{g}}_{n,k}$. Furthermore, $\widehat{\mathbf{g}}_{n,k} \sim \mathcal{CN}(\mathbf{0}, \gamma_k\mathbf{I}_M)$, where $\gamma_k = \frac{\frac{E_{\mathrm{p}}}{N}\beta_k^2}{\sigma^2+\frac{E_{\mathrm{p}}}{N}\beta_k}$ and $\widetilde{\mathbf{g}}_{n,k} \sim \mathcal{CN}(\mathbf{0}, (\beta_k - \gamma_k)\mathbf{I}_M)$. Note that channel estimation remains the same irrespective of whether a chirp or a fixed frequency waveform is used to design the pilot signal.

4.3.2 Downlink Energy Beamforming and Proposed Transmission Strategy

In a multicarrier system having N subbands, instead of transmitting with equal power over all the subbands, it is possible to improve the harvested energy at the sensors by allocating more power to the subbands having relatively higher channel gains [72]. Furthermore, it is possible to transmit a superposition of multiple chirp signals in each subband while maintaining the P_{peak} constraint. We exploit these facts to propose the following strategy for DL-WET based on superposed chirp waveforms in order to beamform energy towards K sensors.

Proposed Transmission Strategy: The estimated channel vectors of every sensor over all subbands are arranged in descending order of their channel gains. Specifically, corresponding to the k^{th} sensor, we sort its subband channel gains as

$$\left\|\widehat{\mathbf{g}}_{[1],k}\right\|^2 \geq \left\|\widehat{\mathbf{g}}_{[2],k}\right\|^2 \geq \ldots \geq \left\|\widehat{\mathbf{g}}_{[N],k}\right\|^2, \tag{4.11}$$

where $\widehat{\mathbf{g}}_{[n],k}$ denotes the estimated channel vector between the M antennas of the AP and the k^{th} sensor over its n^{th} best subband and the subband index associated with the n^{th} best subband $\in \{1, 2, \ldots, N\}$. Furthermore, $\left\|\widehat{\mathbf{g}}_{[n],k}\right\|^2 = \left|\widehat{g}^1_{[n],k}\right|^2 + \left|\widehat{g}^2_{[n],k}\right|^2 + \ldots + \left|\widehat{g}^M_{[n],k}\right|^2$ where $\|\cdot\|$ denotes the Euclidean norm. Based on this, the AP selects the $\widetilde{N}$ best subbands out of the total available subbands N for each of the K sensors. It then allocates power to the subbands of the K sensors such that the transmit power P_{tx} constraint is satisfied with equality. Specifically, $P_{\text{peak}} \geq \frac{P_{\text{tx}}}{NK}$ and the power $P_{[n],k}$ allocated for a signal over the n^{th} best subband of the k^{th} sensor is $0 \leq P_{[n],k} \leq P_{\text{peak}}$. Note that, based on (4.3), a

chirp waveform with unit average power corresponding to the k^{th} sensor over the n^{th} subband equals

$$s'_{cl_{n,k}}(t) = \sqrt{2}s_{\text{cl}_{n,k}}(t), \tag{4.12}$$

where the scaling by $\sqrt{2}$ ensures that the average power is unity.

The following discussion illustrates the key idea behind the advantage that WET based on DL transmission of superposition of chirp waveforms offers over conventional DL-WET transmission strategies based on fixed-frequency waveform in which the frequency of the signal does not vary with time. Figure 4.1(a) shows the instantaneous frequency variation of the waveforms, having a bandwidth B in chirp-2, i.e., $\xi = 2$ configuration, designed using (4.3), where the two chirp waveforms are superposed within the same subband bandwidth B while maintaining orthogonality over the waveform duration T_{c}. From Figure 4.1(a) it can be seen that the instantaneous frequencies of the two chirp waveforms always maintain a separation of $\frac{B}{2}$ so that no two equal signal frequencies corresponding to the two distinct chirps appear at any given time instant. In fact, the proposed design mandates that identical signal frequencies corresponding to distinct chirps do not appear at a given time instant. In other words, the instantaneous frequencies of multiple distinct chirp waveforms that are superposed within a subband are separated by a fixed amount of $\frac{B}{\xi}$ as can be seen from Figure 4.1 and they remain uncorrelated over the waveform duration. This is the reason why the power contained at any frequency at a given time is limited to P_{peak} irrespective of the number of chirp waveforms that are superposed within each subband while maintaining the waveform bandwidth of B. It is to note that, superposition of multiple fixed-frequency cosine waveforms, each of bandwidth B, within a subband of width B cannot be performed while maintaining the peak power constraint or the orthogonality among the waveforms. As an example, mathematically, a fixed-frequency cosine waveform of bandwidth B for k^{th} sensor over the n^{th} subband is give by

$$s_{\text{o1}_{n,k}}(t) = \sqrt{2}\cos\left[2\pi\left(f_{\text{s}} + (n-1)B\right)t\right], \quad 0 \le t \le T_{\text{o}}, \tag{4.13}$$

where $B = \frac{1}{T_{\text{o}}}$. Now, if we want to obtain another fixed-frequency cosine waveform of bandwidth B that is orthogonal to $s_{\text{o1}_{n,k}}(t)$, then the waveform would be given by

$$s_{\text{o2}_{m,k}}(t) = \sqrt{2}\cos\left[2\pi\left(f_{\text{s}} + (m-1)B\right)t\right], \quad 0 \le t \le T_{\text{o}}, \tag{4.14}$$

with $m = n + 1$ such that $\int_0^{T_{\text{o}}} s_{\text{o1}_{n,k}}(t)s_{\text{o2}_{m,k}}(t)dt = 0$. However, from (4.13) and (4.14), it can be

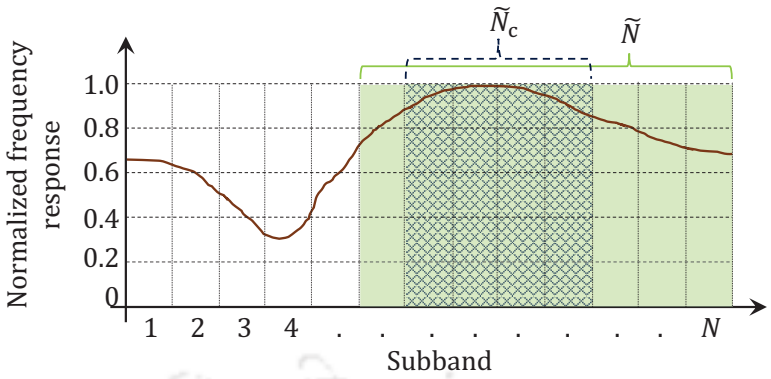

Figure 4.4: Selection of $\widetilde{N}$ and $\widetilde{N}_c$ subbands for energy transfer.

found that the total occupied bandwidth by $s_{o1_{n,k}}(t)$ and $s_{o2_{m,k}}(t)$ is $2B$. Now, given the subband bandwidth of B, if we want to allocate both the waveforms within the same subband (i.e. superpose) while maintaining the signal bandwidth of B, in that case $s_{o2_{m,k}}(t)$ would be rewritten as

$$s_{o2_{m,k}}(t) = s_{o2_{n,k}}(t) = \sqrt{2}\cos\left[2\pi\left(f_s + (n-1)B\right)t\right], \quad 0 \le t \le T_o, \tag{4.15}$$

that is both the waveforms would get overlapped with having identical starting frequency and identical frequency variation over the entire symbol duration, and therefore, the waveforms will be no longer orthogonal, i.e., $\int_0^{T_o} s_{o1_{n,k}}(t)s_{o2_{n,k}}(t)dt \neq 0$. In fact, the superposed fixed-frequency cosine waveforms for k^{th} sensor over the n^{th} subband given by

$$S_{o_{n,k}}(t) = s_{o1_{n,k}}(t) + s_{o2_{n,k}}(t) = 2\left(\sqrt{2}\cos\left[2\pi\left(f_s + (n-1)B\right)t\right]\right), \tag{4.16}$$

will have double the amplitude as compared to the individual signal unlike the proposed superposed chirp waveforms.

To elucidate further, consider that the frequency response of the channel to the k^{th} sensor over its N subbands is as depicted in Figure 4.4. Then, based on the proposed transmission strategy, the top $\widetilde{N}$ subbands having relatively higher channel gains are selected as shown in Figure 4.4. Now, based on chirp-2 configuration, two chirps in a set are superposed within each subband with an instantaneous frequency separation of $\frac{B}{2}$ between the waveforms while satisfying the P_{peak} constraint as explained above. Therefore, using chirp-2 configuration, the AP will end up using only $\widetilde{N}_c$ subbands while satisfying the P_{tx} constraint, where $\widetilde{N}_c = \frac{\widetilde{N}}{2}$. While meeting the average transmit power constraint across all the selected subbands and the peak power constraint, transmission of a superposition of

two chirp waveforms over each of the $\widetilde{N}_{\mathrm{c}}$ subbands having relatively higher channel gains within the pre-selected $\widetilde{N}$ bands, as depicted in Figure 4.4, would result in higher received energy at the sensor nodes as compared to that with fixed-frequency signal where no more than one fixed-frequency waveform of bandwidth B can be placed within each subband of width B without losing orthogonality and violating the P_{peak} constraint. Therefore, in a nutshell, for downlink energy transfer based on superposed chirp waveforms, the maximum number of subbands $\widetilde{N}_{\mathrm{c}}$ required using chirp waveforms under 'ξ-chirp configuration' is calculated as follows

(i) If $\widetilde{N} \bmod \xi = 0$, then $\widetilde{N}_{\mathrm{c}} = \frac{\widetilde{N}}{\xi}$.

(ii) If $\widetilde{N} \bmod \xi \neq 0$, then $\widetilde{N}_{\mathrm{c}} = \left\lfloor \frac{\widetilde{N}}{\xi} \right\rfloor + 1$ with a power scaling factor of $\frac{\widetilde{N} - \left\lfloor \frac{\widetilde{N}}{\xi} \right\rfloor \xi}{\xi}$ for the chirp signals associated with the last subband.

For transmission based on superposed chirp waveforms, let Ξ_{c_k} denote the set of subband entries/indices of the $\widetilde{N}_{\mathrm{c}}$ best subbands for the k^{th} sensor with subband index $n \in \{1, 2, \ldots, N\}$. Given the ordered channel, the AP performs DL beamforming of energy such that signals transmitted from different antennas add up coherently at the sensors, thereby maximizing the received energy. For $\widetilde{N}_{\mathrm{c}} = \frac{\widetilde{N}}{\xi}$ $\big($i.e., $\widetilde{N} \bmod \xi = 0\big)$, the signal transmitted from the AP to K sensors over the n^{th} subband in one symbol period T_{c} is given by

$$\mathbf{x}_{\mathrm{c}_n}(t) = \sqrt{P_{\mathrm{tx}}} \sum_{k=1}^{K} \sqrt{\frac{\eta_{\mathrm{c}_k}}{\widetilde{N}}} \frac{\widehat{\mathbf{g}}_{n,k}^{*}}{\left\|\widehat{\mathbf{g}}_{n,k}\right\|} S_{\mathrm{c}_{n,k}}(t) \delta_{\{n,k\} \in \Xi_{\mathrm{c}_k}}, \quad 0 \leq t \leq T_{\mathrm{c}}, \tag{4.17}$$

where $\mathbf{x}_{\mathrm{c}_n}(t) \in \mathbb{C}^{M \times 1}$, $(\cdot)^*$ denotes the conjugate operation, and $S_{\mathrm{c}_{n,k}}(t) = s'_{\mathrm{c}1_{n,k}}(t) + s'_{\mathrm{c}2_{n,k}}(t) + \ldots + s'_{\mathrm{c}\xi_{n,k}}(t)$. Note that $\delta_{\{n,k\} \in \Xi_{\mathrm{c}_k}}$ is an indicator function that takes the value 1 if the n^{th} subband of the k^{th} sensor belongs to the set Ξ_{c_k} of the entries of the $\widetilde{N}_{\mathrm{c}}$ best subbands corresponding to the k^{th} sensor. Further, based on the channel gain between the AP and the sensors, the same subband may be allocated to multiple sensors, i.e., the same subband index can be a part of Ξ_{c_k} for different values of k. As an example, let the 3^{rd} subband out of N available bands is the 1^{st} best subband of sensor 1, 5^{th} best subband of sensor 2, and 7^{th} best subband of sensor 4 where $\widetilde{N}_{\mathrm{c}} \geq 7$. Therefore, according to the proposed transmission strategy, the set Ξ_{c_k} will hold the index 3 for $k = 1, 2, 4$, and the index will appear in the 1^{st}, 5^{th}, and 7^{th} position of the corresponding list of $\widetilde{N}_{\mathrm{c}}$ indices associated to Ξ_{c_1}, Ξ_{c_2}, and Ξ_{c_4}, respectively. The power control coefficients η_{c_k} must be chosen such that the average transmit power constraint is satisfied at the AP, i.e., $\sum_{n=1}^{N} \mathbb{E}\{\left\|\mathbf{x}_{\mathrm{c}_n}(t)\right\|^2\} \leq P_{\mathrm{tx}}$ where $\mathbb{E}\{\cdot\}$ denotes

the expectation operator. To ensure this, it is shown in Appendix A.3 that $\sum_{k=1}^{K} \eta_{\mathrm{c}_k} \leq 1$.

For the case when $\widetilde{N}$ mod $\xi \neq 0$, using (4.17), the energy beamforming signal transmitted from AP to K sensors over the n^{th} subband, in one symbol period T_{c}, is given by

$$\mathbf{x}_{\mathrm{c}_n}(t) = \sqrt{P_{\mathrm{tx}}} \sum_{k=1}^{K} \sqrt{\frac{\eta_{\mathrm{c}_k}}{\widetilde{N}}} \frac{\widehat{\mathbf{g}}_{n,k}^{*}}{\left\|\widehat{\mathbf{g}}_{n,k}\right\|} S_{\mathrm{c}_{n,k}}(t) \delta_{\{n,k\} \in \Xi_{\mathrm{c}_k}} \delta_{\{n,k\} \in \Xi_{\mathrm{c}_k}^{\widetilde{N}_{\mathrm{c}}}}, \tag{4.18}$$

In the equation above, the amplitude of the chirp waveform over the $\widetilde{N}_{\mathrm{c}}^{\text{th}}$ best subband of sensor k is scaled by α to maintain the average transmit power constraint where $\alpha = \sqrt{\frac{\widetilde{N} - \left\lfloor \frac{\widetilde{N}}{\xi} \right\rfloor \xi}{\xi}}$. Another indicator function $\delta_{\{n,k\} \in \Xi_{\mathrm{c}_k}^{\widetilde{N}_{\mathrm{c}}}}$ is introduced to maintain average transmit power constraint where $\Xi_{\mathrm{c}_k}^{\widetilde{N}_{\mathrm{c}}}$ holds the subband index of $\widetilde{N}_{\mathrm{c}}^{\text{th}}$ best subband for k^{th} sensor. Thereby, $\delta_{\{n,k\} \in \Xi_{\mathrm{c}_k}^{\widetilde{N}_{\mathrm{c}}}} = \alpha$ for $\{n,k\} \in \Xi_{\mathrm{c}_k}^{\widetilde{N}_{\mathrm{c}}}$, else $\delta_{\{n,k\} \in \Xi_{\mathrm{c}_k}^{\widetilde{N}_{\mathrm{c}}}} = 1$. Moreover, The power control coefficients η_{c_k} must be chosen such that $\sum_{n=1}^{N} \mathbb{E}\{\left\|\mathbf{x}_{\mathrm{c}_n}(t)\right\|^2\} \leq P_{\mathrm{tx}}$ and the proof is given in Appendix A.4.

Remark 2. In transmission based on fixed-frequency waveform, the signal transmitted from AP to K sensors over the n^{th} subband, $n \in \{1, 2, \ldots, N\}$ in one symbol period T_{o} is given by

$$\mathbf{x}_{\mathrm{o}_n}(t) = \sqrt{P_{\mathrm{tx}}} \sum_{k=1}^{K} \sqrt{\frac{\eta_{\mathrm{o}_k}}{\widetilde{N}}} \frac{\widehat{\mathbf{g}}_{n,k}^{*}}{\left\|\widehat{\mathbf{g}}_{n,k}\right\|} s_{\mathrm{o}_{n,k}}(t) \delta_{\{n,k\} \in \Xi_{\mathrm{o}_k}}, \quad 0 \leq t \leq T_{\mathrm{o}}, \tag{4.19}$$

where

$$s_{\mathrm{o}_{n,k}}(t) = \sqrt{2} \cos\left[2\pi \left(f_{\mathsf{s}} + (n-1)B\right) t\right], \tag{4.20}$$

and Ξ_{o_k} denotes the set of subband entries of the $\widetilde{N}$ best subbands, $\widetilde{N} \leq N$, for the k^{th} sensor. Furthermore, the power control coefficients in this case must satisfy $\sum_{k=1}^{K} \eta_{\mathrm{o}_k} \leq 1$ to ensure that $\sum_{n=1}^{N} \mathbb{E}\{\left\|\mathbf{x}_{\mathrm{o}_n}(t)\right\|^2\} \leq P_{\mathrm{tx}}$.

4.3.3 Uplink Information Transfer

The signal $\mathbf{y}_{\mathrm{c}_n}(t) \in \mathbb{C}^{M \times 1}$ received by the AP over the n^{th} subband when all the K sensors transmit data signals simultaneously is given by

$$\mathbf{y}_{\mathrm{c}_n}(t) = \sqrt{\frac{P_{\mathrm{UL}}}{N}} \sum_{i=1}^{K} \sqrt{\rho_{\mathrm{c}_i}} \mathbf{g}_{n,i} q_{n,i} s_{\mathrm{c1}_{n,i}}(t) + \mathbf{w}_n(t), \quad 0 \leq t \leq T_{\mathrm{c}}, \tag{4.21}$$

where P_{UL} is the maximum power with which any sensor transmits data on the UL, $0 \leq \rho_{\mathrm{c}_i} \leq 1$ is the power control coefficient corresponding to the i^{th} sensor, $q_{n,i} \sim \mathcal{CN}(0,1)$ denotes the transmit data symbol and $s_{\mathrm{c1}_{n,i}}(t) = e^{j2\pi\left((f_{\mathsf{s}} + (n-1)B)t + \frac{1}{2}\mu t^2\right)}$ is the associated unit power chirp-1 waveform, in complex form, transmitted by the i^{th} sensor on the UL. Note that $T_{\mathrm{c}} = T_{\mathrm{o}}$, and $\Delta f = B$. Furthermore,

the symbols transmitted by different sensors over any subband are assumed to be uncorrelated to each other, and $\mathbf{w}_n(t) \in \mathbb{C}^{M\times 1}$ denotes the noise at the AP on the UL.

Remark 3. During UL data transmission, duration of chirp waveform is equal to the fixed-frequency waveform, i.e., $T_{\mathrm{c}} = T_{\mathrm{o}}$ and the signals are transmitted over all available bands. Thus, UL data signaling with fixed-frequency waveform is identical to the model discussed above with $s_{\mathrm{c1}_{n,i}}(t)$ replaced by $s_{\mathrm{o}_{n,i}}(t) = e^{j2\pi((f_{\mathrm{s}}+(n-1)B)t)}$ and $\mathbf{y}_{\mathrm{c}_n}(t)$ replaced by $\mathbf{y}_{\mathrm{o}_n}(t)$ in (4.21).

4.4 Analysis of Average Harvested Energy

In this section, we analyze the average energy harvested by the sensor nodes, first based on DL-WET via superposition of chirp waveforms over selected subbands, followed by the corresponding analysis for fixed-frequency waveform. The analysis exploits order statistics of the subband channel estimates acquired through UL pilot signaling.

4.4.1 Using Superposed Chirp Waveform

The signal $y_{\mathrm{c}_k}^{[n]}(t)$ received at the k^{th} sensor over its n^{th} best subband based on the signal in (4.17), with $\widetilde{N} \bmod \xi = 0$, transmitted from the AP is given by

$$y_{\mathrm{c}_k}^{[n]}(t) = \sqrt{P_{\mathrm{tx}}}\mathbf{g}_{[n],k}^{\mathrm{T}}\sqrt{\frac{\eta_{\mathrm{c}_k}}{\widetilde{N}}}\frac{\widehat{\mathbf{g}}_{[n],k}^{*}}{\left\|\widehat{\mathbf{g}}_{[n],k}\right\|}S_{\mathrm{c}_{[n],k}}(t) + \sqrt{P_{\mathrm{tx}}}\mathbf{g}_{[n],k}^{\mathrm{T}}\sum_{i=1,i\neq k}^{K}\sqrt{\frac{\eta_{\mathrm{c}_i}}{\widetilde{N}}}\frac{\widehat{\mathbf{g}}_{\{[n],k\},i}^{*}}{\left\|\widehat{\mathbf{g}}_{\{[n],k\},i}\right\|}S_{\mathrm{c}_{\{[n],k\},i}}(t)\delta_{\{[n],k\}\in\Xi_{\mathrm{c}_i}} + w_{[n],k}(t), \quad (4.22)$$

where $\mathbf{g}_{[n],k}^{\mathrm{T}} \in \mathbb{C}^{1\times M}$, $\widehat{\mathbf{g}}_{[n],k} \in \mathbb{C}^{M\times 1}$, and $w_{[n],k}(t) \sim \mathcal{CN}(0,\sigma^2)$ denote respectively the true channel vector, the estimated channel vector, and noise corresponding to the k^{th} sensor over its n^{th} best subband, and $(\cdot)^{\mathrm{T}}$ denotes the transpose operation. The first term in (4.22) corresponds to the desired signal for the k^{th} sensor over its n^{th} best subband. The second term denotes the interference arising due to signals intended for other sensors over the n^{th} best subband of the k^{th} sensor. Furthermore, $\delta_{\{[n],k\}\in\Xi_{\mathrm{c}_i}}$ denotes an indicator function that equals 1 if the index of the n^{th} best subband of the k^{th} sensor belongs to the set Ξ_{c_i} of the best $\widetilde{N}_{\mathrm{c}}$ subband entries corresponding to the i^{th} sensor. To be specific, any sensor $i \neq k$ will contribute to the interference term in $y_{\mathrm{c}_k}^{[n]}(t)$, if the index of the n^{th} best subband of the k^{th} sensor belongs to Ξ_{c_i}.

A sensor receives signal over the entire available bandwidth B_{total} consisting of N subbands. Let $\psi \in [0,1)$ denote the energy conversion efficiency at the sensor. Then, the average energy harvested

by the k^{th} sensor in a symbol duration T_{c} over N subbands equals

$$\overline{E}_{\text{c}_k} = \psi\mathbb{E}\left\{ \int_0^{T_{\text{c}}} \sum_{n=1}^{N} \left| \left[y_{\text{c}_k}^{[n]}(t) \right] \right|^2 dt \right\}. \tag{4.23}$$

Substituting (4.22) in (4.23), we obtain

$$\overline{E}_{\text{c}_k} = \psi\mathbb{E}\Bigg\{ \int_0^{T_{\text{c}}} \Bigg(\sum_{n=1}^{N} \left| \sqrt{P_{\text{tx}}} \mathbf{g}_{[n],k}^{\text{T}} \sqrt{\frac{\eta_{\text{c}_k}}{\widetilde{N}}} \frac{\widehat{\mathbf{g}}_{[n],k}^{*}}{\left\| \widehat{\mathbf{g}}_{[n],k} \right\|} S_{\text{c}_{[n],k}}(t) \right|^2 + \sum_{n=1}^{N} \left| \sqrt{P_{\text{tx}}} \mathbf{g}_{[n],k}^{\text{T}} \sum_{i=1;i\neq k}^{K} \sqrt{\frac{\eta_{\text{c}_i}}{\widetilde{N}}} \frac{\widehat{\mathbf{g}}_{\{[n],k\},i}^{*}}{\left\| \widehat{\mathbf{g}}_{\{[n],k\},i} \right\|} \times S_{\text{c}_{\{[n],k\},i}}(t) \delta_{\{[n],k\}\in\Xi_{\text{c}_i}} \right|^2 \Bigg) dt \Bigg\} + \psi\mathbb{E}\left\{ \int_0^{T_{\text{c}}} \sum_{n=1}^{N} \left| w_{[n],k}(t) \right|^2 dt \right\}. \tag{4.24}$$

Please note that, for each sensor, the signal is transmitted from the AP over its best $\widetilde{N}_{\text{c}}$ subbands only where $\widetilde{N}_{\text{c}} = \frac{\widetilde{N}}{\xi}$. Therefore, not all the sensors will contribute to the power of the interfering signal corresponding to the k^{th} sensor in the second term of (4.24) over all the N subbands. Based on the set Ξ_{c_i} of the best $\widetilde{N}_{\text{c}}$ subband entries corresponding to the i^{th} sensor, the second term of (4.24) can be re-arranged to obtain

$$\overline{E}_{\text{c}_k} = \psi P_{\text{tx}} \frac{\eta_{\text{c}_k}}{\widetilde{N}} \left[\mathbb{E}\left\{ \sum_{n=1}^{\widetilde{N}_{\text{c}}} \left| \frac{\mathbf{g}_{[n],k}^{\text{T}} \widehat{\mathbf{g}}_{[n],k}^{*}}{\left\| \widehat{\mathbf{g}}_{[n],k} \right\|} \right|^2 \right\} \int_0^{T_{\text{c}}} S_{\text{c}_{[n],k}}^2(t) dt \right] + \psi P_{\text{tx}} \mathbb{E}\Bigg\{ \sum_{n=1}^{\widetilde{N}_{\text{c}}} \left| \sum_{i=1;i\neq k}^{K} \sqrt{\frac{\eta_{\text{c}_i}}{\widetilde{N}}} \frac{\mathbf{g}_{\{[n],i\},k}^{\text{T}} \widehat{\mathbf{g}}_{[n],i}^{*}}{\left\| \widehat{\mathbf{g}}_{[n],i} \right\|} \right|^2 \times \int_0^{T_{\text{c}}} S_{\text{c}_{[n],i}}^2(t) dt \Bigg\} + \psi\mathbb{E}\left\{ \sum_{n=1}^{N} w'_{[n],k} \right\}, \tag{4.25}$$

where $w'_{[n],k} = \int_0^{T_{\text{c}}} \left| w_{[n],k}(t) \right|^2 dt$. The use of Lemma 2 allows us to interchange the order of summation and integration in (4.25) above. Using the facts that the chirp waveform has an average power of unity and that the chirp waveforms corresponding to different $l \in \{1, 2, \ldots, \xi\}$ as described in (4.3) are uncorrelated over any subband as stated in Lemma 1, therefore

$$\int_0^{T_{\text{c}}} S_{\text{c}_{[n],k}}^2(t) dt = \int_0^{T_{\text{c}}} S_{\text{c}_{[n],i}}^2(t) dt = \xi T_{\text{c}}. \tag{4.26}$$

Substituting (4.26) in (4.25) and after simplification (4.25) yields

$$\overline{E}_{\text{c}_k} = \frac{\eta_{\text{c}_k} \psi P_{\text{tx}} \xi T_{\text{c}}}{\widetilde{N}} \mathbb{E}\left\{ \sum_{n=1}^{\widetilde{N}_{\text{c}}} \left| \frac{\mathbf{g}_{[n],k}^{\text{T}} \widehat{\mathbf{g}}_{[n],k}^{*}}{\left\| \widehat{\mathbf{g}}_{[n],k} \right\|} \right|^2 \right\} + \psi P_{\text{tx}} \xi T_{\text{c}} \mathbb{E}\Bigg\{ \sum_{n=1}^{\widetilde{N}_{\text{c}}} \left| \sum_{i=1;i\neq k}^{K} \sqrt{\frac{\eta_{\text{c}_i}}{\widetilde{N}}} \frac{\mathbf{g}_{\{[n],i\},k}^{\text{T}} \widehat{\mathbf{g}}_{[n],i}^{*}}{\left\| \widehat{\mathbf{g}}_{[n],i} \right\|} \right|^2 \Bigg\} + \psi\mathbb{E}\left\{ \sum_{n=1}^{N} w'_{[n],k} \right\}. \tag{4.27}$$

Remark 4. For the case when $\widetilde{N} \bmod \xi \neq 0$, using (4.18), (4.22), (4.23), and (4.25), the average

harvested energy at k^{th} sensor based on transmission of superposed chirp waveforms on the DL, in a symbol duration T_{c}, is evaluated as

$$\overline{E}_{c_k} = \frac{\eta_{c_k}\psi P_{\text{tx}}\xi T_{\text{c}}}{\widetilde{N}}\mathbb{E}\Bigg\{\sum_{n=1}^{\widetilde{N}_{\text{c}}-1}\left|\frac{\mathbf{g}_{[n],k}^{\text{T}}\widehat{\mathbf{g}}_{[n],k}^{*}}{\left\|\widehat{\mathbf{g}}_{[n],k}\right\|}\right|^2+\alpha^2\left|\frac{\mathbf{g}_{[\widetilde{N}_{\text{c}}],k}^{\text{T}}\widehat{\mathbf{g}}_{[\widetilde{N}_{\text{c}}],k}^{*}}{\left\|\widehat{\mathbf{g}}_{[\widetilde{N}_{\text{c}}],k}\right\|}\right|^2\Bigg\}$$
$$+\psi P_{\text{tx}}\xi T_{\text{c}}\mathbb{E}\Bigg\{\sum_{n=1}^{\widetilde{N}_{\text{c}}-1}\left|\sum_{i=1;i\neq k}^{K}\sqrt{\frac{\eta_{c_i}}{\widetilde{N}}}\frac{\mathbf{g}_{\{[n],i\},k}^{\text{T}}\widehat{\mathbf{g}}_{[n],i}^{*}}{\left\|\widehat{\mathbf{g}}_{[n],i}\right\|}\right|^2\Bigg\}$$
$$+\psi P_{\text{tx}}\xi T_{\text{c}}\mathbb{E}\Bigg\{\left|\sum_{i=1;i\neq k}^{K}\alpha\sqrt{\frac{\eta_{c_i}}{\widetilde{N}}}\frac{\mathbf{g}_{\{[\widetilde{N}_{\text{c}}],i\},k}^{\text{T}}\widehat{\mathbf{g}}_{[\widetilde{N}_{\text{c}}],i}^{*}}{\left\|\widehat{\mathbf{g}}_{[\widetilde{N}_{\text{c}}],i}\right\|}\right|^2\Bigg\}+\psi\mathbb{E}\Bigg\{\sum_{n=1}^{N}w'_{[n],k}\Bigg\}. \quad (4.28)$$

Based on (4.27) and (4.28), the average harvested energy, i.e., the harvested energy averaged over small-scaling fading realizations, at the k^{th} sensor, can be stated in closed-form as follows.

Theorem 1. The average energy $\overline{E}^{\text{i}}_{\text{c}_k}$ harvested by the k^{th} sensor over duration T_{c} based on DL-WET via superposed chirp waveforms over $\widetilde{N}_{\text{c}}$ best subbands under imperfect CSI at the AP equals

Case (i):

$$\overline{E}^{\text{i}}_{\text{c}_k} = \psi T_{\text{c}}\left[\frac{\eta_{\text{c}_k}P_{\text{tx}}\xi}{\widetilde{N}}\left(\gamma_k\Omega_{\text{c}_k}^{\widetilde{N}_{\text{c}}}+(\beta_k-\gamma_k)\Upsilon_{\text{c}_k}^{\widetilde{N}_{\text{c}}}\right)+P_{\text{tx}}\beta_k(1-\eta_{\text{c}_k})+N\sigma^2\right], \quad (4.29)$$

for $\widetilde{N}$ mod $\xi=0$, i.e., $\widetilde{N}_{\text{c}}=\frac{\widetilde{N}}{\xi}$ where $\Upsilon_{\text{c}_k}^{\widetilde{N}_{\text{c}}}$ and $\Omega_{\text{c}_k}^{\widetilde{N}_{\text{c}}}$ are given by

$$\Upsilon_{\text{c}_k}^{\widetilde{N}_{\text{c}}}=\sum_{n=1}^{\widetilde{N}_{\text{c}}}\frac{N!}{(n-1)!(N-n)!}\sum_{l=0}^{N-n}(-1)^{N-n+l}\binom{N-n}{l}\frac{1}{(N-l)^2}, \quad (4.30)$$

$$\Omega_{\text{c}_k}^{\widetilde{N}_{\text{c}}}=\sum_{n=1}^{\widetilde{N}_{\text{c}}}\frac{N!}{(n-1)!(N-n)!}\sum_{l=0}^{n-1}(-1)^{l}\binom{n-1}{l}(\Gamma(M))^{n-N-l-1}\Lambda(l), \quad (4.31)$$

$$\Lambda(l)=M^{n-N-l}\Gamma(1+M(l+N-n+1))F_A^{(l+N-n)}\left[1+M(l+N-n+1),M,\ldots,M;\right.$$
$$\left.M+1,\ldots,M+1;-1,\ldots,-1\right], \quad (4.32)$$

and $F_A^{(l)}(a,\mathbf{b};\mathbf{c};\mathbf{z})$ is Lauricella function of type A [91, (7)].

Case (ii):

$$\overline{E}^{\text{i}}_{\text{c}_k}=\frac{\eta_{\text{c}_k}\psi P_{\text{tx}}\xi T_{\text{c}}}{\widetilde{N}}\left[\gamma_k\left(\Omega_{\text{c}_k}^{(\widetilde{N}_{\text{c}}-1)}+\alpha^2\Omega'_{\text{c}_k}\right)+(\beta_k-\gamma_k)\left(\Upsilon_{\text{c}_k}^{(\widetilde{N}_{\text{c}}-1)}+\alpha^2\Upsilon'_{\text{c}_k}\right)\right]$$
$$+\frac{\psi P_{\text{tx}}\beta_k\xi T_{\text{c}}}{\widetilde{N}}\left(\widetilde{N}_{\text{c}}-1+\alpha^2\right)(1-\eta_{\text{c}_k})+\psi N\sigma^2T_{\text{c}}, \quad (4.33)$$

for $\widetilde{N} \bmod \xi \neq 0$ where

$$\Omega'_{\mathrm{c}_k} = \frac{N!}{(\widetilde{N}_\mathrm{c}-1)!(N-\widetilde{N}_\mathrm{c})!} \sum_{l=0}^{\widetilde{N}_\mathrm{c}-1} (-1)^l \binom{\widetilde{N}_\mathrm{c}-1}{l} (\Gamma(M))^{\widetilde{N}_\mathrm{c}-N-l-1} \Lambda(l), \tag{4.34}$$

$$\Upsilon'_{\mathrm{c}_k} = \frac{N!}{(\widetilde{N}_\mathrm{c}-1)!(N-\widetilde{N}_\mathrm{c})!} \sum_{l=0}^{N-\widetilde{N}_\mathrm{c}} (-1)^{N-\widetilde{N}_\mathrm{c}+l} \binom{N-\widetilde{N}_\mathrm{c}}{l} \frac{1}{(N-l)^2}. \tag{4.35}$$

and $\Upsilon_{\mathrm{c}_k}^{(\widetilde{N}_\mathrm{c}-1)}$ and $\Omega_{\mathrm{c}_k}^{(\widetilde{N}_\mathrm{c}-1)}$ are obtained from (4.30) and (4.31), respectively by substituting $\widetilde{N}_\mathrm{c} = \widetilde{N}_\mathrm{c}-1$.

Proof: The proof is given in Appendix A.5. □

Remark 5. Note that $\overline{E}^{\mathrm{i}}_{\mathrm{c}_k}$ as expressed in (4.29) and (4.33) is a function of the power P_{tx} with which the AP transmits on the DL, the number of antennas M at the AP, the number of subbands N, the number of sensors K, the chirp configuration factor ξ, the number of selected subbands $\widetilde{N}_\mathrm{c}$, energy conversion efficiency ψ, and variance γ_k of the imperfect channel estimate which in turn depends on the pilot energy E_p. Furthermore, power scaling for the chirp waveforms associated with the last subband for the case when $\widetilde{N} \bmod \xi \neq 0$ results in a different expression in (4.33) as compared to the case $\widetilde{N} \bmod \xi = 0$ that results in (4.29). With perfect CSI at the AP, $\beta_k - \gamma_k = 0$, and the expression for the average harvested energy simplifies and is stated next as a corollary.

Corollary 1. With perfect CSI at the AP, the average energy $\overline{E}^{\mathrm{p}}_{\mathrm{c}_k}$ harvested by k^{th} sensor over symbol duration T_c based on DL energy transmission using superposed chirp waveforms over $\widetilde{N}_\mathrm{c}$ best subbands equals

Case (i): For $\widetilde{N} \bmod \xi = 0$,

$$\overline{E}^{\mathrm{p}}_{\mathrm{c}_k} = \psi T_\mathrm{c} \left[\frac{\eta_{\mathrm{c}_k} P_{\mathrm{tx}} \xi \beta_k \Omega_{\mathrm{c}_k}^{\widetilde{N}_\mathrm{c}}}{\widetilde{N}} + P_{\mathrm{tx}} \beta_k (1-\eta_{\mathrm{c}_k}) + N\sigma^2 \right], \tag{4.36}$$

where $\Omega_{\mathrm{c}_k}^{\widetilde{N}_\mathrm{c}}$ is given in (4.31).

Case (ii): For $\widetilde{N} \bmod \xi \neq 0$,

$$\overline{E}^{\mathrm{p}}_{\mathrm{c}_k} = \frac{\eta_{\mathrm{c}_k} \psi P_{\mathrm{tx}} \xi T_\mathrm{c}}{\widetilde{N}} \left[\gamma_k \left(\Omega_{\mathrm{c}_k}^{(\widetilde{N}_\mathrm{c}-1)} + \alpha^2 \Omega'_{\mathrm{c}_k} \right) \right] + \frac{\psi P_{\mathrm{tx}} \beta_k \xi T_\mathrm{c}}{\widetilde{N}} \left(\widetilde{N}_\mathrm{c} - 1 + \alpha^2 \right) (1-\eta_{\mathrm{c}_k}) + \psi N \sigma^2 T_\mathrm{c}, \tag{4.37}$$

where Ω'_{c_k} is given in (4.34) and $\Omega_{\mathrm{c}_k}^{(\widetilde{N}_\mathrm{c}-1)}$ is calculated from (4.31) with $\widetilde{N}_\mathrm{c} = \widetilde{N}_\mathrm{c} - 1$.

Proof: Under perfect CSIT, $\gamma_k = \beta_k$. Replacing γ_k with β_k in (4.29) and (4.33), (4.36) and (4.37), respectively, are obtained. □

Remark 6. Given $\overline{E}^{\mathrm{i}}_{\mathrm{c}_k}$ and $\overline{E}^{\mathrm{p}}_{\mathrm{c}_k}$, the average harvested energy using superposed chirps over the

DL-WET duration τ_{DL} equals

$$\overline{E}_{\mathrm{c}_k}^{\partial,\mathrm{DL}} = \frac{\tau_{\mathrm{DL}}}{T_{\mathrm{c}}}\overline{E}_{\mathrm{c}_k}^{\partial}, \quad \partial \in \{\mathrm{i},\mathrm{p}\}. \tag{4.38}$$

where $\partial \in \{\mathrm{i},\mathrm{p}\}$ denotes either the imperfect CSI ($\partial = \mathrm{i}$) or the perfect CSI ($\partial = \mathrm{p}$).

4.4.2 Using Fixed-frequency Waveform

Based on Remark 2, the signal received at the k^{th} sensor over the n^{th} best subband for fixed-frequency waveform based transmission using (4.19) and (4.22) is given as

$$y_{\mathrm{o}_k}^{[n]}(t) = \sqrt{P_{\mathrm{tx}}}\mathbf{g}_{[n],k}^{\mathrm{T}}\sqrt{\frac{\eta_{\mathrm{o}_k}}{\widetilde{N}}}\frac{\widehat{\mathbf{g}}_{[n],k}^{*}}{\left\|\widehat{\mathbf{g}}_{[n],k}\right\|}s_{\mathrm{o}_{[n],k}}(t) + \sqrt{P_{\mathrm{tx}}}\mathbf{g}_{[n],k}^{\mathrm{T}}\sum_{i=1,i\neq k}^{K}\sqrt{\frac{\eta_{\mathrm{o}_i}}{\widetilde{N}}}\frac{\widehat{\mathbf{g}}_{\{[n],k\},i}^{*}}{\left\|\widehat{\mathbf{g}}_{\{[n],k\},i}\right\|}s_{\mathrm{o}_{\{[n],k\},i}}(t)\delta_{\{[n],k\}\in\Xi_{\mathrm{o}_i}} + w_{[n],k}(t), \tag{4.39}$$

where $\delta_{\{[n],k\}\in\Xi_{\mathrm{o}_i}}$ is an indicator function that equals 1 if the index of the n^{th} best subband of the k^{th} sensor belongs to the set Ξ_{o_i} of the best $\widetilde{N}$ subband entries corresponding to the i^{th} sensor. To be specific, any sensor $i \neq k$ will contribute to the interference term in $y_{\mathrm{o}_k}^{[n]}(t)$, if the index of the n^{th} best subband of the k^{th} sensor belongs to Ξ_{o_i}. Accordingly, using (4.39), the energy harvested by the k^{th} sensor over duration T_{o} and over N subbands, averaged over channel realizations, is given by

$$\overline{E}_{\mathrm{o}_k} = \psi\mathbb{E}\left\{\int_0^{T_{\mathrm{o}}}\sum_{n=1}^{N}\left|\left[y_{\mathrm{o}_k}^{[n]}(t)\right]\right|^2 dt\right\}. \tag{4.40}$$

As discussed, for each sensor, the signal is transmitted from the AP over its best $\widetilde{N}$ subbands only. Therefore, not all the sensors will contribute to the power of the interfering signal corresponding to the k^{th} sensor in the second term of (4.39) over all the N subbands. Based on the set Ξ_{o_i} of the best $\widetilde{N}$ subband entries corresponding to the i^{th} sensor, (4.40) can be re-arranged in a similar fashion as done in Section 4.4.1 for superposed chirps based transmission to obtain

$$\overline{E}_{\mathrm{o}_k} = \frac{\eta_{\mathrm{o}_k}\psi P_{\mathrm{tx}}T_{\mathrm{o}}}{\widetilde{N}}\mathbb{E}\left\{\sum_{n=1}^{\widetilde{N}}\left|\frac{\mathbf{g}_{[n],k}^{\mathrm{T}}\widehat{\mathbf{g}}_{[n],k}^{*}}{\left\|\widehat{\mathbf{g}}_{[n],k}\right\|}\right|^2\right\} + \psi P_{\mathrm{tx}}T_{\mathrm{o}}\mathbb{E}\left\{\sum_{n=1}^{\widetilde{N}}\left|\sum_{i=1,i\neq k}^{K}\sqrt{\frac{\eta_{\mathrm{o}_i}}{\widetilde{N}}}\frac{\mathbf{g}_{\{[n],i\},k}^{\mathrm{T}}\widehat{\mathbf{g}}_{[n],i}^{*}}{\left\|\widehat{\mathbf{g}}_{[n],i}\right\|}\right|^2\right\} + \psi\mathbb{E}\left\{\sum_{n=1}^{N}w'_{[n],k}\right\}, \tag{4.41}$$

where $\int_0^{T_{\mathrm{o}}} s_{\mathrm{o}_{[n],k}}^2(t)\,dt = T_{\mathrm{o}}$. Given (4.41), the average energy harvested by the k^{th} sensor in a symbol duration T_{o} over N subbands based on transmission of fixed-frequency waveform can be stated in closed-form as follows.

Theorem 2. The average energy $\overline{E}^{\mathrm{i}}_{\mathrm{o}_k}$ harvested by the k^{th} sensor over duration T_{o} based on DL-WET via fixed-frequency waveform over $\widetilde{N}$ best subbands under imperfect CSI equals

$$\overline{E}^{\mathrm{i}}_{\mathrm{o}_k} = \psi T_{\mathrm{o}} \left[\frac{\eta_{\mathrm{o}_k} P_{\mathrm{tx}}}{\widetilde{N}} \left(\gamma_k \Omega^{\widetilde{N}}_{\mathrm{o}_k} + (\beta_k - \gamma_k) \Upsilon^{\widetilde{N}}_{\mathrm{o}_k} \right) + P_{\mathrm{tx}} \beta_k (1 - \eta_{\mathrm{o}_k}) + N\sigma^2 \right], \tag{4.42}$$

where

$$\Omega^{\widetilde{N}}_{\mathrm{o}_k} = \sum_{n=1}^{\widetilde{N}} \frac{N!}{(n-1)!(N-n)!} \sum_{l=0}^{n-1} (-1)^l \binom{n-1}{l} (\Gamma(M))^{n-N-l-1} \Lambda(l), \tag{4.43}$$

$\Lambda(l)$ is given in (4.32) and

$$\Upsilon^{\widetilde{N}}_{\mathrm{o}_k} = \sum_{n=1}^{\widetilde{N}} \frac{N!}{(n-1)!(N-n)!} \sum_{l=0}^{N-n} (-1)^{N-n+l} \binom{N-n}{l} \frac{1}{(N-l)^2}. \tag{4.44}$$

Proof: The proof exploits order statistics and follows a similar methodology as in Appendix A.5.1 with $T_{\mathrm{c}} = T_{\mathrm{o}}$, $\xi = 1$, $\eta_{\mathrm{c}_k} = \eta_{\mathrm{o}_k}$. Further, the expressions for $\Omega^{\widetilde{N}}_{\mathrm{o}_k}$ and $\Upsilon^{\widetilde{N}}_{\mathrm{o}_k}$ given in (4.43) and (4.44) are obtained from the analysis of (4.31) and (4.30), respectively as given in Appendix A.5.1. □

Similar to superposed chirps based transmission, it may be noted that the average harvested energy in (4.42) is a function of the transmit power P_{tx} of the AP, the number of antennas M at the AP, the number of subbands N, the number of sensors K, the number of the best subbands selected $\widetilde{N}$, energy conversion efficiency ψ, and the pilot energy E_{p} through γ_k. As discussed, with perfect CSI, $\beta_k - \gamma_k = 0$, and the expression for average harvested energy simplifies and is stated next as a corollary.

Corollary 2. With perfect CSI at the AP, the average energy $\overline{E}^{\mathrm{p}}_{\mathrm{o}_k}$ harvested by the k^{th} sensor over duration T_{o} based on DL-WET via fixed-frequency waveform over $\widetilde{N}$ best subbands equals

$$\overline{E}^{\mathrm{p}}_{\mathrm{o}_k} = \psi T_{\mathrm{o}} \left[\frac{\eta_{\mathrm{o}_k} P_{\mathrm{tx}} \beta_k \Omega^{\widetilde{N}}_{\mathrm{o}_k}}{\widetilde{N}} + P_{\mathrm{tx}} \beta_k (1 - \eta_{\mathrm{o}_k}) + N\sigma^2 \right], \tag{4.45}$$

where $\Omega^{\widetilde{N}}_{\mathrm{o}_k}$ is given in (4.43).

Proof: Under perfect CSI, $\gamma_k = \beta_k$. Replacing γ_k with β_k in (4.42), (4.45) is obtained. □

Remark 7. Given $\overline{E}^{\mathrm{i}}_{\mathrm{o}_k}$ and $\overline{E}^{\mathrm{p}}_{\mathrm{o}_k}$, average harvested energy for DL-WET via fixed frequency waveform over duration τ_{DL} equals

$$\overline{E}^{\partial,\mathrm{DL}}_{\mathrm{o}_k} = \frac{\tau_{\mathrm{DL}}}{T_{\mathrm{o}}} \overline{E}^{\partial}_{\mathrm{o}_k} = \frac{\tau_{\mathrm{DL}}}{T_{\mathrm{c}}} \xi \overline{E}^{\partial}_{\mathrm{o}_k}, \tag{4.46}$$

and the gain in harvested energy using superposed chirps over fixed-frequency waveform is given by

$$\text{gain}(\%) = \frac{\overline{E}_{\mathrm{c}_k}^{\partial,\mathrm{DL}} - \overline{E}_{\mathrm{o}_k}^{\partial,\mathrm{DL}}}{\overline{E}_{\mathrm{o}_k}^{\partial,\mathrm{DL}}} \times 100, \tag{4.47}$$

where $\partial \in \{\mathrm{i}, \mathrm{p}\}$ denotes either the imperfect CSI ($\partial = \mathrm{i}$) or the perfect CSI ($\partial = \mathrm{p}$).

4.5 Analysis of Average Uplink Information Rate

From (4.21) and using the fact that $\mathbf{g}_{n,i} = \widehat{\mathbf{g}}_{n,i} - \widetilde{\mathbf{g}}_{n,i}$, the signal received at the AP due to simultaneous transmission by K sensors on the UL is given by

$$\mathbf{y}_{\mathrm{c}_n}(t) = \sqrt{\frac{P_{\mathrm{UL}}}{N}} \sum_{i=1}^{K} \sqrt{\rho_{\mathrm{c}_i}} \widehat{\mathbf{g}}_{n,i} q_{n,i} s_{\mathrm{c1}_{n,i}}(t) - \sqrt{\frac{P_{\mathrm{UL}}}{N}} \sum_{i=1}^{K} \sqrt{\rho_{\mathrm{c}_i}} \widetilde{\mathbf{g}}_{n,i} q_{n,i} s_{\mathrm{c1}_{n,i}}(t) + \mathbf{w}_n(t). \tag{4.48}$$

In order to decode the signal transmitted by the k^{th} sensor over the n^{th} subband, the AP uses maximum-ratio (MR) decoder given by $\mathbf{a}_{\mathrm{c}_{n,k}} = \widehat{\mathbf{h}}_{n,k} = \frac{\widehat{\mathbf{g}}_{n,k}}{\sqrt{\gamma_k}}$ to obtain

$$\mathbf{a}_{\mathrm{c}_{n,k}}^{\mathrm{H}} \mathbf{y}_{\mathrm{c}_n}(t) = \sqrt{\frac{P_{\mathrm{UL}}}{N}} \mathbf{a}_{\mathrm{c}_{n,k}}^{\mathrm{H}} \sum_{i=1}^{K} \sqrt{\rho_{\mathrm{c}_i}} \widehat{\mathbf{g}}_{n,i} q_{n,i} s_{\mathrm{c1}_{n,i}}(t) - \sqrt{\frac{P_{\mathrm{UL}}}{N}} \mathbf{a}_{\mathrm{c}_{n,k}}^{\mathrm{H}} \sum_{i=1}^{K} \sqrt{\rho_{\mathrm{c}_i}} \widetilde{\mathbf{g}}_{n,i} q_{n,i} s_{\mathrm{c1}_{n,i}}(t) + \mathbf{a}_{\mathrm{c}_{n,k}}^{\mathrm{H}} \mathbf{w}_n(t), \tag{4.49}$$

where $(\cdot)^{\mathrm{H}}$ denotes the conjugate transpose operation. Given $\mathbf{a}_{\mathrm{c}_{n,k}}^{\mathrm{H}} \mathbf{y}_{\mathrm{c}_n}(t)$, the demodulated signal $r_{\mathrm{c}_{n,k}}$ corresponding to the k^{th} sensor over the n^{th} subband as obtained at the AP is given by

$$\begin{aligned} r_{\mathrm{c}_{n,k}} &= \int_0^{T_{\mathrm{c}}} \left(\mathbf{a}_{\mathrm{c}_{n,k}}^{\mathrm{H}} \mathbf{y}_{\mathrm{c}_n}(t) \right) \frac{1}{\sqrt{T_{\mathrm{c}}}} s_{\mathrm{c1}_{n,k}}^{*}(t)\, dt \\ &= \sqrt{\frac{P_{\mathrm{UL}} T_{\mathrm{c}}}{N}} \rho_{\mathrm{c}_k} \gamma_k \left(\widehat{\mathbf{h}}_{n,k}^{\mathrm{H}} \widehat{\mathbf{h}}_{n,k} \right) q_{n,k} + \sqrt{\frac{P_{\mathrm{UL}} T_{\mathrm{c}}}{N}} \sum_{i=1; i \neq k}^{K} \sqrt{\rho_{\mathrm{c}_i} \gamma_i} \left(\widehat{\mathbf{h}}_{n,k}^{\mathrm{H}} \widehat{\mathbf{h}}_{n,i} \right) q_{n,i} + \widehat{\mathbf{h}}_{n,k}^{\mathrm{H}} \mathbf{w}_{n,k} \\ &\quad - \sqrt{\frac{P_{\mathrm{UL}} T_{\mathrm{c}}}{N}} \sum_{l=1}^{K} \sqrt{\rho_{\mathrm{c}_l}} \left(\widehat{\mathbf{h}}_{n,k}^{\mathrm{H}} \widetilde{\mathbf{g}}_{n,l} \right) q_{n,l}, \end{aligned} \tag{4.50}$$

where $\mathbf{w}_{n,k} = \frac{1}{\sqrt{T_{\mathrm{c}}}} \int_0^{T_{\mathrm{c}}} \mathbf{w}_n(t) s_{\mathrm{c1}_{n,k}}^{*}(t) dt$. The first term in (4.50) corresponds to the desired signal from the k^{th} sensor over the n^{th} subband. The second term captures the interference arising due to signals transmitted by other sensors on the UL. The third term is due to AWGN at the AP and the last term captures the effects of channel estimation error. Applying use-and-forget technique, the signal-to-interference-plus-noise ratio corresponding to the k^{th} sensor over the n^{th} subband can be obtained

as [92],

$$\begin{aligned}\mathrm{SINR}_{\mathrm{c}_{n,k}}^{\mathrm{MR,UL}} &= \frac{\frac{P_{\mathrm{UL}}T_{\mathrm{c}}}{N}\rho_{\mathrm{c}_k}\gamma_k M}{\sigma^2 + \frac{P_{\mathrm{UL}}T_{\mathrm{c}}}{NM}\left[\sum_{i=1,i\neq k}^{K}\rho_{\mathrm{c}_i}\gamma_i M + \sum_{l=1}^{K}\rho_{\mathrm{c}_l}\left(\beta_l - \gamma_l\right)M + \rho_{\mathrm{c}_k}\gamma_k M\right]} \\ &= \frac{\frac{P_{\mathrm{UL}}T_{\mathrm{c}}M}{N}\rho_{\mathrm{c}_k}\gamma_k}{\sigma^2 + \frac{P_{\mathrm{UL}}T_{\mathrm{c}}}{N}\sum_{l=1}^{K}\rho_{\mathrm{c}_l}\beta_l}. \end{aligned} \tag{4.51}$$

The amount of information $R_{\mathrm{c}_k}^{\mathrm{MR,UL}}$ (in bits) that is conveyed using chirp based transmission from the k^{th} sensor over N subbands for a duration of τ_{UL} seconds is given by

$$R_{\mathrm{c}_k}^{\mathrm{MR,UL}} = \frac{\tau_{\mathrm{UL}}}{T_{\mathrm{c}}}\sum_{n=1}^{N}\log_2\left(1 + \mathrm{SINR}_{\mathrm{c}_{n,k}}^{\mathrm{MR,UL}}\right). \tag{4.52}$$

Remark 8. The corresponding UL information (in bits) for fixed-frequency waveform based transmission is the same as in (4.52) because $T_{\mathrm{c}} = T_{\mathrm{o}}$.

4.6 Max-Min Optimal Power Allocation for WET

In this section, analysis on transmit power allocation policy that a power constrained AP must adopt for DL-WET to a swarm of sensor nodes is performed. The optimal solution through 'max-min' optimization is obtained first for DL-WET via superposed chirp waveforms followed by the corresponding analysis for fixed-frequency waveform based transmission.

4.6.1 Optimization Problem

Given that the AP is subject to an average transmit power constraint of P_{tx} and the knowledge of the system parameters ξ, M, N, K, $\widetilde{N}$, and ψ, the objective is to determine the max-min optimal power allocation coefficients to ensure that every sensor harvests the same amount of energy $\overline{E}_{\nu}^{\partial}$ on an average irrespective of its distance from the AP. Also, $\nu \in \{\mathrm{c},\mathrm{o}\}$ depending respectively on the use of superposed chirp ($\nu = \mathrm{c}$) waveforms or fixed-frequency ($\nu = \mathrm{o}$) waveform for DL-WET, and $\partial \in \{\mathrm{i},\mathrm{p}\}$ denotes either the estimated CSI ($\partial = \mathrm{i}$) or the perfect CSI ($\partial = \mathrm{p}$). Mathematically, the max-min optimization problem can be stated as follows:

$$\begin{aligned} \max_{\{\eta_{\nu_k}\}} \quad & \overline{E}_{\nu}^{\partial}, \quad \nu \in \{\mathrm{c},\mathrm{o}\}, \quad \partial \in \{\mathrm{i},\mathrm{p}\} \\ \text{s.t.} \quad & \overline{E}_{\nu_k}^{\partial} \geq \overline{E}_{\nu}^{\partial}, \quad k = 1,2,\ldots,K, \\ & \sum_{k=1}^{K}\eta_{\nu_k} \leq 1, \text{ and } \eta_{\nu_k} \geq 0, \quad k = 1,2,\ldots,K. \end{aligned} \tag{4.53}$$

4.6.2 Transmission of Superposed Chirp Waveforms on the DL

The solution to the max-min problem in (4.53) is given next, for superposed chirp waveforms, i.e., $\nu = \mathrm{c}$, in closed-form for both estimated CSI, i.e., $\partial = \mathrm{i}$ and perfect CSI, i.e., $\partial = \mathrm{p}$ in Proposition 1 and Corollary 3, respectively.

Proposition 1. With estimated CSI, the max-min power control coefficient $\overline{\eta}^{\mathrm{i}}_{\mathrm{c}_k}$ corresponding to the k^{th} sensor for DL-WET via superposed chirp waveforms is given by

Case (i)

$$\overline{\eta}^{\mathrm{i}}_{\mathrm{c}_k} = \frac{\widetilde{N}\left[\frac{1+\sum_{j=1}^{K}\frac{\widetilde{N}\beta_j}{\xi\left[\gamma_j\Omega_{\mathrm{c}_j}^{\widetilde{N}_{\mathrm{c}}}+(\beta_j-\gamma_j)\Upsilon_{\mathrm{c}_j}^{\widetilde{N}_{\mathrm{c}}}\right]-\widetilde{N}\beta_j}}{\sum_{j=1}^{K}\frac{\widetilde{N}}{\psi P_{\mathrm{tx}}T_{\mathrm{c}}\left(\xi\left[\gamma_j\Omega_{\mathrm{c}_j}^{\widetilde{N}_{\mathrm{c}}}+(\beta_j-\gamma_j)\Upsilon_{\mathrm{c}_j}^{\widetilde{N}_{\mathrm{c}}}\right]-\widetilde{N}\beta_j\right)}} - \psi P_{\mathrm{tx}}\beta_k T_{\mathrm{c}}\right]}{\psi P_{\mathrm{tx}}\xi T_{\mathrm{c}}\left[\gamma_k\Omega_{\mathrm{c}_k}^{\widetilde{N}_{\mathrm{c}}}+(\beta_k-\gamma_k)\Upsilon_{\mathrm{c}_k}^{\widetilde{N}_{\mathrm{c}}}\right]-\psi P_{\mathrm{tx}}\widetilde{N}\beta_k T_{\mathrm{c}}}, \tag{4.54}$$

for $\widetilde{N} \bmod \xi = 0$, where $\Omega_{\mathrm{c}_k}^{\widetilde{N}_{\mathrm{c}}}$ and $\Upsilon_{\mathrm{c}_k}^{\widetilde{N}_{\mathrm{c}}}$ are given in (4.31) and (4.30), respectively.

Case (ii)

$$\overline{\eta}^{\mathrm{i}}_{\mathrm{c}_k} = \frac{\widetilde{N}\left[\frac{1+\sum_{j=1}^{K}\frac{\beta_j\left(\widetilde{N}_{\mathrm{c}}-1+\alpha^2\right)}{\vartheta_j-\beta_j\left(\widetilde{N}_{\mathrm{c}}-1+\alpha^2\right)}}{\sum_{j=1}^{K}\frac{\widetilde{N}}{\psi P_{\mathrm{tx}}\xi T_{\mathrm{c}}\left[\vartheta_j-\beta_j\left(\widetilde{N}_{\mathrm{c}}-1+\alpha^2\right)\right]}} - \frac{\psi P_{\mathrm{tx}}\beta_k\xi T_{\mathrm{c}}}{\widetilde{N}}\left(\widetilde{N}_{\mathrm{c}}-1+\alpha^2\right)\right]}{\psi P_{\mathrm{tx}}\xi T_{\mathrm{c}}\left[\vartheta_k-\beta_k\left(\widetilde{N}_{\mathrm{c}}-1+\alpha^2\right)\right]}, \tag{4.55}$$

for $\widetilde{N} \bmod \xi \neq 0$, where $\vartheta_k = \gamma_k\left(\Omega_{\mathrm{c}_k}^{(\widetilde{N}_{\mathrm{c}}-1)}+\alpha^2\Omega'_{\mathrm{c}_k}\right)+(\beta_k-\gamma_k)\left(\Upsilon_{\mathrm{c}_k}^{(\widetilde{N}_{\mathrm{c}}-1)}+\alpha^2\Upsilon'_{\mathrm{c}_k}\right)$. Furthermore, Ω'_{c_k} and Υ'_{c_k} are given in (4.34) and (4.35), respectively. $\Upsilon_{\mathrm{c}_k}^{(\widetilde{N}_{\mathrm{c}}-1)}$ and $\Omega_{\mathrm{c}_k}^{(\widetilde{N}_{\mathrm{c}}-1)}$ are obtained from (4.30) and (4.31), respectively by substituting $\widetilde{N}_{\mathrm{c}} = \widetilde{N}_{\mathrm{c}} - 1$.

Proof: The proof is given in Appendix A.6. □

From (4.54) and (4.55), it is evident that $\overline{\eta}^{\mathrm{i}}_{\mathrm{c}_k}$ is a function of the variance of the estimates of the subband channel gain. With perfect CSI at the AP, $\beta_k - \gamma_k = 0$, the expressions for $\overline{\eta}^{\mathrm{i}}_{\mathrm{c}_k}$ simplify and are stated next as a corollary.

Corollary 3. With perfect CSI, the max-min power control coefficient $\overline{\eta}^{\mathrm{p}}_{\mathrm{c}_k}$ corresponding to the k^{th} sensor for DL-WET based on superposed chirp waveforms is given by

Case (i)

$$\overline{\eta}^{\mathrm{p}}_{\mathrm{c}_k} = \frac{\widetilde{N}}{\psi P_{\mathrm{tx}}\beta_k T_{\mathrm{c}}\left(\xi\Omega_{\mathrm{c}_k}^{\widetilde{N}_{\mathrm{c}}}-\widetilde{N}\right)}\left[\frac{1+\sum_{j=1}^{K}\frac{\widetilde{N}}{\xi\Omega_{\mathrm{c}_j}^{\widetilde{N}_{\mathrm{c}}}-\widetilde{N}}}{\sum_{j=1}^{K}\frac{\widetilde{N}}{\psi P_{\mathrm{tx}}\beta_j T_{\mathrm{c}}\left(\xi\Omega_{\mathrm{c}_j}^{\widetilde{N}_{\mathrm{c}}}-\widetilde{N}\right)}} - \psi P_{\mathrm{tx}}\beta_k T_{\mathrm{c}}\right], \tag{4.56}$$

for $\widetilde{N} \bmod \xi = 0$.

Case (ii)

$$\overline{\eta}_{\mathrm{c}_k}^{\mathrm{p}} = \frac{\widetilde{N}\left[\frac{1+\sum_{j=1}^{K}\frac{\beta_j\left(\widetilde{N}_{\mathrm{c}}-1+\alpha^2\right)}{\vartheta_j'-\beta_j\left(\widetilde{N}_{\mathrm{c}}-1+\alpha^2\right)}}{\sum_{j=1}^{K}\frac{\widetilde{N}}{\psi P_{\mathrm{tx}}\xi T_{\mathrm{c}}\left[\vartheta_j'-\beta_j\left(\widetilde{N}_{\mathrm{c}}-1+\alpha^2\right)\right]}} - \frac{\psi P_{\mathrm{tx}}\beta_k\xi T_{\mathrm{c}}}{\widetilde{N}}\left(\widetilde{N}_{\mathrm{c}}-1+\alpha^2\right)\right]}{\psi P_{\mathrm{tx}}\xi T_{\mathrm{c}}\left[\vartheta_k'-\beta_k\left(\widetilde{N}_{\mathrm{c}}-1+\alpha^2\right)\right]}, \tag{4.57}$$

for $\widetilde{N} \bmod \xi \neq 0$, where $\vartheta_k' = \gamma_k\left(\Omega_{\mathrm{c}_k}^{(\widetilde{N}_{\mathrm{c}}-1)} + \alpha^2\Omega_{\mathrm{c}_k}'\right)$.

Proof: For perfect CSI, $\gamma_k = \beta_k$. Replacing γ_k with β_k in (4.54) and (4.55), (4.56) and (4.57), respectively, are obtained. □

Once the max-min power control coefficients are evaluated, the corresponding max-min average energy harvested based on DL-WET via superposed chirp waveforms is obtained from (4.29) and (4.33) under estimated CSI by substituting $\eta_{\mathrm{c}_k} = \overline{\eta}_{\mathrm{c}_k}^{\mathrm{i}}$, and from (4.36) and (4.37) under perfect CSI by substituting $\eta_{\mathrm{c}_k} = \overline{\eta}_{\mathrm{c}_k}^{\mathrm{p}}$.

4.6.3 Transmission of Fixed-Frequency Waveform on the DL

The closed-form solution to the max-min optimization problem as stated in (4.53) for fixed-frequency waveform, i.e., $\nu = \mathrm{o}$ under both estimated CSI, i.e., $\partial = \mathrm{i}$ and perfect CSI, i.e., $\partial = \mathrm{p}$ at the AP is stated in Proposition 2 and Corollary 4, respectively.

Proposition 2. With estimated CSI at the AP, the max-min power control coefficient $\overline{\eta}_{\mathrm{o}_k}^{\mathrm{i}}$ corresponding to the k^{th} sensor for DL-WET via fixed-frequency waveform is given by

$$\overline{\eta}_{\mathrm{o}_k}^{\mathrm{i}} = \frac{\widetilde{N}\left[\frac{1+\sum_{j=1}^{K}\frac{\widetilde{N}\beta_j}{\left[\gamma_j\Omega_{\mathrm{o}_j}^{\widetilde{N}}+(\beta_j-\gamma_j)\Upsilon_{\mathrm{o}_j}^{\widetilde{N}}\right]-\widetilde{N}\beta_j}}{\sum_{j=1}^{K}\frac{\widetilde{N}}{\psi P_{\mathrm{tx}}T_{\mathrm{o}}\left(\left[\gamma_j\Omega_{\mathrm{o}_j}^{\widetilde{N}}+(\beta_j-\gamma_j)\Upsilon_{\mathrm{o}_j}^{\widetilde{N}}\right]-\widetilde{N}\beta_j\right)}} - \psi P_{\mathrm{tx}}\beta_k T_{\mathrm{o}}\right]}{\psi P_{\mathrm{tx}}T_{\mathrm{o}}\left[\gamma_k\Omega_{\mathrm{o}_k}^{\widetilde{N}}+(\beta_k-\gamma_k)\Upsilon_{\mathrm{o}_k}^{\widetilde{N}}\right] - \psi P_{\mathrm{tx}}\widetilde{N}\beta_k T_{\mathrm{o}}}. \tag{4.58}$$

Proof: This can be proved along similar lines as in Appendix A.6.1 with $T_{\mathrm{c}} = T_{\mathrm{o}}$, $\xi = 1$, $\eta_{\mathrm{c}_k} = \eta_{\mathrm{o}_k}$. Further, the expressions for $\Omega_{\mathrm{o}_k}^{\widetilde{N}}$ and $\Upsilon_{\mathrm{o}_k}^{\widetilde{N}}$ are given in (4.43) and (4.44), respectively. □

With perfect CSI at the AP, $\beta_k - \gamma_k = 0$, the result above simplifies and is stated next as a corollary.

Corollary 4. With perfect CSI at the AP, the max-min power control coefficient $\overline{\eta}_{\mathrm{o}_k}^{\mathrm{p}}$ corresponding to the k^{th} sensor for DL-WET via fixed-frequency waveform is given by

$$\overline{\eta}_{\mathrm{o}_k}^{\mathrm{p}} = \frac{\widetilde{N}}{\psi P_{\mathrm{tx}}\beta_k T_{\mathrm{o}}\left(\Omega_{\mathrm{o}_k}^{\widetilde{N}}-\widetilde{N}\right)}\left[\frac{1+\sum_{j=1}^{K}\frac{\widetilde{N}}{\Omega_{\mathrm{o}_j}^{\widetilde{N}}-\widetilde{N}}}{\sum_{j=1}^{K}\frac{\widetilde{N}}{\psi P_{\mathrm{tx}}\beta_j T_{\mathrm{o}}\left(\Omega_{\mathrm{o}_j}^{\widetilde{N}}-\widetilde{N}\right)}} - \psi P_{\mathrm{tx}}\beta_k T_{\mathrm{o}}\right]. \tag{4.59}$$

Proof: For perfect CSI, $\gamma_k = \beta_k$. Replacing γ_k with β_k in (4.58), (4.59) is obtained. □

Based on Proposition 2 and Corollary 4, the corresponding max-min energy harvested by the sensor under estimated CSI is computed by substituting $\eta_{\mathrm{o}_k} = \overline{\eta}^{\mathrm{i}}_{\mathrm{o}_k}$ in (4.42) and under perfect CSI is computed by substituting $\eta_{\mathrm{o}_k} = \overline{\eta}^{\mathrm{p}}_{\mathrm{o}_k}$ in (4.45) for fixed-frequency waveform.

4.6.4 Optimization Scenarios for WET

Following the transmission strategy presented in Section 4.3.2, out of the available N subbands, $\widetilde{N}$ and $\widetilde{N}_{\mathrm{c}}$ best subbands are selected, over which signals are transmitted, while using fixed-frequency and superposed chirp waveforms, respectively. Using the associated max-min power control coefficients $\{\overline{\eta}_{\mathrm{c}_k}\}\ \forall\ k \in \{1, 2, \ldots, K\}$, calculated using (4.54), (4.55), (4.56), (4.57), and $\{\overline{\eta}_{\mathrm{o}_k}\}\ \forall\ k \in \{1, 2, \ldots, K\}$, calculated using (4.58), (4.59) based on the CSI type, the value of P_{peak} for the waveforms is defined as

$$P_{\mathrm{peak}} = \frac{\overline{\eta}_{\mathrm{c}_{k'}} P_{\mathrm{tx}}}{\widetilde{N}_{\mathrm{c}}\xi}, \quad \widetilde{N}_{\mathrm{c}} = \frac{\widetilde{N}}{\xi}, \qquad \text{for Superposed Chirp,} \tag{4.60}$$

$$P_{\mathrm{peak}} = \frac{\overline{\eta}_{\mathrm{o}_{k'}} P_{\mathrm{tx}}}{\widetilde{N}}, \quad \widetilde{N} \leq N, \qquad \text{for Fixed-frequency,} \quad k' \in \{1, 2, \ldots, K\}, \tag{4.61}$$

where k' represents the farthest sensor from AP, i.e.,

$$k' = k, \quad \text{for} \quad \beta_k = \min\{\beta_1, \beta_2, \ldots, \beta_K\}. \tag{4.62}$$

Furthermore, for the k^{th} sensor, for each chirp in the superposed waveform, the associated $P_{n,k}$ is calculated from (4.60) as $P_{n,k} = \frac{\overline{\eta}_{\mathrm{c}_k} P_{\mathrm{tx}}}{\widetilde{N}_{\mathrm{c}}\xi}$ and for fixed-frequency waveform the associated $P_{n,k}$ is calculated from (4.61) as $P_{n,k} = \frac{\overline{\eta}_{\mathrm{o}_k} P_{\mathrm{tx}}}{\widetilde{N}}$ where $0 \leq P_{n,k} \leq P_{\mathrm{peak}}\ \forall\ n, k$.

Alternatively, if the P_{peak} level is fixed at $\overline{P}_{\mathrm{peak}}$ then one can compute the number of subbands $\widetilde{N}_{\mathrm{c}}$ and $\widetilde{N}$ that are required for superposed chirp waveforms and fixed-frequency waveform such that P_{tx} constraint is satisfied. In this context, two algorithms, Algorithm 1 for the selection of $\widetilde{N}_{\mathrm{c}}$ and Algorithm 2 for the selection of $\widetilde{N}$ are designed and presented below while maintaining the max-min optimality. In case of $\overline{P}_{\mathrm{peak}} - P_{\mathrm{peak}} = 0$, for the k' user, associated waveform power $P_{n,k'} = \overline{P}_{\mathrm{peak}}$ else $P_{n,k'} < \overline{P}_{\mathrm{peak}}$. Once $\widetilde{N}_{\mathrm{c}}$ and $\widetilde{N}$ is obtained, P_{peak}, the power control coefficients, and average harvested energy is calculated from (4.60), (4.54), (4.55), (4.29), (4.33) for superposed chirp waveforms, and from (4.61), (4.58), (4.42) for fixed-frequency waveform.

Algorithm 1 Selection of $\widetilde{N}_{\mathrm{c}}$ Best Subbands for Superposed Chirp Waveforms for a Given $\overline{P}_{\mathrm{peak}}$

Initialize:
  $\widetilde{N} \leftarrow N$, ξ, $\overline{P}_{\mathrm{peak}} \geq \frac{P_{\mathrm{tx}}}{NK}$
repeat
  $\widetilde{N} \leftarrow \widetilde{N} - 1$
  if $\left(\widetilde{N} \bmod \xi\right) = 0$ **then**
    $\widetilde{N}_{\mathrm{c}} = \frac{\widetilde{N}}{\xi}$, and calculate P_{peak} from (4.54), (4.56), and (4.60);
  else
    $\widetilde{N}_{\mathrm{c}} = \left\lfloor \frac{\widetilde{N}}{\xi} \right\rfloor + 1$, and calculate P_{peak} from (4.55), (4.57), and (4.60);
  end if
until $\left(\overline{P}_{\mathrm{peak}} - P_{\mathrm{peak}}\right) \leq 0$ or $\widetilde{N}_{\mathrm{c}} = 1$
if $\left(\overline{P}_{\mathrm{peak}} - P_{\mathrm{peak}}\right) \leq 0$ **then**
  if $\left(\overline{P}_{\mathrm{peak}} - P_{\mathrm{peak}}\right) < 0$ **then**
    $\widetilde{N} = \widetilde{N} + 1$;
  end if
  $\widetilde{N}_{\mathrm{c}} = \frac{\widetilde{N}}{\xi}$, for $\widetilde{N} \bmod \xi = 0$; or $\widetilde{N}_{\mathrm{c}} = \left\lfloor \frac{\widetilde{N}}{\xi} \right\rfloor + 1$, for $\widetilde{N} \bmod \xi \neq 0$;
end if

Algorithm 2 Selection of $\widetilde{N}$ Best Subbands for Fixed-frequency Waveform for a Given $\overline{P}_{\mathrm{peak}}$

Initialize:
  $\widetilde{N} \leftarrow N$, $\overline{P}_{\mathrm{peak}} \geq \frac{P_{\mathrm{tx}}}{NK}$
repeat
  $\widetilde{N} \leftarrow \widetilde{N} - 1$, and calculate P_{peak} from (4.58), (4.59), and (4.61),
until $\left(\overline{P}_{\mathrm{peak}} - P_{\mathrm{peak}}\right) \leq 0$ or $\widetilde{N} = 1$
if $\left(\overline{P}_{\mathrm{peak}} - P_{\mathrm{peak}}\right) < 0$ **then**
  $\widetilde{N} = \widetilde{N} + 1$;
end if

4.7 Performance Analysis and Numerical Results for Rayleigh Fading Channel

In this section, we present numerical results to understand the potential of using chirp waveform for WET and the benefits that it offers in comparison to fixed-frequency waveform. We also illustrate the impact of several design parameters such as ξ, M, N, $\widetilde{N}$, and channel estimation error on the system performance. The large-scale fading coefficient for the k^{th} sensor node is modeled as $\beta_k = 10^{-3} d_k^{-3}$ [64], where d_k is the distance, in m, between the AP and the k^{th} sensor. Unless mentioned otherwise, we consider a carrier frequency of 2.4 GHz, $B_{\mathrm{total}} = 6.4$ MHz, $N = 32$ and $B = 200$ kHz. Furthermore, we take $P_{\mathrm{tx}} = 1$ W, $\tau_{\mathrm{ch}} = 190.5$ ms, $\psi = 0.5$, $\sigma^2 = k_B T_{\mathrm{e}} 10^{F/10} = 10^{-20}$ J, where $k_B = 1.38 \times 10^{-23}$ J/K, $T_{\mathrm{e}} = 300$ K, and the receiver noise figure $F = 7$ dB [63]. In order to confirm our mathematical analysis, the Monte-Carlo simulations are carried out over 10^5 independent channel realizations.

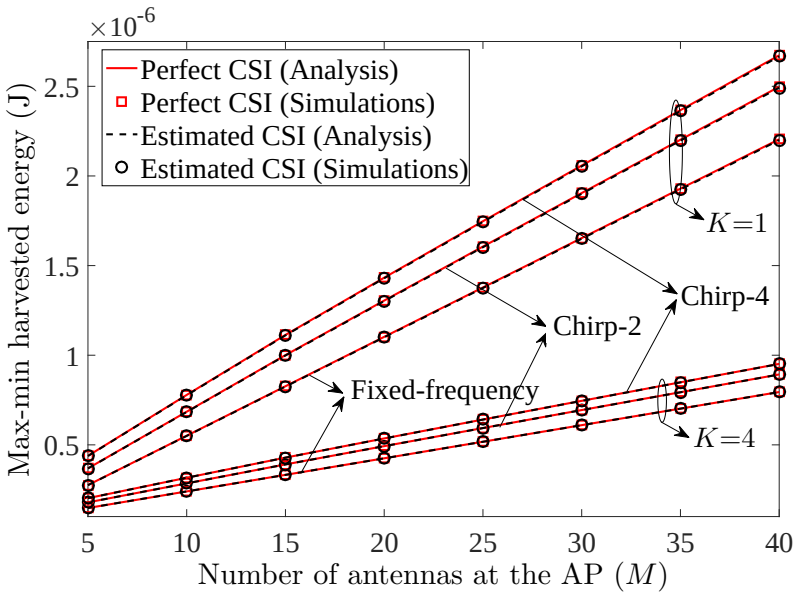

Figure 4.5: Effect of M, K and ξ on max-min harvested energy ($\widetilde{N} = N = 32$, $\xi = 2, 4$, and $K = 4$ placed at distances of 9.5, 10.4, 11.3, and 12 meters from the AP, $K = 1$ placed at a distance of 12 meter from the AP).

4.7.1 Analysis on Max-Min Harvested Energy

The max-min harvested energy is plotted in Figure 4.5 as a function M with $N = \widetilde{N} = 32$ for $K = 1$ sensor placed at a distance of 12 m and for $K = 4$ sensors placed at distances of 9.5, 10.4, 11.3 and 12 m from the AP. The value $K = 1$ or $K = 4$ is taken just for illustration. Note that our mathematical analysis is in general valid for any arbitrary value of K. The results are shown for fixed-frequency and superposed chirp waveforms with $\xi = 2$ and $\xi = 4$. It is observed that the analysis matches with the simulations. The max-min harvested energy under imperfect CSI at a pilot power $P_{\mathrm{p}} = 0.1$ mW and $\tau_{\mathrm{p}} = K$ is very close to that obtained under perfect CSI. Furthermore, the max-min harvested energy with superposed chirp waveforms increases relative to that obtained with fixed-frequency waveform as chirp configuration parameter ξ increases. This is primarily because as ξ increases, more and more superposed chirp waveforms are transmitted within the same bandwidth without violating orthogonality or the peak power constraint. And more energy is pushed through the subbands with relatively higher channel gain, thus exploiting gains due to frequency diversity. As expected, the max-min harvested energy reduces as K increases and increases as M increases due to increase in the beamforming gain.

In Figure 4.6 the gain in max-min harvested energy obtained using superposed chirp waveforms relative to fixed-frequency waveform as a function of M is plotted. We plot the gains obtained with

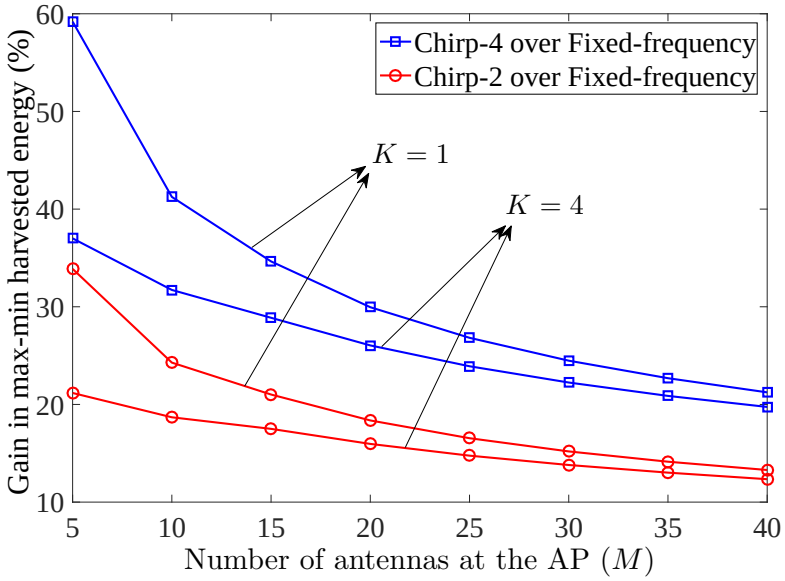

Figure 4.6: Gain in max-min harvested energy by using chirp-2 or chirp-4 over fixed-frequency as a function of M ($\widetilde{N} = N = 32$, and $K = 1, 4$).

chirp-4 and chirp-2 over fixed-frequency waveform for both $K = 1$ and $K = 4$ sensors in the network. It is observed that the use of chirp over fixed-frequency waveform provides gain in the harvested energy of about 14% – 60% depending on the values of ξ, M, $\widetilde{N}$, K and the distance of the sensors from the AP. For example, for $K = 4$, and with $M = 20$, 26% gain in harvested energy is obtained using chirp-4 over fixed frequency waveform. Furthermore, as M increases, the variance of the channel estimate reduces, i.e., the channel gain of different subbands approaches towards its mean channel gain. Therefore, the achievable gain using superposed chirps over fixed-frequency waveform reduces due to diminishing gains from frequency-diversity.

In Figure 4.7 max-min harvested energy is plotted as a function of M for different pilot powers and with imperfect CSI for $\widetilde{N} = N = 32$ and $K = 4$ sensors placed at distances of 9.5, 10.4, 11.3 and 12 m from the AP. It is found that the max-min harvested energy degrades relative to perfect CSI as the pilot power P_{p} is reduced from 1 mW to 1 μW due to degradation in the quality of channel estimates. Since, the analytical results are in close agreement with the Monte-Carlo simulation results, henceforth only analytical results are shown for the remaining results to avoid clutter.

In Figure 4.8 the cumulative distribution function (CDF) of the minimum harvested energy is plotted for two different power allocation strategies, namely, max-min and equal power under imperfect CSI with $P_{\mathrm{p}} = 0.1$ mW, $M = 32$ and $N = 32$. The results for DL-WET via chirp-2 and fixed frequency

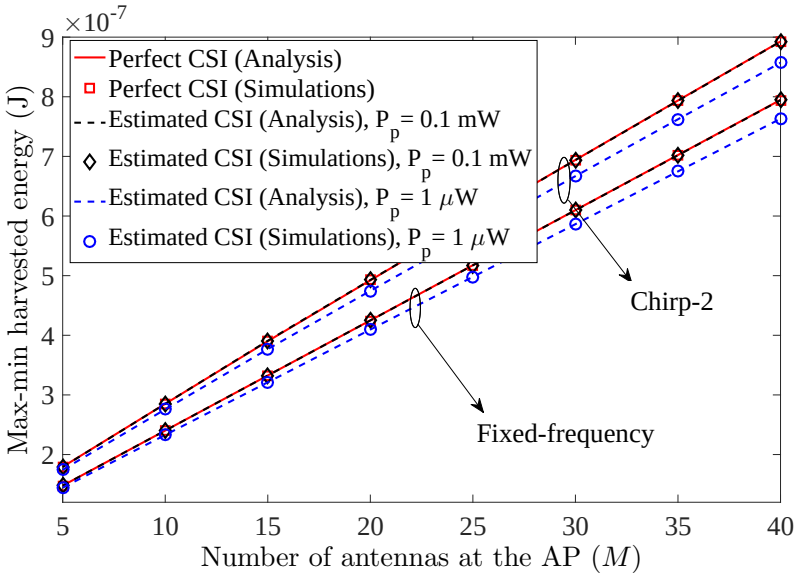

Figure 4.7: Effect of channel estimation error on max-min harvested energy ($\widetilde{N} = N = 32$, $K = 4$ sensors placed at distances of 9.5, 10.4, 11.3 and 12 meters from the AP).

waveform are obtained with and without subband selection. It is observed that the probability that the minimum harvested energy is above a certain threshold is the highest with chirp-2 based DL-WET when max-min power control and subband selection is employed. It is because under max-min power control policy the power is distributed among the sensors so as to ensure that the minimum energy

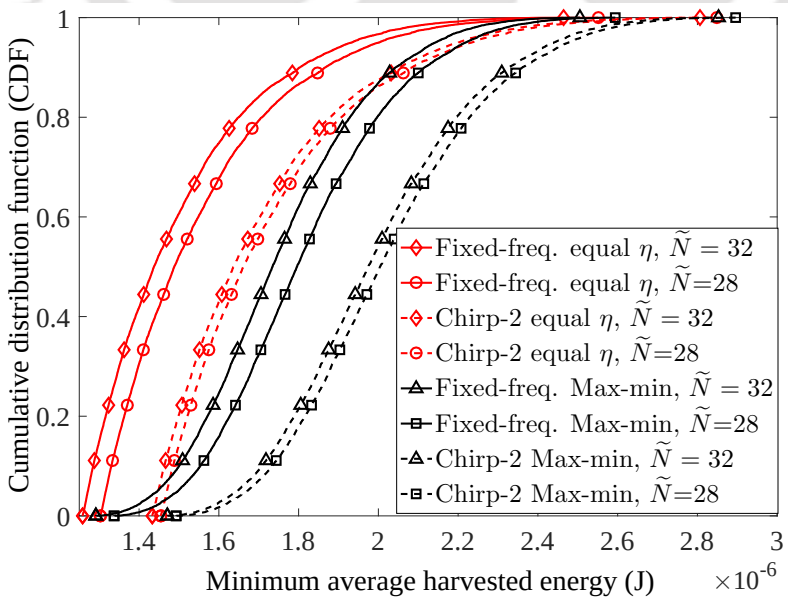

Figure 4.8: CDF of minimum harvested energy for $M = 32$, $N = 32$, $\widetilde{N} = 32, 28$, $P_{\mathrm{p}} = 0.1$ mW, and $K = 3$ sensors distributed uniformly between 7.5 – 9.5 meters from the AP.

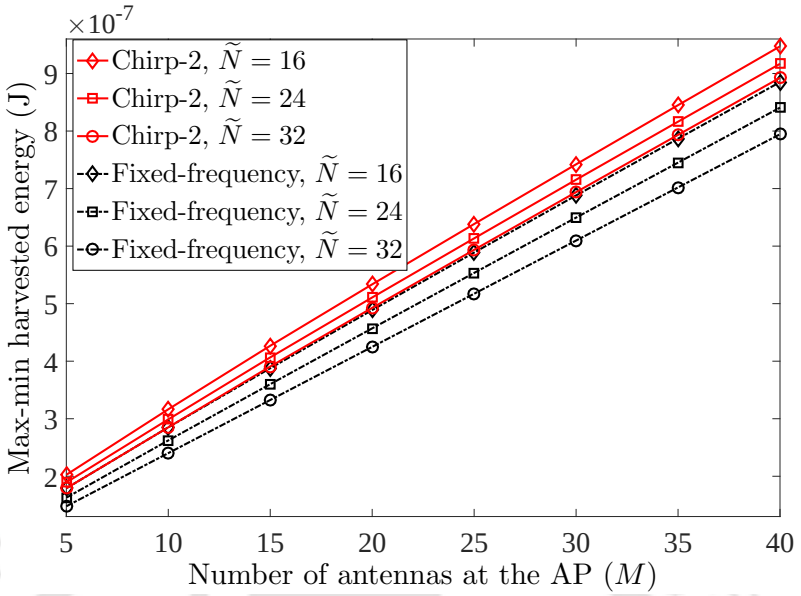

Figure 4.9: Effect of subband selection on max-min harvested energy for $N = 32$, $P_{\mathrm{p}} = 0.1$ mW, and $K = 4$ sensors placed at distances of 9.5, 10.4, 11.3 and 12 meters from the AP.

harvested is maximized. This is unlike equal power policy in which the farthest sensor harvests very small amount of energy. Furthermore, unlike fixed-frequency waveform, with chirp-2 waveforms and subband selection more energy can be pushed over the subbands with relatively higher channel gains without affecting orthogonality while maintaining the average and the peak power constraints.

In Figure 4.9 the max-min harvested energy versus M is plotted under imperfect CSI with $P_{\mathrm{p}} = 0.1$ mW, $N = 32$ for DL-WET via both chirp-2 and fixed-frequency waveform transmission on the DL to $K = 4$ sensors located at distances of 9.5, 10.4, 11.3 and 12 m from the AP. The results are plotted for three different values of $\widetilde{N}$, namely, 32, 24, and 16. Note that $\widetilde{N} = N = 32$ refers to no subband selection. It is observed that the max-min harvested energy increases as $\widetilde{N}$ decreases for both fixed-frequency and chirp-2 transmission, since higher and higher energy is pushed through the subbands with relatively better channel gains while maintaining the average transmit power constraint of P_{tx}. For DL-WET via superposed chirps, $\widetilde{N}_{\mathrm{c}} < \widetilde{N}$ as $\xi > 1$, it therefore obtains higher max-min harvested energy compared to fixed-frequency waveform.

In Figure 4.10 the max-min harvested energy versus M is plotted for $K = 4$ sensors placed at distances of 7.5, 8.3, 9.2, and 10 m from the AP and for $K = 1$ sensor placed at a distance of 12 m from the AP where a fixed $\overline{P}_{\mathrm{peak}}$ of 15.6 mW for $K = 4$ and $\overline{P}_{\mathrm{peak}}$ of 42.1 mW for $K = 1$ are considered such that $\overline{P}_{\mathrm{peak}} > \frac{P_{\mathrm{tx}}}{NK}$ is satisfied. Accordingly, $\widetilde{N}_{\mathrm{c}}$ and $\widetilde{N}$ subbands are computed for superposed chirp

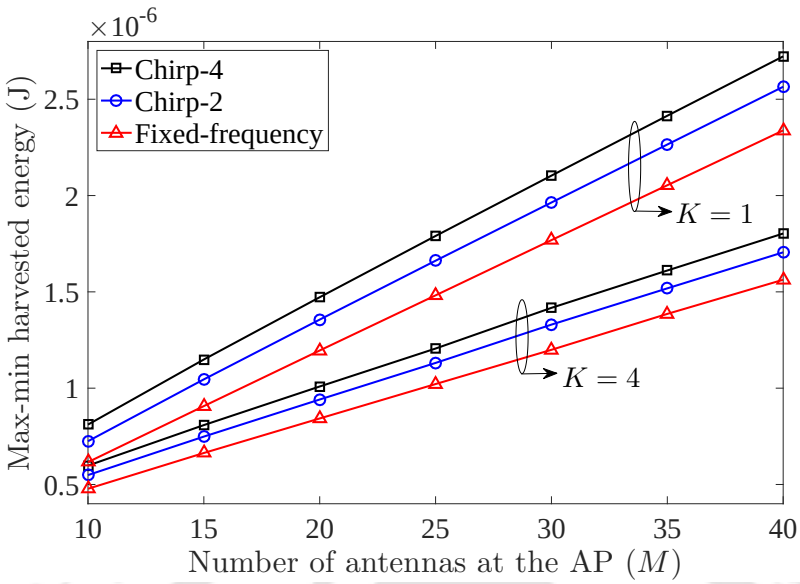

Figure 4.10: Max-min harvested energy versus M with $\widetilde{N}_{\mathrm{c}}$ and $\widetilde{N}$ obtained from Algorithm 1 and Algorithm 2, for $K = 4$ with $\overline{P}_{\mathrm{peak}} = 15.6$ mW, and for $K = 1$ with $\overline{P}_{\mathrm{peak}} = 42.1$ mW.

waveforms and fixed-frequency waveform, respectively based on proposed Algorithm 1 and Algorithm 2 such that the P_{tx} constraint is satisfied with equality. Even in this setting, where $\overline{P}_{\mathrm{peak}}$ has a fixed value and $\widetilde{N}_{\mathrm{c}}$ or $\widetilde{N}$ are obtained accordingly, a similar trend is observed in terms of harvested energy with DL-WET via chirp waveforms outperforming DL-WET via fixed-frequency waveform.

Figure 4.11 plots the average energy harvested by the sensor as a function of its distance from the AP based on DL-WET via chirp-4, chirp-2, and fixed frequency waveform transmission. $N = 32$, $\widetilde{N} = 24$ is considered and the results are shown for two different values of M, namely, 5 and 10. It is observed that the range of WET can be extended using chirp waveform based transmissions relative to fixed-frequency waveform or by increasing the number of antennas at the AP while maintaining the average harvested energy at the same target level. The range of WET increases as ξ is increased. For example, DL-WET based on chirp-4 waveform transmission can extend the range of energy transfer by 1.5 m over DL-WET based on fixed-frequency waveform transmission with $M = 5$ antennas at the AP while maintaining the average energy harvested at 7×10^{-7} J.

Design of multisine waveforms for WET operation based on a set of fixed-frequency unmodulated waveforms is presented in [22]. A comparison, in terms of average harvested energy at the sensor, placed at a distance of 12 m from the AP is performed among DL-WET via superposed chirp, via fixed-frequency, and via multisine waveforms [22] while considering a fixed $\overline{P}_{\mathrm{peak}}$ of 42.1 mW and $N = 32$.

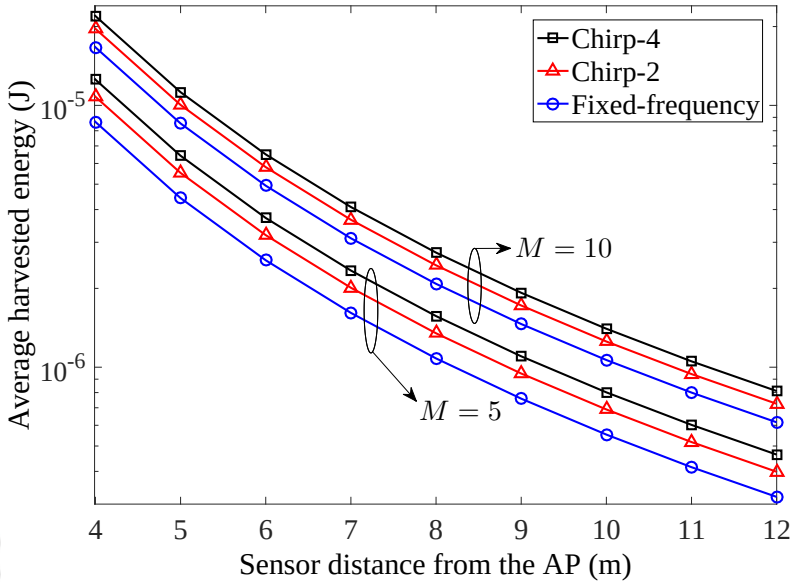

Figure 4.11: Effect of distance on the average harvested energy ($N = 32$, $\widetilde{N} = 24$ and $K = 1$).

The associated $\widetilde{N}_{\mathrm{c}}$ and $\widetilde{N}$ for superposed chirps and fixed-frequency waveform are obtained using proposed Algorithm 1 and Algorithm 2, and the average harvested energy is plotted in Figure 4.12, for different M and this result provides the following important insights: (1) Fixed-frequency waveform with selected subbands ($\widetilde{N}$) provides improved harvested energy over multisine [22]. For a given $\overline{P}_{\mathrm{peak}}$, DL-WET via multisine adapts the signal amplitude and phase proportional to the associated subband gain, it however uses all the N subbands for transmission. In contrast, for DL-WET via fixed-frequency waveform with subband selection we use Algorithm 2 to compute $\widetilde{N}$ while satisfying both $\overline{P}_{\mathrm{peak}}$ and P_{tx} constraints. Thus, unlike multisine using fixed-frequency waveform, no power is transferred over $N - \widetilde{N}$ weaker set of subbands and it thereby provides greater harvested energy, and the same is observed from Figure 4.12. However, compared to fixed-frequency waveform with no subband selection, both multisine and fixed-frequency waveform with selected subbands perform better as expected. (2) With the proposed DL-WET via superposed chirps, a superposition of multiple chirp waveforms is transmitted over a subband and it therefore uses fewer subbands $\widetilde{N}_{\mathrm{c}} < \widetilde{N}$ having relatively better channel gains over fixed-frequency waveform and achieves higher harvested energy as observed from the previous results. Thus, relative to multisine, superposed chirps perform better, in terms of harvested energy, as observed from Figure 4.12 where Algorithm 1 is used for the selection of $\widetilde{N}_{\mathrm{c}}$. (3) From Figure 4.12, it is found that DL-WET via chirp-4 and DL-WET via fixed frequency with subband selection provide an improvement of respectively about 40% and 5% in harvested energy

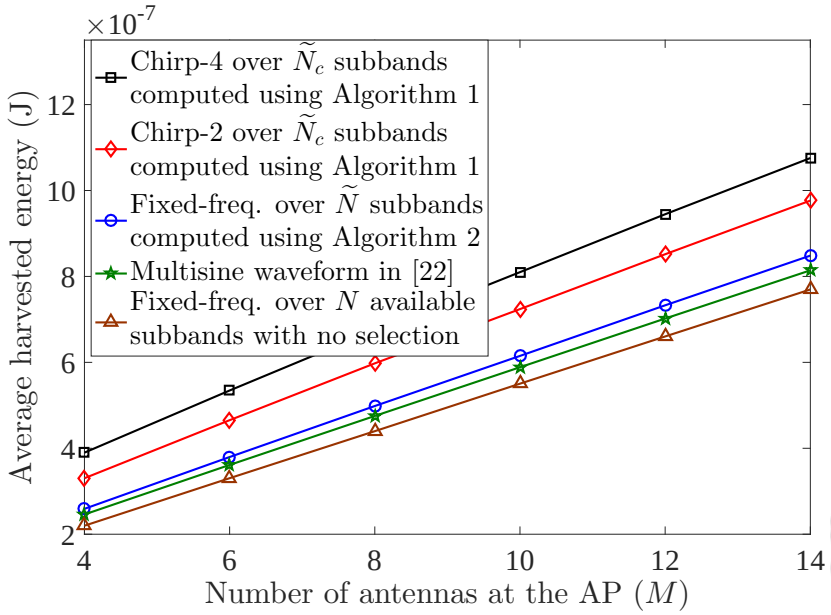

Figure 4.12: Average energy harvested versus M for a sensor ($K = 1$) placed at a distance of 12 meter from the AP while using chirp and fixed-frequency waveform with selected subbands, multisine [22], and fixed-frequency waveform with available subbands and no selection, with $N = 32$ and $\overline{P}_{\text{peak}} = 42.1$ mW.

over DL-WET via multisine [22] with $M = 8$ antennas at the AP. From the above observations, it can be concluded that the proposed waveform design using chirp is capable of providing superior performance in terms of harvested energy at the sensor over available designs, i.e., OFDM, multisine etc., and thereby improving the ETE. Further, in case of a WET system operating over fixed-frequency waveform, selecting set of subbands $\widetilde{N}$ with higher channel gains, based on $\overline{P}_{\text{peak}}$, also leads to improved harvested energy over multisine but it is lower than the chirp.

4.7.2 Analysis on Energy-Information Transfer Trade-off

The trade-off between the UL max-min information transfer (in bits) and the max-min harvested energy on the DL is illustrated in Figure 4.13 for chirp-4, chirp-2, and fixed-frequency waveform based transmission for $M = 20$, $N = 32$, and $K = 1$ sensor placed at a distance of 12 m and for $K = 4$ sensors placed at distances of 9.5, 10.4, 11.3 and 12 m, respectively from the AP. For information transfer, we choose the max-min power control coefficient corresponding to the k^{th} sensor as $\rho_{c_k} = \frac{1}{\gamma_k}\left(\min_i \gamma_i\right)$ where $i = 1, 2, \ldots, K$ [92]. It is observed that DL-WET via chirp-4 achieves the highest max-min harvested energy relative to DL-WET via chirp-2 and DL-WET via fixed frequency waveform based transmission while keeping the max-min information transfer in bits fixed at a certain level. Furthermore, with the increase in K, the energy-information transfer region contracts, i.e., the max-min harvested energy

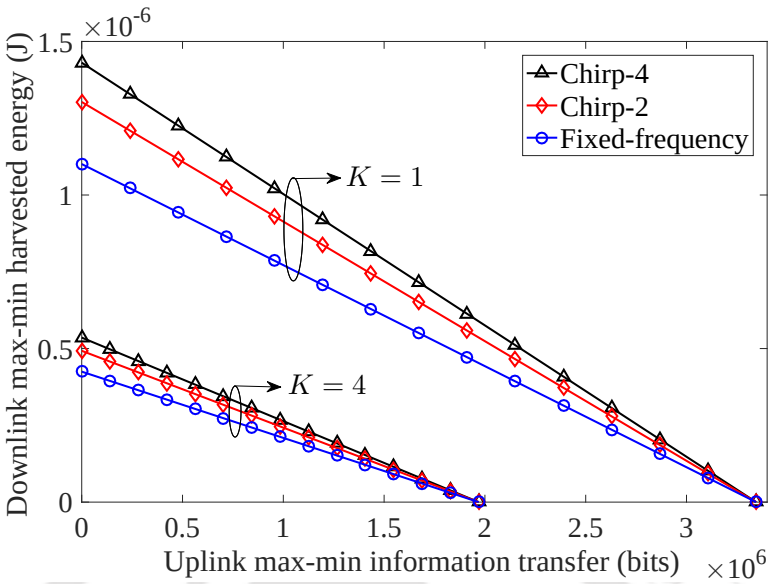

Figure 4.13: Energy-information transfer region for $M = 20$, $N = 32$, and $K = 4$ placed at distances of 9.5, 10.4, 11.3, and 12 meters from the AP, $K = 1$ placed at a distance of 12 meter from the AP.

on the DL decreases due to smaller fraction of power per sensor given a fixed P_{tx} while the max-min fair information transfer on the UL reduces due to increased interference. Therefore, for a fixed K, DL-WET based on the transmission of the proposed superposed chirp waveforms provides a broader energy-information transfer region over the transmission based on fixed-frequency waveform.

4.8 Summary

In this chapter, the application of chirp waveform is investigated for wireless energy and information transfer to a group of energy constrained sensors operating over multiple subbands. We have proposed a generic waveform design for WET based on the superposition of chirp waveforms while remaining orthogonal or uncorrelated across subbands, which is otherwise not feasible for fixed-frequency waveform. Further, key properties of such waveforms are established for optimizing WET. Packing multiple chirps in a subband enables to exploit channel diversity gain during DL-WET from a multi-antenna AP to the sensors, and has provided gain in harvested energy over fixed-frequency waveform while maintaining the peak power constraint. New closed form expressions are derived for the average energy harvested by the sensors on the DL based on the transmission of both superposed chirp waveforms and fixed-frequency waveform. The analysis has used order statistics and the performances are evaluated considering both estimated and perfect CSI. Moreover, the results have captured the

effects of subband selection, number of antennas at the AP and the number of sensors in the network. Corresponding max-min optimal power control coefficients are derived to maximize the minimum harvested energy and achieve fairness for DL energy among sensors for the two proposed transmission schemes. Firstly, with a fixed number of subbands and no peak power constraint, and secondly, with fixed peak power constraint and having variable subbands for which we have designed two subband selection algorithms. As a benchmark, associated results considering perfect CSI are also presented. The max-min information transmitted on the UL by the sensors is also analyzed.

From the analysis and simulations it is proved that DL-WET via superposed chirp waveforms provides considerable improvement in the max-min harvested energy at the sensor nodes compared to fixed-frequency waveform. Specifically, in case of an AP is equipped with limited antennas, the gains in harvested energy become large. The difference in performances for the average energy harvested by the sensors among estimated and perfect CSI has appeared to be negligibly small. It is shown that, by restricting the operational subbands, i.e., $\widetilde{N} < N$, the max-min harvested energy at the sensor nodes can be improved for both superposed chirp and fixed-frequency waveforms. For DL-WET scenario with fixed peak power and variable subbands, it has been observed that the proposed algorithms have achieved the desired output. Further, it is proved that the use of the superposed chirp waveforms improves the effective operational range of energy transfer over fixed-frequency waveform and thereby increases the ETE of the system. In comparison to other waveforms, the analysis indicates the proposed superposed chirp waveforms to be a superior choice for WET applications over multisine, fixed-frequency waveform in terms of harvested energy and associated gain. From the energy-information analysis for multisensor WEIT system, it can be concluded that superposed chirp waveforms achieve a broader energy-information transfer region over fixed-frequency waveform. Thus, using the presented superposed chirp waveforms in combination with the proposed transmission schemes in a multisensor WEIT system, it is possible to attain overall improvements in terms of harvested energy, operational span, and a wider energy-information transfer region compared to fixed-frequency waveform.

5

Conclusion and Future Work

Contents

The objective of the works that have been presented in this thesis is to design waveforms based on chirp and associated systems to enhance system performances for wireless communication, radar, IoT, and WEIT applications, for which we have proposed novel waveform designs by exploiting key properties of chirp and carried out performance evaluation of the systems through analytical and numerical analysis. The main conclusion and the contributions of this thesis are summarized in Section 5.1 and possible future directions in which this work can be extended are outlined in Section 5.2.

5.1 Conclusion

The main contributions and conclusions of each chapter are summarized below.

- A brief survey of chirp waveform and its properties, wireless communication and radar systems, IoT and WET, and metrics of performance analysis for the systems has been presented in Chapter 1 along with the motivation and contribution of the thesis. This chapter provides an in-depth review of related works available in the literature which includes designs based on chirp waveform for the applications of communication, radar, and IoT systems along with associated analysis of its performance followed by some of the existing works on WET and WEIT.

- Design of waveforms based on chirp and the systems employing the waveforms has been proposed in Chapter 2 for improving the data rate and error performance over a single user and multiuser wireless communication environments. The chapter includes the following studies.

  - Single user communication systems using SAW devices and employing fixed-frequency and chirp waveforms for a transmission of 2 bits and 3 bits per symbol, respectively, have been designed and analyzed. Closed-form expressions of SER have been derived for the proposed systems and the results have indicated that the SAW-chirp communication system performs better over the reported systems adapted for transmission of 3-bit data symbols.

  - The design of PN-coded LC and NLC waveforms has been presented to reduce the MAI in a multiuser communication. A dependency on the number of available users on the system performance has been observed from the results.

  - Design of LC waveforms with equal chirp rate has been studied, and an appropriate condition of orthogonality has been derived to attain a set of orthogonal up-chirp and a set of orthogonal down-chirp waveforms for a multiuser chirp communication system. Closed

form expressions of BER performance have been derived for which analytical analysis has been carried out to compute the correlation performance between the up-chirp and down-chirp waveforms. The studies over Rayleigh fading channel indicate that the system with the proposed waveforms has an improved MAI performance and performed better over reported work while using the same bandwidth.

- A combination of chirp-BOK waveform with PSK modulation has been proposed and a PSK-chirp-BOK system employing the waveform has been designed to double the transmission rate without increasing bandwidth and the number of correlators at the receiver, and thus saving valuable spectral resources. The performance of the system has been analyzed in terms of SEP considering a set of linear up-PSK and down-PSK chirps over a Nakagami-m channel in a multiuser environment and under the influence of co-channel interference. Associated closed-form expressions have been derived in terms of the confluent hypergeometric function. The derivation has involved the analysis for correlation performance between the up-PSK and down-PSK chirps and the PDF of a sum of random variables that are expressed in terms of Gauss hypergeometric function. To eliminate MAI, a set of complete orthogonal waveforms using up-chirps and segmented up-chirps has been proposed in place of the up-chirps and down-chirps in multiuser systems. The impact of different system parameters such as waveform type, number of users, channel conditions on system performance has been analyzed. The results show that the proposed orthogonal chirps combined with the modulation technique have provided considerable improvement in SER performance over the reported designs. Furthermore, a transmission scheme using TDM of the same chirp set has been proposed to attain bandwidth gain, and the demodulation of the overlapped chirps at the receiver has been presented through an FrFT based filtering process. It has been inferred from the results that the proposed filtering process has successfully removed the interfering chirps and the receiver performs as good as the system having orthogonal chirps without time overlap.

■ The designs of chirp waveforms for MIMO and multiuser radar systems have been proposed in Chapter 3 with the aim of improving the ASP and CCP levels over reported designs. Chirp waveform design has also been investigated for LEO satellite IoT applications. The chapter includes the following studies.

- A combination of LC waveform with binary PN-code sequence has been proposed for designing a set of DFCWs in which HFH sequences are used to control the frequency-firing order of the waveforms for MIMO and multiuser radar applications. Analytical evaluation of the auto-ambiguity and cross-ambiguity functions has been obtained to analyze the performance of the waveforms. Minimization of CCP levels among the waveforms has been achieved through an optimization process designed to select appropriate HFH sequences and PN-code sequences in two consecutive stages. The results have shown that the proposed design technique and the optimization process have provided better ASP and CCP level performance over existing DFCW-LC.
- To realize a chirp waveform with adaptive design parameters, for MIMO and multiuser radar, a parameterized mathematical model has been presented to construct parameterized NLC waveforms. A GA based optimization process for the appropriate selection of input parameters of NLC waveforms is presented to accomplish the required ASP and CCP levels. Associated numerical analysis of autocorrelation and cross-correlation for the parameterized NLC waveforms, for which we have derived analytical expressions, has proved that the proposed NLC waveforms through the optimization process attain the desired output with improved ASP and CCP performances over the existing designs while using fewer input variables. Construction of a set of DFCWs using a tangential-type NLC waveform, obtained from the model, has been presented, and a joint optimization of the frequency hopping sequences and the chirp type at each frequency slot of the DFCWs-NLC has been performed to minimize CCP levels among the DFCWs without degrading the ASP level. The analysis has been performed on a set of eight DFCWs and the results conclude that the proposed design can provide significant gain in ASP and CCP levels over the reported DFCW designs, i.e., an average gain of ≈ 5.0 dB and ≈ 5.47 dB in ASP and CCP levels while considering waveforms for MIMO radar, and an average gain of ≈ 4.51 dB and ≈ 4.41 dB in ASP and CCP levels while considering waveforms for multiuser radar.
- The concepts of SC waveform and multiple chirp rate waveform have been combined to propose SC-MCR for LEO satellite IoT communication. A generalized mathematical formulation has been presented for the construction of the waveforms, and the correlation analysis between the SC-MCR waveforms has indicated improved cross-correlation perfor-

mance over the SC waveform. In addition, extending SC-MCR in time domain, TDM-SC-MCS has been presented to increase the overall system data rate. Performance of an M-ary system has been analyzed in terms of SEP over an RLS channel in a multiuser environment and the results indicate that both SC-MCR and TDM-SC-MCR waveforms outperform SC waveforms and provide more reliable communication.

- Chapter 4 investigates the design of chirp waveforms for the application of WET and WEIT. We have illustrated and quantified the advantages offered by DL-WET from a multi-antenna AP to a group of sensors based on superposed chirp waveforms over that via fixed-frequency waveform with subband selection under imperfect CSI. Specifically, a generic waveform design has been proposed for WET based on the superposition of chirp waveforms and key properties of such waveforms for optimizing WET have been established. New mathematical expressions have also been derived using order statistics for the average energy harvested by the sensors when DL-WET is done via superposed chirps and via fixed-frequency waveform transmission. We have also derived the corresponding max-min optimal power control coefficients to maximize the minimum harvested energy in the sensor network. As a benchmark, results have been presented considering perfect CSI also. The max-min information transmitted on the UL by the sensors has also been analyzed. From the results, it has been proved that DL-WET via superposed chirp waveforms provides considerable improvement in the max-min harvested energy and the operational range of energy transfer and achieves a broader energy-information transfer region over DL-WET via fixed-frequency waveform. Thus, the designed superposed chirp waveforms in combination with the proposed transmission scheme can effectively prolong the operational span of the energy constrained sensor nodes over conventional fixed-frequency waveform based transmission.

5.2 Scopes of Future Extension of the Works

Some of the possible future research directions of the works listed in this thesis, i.e., design and application of chirp waveform in the areas of communication, radar, and WET, are as follows:

(1) Investigation on possible designs of chirp waveform for a joint radar-communication system, and analyze the effect of interference on the system performance.

(2) The WEIT analysis in Chapter 4 is presented over Rayleigh fading. The analysis can further be extended considering Rician fading channel. Additionally, the outage performance analysis of the system would be an interesting problem to solve.

(3) The WEIT system in Chapter 4 has considered a linear energy harvesting model. The analysis of the system can be extended by incorporating a nonlinear energy harvesting model, and its effect on the average harvested energy, energy-information transfer region can be investigated.

(4) The WEIT system has considered the transfer of information in the uplink only. The system design can be extended considering simultaneous transmission of energy and information on the downlink and the associated analysis can be performed considering a PS or TS scheme at the sensor nodes. Moreover, the effect of subband selection on these schemes would be worth exploring.

(5) A WEIT system with homogeneous users has been considered in this thesis. The system can be generalized by incorporating heterogeneous users where the main challenge would be to explore efficient interference cancellation schemes at the user ends such that both information and energy transfer efficiency can be maximized.

(6) The WEIT system has considered a single multiantenna AP. The system model and analysis can be extended by incorporating intelligent reflecting surface (IRS) for WET and WEIT operations. In addition, the performance of such system with or without subband selection can further be investigated.

A

Appendix

Contents

A.1 Proof of Lemma 1

A chirp signal $s_{c_n}(t) = \cos\left[2\pi\left(\left(f_s + (n-1)\Delta f\right)t + \frac{1}{2}\mu t^2\right)\right]$ in equivalent complex form is given by $s_{c_n}(t) = \Re\left[e^{j2\pi\left(\left(f_s+(n-1)\Delta f\right)t+\frac{1}{2}\mu t^2\right)}\right]$. Without loss of generality, the proof is given for $\xi = 3$, and the corresponding chirp signals based on (4.3) are given as

$$
\begin{aligned}
s_{c1_{n,k}}(t) &= \cos\left[2\pi\left(\left(f_s + (n-1)\Delta f\right)t + \frac{1}{2}\mu t^2\right)\right], \quad 0 \le t \le T_c \\
s_{c2_{n,k}}(t) &= \begin{cases} \cos\left[2\pi\left(\left(f_s + \frac{B}{3} + (n-1)\Delta f\right)t + \frac{1}{2}\mu t^2\right)\right], & 0 \le t \le \frac{2T_c}{3}, \\ \cos\left[2\pi\left(\left(f_s - \frac{2B}{3} + (n-1)\Delta f\right)t + \frac{1}{2}\mu t^2\right)\right], & \frac{2T_c}{3} < t \le T_c, \end{cases} \\
s_{c3_{n,k}}(t) &= \begin{cases} \cos\left[2\pi\left(\left(f_s + \frac{2B}{3} + (n-1)\Delta f\right)t + \frac{1}{2}\mu t^2\right)\right], & 0 \le t \le \frac{T_c}{3}, \\ \cos\left[2\pi\left(\left(f_s - \frac{B}{3} + (n-1)\Delta f\right)t + \frac{1}{2}\mu t^2\right)\right], & \frac{T_c}{3} < t \le T_c. \end{cases}
\end{aligned} \tag{A.1}
$$

The L.H.S. of (4.4) is calculated using (A.1) as

$$
\int_0^{T_c}\left(s_{c1_{n,k}}(t) + s_{c2_{n,k}}(t) + s_{c3_{n,k}}(t)\right)^2 dt = \int_0^{T_c}\left(s^2_{c1_{n,k}}(t) + s^2_{c2_{n,k}}(t) + s^2_{c3_{n,k}}(t) + 2R_{c1c2c3}(t)\right)dt, \tag{A.2}
$$

where $R_{c1c2c3}(t) = s_{c2_{n,k}}(t)s_{c1_{n,k}}(t) + s_{c3_{n,k}}(t)s_{c2_{n,k}}(t) + s_{c3_{n,k}}(t)s_{c1_{n,k}}(t)$. For the chirps to remain uncorrelated to each other, $R_{c1c2c3}(t)$ should be zero. Now, substituting every term of $R_{c1c2c3}(t)$ using (A.1), in equivalent complex form, and after simplification we obtain

$$
\begin{aligned}
R_{c1c2c3}(t) &= \int_0^{\frac{T_c}{3}} \Re\left[e^{j2\pi\frac{B}{3}t} + e^{j2\pi\frac{B}{3}t} + e^{j2\pi\frac{2B}{3}t}\right]dt + \int_{\frac{T_c}{3}}^{\frac{2T_c}{3}} \Re\left[e^{j2\pi\frac{B}{3}t} + e^{-j2\pi\frac{2B}{3}t} + e^{-j2\pi\frac{B}{3}t}\right]dt \\
&\quad + \int_{\frac{2T_c}{3}}^{T_c} \Re\left[e^{-j2\pi\frac{2B}{3}t} + e^{j2\pi\frac{B}{3}t} + e^{-j2\pi\frac{B}{3}t}\right]dt \\
&= \int_0^{\frac{T_c}{3}} \left(2\cos\left(2\pi B\frac{t}{3}\right) + \cos\left(4\pi B\frac{t}{3}\right)\right)dt + \int_{\frac{T_c}{3}}^{T_c} \left(\cos\left(4\pi B\frac{t}{3}\right) + 2\cos\left(2\pi B\frac{t}{3}\right)\right)dt \\
&= 2\frac{\sin\left(\frac{2\pi}{3}\right)}{2\pi\frac{B}{3}} + \frac{\sin\left(\frac{4\pi}{3}\right)}{2\pi\frac{2B}{3}} - \frac{\sin\left(\frac{4\pi}{3}\right)}{2\pi\frac{2B}{3}} - 2\frac{\sin\left(\frac{2\pi}{3}\right)}{2\pi\frac{B}{3}} = 0.
\end{aligned} \tag{A.3}
$$

As $R_{c1c2c3}(t) = 0$, the superposed chirp waveforms, designed based on (4.3) exhibit zero cross-correlation among them and satisfy the relation given in (4.4). In a similar process, (4.4) can be proved for other values of ξ, i.e., all the chirps in a 'ξ-chirp' configuration, designed using (4.3), as a composite signal remain uncorrelated.

A.2 Proof of Lemma 2

Without loss of generality, the proof is given for $\xi = 3$. Expanding the L.H.S. of (4.5) gives

$$\int_0^{T_c} S_{c_{m,k}}(t) S_{c_{n,k}}(t) dt = \int_0^{T_c} \left(s_{c1_{m,k}}(t) + s_{c2_{m,k}}(t) + s_{c3_{m,k}}(t)\right)\left(s_{c1_{n,k}}(t) + s_{c2_{n,k}}(t) + s_{c3_{n,k}}(t)\right) dt \tag{A.4}$$

Substituting the terms using (4.3) in equivalent complex form, and after simplification, the R.H.S. of (A.4) can be evaluated as

$$\begin{aligned}
&\int_0^{T_c} S_{c_{m,k}}(t) S_{c_{n,k}}(t) dt \\
&= 3\int_0^{T_c} \Re\left[e^{j2\pi(m-n)t}\right] dt + 2\int_0^{T_c} \Re\left[e^{j2\pi\left(-\frac{B}{3}+(m-n)\Delta f\right)t}\right] dt + 2\int_0^{T_c} \Re\left[e^{j2\pi\left(\frac{B}{3}+(m-n)\Delta f\right)t}\right] dt \\
&\quad + \int_0^{T_c} \Re\left[e^{j2\pi\left(\frac{2B}{3}+(m-n)\Delta f\right)t}\right] dt + \int_0^{T_c} \Re\left[e^{j2\pi\left(-\frac{2B}{3}+(m-n)\Delta f\right)t}\right] dt \\
&= 3\int_0^{T_c} \cos\left[2\pi r t\right] dt + 2\int_0^{T_c} \cos\left[2\pi\left(-\frac{B}{3}+r\Delta f\right)t\right] dt + \int_0^{T_c} \cos\left[2\pi\left(-\frac{2B}{3}+r\Delta f\right)t\right] dt \\
&\quad + 2\int_0^{T_c} \cos\left[2\pi\left(\frac{B}{3}+r\Delta f\right)t\right] + \cos\left[2\pi\left(\frac{2B}{3}+r\Delta f\right)t\right] dt \\
&= \frac{1}{2\pi}\left[\frac{3\sin(6\pi)}{\Delta f} + \frac{2\sin(4\pi)}{\left(-\frac{B}{3}+\Delta f\right)} + \frac{2\sin(8\pi)}{\left(\frac{B}{3}+\Delta f\right)} + \frac{\sin(10\pi)}{\left(\frac{2B}{3}+\Delta f\right)} + \frac{\sin(2\pi)}{\left(-\frac{2B}{3}+\Delta f\right)}\right] = 0,
\end{aligned} \tag{A.5}$$

where $|m-n| = r > 0$ and an integer. Also, $\min(r) = 1$. From (A.5), it is found that the superposed chirp waveforms, designed using (4.3), transmitted in different subbands remain mutually orthogonal. Based on similar arguments, the relation in (4.5) can be proved for other values of ξ.

A.3 Proof of $\sum_{k=1}^{K} \eta_{\mathbf{c}_k} \leq 1$ for $\widetilde{N}$ mod $\xi = 0$

For each sensor the transmitted signals in different subbands are mutually orthogonal and using (4.17) the average transmit power of the AP, for $\widetilde{N}$ mod $\xi = 0$, is given by

$$\sum_{n=1}^{N} \mathbb{E}\left\{\left\|\mathbf{x}_{c_n}(t)\right\|^2\right\} = \frac{1}{T_c} P_{tx} \int_0^{T_c} \mathbb{E}\left\{\left\|\sum_{k=1}^{K}\sum_{n=1}^{N} \sqrt{\frac{\eta_{c_k}}{\widetilde{N}}} \frac{\widehat{\mathbf{g}}_{n,k}^*}{\left\|\widehat{\mathbf{g}}_{n,k}\right\|} S_{c_{n,k}}(t) \delta_{\{n,k\}\in\Xi_{c_k}}\right\|^2\right\} dt, \tag{A.6}$$

where the expectation above is with respect to the estimated channel vector $\widehat{\mathbf{g}}_{n,k}$. For each sensor, the signal is transmitted over its best $\widetilde{N}_c$ subbands only where $\widetilde{N}_c = \frac{\widetilde{N}}{\xi}$. Therefore, rearranging the inner summation term according to the indices corresponding to the $\widetilde{N}_c$ best subbands for each sensor,

(A.6) can be expressed as

$$\sum_{n=1}^{N}\mathbb{E}\left\{\left\|\mathbf{x}_{\mathrm{c}_n}(t)\right\|^2\right\}=P_{\mathrm{tx}}\sum_{k=1}^{K}\sum_{n=1}^{\widetilde{N}_{\mathrm{c}}}\mathbb{E}\left\{\frac{\eta_{\mathrm{c}_k}}{\widetilde{N}}\left\|\frac{\widehat{\mathbf{g}}^*_{[n],k}}{\left\|\widehat{\mathbf{g}}_{[n],k}\right\|}\right\|^2\right\}\times\left[\frac{1}{T_{\mathrm{c}}}\int_0^{T_{\mathrm{c}}}\left(s'^2_{\mathrm{c}1_{[n],k}}(t)+s'^2_{\mathrm{c}2_{[n],k}}(t)+\cdots+s'^2_{\mathrm{c}\xi_{[n],k}}(t)\right)dt\right],\quad(\mathrm{A.7})$$

where the chirps in a subband are uncorrelated as given by Lemma 1 and are deterministic. Since each chirp waveform maintains an average power of unity, (A.7) simplifies to

$$\sum_{n=1}^{N}\mathbb{E}\left\{\left\|\mathbf{x}_{\mathrm{c}_n}(t)\right\|^2\right\}=P_{\mathrm{tx}}\sum_{k=1}^{K}\frac{\eta_{\mathrm{c}_k}}{\widetilde{N}}\sum_{n=1}^{\widetilde{N}_{\mathrm{c}}}\mathbb{E}\left\{\frac{\left\|\widehat{\mathbf{g}}_{[n],k}\right\|^2}{\left\|\widehat{\mathbf{g}}_{[n],k}\right\|^2}\right\}\xi=P_{\mathrm{tx}}\sum_{k=1}^{K}\frac{\eta_{\mathrm{c}_k}}{\widetilde{N}}\widetilde{N}_{\mathrm{c}}\xi=P_{\mathrm{tx}}\sum_{k=1}^{K}\eta_{\mathrm{c}_k}\leq P_{\mathrm{tx}}.\quad(\mathrm{A.8})$$

As the total transmit power is constrained to P_{tx}, from (A.8) we have $\sum_{k=1}^{K}\eta_{\mathrm{c}_k}\leq 1$.

A.4 Proof of $\sum_{k=1}^{K}\eta_{\mathrm{c}_k}\leq 1$ for $\widetilde{N}$ mod $\xi\neq 0$

The average transmit power from the AP for $\widetilde{N}$ mod $\xi\neq 0$ is given using (4.18) as

$$\sum_{n=1}^{N}\mathbb{E}\left\{\left\|\mathbf{x}_{\mathrm{c}_n}(t)\right\|^2\right\}=\frac{1}{T_{\mathrm{c}}}P_{\mathrm{tx}}\int_0^{T_{\mathrm{c}}}\mathbb{E}\left\{\left\|\sum_{k=1}^{K}\sum_{n=1}^{N}\sqrt{\frac{\eta_{\mathrm{c}_k}}{\widetilde{N}}}\frac{\widehat{\mathbf{g}}^*_{n,k}}{\left\|\widehat{\mathbf{g}}_{n,k}\right\|}S_{\mathrm{c}_{n,k}}(t)\delta_{\{n,k\}\in\Xi_{\mathrm{c}_k}}\delta_{\{n,k\}\in\Xi^{\widetilde{N}_{\mathrm{c}}}_{\mathrm{c}_k}}\right\|^2\right\}dt\quad(\mathrm{A.9})$$

where the expectation above is with respect to $\widehat{\mathbf{g}}_{n,k}$. For each sensor, the signal is transmitted over its best $\widetilde{N}_{\mathrm{c}}$ subbands only where $\widetilde{N}_{\mathrm{c}}=\left\lfloor\frac{\widetilde{N}}{\xi}\right\rfloor+1$, and the transmitted signals in different subbands are mutually orthogonal. Therefore, rearranging the inner summation term according to the indices corresponding to the $\widetilde{N}_{\mathrm{c}}$ best subbands for each sensor, (A.9) can be expressed using (A.7) as

$$\sum_{n=1}^{N}\mathbb{E}\left\{\left\|\mathbf{x}_{\mathrm{c}_n}(t)\right\|^2\right\}=P_{\mathrm{tx}}\sum_{k=1}^{K}\sum_{n=1}^{\widetilde{N}_{\mathrm{c}}-1}\mathbb{E}\left\{\frac{\eta_{\mathrm{c}_k}}{\widetilde{N}}\left\|\frac{\widehat{\mathbf{g}}^*_{[n],k}}{\left\|\widehat{\mathbf{g}}_{[n],k}\right\|}\right\|^2\right\}\left[\frac{1}{T_{\mathrm{c}}}\int_0^{T_{\mathrm{c}}}S^2_{\mathrm{c}_{[n],k}}(t)dt\right]+P_{\mathrm{tx}}\sum_{k=1}^{K}\mathbb{E}\left\{\frac{\eta_{\mathrm{c}_k}}{\widetilde{N}}\left\|\frac{\widehat{\mathbf{g}}^*_{[\widetilde{N}_{\mathrm{c}}],k}}{\left\|\widehat{\mathbf{g}}_{[\widetilde{N}_{\mathrm{c}}],k}\right\|}\right\|^2\right\}\left[\frac{1}{T_{\mathrm{c}}}\int_0^{T_{\mathrm{c}}}\alpha^2S^2_{\mathrm{c}_{[\widetilde{N}_{\mathrm{c}}],k}}(t)dt\right].\quad(\mathrm{A.10})$$

Since the chirps in a subband are uncorrelated as given by Lemma 1 and deterministic, and each chirp waveform maintains an average power of unity, using (A.7) and (A.8), (A.10) can be simplified as

$$\begin{aligned}\sum_{n=1}^{N}\mathbb{E}\left\{\left\|\mathbf{x}_{\mathrm{c}_n}(t)\right\|^2\right\}&=P_{\mathrm{tx}}\sum_{k=1}^{K}\frac{\eta_{\mathrm{c}_k}}{\widetilde{N}}\left[\sum_{n=1}^{\widetilde{N}_{\mathrm{c}}-1}\mathbb{E}\left\{\frac{\left\|\widehat{\mathbf{g}}_{[n],k}\right\|^2}{\left\|\widehat{\mathbf{g}}_{[n],k}\right\|^2}\right\}\xi+\alpha^2\mathbb{E}\left\{\frac{\left\|\widehat{\mathbf{g}}_{[\widetilde{N}_{\mathrm{c}}],k}\right\|^2}{\left\|\widehat{\mathbf{g}}_{[\widetilde{N}_{\mathrm{c}}],k}\right\|^2}\right\}\xi\right]\\&=P_{\mathrm{tx}}\sum_{k=1}^{K}\frac{\eta_{\mathrm{c}_k}}{\widetilde{N}}\left[\left(\widetilde{N}_{\mathrm{c}}-1\right)\xi+\left(\frac{\widetilde{N}-\left\lfloor\frac{\widetilde{N}}{\xi}\right\rfloor\xi}{\xi}\right)\xi\right]=P_{\mathrm{tx}}\sum_{k=1}^{K}\eta_{\mathrm{c}_k}\leq P_{\mathrm{tx}}.\end{aligned}\quad(\mathrm{A.11})$$

As the total transmit power is constrained to P_{tx}, from (A.11) we have $\sum_{k=1}^{K} \eta_{\text{c}_k} \leq 1$.

A.5 Proof of Theorem 1

In order to compute the average energy $\overline{E}_{\text{c}_k}$ harvested by the k^{th} sensor, simplifications of the three terms in (4.27) and the four terms in (4.28) are performed in Appendix A.5.1 and in Appendix A.5.2, respectively to obtain the closed-form solutions. Further, results on order statistics to be used for the analysis of (4.27) and (4.28) are derived here.

Consider that $X_1, X_2, \ldots, X_N$ are random samples from a continuous population with corresponding CDF $F_X(x)$ and PDF $f_X(x)$. Now, if $X_{[1]} \geqslant X_{[2]} \geqslant \ldots \geqslant X_{[N]}$, then using [93, Ch. 2] on order statistics, the CDF of the n^{th} largest random variable, $n = 1, 2, \ldots, N$, can be evaluated as

$$F_{X_{[n]}}(x) = \sum_{v=0}^{n-1} \binom{N}{v} \left(1 - F_{X_n}(x)\right)^v \left(F_{X_n}(x)\right)^{N-v}, \tag{A.12}$$

and the associated PDF of the n^{th} largest random $X_{[n]}$, $f_{X_{[n]}}(x)$ is calculated using (A.12) as

$$\begin{aligned} f_{X_{[n]}}(x) = &\binom{N}{n-1} (N - (n-1)) \left(F_X(x)\right)^{N-(n-1)-1} \left(1 - F_X(x)\right)^{n-1} f_X(x) \\ &+ \left[\sum_{v=0}^{n-2} \binom{N}{v} (N - v) - \sum_{v=0}^{n-2} \binom{N}{v+1} (v+1)\right] \left(F_X(x)\right)^{N-v-1} \left(1 - F_X(x)\right)^v f_X(x). \end{aligned} \tag{A.13}$$

In the second term of (A.13) $\binom{N}{v}(N - v) = \binom{N}{v+1}(v+1)$, thereby $f_{X_{[n]}}(x)$ simplifies to

$$f_{X_{[n]}}(x) = \frac{N!}{(n-1)!(N-n)!} \left(F_X(x)\right)^{N-n} \left(1 - F_X(x)\right)^{n-1} f_X(x). \tag{A.14}$$

A.5.1 Proof for Case (i)

Using (4.10), we have $\mathbf{g}_{[n],k} = \widehat{\mathbf{g}}_{[n],k} - \widetilde{\mathbf{g}}_{[n],k}$, where $\widehat{\mathbf{g}}_{[n],k} = \sqrt{\gamma_k}\widehat{\mathbf{h}}_{[n],k}$ and $\widetilde{\mathbf{g}}_{[n],k} = \sqrt{\beta_k - \gamma_k}\widetilde{\mathbf{h}}_{[n],k}$. Now, to compute the average energy $\overline{E}_{\text{c}_k}$ harvested by the k^{th} sensor given by (4.27) for $\widetilde{N} \bmod \xi = 0$, the first term from (4.27) is expressed as

$$\begin{aligned} \text{Term I} &= \frac{\eta_{\text{c}_k} \psi P_{\text{tx}} \xi T_{\text{c}}}{\widetilde{N}} \sum_{n=1}^{\widetilde{N}_{\text{c}}} \left[\mathbb{E}\left\{\frac{\widehat{\mathbf{g}}_{[n],k}^{\text{T}} \left(\widehat{\mathbf{g}}_{[n],k}^{*} \widehat{\mathbf{g}}_{[n],k}^{\text{T}}\right) \widehat{\mathbf{g}}_{[n],k}^{*}}{\left\|\widehat{\mathbf{g}}_{[n],k}\right\|^2}\right\} + \mathbb{E}\left\{\frac{\widehat{\mathbf{g}}_{[n],k}^{\text{T}} \left(\widetilde{\mathbf{g}}_{[n],k}^{*} \widetilde{\mathbf{g}}_{[n],k}^{\text{T}}\right) \widehat{\mathbf{g}}_{[n],k}^{*}}{\left\|\widehat{\mathbf{g}}_{[n],k}\right\|^2}\right\}\right] \\ &= \frac{\eta_{\text{c}_k} \psi P_{\text{tx}} \xi T_{\text{c}}}{\widetilde{N}} \left[\sum_{n=1}^{\widetilde{N}_{\text{c}}} \mathbb{E}\left\{\left\|\widehat{\mathbf{g}}_{[n],k}\right\|^2\right\} + \sum_{n=1}^{\widetilde{N}_{\text{c}}} \mathbb{E}\left\{\frac{\widehat{\mathbf{g}}_{[n],k}^{\text{T}} \left(\widetilde{\mathbf{g}}_{[n],k}^{*} \widetilde{\mathbf{g}}_{[n],k}^{\text{T}}\right) \widehat{\mathbf{g}}_{[n],k}^{*}}{\left\|\widehat{\mathbf{g}}_{[n],k}\right\|^2}\right\}\right] \\ &= \frac{\eta_{\text{c}_k} \psi P_{\text{tx}} \xi T_{\text{c}}}{\widetilde{N}} \left[\gamma_k \left(\sum_{n=1}^{\widetilde{N}_{\text{c}}} \mathbb{E}\left\{\left\|\widehat{\mathbf{h}}_{[n],k}\right\|^2\right\}\right) + \sum_{n=1}^{\widetilde{N}_{\text{c}}} \mathbb{E}\left\{\frac{\widehat{\mathbf{g}}_{[n],k}^{\text{T}} \left(\widetilde{\mathbf{g}}_{[n],k}^{*} \widetilde{\mathbf{g}}_{[n],k}^{\text{T}}\right) \widehat{\mathbf{g}}_{[n],k}^{*}}{\left\|\widehat{\mathbf{g}}_{[n],k}\right\|^2}\right\}\right]. \end{aligned} \tag{A.15}$$

From (A.15), the squared norm of $\widehat{\mathbf{h}}_{n,k}$ is given by

$$\left\|\widehat{\mathbf{h}}_{n,k}\right\|^2 = \left|\widehat{h}^1_{n,k}\right|^2 + \left|\widehat{h}^2_{n,k}\right|^2 + \ldots + \left|\widehat{h}^M_{n,k}\right|^2, \tag{A.16}$$

where $\widehat{h}^m_{n,k}$ is CSCG random variable and $\left|\widehat{h}^m_{n,k}\right|^2$ is exponential distributed with parameter 1, i.e., $\left|\widehat{h}^m_{n,k}\right|^2 \sim \exp(1)$. Let $X_{n,k} = \left\|\widehat{\mathbf{h}}_{n,k}\right\|^2$. Since $X_{n,k}$ is the sum of M independent exponential random variables, $X_{n,k}$ is a Gamma random variable with shape parameter M and rate parameter 1, i.e., $X_{n,k} \sim \Gamma(M,1)$. The CDF and the PDF of $X_{n,k}$ are respectively given by [84]

$$\begin{aligned} F_{X_{n,k}}(x_{n,k}) &= \frac{\gamma(M, x_{n,k})}{\Gamma(M)}, \\ f_{X_{n,k}}(x_{n,k}) &= \frac{1}{\Gamma(M)} {x_{n,k}}^{M-1} e^{-x_{n,k}}, \quad x_{n,k} > 0,\ M > 0, \end{aligned} \tag{A.17}$$

where $\gamma(\cdot,\cdot)$ is lower incomplete gamma function [78].

Now, using (A.14) and (A.15), $\mathbb{E}\left\{\left\|\widehat{\mathbf{h}}_{[n],k}\right\|^2\right\}$ can be written as

$$\mathbb{E}\left\{\left\|\widehat{\mathbf{h}}_{[n],k}\right\|^2\right\} = \mathbb{E}\left\{X_{[n],k}\right\} = \int_0^\infty x_{n,k} f_{X_{[n],k}}(x_{n,k})\, dx_{n,k}. \tag{A.18}$$

Note that the PDF $f_{X_{[n],k}}(x_{n,k})$ depends on $F_{X_{n,k}}(x_{n,k})$ and $f_{X_{n,k}}(x_{n,k})$ which, in our case, is given by (A.17). Thus, substituting (A.14) and (A.17) in (A.18), $\mathbb{E}\left\{\left\|\widehat{\mathbf{h}}_{[n],k}\right\|^2\right\}$ is evaluated as

$$\begin{aligned} \mathbb{E}\left\{\left\|\widehat{\mathbf{h}}_{[n],k}\right\|^2\right\} &= \frac{N!}{(n-1)!(N-n)!} \int_0^\infty \left(\frac{\gamma(M,x_{n,k})}{\Gamma(M)}\right)^{N-n} \left(1 - \frac{\gamma(M,x_{n,k})}{\Gamma(M)}\right)^{n-1} \frac{{x_{n,k}}^M}{\Gamma(M)} e^{-x_{n,k}} dx_{n,k} \\ &= \frac{N!}{(n-1)!(N-n)!} \sum_{l=0}^{n-1} (-1)^l \binom{n-1}{l} (\Gamma(M))^{n-N-l-1} \int_0^\infty {x_{n,k}}^M e^{-x_{n,k}} \left(\gamma(M,x_{n,k})\right)^{l+N-n} dx_{n,k} \\ &= \frac{N!}{(n-1)!(N-n)!} \sum_{l=0}^{n-1} (-1)^l \binom{n-1}{l} (\Gamma(M))^{n-N-l-1} \Lambda(l), \end{aligned} \tag{A.19}$$

where $\Lambda(l)$ can be expressed using Lauricella function of type A [91, (7)] as in (4.32). This is used to compute $\Omega^{\widetilde{N}_c}_{c_k} = \sum_{n=1}^{\widetilde{N}_c} \mathbb{E}\left\{\left\|\widehat{\mathbf{h}}_{[n],k}\right\|^2\right\}$ in (A.15) and is given in closed-form in (4.31).

From (A.15), $\mathbb{E}\left\{\widetilde{\mathbf{g}}^*_{[n],k}\widetilde{\mathbf{g}}^{\mathrm{T}}_{[n],k}\right\}$ is expressed as

$$\mathbb{E}\left\{\widetilde{\mathbf{g}}^*_{[n],k}\widetilde{\mathbf{g}}^{\mathrm{T}}_{[n],k}\right\} = (\beta_k - \gamma_k)\, \mathbb{E}\left\{\mathrm{diag}\left\{\left|\widetilde{h}^1_{[n],k}\right|^2, \left|\widetilde{h}^2_{[n],k}\right|^2, \ldots, \left|\widetilde{h}^M_{[n],k}\right|^2\right\}\right\}. \tag{A.20}$$

Furthermore, using (A.14) and (A.18), $\mathbb{E}\left\{\left|\widetilde{h}_{[n],k}\right|^2\right\}$ is evaluated as

$$\begin{aligned}\mathbb{E}\left\{\left|\widetilde{h}_{[n],k}\right|^2\right\} &= \frac{N!}{(n-1)!(N-n)!}\int_0^\infty x_{n,k}\left(1-e^{-x_{n,k}}\right)^{N-n}\left(e^{-x_{n,k}}\right)^{n-1}e^{-x_{n,k}}dx_{n,k}\\ &= \frac{N!}{(n-1)!(N-n)!}\int_0^\infty x_{n,k}\left(e^{-x_{n,k}}\right)^{n}\left(1-e^{-x_{n,k}}\right)^{N-n}dx_{n,k}\\ &= \frac{N!}{(n-1)!(N-n)!}\sum_{l=0}^{N-n}(-1)^{N-n+l}\binom{N-n}{l}\frac{1}{(N-l)^2},\end{aligned} \tag{A.21}$$

where the integral above is evaluated using [78, (3.432.1)]. Let $\Upsilon_{[n],k} = \mathbb{E}\left\{\left|\widetilde{h}_{[n],k}\right|^2\right\}$. Substituting (A.21) in (A.20), (A.15) can be simplified as

$$\text{Term I} = \frac{\eta_{\mathrm{c}_k}\psi P_{\mathrm{tx}}\xi T_{\mathrm{c}}}{\widetilde{N}}\left[\gamma_k\Omega_{\mathrm{c}_k}^{\widetilde{N}_{\mathrm{c}}} + \sum_{n=1}^{\widetilde{N}_{\mathrm{c}}}(\beta_k-\gamma_k)\,\Upsilon_{[n],k}\right] = \frac{\eta_{\mathrm{c}_k}\psi P_{\mathrm{tx}}\xi T_{\mathrm{c}}}{\widetilde{N}}\left[\gamma_k\Omega_{\mathrm{c}_k}^{\widetilde{N}_{\mathrm{c}}} + (\beta_k-\gamma_k)\,\Upsilon_{\mathrm{c}_k}^{\widetilde{N}_{\mathrm{c}}}\right], \tag{A.22}$$

where $\Upsilon_{\mathrm{c}_k}^{\widetilde{N}_{\mathrm{c}}} = \sum_{n=1}^{\widetilde{N}_{\mathrm{c}}}\Upsilon_{[n],k}$ is given in (4.30).

Next, expanding the second term of (4.27) gives

$$\begin{aligned}\text{Term II} = &\underbrace{\psi P_{\mathrm{tx}}\xi T_{\mathrm{c}}\sum_{n=1}^{\widetilde{N}_{\mathrm{c}}}\sum_{i=j=1;i,j\neq k}^{K}\frac{\eta_{\mathrm{c}_i}}{\widetilde{N}}\mathbb{E}\left\{\frac{\widehat{\mathbf{g}}_{[n],i}^{\mathrm{T}}\left(\mathbf{g}_{\{[n],i\},k}^{*}\mathbf{g}_{\{[n],i\},k}^{\mathrm{T}}\right)\widehat{\mathbf{g}}_{[n],i}^{*}}{\left\|\widehat{\mathbf{g}}_{[n],i}\right\|^2}\right\}}_{\mathrm{R1}}\\ &+\underbrace{\psi P_{\mathrm{tx}}\xi T_{\mathrm{c}}\sum_{n=1}^{\widetilde{N}_{\mathrm{c}}}\sum_{i=1;i\neq k}^{K}\sum_{j=1;j\neq i,k}^{K}\frac{\sqrt{\eta_{\mathrm{c}_i}\eta_{\mathrm{c}_j}}}{\widetilde{N}}\mathbb{E}\left\{\frac{\widehat{\mathbf{g}}_{[n],i}^{\mathrm{T}}\left(\mathbf{g}_{\{[n],i\},k}^{*}\mathbf{g}_{\{[n],j\},k}^{\mathrm{T}}\right)\widehat{\mathbf{g}}_{[n],j}^{*}}{\left\|\widehat{\mathbf{g}}_{[n],i}\right\|\left\|\widehat{\mathbf{g}}_{[n],j}\right\|}\right\}}_{\mathrm{R2}}.\end{aligned} \tag{A.23}$$

All channel realizations are independent to each other and the ordered subbands for i^{th} user is not the same as that of the ordered subbands for k^{th} user. Thus, $\{[n],i\},k$ can be any arbitrary subband $\{[n],i\} \in \{1,2,\ldots,N\}$ for the k^{th} user and for term II, $\mathbb{E}\left\{\mathbf{g}_{\{[n],i\},k}^{*}\mathbf{g}_{\{[n],i\},k}^{\mathrm{T}}\right\} = \beta_k\mathbf{I}_M$. Using this result, R1 simplifies to

$$\begin{aligned}\mathrm{R1} &= \psi P_{\mathrm{tx}}\xi T_{\mathrm{c}}\sum_{n=1}^{\widetilde{N}_{\mathrm{c}}}\sum_{i=1;i\neq k}^{K}\frac{\eta_{\mathrm{c}_i}}{\widetilde{N}}\mathbb{E}\left\{\frac{\widehat{\mathbf{g}}_{[n],i}^{\mathrm{T}}\left(\beta_k\mathbf{I}_M\right)\widehat{\mathbf{g}}_{[n],i}^{*}}{\left\|\widehat{\mathbf{g}}_{[n],i}\right\|^2}\right\}\\ &= \frac{\psi P_{\mathrm{tx}}\xi\beta_k T_{\mathrm{c}}}{\widetilde{N}}\widetilde{N}_{\mathrm{c}}\sum_{i=1;i\neq k}^{K}\eta_{\mathrm{c}_i} = \psi P_{\mathrm{tx}}\beta_k T_{\mathrm{c}}\left(1-\eta_{\mathrm{c}_k}\right),\end{aligned} \tag{A.24}$$

where $\sum_{i=1}^{K}\eta_{\mathrm{c}_i} = 1$. For the term R2, there exist two scenarios as outlined next.

Scenario 1: If $\{[n],i\}=\{[n],j\}=l$, then using (A.24)

$$\mathrm{R2}=\psi P_{\mathrm{tx}}\xi T_{\mathrm{c}}\sum_{n=1}^{\widetilde{N}_{\mathrm{c}}}\sum_{i=1;i\neq k}^{K}\sum_{j=1;j\neq i,k}^{K}\frac{\sqrt{\eta_{\mathrm{c}_i}\eta_{\mathrm{c}_j}}}{\widetilde{N}}\mathbb{E}\left\{\frac{\widehat{\mathbf{g}}_{[n],i}^{\mathrm{T}}\left(\mathbf{g}_{l,k}^{*}\mathbf{g}_{l,k}^{\mathrm{T}}\right)\widehat{\mathbf{g}}_{[n],j}^{*}}{\left\|\widehat{\mathbf{g}}_{[n],i}\right\|\left\|\widehat{\mathbf{g}}_{[n],j}\right\|}\right\}$$
$$=\psi P_{\mathrm{tx}}\xi\beta_k T_{\mathrm{c}}\sum_{n=1}^{\widetilde{N}_{\mathrm{c}}}\sum_{i=1;i\neq k}^{K}\sum_{j=1;j\neq i,k}^{K}\frac{\sqrt{\eta_{\mathrm{c}_i}\eta_{\mathrm{c}_j}}}{\widetilde{N}}\mathbb{E}\left\{\frac{\widehat{\mathbf{g}}_{[n],i}^{\mathrm{T}}\widehat{\mathbf{g}}_{[n],j}^{*}}{\left\|\widehat{\mathbf{g}}_{[n],i}\right\|\left\|\widehat{\mathbf{g}}_{[n],j}\right\|}\right\}=0, \tag{A.25}$$

where the last line is obtained from the facts that the index of the n^{th} best subband of the i^{th} user may be different from the index of the n^{th} best subband of the j^{th} user and that the channels corresponding to different users are independent, thus $\mathbb{E}\left\{\widehat{\mathbf{g}}_{[n],i}^{\mathrm{T}}\widehat{\mathbf{g}}_{[n],j}^{*}\right\}=0$.

Scenario 2: If $\{[n],i\}\neq\{[n],j\}$

As all the channels are independent, $\mathbb{E}\left\{\mathbf{g}_{\{[n],i\},k}^{*}\mathbf{g}_{\{[n],j\},k}^{\mathrm{T}}\right\}=0$, and

$$\mathrm{R2}=\psi P_{\mathrm{tx}}\xi T_{\mathrm{c}}\sum_{n=1}^{\widetilde{N}_{\mathrm{c}}}\sum_{i=1;i\neq k}^{K}\sum_{j=1;j\neq i,k}^{K}\frac{\sqrt{\eta_{\mathrm{c}_i}\eta_{\mathrm{c}_j}}}{\widetilde{N}}\mathbb{E}\left\{\frac{\widehat{\mathbf{g}}_{[n],i}^{\mathrm{T}}\left(\mathbf{g}_{\{[n],i\},k}^{*}\mathbf{g}_{\{[n],j\},k}^{\mathrm{T}}\right)\widehat{\mathbf{g}}_{[n],j}^{*}}{\left\|\widehat{\mathbf{g}}_{[n],i}\right\|\left\|\widehat{\mathbf{g}}_{[n],j}\right\|}\right\}=0. \tag{A.26}$$

And Term III of (4.27) is calculated as

$$\text{Term III}=\psi\mathbb{E}\left\{\sum_{n=1}^{N}w'_{[n],k}\right\}=\psi N\sigma^2 T_{\mathrm{c}}. \tag{A.27}$$

Finally, substituting the simplified expressions for Term I, II, and III from (A.22), (A.24), (A.25), (A.26), and (A.27) in (4.27), $\overline{E}_{\mathrm{c}_k}$ is given by (4.29).

A.5.2 Proof for Case (ii)

A process similar to Appendix A.5.1 is considered to evaluate the average energy $\overline{E}_{\mathrm{c}_k}$ harvested by the k^{th} sensor using (4.28) for $\widetilde{N}$ mod $\xi\neq 0$. Out of four terms in (4.28), the first term is expressed using (A.15) and (A.22) as

$$\text{Term I}=\frac{\eta_{\mathrm{c}_k}\psi P_{\mathrm{tx}}\xi T_{\mathrm{c}}}{\widetilde{N}}\mathbb{E}\left\{\sum_{n=1}^{\widetilde{N}_{\mathrm{c}}-1}\left|\frac{\mathbf{g}_{[n],k}^{\mathrm{T}}\widehat{\mathbf{g}}_{[n],k}^{*}}{\left\|\widehat{\mathbf{g}}_{[n],k}\right\|}\right|^2+\alpha^2\left|\frac{\mathbf{g}_{[\widetilde{N}_{\mathrm{c}}],k}^{\mathrm{T}}\widehat{\mathbf{g}}_{[\widetilde{N}_{\mathrm{c}}],k}^{*}}{\left\|\widehat{\mathbf{g}}_{[\widetilde{N}_{\mathrm{c}}],k}\right\|}\right|^2\right\}$$
$$=\frac{\eta_{\mathrm{c}_k}P_{\mathrm{tx}}\xi T_{\mathrm{c}}\psi}{\widetilde{N}}\left[\gamma_k\sum_{n=1}^{\widetilde{N}_{\mathrm{c}}-1}\mathbb{E}\left\{\left\|\widehat{\mathbf{h}}_{[n],k}\right\|^2\right\}+(\beta_k-\gamma_k)\sum_{n=1}^{\widetilde{N}_{\mathrm{c}}-1}\Upsilon_{[n],k}\right.$$
$$\left.+\alpha^2\left[\gamma_k\left(\mathbb{E}\left\{\left\|\widehat{\mathbf{h}}_{[\widetilde{N}_{\mathrm{c}}],k}\right\|^2\right\}\right)+(\beta_k-\gamma_k)\Upsilon_{[\widetilde{N}_{\mathrm{c}}],k}\right]\right]$$
$$=\frac{\eta_{\mathrm{c}_k}P_{\mathrm{tx}}\xi T_{\mathrm{c}}\psi}{\widetilde{N}}\left[\gamma_k\Omega_{\mathrm{c}_k}^{(\widetilde{N}_{\mathrm{c}}-1)}+(\beta_k-\gamma_k)\Upsilon_{\mathrm{c}_k}^{(\widetilde{N}_{\mathrm{c}}-1)}+\alpha^2\left[\gamma_k\Omega'_{\mathrm{c}_k}+(\beta_k-\gamma_k)\Upsilon'_{\mathrm{c}_k}\right]\right], \tag{A.28}$$

where $\Omega_{\mathrm{c}_k}^{(\widetilde{N}_\mathrm{c}-1)} = \sum_{n=1}^{\widetilde{N}_\mathrm{c}-1} \mathbb{E}\left\{\left\|\widehat{\mathbf{h}}_{[n],k}\right\|^2\right\}$ and $\Upsilon_{\mathrm{c}_k}^{(\widetilde{N}_\mathrm{c}-1)} = \sum_{n=1}^{\widetilde{N}_\mathrm{c}-1} \Upsilon_{[n],k}$ are calculated using (A.19) and (A.21), respectively with substituting $\widetilde{N}_\mathrm{c} = \widetilde{N}_\mathrm{c} - 1$. Further, $\Omega'_{\mathrm{c}_k} = \mathbb{E}\left\{\left\|\widehat{\mathbf{h}}_{[\widetilde{N}_\mathrm{c}],k}\right\|^2\right\}$ and $\Upsilon'_{\mathrm{c}_k} = \Upsilon_{[\widetilde{N}_\mathrm{c}],k}$ are calculated using (A.19) and (A.21) and are given in closed-form in (4.34) and (4.35), respectively.

For the second and third term in (4.28), the average values are evaluated using (A.24), (A.25), and (A.26) as

$$\begin{aligned}\text{Term II \& III} &= \psi P_{\mathrm{tx}}\xi T_\mathrm{c}\left[\mathbb{E}\left\{\sum_{n=1}^{\widetilde{N}_\mathrm{c}-1}\left|\sum_{\substack{i=1\\ i\neq k}}^{K}\sqrt{\frac{\eta_{\mathrm{c}_i}}{\widetilde{N}}}\frac{\mathbf{g}_{\{[n],i\},k}^{\mathrm{T}}\widehat{\mathbf{g}}_{[n],i}^{*}}{\left\|\widehat{\mathbf{g}}_{[n],i}\right\|}\right|^2\right\} + \mathbb{E}\left\{\left|\sum_{\substack{i=1\\ i\neq k}}^{K}\alpha\sqrt{\frac{\eta_{\mathrm{c}_i}}{\widetilde{N}}}\frac{\mathbf{g}_{\{[\widetilde{N}_\mathrm{c}],i\},k}^{\mathrm{T}}\widehat{\mathbf{g}}_{[\widetilde{N}_\mathrm{c}],i}^{*}}{\left\|\widehat{\mathbf{g}}_{[\widetilde{N}_\mathrm{c}],i}\right\|}\right|^2\right\}\right] \\ &= \psi P_{\mathrm{tx}}\xi T_\mathrm{c}\left[\sum_{i=1;i,\neq k}^{K}\beta_k\frac{\eta_{\mathrm{c}_i}}{\widetilde{N}}\left(\widetilde{N}_\mathrm{c}-1\right) + \alpha^2\sum_{i=1;i,\neq k}^{K}\beta_k\frac{\eta_{\mathrm{c}_i}}{\widetilde{N}}\right] \\ &= \frac{\psi P_{\mathrm{tx}}\beta_k\xi T_\mathrm{c}}{\widetilde{N}}\left[\widetilde{N}_\mathrm{c}-1+\alpha^2\right](1-\eta_{\mathrm{c}_k}). \end{aligned} \tag{A.29}$$

For the last term, the average is calculated using (A.27) as $\psi N\sigma^2 T_\mathrm{c}$.

Finally, substituting the simplified expressions for all four terms in (4.28), $\overline{E}_{\mathrm{c}_k}$ is given by (4.33).

A.6 Proof of Proposition 1

A.6.1 Proof for Case (i)

After rearranging (4.29), for the case of $\widetilde{N}$ mod $\xi = 0$, we obtain

$$\eta_{\mathrm{c}_k} = \frac{\overline{E}_{\mathrm{c}_k}^{\mathrm{i}} - \psi N\sigma^2 T_\mathrm{c} - \psi P_{\mathrm{tx}}\beta_k T_\mathrm{c}}{\frac{\psi P_{\mathrm{tx}}\xi T_\mathrm{c}\left[\gamma_k\Omega_{\mathrm{c}_k}^{\widetilde{N}_\mathrm{c}}+(\beta_k-\gamma_k)\Upsilon_{\mathrm{c}_k}^{\widetilde{N}_\mathrm{c}}\right]}{\widetilde{N}} - \psi P_{\mathrm{tx}}\beta_k T_\mathrm{c}}. \tag{A.30}$$

At the optimum solution the power constraint must be satisfied with equality, i.e., $\sum_{k=1}^{K}\eta_{\mathrm{c}_k} = 1$. This is because if $\sum_{k=1}^{K}\eta_{\mathrm{c}_k} < 1$, one can scale up η_{c_k} corresponding to every sensor by a common factor such that $\sum_{k=1}^{K}\eta_{\mathrm{c}_k}$ increases to 1 which in turn would increase the energy harvested by every sensor. This would contradict the max-min optimality of the solution. Now, taking summation on both sides of (A.30) gives

$$\sum_{k=1}^{K}\frac{\overline{E}_{\mathrm{c}_k}^{\mathrm{i}} - \psi N\sigma^2 T_\mathrm{c} - \psi P_{\mathrm{tx}}\beta_k T_\mathrm{c}}{\frac{\psi P_{\mathrm{tx}}\xi T_\mathrm{c}\left[\gamma_k\Omega_{\mathrm{c}_k}^{\widetilde{N}_\mathrm{c}}+(\beta_k-\gamma_k)\Upsilon_{\mathrm{c}_k}^{\widetilde{N}_\mathrm{c}}\right]}{\widetilde{N}} - \psi P_{\mathrm{tx}}\beta_k T_\mathrm{c}} = 1. \tag{A.31}$$

Furthermore, at the max-min optimum solution, we must have $\overline{E}_{\mathrm{c}_k}^{\mathrm{i}} = \overline{E}_{\mathrm{c}}^{\mathrm{i}}\ \forall\ k$, for some $\overline{E}_{\mathrm{c}}^{\mathrm{i}}$.

Using this fact and by simplifying (A.31), we obtain

$$\overline{E}_{\mathrm{c}}^{\mathrm{i}} = \frac{1+\sum_{j=1}^{K}\frac{\psi P_{\mathrm{tx}}\beta_j T_{\mathrm{c}}}{\frac{\psi P_{\mathrm{tx}}\xi T_{\mathrm{c}}\left[\gamma_j \Omega_{\mathrm{c}_j}^{\widetilde{N}_{\mathrm{c}}}+(\beta_j-\gamma_j)\Upsilon_{\mathrm{c}_j}^{\widetilde{N}_{\mathrm{c}}}\right]}{\widetilde{N}}-\psi P_{\mathrm{tx}}\beta_j T_{\mathrm{c}}}}{\sum_{j=1}^{K}\frac{1}{\frac{\psi P_{\mathrm{tx}}\xi T_{\mathrm{c}}\left[\gamma_j \Omega_{\mathrm{c}_j}^{\widetilde{N}_{\mathrm{c}}}+(\beta_j-\gamma_j)\Upsilon_{\mathrm{c}_j}^{\widetilde{N}_{\mathrm{c}}}\right]}{\widetilde{N}}-\psi P_{\mathrm{tx}}\beta_j T_{\mathrm{c}}}} + \psi N\sigma^2 T_{\mathrm{c}}. \tag{A.32}$$

Also, based on the fact that at the optimum, $\overline{E}_{\mathrm{c}_k}^{\mathrm{i}} = \overline{E}_{\mathrm{c}}^{\mathrm{i}}, \forall\ k$, from (A.30) we obtain

$$\eta_{\mathrm{c}_k} = \frac{\overline{E}_{\mathrm{c}}^{\mathrm{i}} - \psi N\sigma^2 T_{\mathrm{c}} - \psi P_{\mathrm{tx}}\beta_k T_{\mathrm{c}}}{\frac{\psi P_{\mathrm{tx}}\xi T_{\mathrm{c}}\left[\gamma_k \Omega_{\mathrm{c}_k}^{\widetilde{N}_{\mathrm{c}}}+(\beta_k-\gamma_k)\Upsilon_{\mathrm{c}_k}^{\widetilde{N}_{\mathrm{c}}}\right]}{\widetilde{N}} - \psi P_{\mathrm{tx}}\beta_k T_{\mathrm{c}}}. \tag{A.33}$$

Substituting $\overline{E}_{\mathrm{c}}^{\mathrm{i}}$ from (A.32) in (A.33) and after some algebraic rearrangements, the max-min power control coefficient $\overline{\eta}_{\mathrm{c}_k}$ is obtained in closed-form given in (4.54).

A.6.2 Proof for Case (ii)

After rearranging (4.33), for the case of $\widetilde{N}$ mod $\xi \neq 0$, gives

$$\eta_{\mathrm{c}_k} = \frac{\overline{E}_{\mathrm{c}_k}^{\mathrm{i}} - \psi N\sigma^2 T_{\mathrm{c}} - \frac{\psi P_{\mathrm{tx}}\beta_k \xi T_{\mathrm{c}}}{\widetilde{N}}\left(\widetilde{N}_{\mathrm{c}} - 1 + \alpha^2\right)}{\frac{\psi P_{\mathrm{tx}}\xi T_{\mathrm{c}}}{\widetilde{N}}\left[\vartheta_k - \beta_k\left(\widetilde{N}_{\mathrm{c}} - 1 + \alpha^2\right)\right]}, \tag{A.34}$$

where $\vartheta_k = \gamma_k\left(\Omega_{\mathrm{c}_k}^{(\widetilde{N}_{\mathrm{c}}-1)} + \alpha^2\Omega'_{\mathrm{c}_k}\right) + (\beta_k-\gamma_k)\left(\Upsilon_{\mathrm{c}_k}^{(\widetilde{N}_{\mathrm{c}}-1)} + \alpha^2\Upsilon'_{\mathrm{c}_k}\right)$. Following a similar process given in Appendix (A.6.1), using (A.31) and (A.32), from (A.34) we obtain

$$\overline{E}_{\mathrm{c}}^{\mathrm{i}} = \frac{1+\sum_{j=1}^{K}\frac{\psi P_{\mathrm{tx}}\beta_j \xi T_{\mathrm{c}}\left(\widetilde{N}_{\mathrm{c}}-1+\alpha^2\right)}{\psi P_{\mathrm{tx}}\xi T_{\mathrm{c}}\left[\vartheta_j-\beta_j\left(\widetilde{N}_{\mathrm{c}}-1+\alpha^2\right)\right]}}{\sum_{j=1}^{K}\frac{\widetilde{N}}{\psi P_{\mathrm{tx}}\xi T_{\mathrm{c}}\left[\vartheta_j-\beta_j\left(\widetilde{N}_{\mathrm{c}}-1+\alpha^2\right)\right]}} + \psi N\sigma^2 T_{\mathrm{c}}. \tag{A.35}$$

Furthermore, at the max-min optimum solution, we must have $\overline{E}_{\mathrm{c}_k}^{\mathrm{i}} = \overline{E}_{\mathrm{c}}^{\mathrm{i}}\ \forall\ k$, for some $\overline{E}_{\mathrm{c}}^{\mathrm{i}}$. Using this fact and by simplifying (A.34), we obtain

$$\eta_{\mathrm{c}_k} = \frac{\overline{E}_{\mathrm{c}}^{\mathrm{i}} - \psi N\sigma^2 T_{\mathrm{c}} - \frac{\psi P_{\mathrm{tx}}\beta_k \xi T_{\mathrm{c}}}{\widetilde{N}}\left(\widetilde{N}_{\mathrm{c}} - 1 + \alpha^2\right)}{\frac{\psi P_{\mathrm{tx}}\xi T_{\mathrm{c}}}{\widetilde{N}}\left[\vartheta_k - \beta_k\left(\widetilde{N}_{\mathrm{c}} - 1 + \alpha^2\right)\right]}. \tag{A.36}$$

Substituting $\overline{E}_{\mathrm{c}}^{\mathrm{i}}$ from (A.35) in (A.36) and after some algebraic rearrangements, the max-min power control coefficient $\overline{\eta}_{\mathrm{c}_k}$ is obtained in closed-form, for $\widetilde{N}$ mod $\xi \neq 0$ scenario, as given in (4.55).

Bibliography

[1] C. E. Cook and M. Bernfeld, *Radar Signals: An Introduction to Theory and Application.* Academic Press, 1967.

[2] C. Campbell, *Surface Acoustic Wave Devices and Their Signal Processing Applications.* Academic Press, 1989.

[3] M. A. Khan, R. K. Rao, and X. Wang, "Performance of multiuser MIMO communication system using chirp modulation," in *Int. Symp. Performance Evaluation of Computer and Telecommun. Systems (SPECTS)*, Jul. 2013, pp. 115–119.

[4] M. Alsharef and R. K. Rao, "M-ary chirp modulation for coherent and non-coherent data transmission," in *IEEE Canadian Conf. Electrical and Computer Engineering (CCECE)*, May 2015, pp. 213–219.

[5] T. Elshabrawy and J. Robert, "Interleaved chirp spreading LoRa-based modulation," *IEEE Internet Things J.*, vol. 6, no. 2, pp. 3855–3863, Apr. 2019.

[6] X. Wang, M. Fei, and X. Li, "Performance of chirp spread spectrum in wireless communication systems," in *IEEE Int. Conf. Commun. Systems*, Nov. 2008, pp. 466–469.

[7] Z. Popovi, E. A. Falkenstein, D. Costinett, and R. Zane, "Low-power far-field wireless powering for wireless sensors," *Proc. IEEE*, vol. 101, no. 6, pp. 1397–1409, Jun. 2013.

[8] "Cisco visual networking index: Forecast and trends, 2017-2022," *White Paper*, 2018.

[9] A. Springer, M. Huemer, L. Reindl, C. C. W. Ruppel, A. Pohl, F. Seifert, W. Gugler, and R. Weigel, "A robust ultra-broad-band wireless communication system using SAW chirped delay lines," *IEEE Trans. Microw. Theory Tech.*, vol. 46, no. 12, pp. 2213–2219, Dec. 1998.

[10] A. Hein, *Processing of SAR Data - Fundamentals, Signal Processing, Interferometry.* Verlag Berlin Heidelberg: Springer, 2004.

[11] C. Gao, K. C. Teh, A. Liu, and H. Sun, "Piecewise LFM waveform for MIMO radar," *IEEE Trans. Aerosp. Electron. Syst.*, vol. 52, no. 2, pp. 590–602, Apr. 2016.

[12] M. Y. Chua and V. C. Koo, "FPGA-based chirp generator for high resolution UAV SAR," *Prog. Electromagn. Res.*, vol. 99, pp. 71–88, Jan. 2009.

[13] D. Morgan, *Surface Acoustic Wave Filters: With Applications to Electronic Communications and Signal Processing*, 2nd ed. NewYork, NY, USA: Academic Press, 2010.

[14] C. S. Hartmann, D. T. Bell, and R. C. Rosenfeld, "Impulse model design of acoustic surface-wave filters," *IEEE Trans. Microw. Theory Tech.*, vol. 21, no. 4, pp. 162–175, Apr. 1973.

[15] S. Haykin, *Communication Systems*, 4th ed. New York: Wiley, 2001.

[16] A. Goldsmith, *Wireless Communications.* Cambridge University Press, 2005.

[17] M. I. Skolnik, *Introduction To Radar Systems*, 3rd ed. McGraw-Hill Education, 2001.

[18] Q. M. Qadir, T. A. Rashid, N. K. Al-Salihi, B. Ismael, A. A. Kist, and Z. Zhang, "Low power wide area networks: A survey of enabling technologies, applications and interoperability needs," *IEEE Access*, vol. 6, pp. 77 454–77 473, Nov. 2018.

[19] N. Dhieb, H. Ghazzai, H. Besbes, and Y. Massoud, "Scalable and secure architecture for distributed IoT systems," in *IEEE Technology Engineering Management Conference (TEMSCON)*, Jul. 2020, pp. 1–6.

[20] J. Ding, M. Nemati, C. Ranaweera, and J. Choi, "IoT connectivity technologies and applications: A survey," *IEEE Access*, vol. 8, pp. 67 646–67 673, Apr. 2020.

[21] X. Lu, P. Wang, D. Niyato, D. I. Kim, and Z. Han, "Wireless charging technologies: Fundamentals, standards, and network applications," *IEEE Commun. Surv. Tuts.*, vol. 18, no. 2, pp. 1413–1452, Nov. 2015.

[22] B. Clerckx and E. Bayguzina, "Waveform design for wireless power transfer," *IEEE Trans. Signal Process.*, vol. 64, no. 23, pp. 6313–6328, Dec. 2016.

[23] J. Xu, S. Bi, and R. Zhang, "Multiuser MIMO wireless energy transfer with coexisting opportunistic communication," *IEEE Commun. Lett.*, vol. 4, no. 3, pp. 273–276, Jun. 2015.

[24] X. Zhou, R. Zhang, and C. K. Ho, "Wireless information and power transfer in multiuser OFDM systems," *IEEE Trans. Wireless Commun.*, vol. 13, no. 4, pp. 2282–2294, Apr. 2014.

[25] S. E. El-Khamy, S. E. Shaaban, and E. A. Tabet, "Efficient multiple-access communications using multi-user chirp modulation signals," in *Int. Symp. Spread Spectrum Techniques and Applications*, Sep. 1996, pp. 1209–1213.

[26] Y. Takeuchi and K. Yamanouchi, "A chirp spread spectrum DPSK modulator and demodulator for a time shift multiple access communication system by using SAW devices," in *Proc. IEEE MTT-S Int. Microw. Symp.*, Jun. 1998, pp. 507–510.

[27] J. Pinkney, R. Behin, A. Sesay, and S. Nichols, "High-speed DQPSK chirp spread spectrum system for indoor wireless applications," *Electron. Lett.*, vol. 34, no. 20, pp. 1910–1911, Nov. 1998.

[28] A. Springer, W. Gugler, M. Huemer, R. Koller, and R. Weigel, "A wireless spread-spectrum communication system using SAW chirped delay lines," *IEEE Trans. Microw. Theory Tech.*, vol. 49, no. 4, pp. 754–760, Apr. 2001.

[29] Y. P. Lee, S. Yoo, S. Y. Kim, and S. Yoon, "Anti-jamming performance analysis of CSS-based communication systems," in *Int. Tech. Conf. on Circuits/Systems, Computers and Communications (ITC-CSCC)*, Jul. 2008, pp. 101–104.

[30] Z. Feng and J. An, "BER performance of chirp QPSK in multipath channel," in *Int. Conf. Symp. on Electronics, Communications and Control (ICECC)*, Sep. 2011, pp. 1349–1352.

[31] A. C. Pecci, C. Laot, and A. Bourre, "Quadratic chirp modulation for underwater acoustic digital communications," in *OCEANS 2015 - Genova*, May 2015, pp. 1–7.

[32] H. Shen, S. Machineni, C. Gupta, and A. Papandreou-Suppappola, "Time-varying multichirp rate modulation for multiple access systems," *IEEE Signal Process. Lett.*, vol. 11, no. 5, pp. 497–500, May 2004.

[33] E. Cheng, S. Chen, and F. Yuan, "Design and detection of multilinear chirp signals for underwater acoustic sensor networks," *Intl. Jour. Distrib. Sensor Net.*, pp. Article ID. 371 579, 1–13, May 2015.

[34] M. A. Khan, R. K. Rao, and X. Wang, "Performance of quadratic and exponential multiuser chirp spread spectrum communication systems," in *Int. Symp. Performance Evaluation of Computer and Telecommun. Systems (SPECTS)*, Sep. 2013, pp. 58–63.

[35] ——, "Non-linear trigonometric and hyperbolic chirps in multiuser spread spectrum communication systems," in *IEEE Int. Conf. on Emerging Technologies (ICET)*, Dec. 2013, pp. 1–6.

[36] M. Alsharef, A. Hamed, and R. K. Rao, "Error rate performance of digital chirp communication system over fading channels," in *World Congress on Engineering and Computer Science (WCECS)*, Oct. 2015, pp. 1–6.

[37] M. A. Khan, R. K. Rao, and X. Wang, "Closed-form error probability for M-ary chirp modulation in frequency-selective and -nonselective fading channels," in *IEEE Canadian Conf. Electrical and Computer Engineering (CCECE)*, May 2013, pp. 1–4.

[38] C. Li, X. Shen, Z. Jiang, and X. Wang, "Mobile underwater acoustic communication based on passive time reversal," in *IEEE Int. Conf. Signal Processing, Communication and Computing (ICSPCC)*, Oct. 2017, pp. 1–5.

[39] B. Liu, "Orthogonal discrete frequency-coding waveform set design with minimized autocorrelation sidelobes," *IEEE Trans. Aerosp. Electron. Syst.*, vol. 45, no. 4, pp. 1650–1657, Oct. 2009.

[40] N. Touati, C. Tatkeu, A. Rivenq, C. Thierry, and Y. El Hillali, "Multi-user radar waveforms based on doubly coded Costas signals," *IET Radar, Sonar Navigat.*, vol. 11, no. 2, pp. 277–284, Feb. 2017.

[41] H. Deng, "Discrete frequency-coding waveform design for netted radar systems," *IEEE Signal Process. Lett.*, vol. 11, no. 2, pp. 179–182, Jan. 2004.

[42] W. Mehany and L. Jiao, "Improved design of orthogonal discrete frequency-coding waveform based on modified genetic algorithm for MIMO-SAR," in *IEEE Int. Conf. Signal Processing, Communication and Computing (ICSPCC)*, Jun. 2014, pp. 341–345.

[43] G. Chang, X. Yu, and C. Yu, "Discrete frequency and phase coding waveform for MIMO radar," *Radioengineering*, vol. 26, no. 3, pp. 835–841, Sep. 2017.

[44] D. Deb, R. Bhattacharjee, and A. Vengadarajan, "Design of orthogonal waveforms for MIMO radar with phase randomised frequency hopping (FH) sequence," in *IEEE Int. Conf. on Electrical, Computer and Electronics Engineering (UPCON)*, Dec. 2016, pp. 235–238.

[45] H. A. Khan, Y. Zhang, C. Ji, C. J. Stevens, D. J. Edwards, and D. O'Brien, "Optimizing polyphase sequences for orthogonal netted radar," *IEEE Signal Process. Lett.*, vol. 13, no. 10, pp. 589–592, Sep. 2006.

[46] E. H. Kim and K. H. Kim, "Random phase code for automotive MIMO radars using combined frequency shift keying-linear FMCW waveform," *IET Radar, Sonar Navigat.*, vol. 12, no. 10, pp. 1090–1095., Oct. 2018.

[47] J. Liu, Y. Zhang, and X. Dong, "Linear-FM random radar waveform compressed by dechirping method," *IET Radar, Sonar Navigat.*, vol. 13, no. 7, pp. 1107–1115, Mar. 2019.

[48] W. Wang, "MIMO SAR OFDM chirp waveform diversity design with random matrix modulation," *IEEE Trans. Geosci. Remote Sens.*, vol. 53, no. 3, pp. 1615–1625, Mar. 2015.

[49] F. A. Qazi and A. T. Fam, "Discrete frequency-coding waveform sets based on piecewise linear FM," in *Proc. IEEE Radar Conf.*, May 2014, pp. 0469–0473.

[50] B. P. A. Rohman, R. Indrawijaya, D. Kurniawan, O. Heriana, and C. B. A. Wael, "Sidelobe suppression on pulse compression using curve-shaped nonlinear frequency modulation," in *Int. Conf. Information Technology, Information Systems and Electrical Engineering (ICITISEE)*, Aug. 2016, pp. 49–53.

[51] H. S. Mir and U. K. Thomas Wong, "Low-rate sampling technique for range-windowed radar/sonar using nonlinear frequency modulation," *IEEE Trans. Aerosp. Electron. Syst.*, vol. 51, no. 3, pp. 1972–1979, Jul. 2015.

[52] C. Gao, K. C. Teh, and A. Liu, "Frequency diversity waveform with NLFM signals," in *Int. Conf. on Information, Commun. and Signal Processing (ICICS)*, Dec. 2015, pp. 1–4.

[53] X. Lan, M. Zhang, and L. Wang, "OFDM chirp waveform design based on imitating the time-frequency structure of NLFM for low correlation interference in MIMO radar," *IEEE Geoscience and Remote Sensing Letters*, vol. 18, no. 2, pp. 286–290, Feb. 2021.

[54] T. Elshabrawy and J. Robert, "Closed-form approximation of LoRa modulation BER performance," *IEEE Commun. Lett.*, vol. 22, no. 9, pp. 1778–1781, Sep. 2018.

[55] D. Croce, M. Gucciardo, S. Mangione, G. Santaromita, and I. Tinnirello, "Impact of LoRa imperfect orthogonality: Analysis of link-level performance," *IEEE Commun. Lett.*, vol. 22, no. 4, pp. 796–799, Apr. 2018.

[56] X. Tang, H. Li, Y. Zhang, and X. Zhao, "Performance analysis of LoRa modulation with residual frequency offset," in *IEEE 4th International Conference on Computer and Communications (ICCC)*, Dec. 2018, pp. 835–839.

[57] O. Afisiadis, M. Cotting, A. Burg, and A. Balatsoukas-Stimming, "On the error rate of the LoRa modulation with interference," *IEEE Trans. Wireless Commun.*, vol. 19, no. 2, pp. 1292–1304, Feb. 2020.

[58] Y. Qian, L. Ma, and X. Liang, "Symmetry chirp spread spectrum modulation used in LEO satellite Internet of Things," *IEEE Commun. Lett.*, vol. 22, no. 11, pp. 2230–2233, Nov. 2018.

[59] ——, "The acquisition method of symmetry chirp signal used in LEO satellite Internet of Things," *IEEE Commun. Lett.*, vol. 23, no. 9, pp. 1572–1575, Jul. 2019.

[60] X. Zhou, R. Zhang, and C. K. Ho, "Wireless information and power transfer: Architecture design and rate-energy tradeoff," *IEEE Trans. Commun.*, vol. 61, no. 11, pp. 4754–4767, Nov. 2013.

[61] R. Morsi, V. Jamali, A. Hagelauer, D. W. K. Ng, and R. Schober, "Conditional capacity and transmit signal design for SWIPT systems with multiple nonlinear energy harvesting receivers," *IEEE Trans. Commun.*, vol. 68, no. 1, pp. 582–601, Jan. 2020.

[62] X. Chen, Z. Zhang, H. Chen, and H. Zhang, "Enhancing wireless information and power transfer by exploiting multi-antenna techniques," *IEEE Commun. Mag.*, vol. 53, no. 4, pp. 133–141, Apr. 2015.

[63] S. Kashyap, E. Björnson, and E. G. Larsson, "On the feasibility of wireless energy transfer using massive antenna arrays," *IEEE Trans. Wireless Commun.*, vol. 15, no. 5, pp. 3466–3480, Jun. 2016.

[64] G. Yang, C. K. Ho, R. Zhang, and Y. L. Guan, "Throughput optimization for massive MIMO systems powered by wireless energy transfer," *IEEE J. Sel. Areas Commun.*, vol. 33, no. 8, pp. 1640–1650, Aug. 2015.

[65] L. Zhao, X. Wang, and K. Zheng, "Downlink hybrid information and energy transfer with massive MIMO," *IEEE Trans. Commun.*, vol. 15, no. 2, pp. 1309–1322, Feb. 2016.

[66] D. Kudathanthirige, R. Shrestha, and G. A. Aruma Baduge, "Max-Min fairness optimal rate-energy trade-off of SWIPT for massive MIMO downlink," *IEEE Commun. Lett.*, vol. 23, no. 4, pp. 688–691, Apr. 2019.

[67] A. S. Boaventura and N. B. Carvalho, "Maximizing DC power in energy harvesting circuits using multisine excitation," in *Proc. IEEE MTT-S Int. Microw. Symp.*, Jun. 2011, pp. 1–4.

[68] D. W. K. Ng, E. S. Lo, and R. Schober, "Wireless information and power transfer: Energy efficiency optimization in OFDMA systems," *IEEE Trans. Wireless Commun.*, vol. 12, no. 12, pp. 6352–6370, Dec. 2013.

[69] W. Lu, Y. Gong, J. Wu, H. Peng, and J. Hua, "Simultaneous wireless information and power transfer based on joint subcarrier and power allocation in OFDM systems," *IEEE Access*, vol. 5, pp. 2763–2770, Feb. 2017.

[70] Y. Huang and B. Clerckx, "Large-scale multiantenna multisine wireless power transfer," *IEEE Trans. Signal Process.*, vol. 65, no. 21, pp. 5812–5827, Nov. 2017.

[71] B. Clerckx, "Wireless information and power transfer: Nonlinearity, waveform design, and rate-energy tradeoff," *IEEE Trans. Signal Process.*, vol. 66, no. 4, pp. 847–862, Feb. 2018.

[72] Y. Zeng and R. Zhang, "Optimized training for net energy maximization in multi-antenna wireless energy transfer over frequency-selective channel," *IEEE Trans. Commun.*, vol. 63, no. 6, pp. 2360–2373, Jun. 2015.

[73] G. N. Saddik, R. S. Singh, and E. R. Brown, "Ultra-wideband multifunctional communications/radar system," *IEEE Trans. Microw. Theory Tech.*, vol. 55, no. 7, pp. 1431–1437, Jul. 2007.

[74] T. Ikeda, M. Furusawa, and K. Toda, "Quadrature phase shift keying modulation and demodulation system using Rayleigh wave devices," *Jpn. J. Appl. Phys.*, vol. 29, no. 1, pp. 151–153, 1990.

[75] S. O. Haykin and M. Moher, *Modern Wireless Communications*. Prentice Hall, 2004.

[76] W. Osborne and M. Luntz, "Coherent and noncoherent detection CPFSK," *IEEE Trans. Commun.*, vol. 22, no. 8, pp. 1023–1036, Aug. 1974.

[77] M. A. Alsharef, *Constant-Envelope Multi-Level Chirp Modulation: Properties, Receivers, and Performance*. PhD thesis, The University of Western Ontario, 2016.

[78] I. S. Gradshteyn and I. M. Ryzhik, *Table of Integrals, Series, and Products*, 7th ed. San Diego, CA: Academic Press, 2007.

[79] T. Eng and L. B. Milstein, "Coherent DS-CDMA performance in Nakagami multipath fading," *IEEE Trans. Commun.*, vol. 43, no. 2, pp. 1134–1143, Apr. 1995.

[80] M. Abramowitz and I. A. Stegun, *Handbook of Mathematical Functions, with Formulas, Graphs, and Mathematical Tables*. New York: Dover Publications, Inc., 1974.

[81] X. Ouyang, O. A. Dobre, Y. L. Guan, and J. Zhao, "Chirp spread spectrum toward the Nyquist signaling rate–orthogonality condition and applications," *IEEE Signal Process. Lett.*, vol. 24, no. 10, pp. 1488–1492, Oct. 2017.

[82] S. Pei, C. Tseng, M. Yeh, and J. Shyu, "Discrete fractional Hartley and Fourier transforms," *IEEE Trans. Circuits Syst. II, Analog Digit. Signal Process.*, vol. 45, no. 6, pp. 665–675, Jun. 1998.

[83] C. Capus and K. Brown, "Short-time fractional Fourier methods for the time-frequency representation of chirp signals," *J. Acoust. Soc. America*, vol. 113, no. 6, pp. 3253–3263, Jun. 2003.

[84] M. Simon and M.-S. Alouini, *Digital Communication over Fading Channels*, 2nd ed. Wiley-Interscience, 2005.

[85] X. Xia, J. Liu, and M. Lee, "A generalized hyperbolic frequency hopping sequences," in *Proc. Int. Conf. Intelligent Signal Processing and Communication Systems*, Nov. 2004, pp. 645–647.

[86] S. Cheng, W. Wang, and H. Shao, "Spread spectrum-coded OFDM chirp waveform diversity design," *IEEE Sensors Journal*, vol. 15, no. 10, pp. 5694–5700, Jun. 2015.

[87] M. Mitchell, *An Introduction to Genetic Algorithms*. Cambridge, MA: MIT Press, 1998.

[88] Q. Wang and J. Jiang, "Performances of trigonometric chirp spread spectrum modulation in AWGN and Rayleigh channels," in *Proc. of the 8th ACM Workshop on Performance Monitoring and Measurement of Heterogeneous Wireless and Wired Networks*, Nov. 2013, pp. 203–210.

[89] S. P. Sira, A. Papandreou-Suppappola, and D. Morrell, "Dynamic configuration of time-varying waveforms for agile sensing and tracking in clutter," *IEEE Trans. Signal Process.*, vol. 55, no. 7, pp. 3207–3217, Jun. 2007.

[90] G. E. Corazza and F. Vatalaro, "A statistical model for land mobile satellite channels and its application to nongeostationary orbit systems," *IEEE Trans. Veh. Technol.*, vol. 43, no. 3, pp. 738–742, Aug. 1994.

[91] S. Nadarajah, "Explicit expressions for moments of χ^2 order statistics," *Bull. Inst. Math. Acad. Sin. (N.S.)*, vol. 3, no. 3, pp. 433–444, 2008.

[92] T. L. Marzetta, E. G. Larsson, H. Yang, and H. Q. Ngo, *Fundamentals of Massive MIMO*. Cambridge, U.K.:Cambridge Univ. Press, 2016.

[93] M. Ahsanullah, V. B. Nevzorov, and M. Shakil, *An Introduction to Order Statistics*. Paris, France: Atlantis Press, 2013.

List of Publications

Journal Publications:

- A. Roy, H. B. Nemade, R. Bhattacharjee, and V. Kushwah, "DQPSK modulation and demodulation using SAW device," *IET Commun.,* vol. 11, no. 7, pp. 2630–2636, Dec. 2017. **(Chapter 2)**
- A. Roy, H. B. Nemade, and R. Bhattacharjee, "Multiuser PSK-chirp-BOK communication system under co-channel interference," *IEEE Trans. Circuits Syst. II, Exp. Briefs,* vol. 67, no. 3, pp. 465–469, Mar. 2020. **(Chapter 2)**
- A. Roy, H. B. Nemade, and R. Bhattacharjee, "Radar waveform diversity using nonlinear chirp with improved sidelobe level performance," *AEÜ−International Journal of Electronics and Communication* vol. 136, pp. 153768, Jul. 2021. **(Chapter 3)**
- A. Roy, H. B. Nemade, and R. Bhattacharjee, "Symmetry chirp modulation waveform design for LEO satellite IoT communication," *IEEE Commun. Lett.,* vol. 23, no. 10, pp. 1836–1839, Oct. 2019. **(Chapter 3)**

Conference Publications:

- A. Roy, H. B. Nemade, and R. Bhattacharjee, "A chirp communication system using SAW-chirp devices for multibit symbol transmission," in *IEEE Region 10 Conference (TENCON)*, Oct. 2019, pp. 1466–1471. **(Chapter 2)**
- A. Roy, H. B. Nemade, and R. Bhattacharjee, "Performance of multiuser communication system using phase coded linear chirp modulation," in *National Conference on Communications (NCC)*, Mar. 2017, pp. 1–6. **(Chapter 2)**
- A. Roy, H. B. Nemade, and R. Bhattacharjee, "Phase coded nonlinear chirp modulation in multiuser communication systems," in *International Conference on Innovations in Electronics, Signal Processing and Communication (IESC)*, Apr. 2017, pp. 89–94. **(Chapter 2)**

- A. Roy, S. Sen, H. B. Nemade, and R. Bhattacharjee, "Multiuser communication using chirp signals of equal chirp rate," in *National Conference on Communications (NCC)*, Feb. 2018, pp. 1–6. **(Chapter 2)**

- A. Roy, D. Deb, H. B. Nemade, and R. Bhattacharjee, "Design of discrete frequency-coding waveforms using phase-coded linear chirp for multiuser and MIMO radar systems," in *National Conference on Communications (NCC)*, Feb. 2019, pp. 1–6. **(Chapter 3)**

Manuscripts Under Preparation:

- A. Roy, S. Kashyap, and R. Bhattacharjee, "Wireless energy transfer over OFDM with superposed chirp employing joint subband selection and max-min power control," to be submitted in *IEEE Transactions on Communications*. **(Chapter 4)**

Bio-Data

1	Name:	Arijit Roy
2	Educational Qualification:	June-2011, B.Tech. in Electronics and Communication Engineering (8.66/10 CGPA), RCC Institute of Information Technology, Kolkata, West Bengal, India June-2013, M.Tech. in Communication Engineering (8.42/10 CGPA), Indian Institute of Technology Guwahati, Guwahati, Assam, India May-2021, PhD (Thesis Submitted), Indian Institute of Technology Guwahati, Guwahati, Assam, India
3	Permanent Address:	6, Vivekananda Road Kalianivas East Post: Nona Chandan Pukur District: North 24 Parganas West Bengal, India Pincode-700122
4	Contact Address:	Communication Lab 2, Dept. of EEE, Indian Institute of Technology Guwahati, Guwahati, Assam, India Pincode-781039
5	Contact Number:	(+91)-7002020683